The Role of Protostellar Heating in Star Formation

Michael O. Jones

Submitted by Michael Oliver Jones to the University of Exeter as a thesis for the degree of Doctor of Philosophy in Physics, Monday 18th June 2018.

I certify that all material in this thesis which is not my own work has been identified and that no material has previously been submitted and approved for the award of a degree by this or any other University.

Signed: .....
Michael Oliver Jones

Date: .....

Abstract

Previous studies have shown that thermal feedback from protostars plays a key role in the process of low-mass star formation. In this thesis, we explore the effects of protostellar heating on the formation of stellar clusters. We describe new methods for modelling protostellar accretion luminosities and protostellar evolution in calculations of star formation. We then present results of a series of numerical simulations of stellar cluster formation which include these effects, and examine their impact.

We begin by investigating the dependence of stellar properties on the initial density of molecular clouds. We find that the dependence of the median stellar mass on the initial density of the cloud is weaker than the dependence of the thermal Jeans mass when radiative effects are included. We suggest that including protostellar accretion luminosities and protostellar evolution may weaken this dependence further, and may account for the observed invariance of the median stellar mass in Galactic star-forming regions.

Next, we investigate the effects of including accretion feedback from sink particles on the formation of small stellar groups. We find that including accretion feedback in calculations suppresses fragmentation even further than calculations that only include radiative transfer within the gas. Including feedback also produces a higher median stellar mass, which is insensitive to the sink particle accretion radius used.

Finally, we compare calculations of small stellar clusters which model the evolution of protostars using a live stellar model with those which use a fixed stellar structure. We find that the dynamics of the clusters are primarily determined by the accretion luminosities of protostars, but that the relative effects of protostellar evolution depend on the accretion rate and advection of energy into the protostar. We also demonstrate how such calculations may be used to study the properties of young stellar populations.

Declaration of Authorship

Portions of this thesis have been published in peer-reviewed papers or are being prepared for publication. The content of Chapter 4 and Section 1.3 of Chapter 1 is derived from the paper 'The dependence of stellar properties on initial cloud density' which has been published in the *Monthly Notices of the Royal Astronomical Society* in 2018. The content of Chapter 5 and Sections 1.4 of Chapter 1 and 3.2 of Chapter 3 is derived from the paper 'Sink particle radiative feedback in smoothed particle hydrodynamics models of star formation' which has been accepted for publication in the *Monthly Notices of the Royal Astronomical Society* in 2018. The content of Section 3.2.1 was originally written by Matthew R. Bate. All other published content was written by the author of this thesis.

Contents

List of Figures

List of Tables

Acknowledgements

First and foremost, I would like to thank my supervisor, Professor Matthew R. Bate, without whose guidance and considerable patience this thesis would not have been possible. I would also like to thank Professor Tim J. Harries for his supervision during the spring and summer of 2017; Dr. Ben Lewis and Dr. James Wurster for their many insights into programming and the minutiae of SPH; Dr. Felix Sainsbury-Martinez for his assistance with the formatting of this thesis; and my friends and colleagues in the Astrophysics Group at the University of Exeter for all of their help and advice.

Finally, I would like to thank my family, whose love and support has sustained me throughout the entire process.

Michael Oliver Jones
Exeter, United Kingdom
Friday 15th June 2018

"And there were all the stars, looking remarkably like powdered diamonds spilled on black velvet, the stars that lured and ultimately called the boldest towards them...

The whole Creation was waiting for Rincewind to drop in.

He did so.

There didn't seem to be any alternative."

Terry Pratchett, ***The Colour of Magic***

Chapter 1

Introduction

Throughout human history, stars have been an enduring fixture in the night sky. Their nature, positions and arrangements were of great importance to many of the earliest civilisations, who used them for navigation and farming, and imbued them with a religious and cultural significance. During the scientific revolution, the advent of the telescope in the early 17th Century made it possible to study stars and planets in intimate detail, giving rise to the scientific discipline of astronomy as it exists today. As such, stars are quite possibly the most well studied celestial phenomenon in the history of astronomy. Despite this, many questions still exist regarding their formation and evolution.

Aristotle's seminal work 'On the Heavens' (Greek: Περὶ οὐρανοῦ, Latin: *De Caelo*) dominated intellectual thought on the nature of the universe for much of the last two millennia. However, it was only one of many theories proposed to describe the cosmos. While the Aristotelian theory viewed the realms beyond the Earth as being composed of perfect and eternal heavenly spheres, many other rudimentary cosmologies envisaged universes that were chaotic and ever-changing. Modern scientific understanding has perhaps more in common with these alternative theories, describing a universe that is deeply intricate but also highly dynamic. Such a description is particularly apt for the process of star formation, which involves myriad phenomena across a vast range of scales, both temporal and spatial.

A long standing goal of theoretical astrophysics is the construction of a complete theory of star formation. **Such a theory would unite the seemingly disparate galactic and stellar and scales, and allow us to view them as a comprehensive whole.** The sequence of events that leads to the formation of stars begins long before the collapse of the pre-stellar core, and at scales far larger than the typical size of a protostar. Vast complexes of clouds, filaments and cavities interact with one another, forming clusters which eventually give rise to the stars we observe. Herein lies the challenge in constructing theories of star formation. A complete theory must not only account for the properties of individual protostars, but also those of the systems in which they form. To do so, the mechanisms

governing each stage of star formation must be considered.

1.1 Molecular clouds

Observational surveys find that the sites of star formation across the Milky Way galaxy and throughout the universe are correlated with the presence of molecular gas (Kennicutt 1989, 1998). This gas is primarily found in structures known as molecular clouds. First predicted to exist by Spitzer (1949), molecular clouds are dense regions of the interstellar medium (ISM) comprised primarily of molecular hydrogen (H_2), as well as helium and ionised hydrogen (Fukui and Kawamura 2010).

H_2 forms in the ISM predominantly through surface interactions with dust grains (McCrea and McNally 1960; Gould and Salpeter 1963; Wakelam et al. 2017). Due to the lack of a permanent electric dipole, H_2 spectral lines are often difficult to observe. Instead, the presence of molecular hydrogen is commonly inferred from the presence of 'tracers'. These are other atomic or molecular gases present in the ISM which typically form in the same regions as molecular hydrogen. A commonly used tracer for molecular hydrogen is carbon monoxide (CO), although other tracers such as hydrogen cyanide (HCN), ammonia (NH3) and carbon monosulphide (CS) exist, and can be used to reveal different structures, such as active sites of star formation (see Myers et al. 1983; Snell et al. 1984).

The first CO maps of the galactic plane showed that large regions of molecular gas, known as giant molecular clouds (GMCs) extend over significant portions of the ISM (Lada 1976; Blair et al. 1978; Blitz and Thaddeus 1980), and contribute significantly to its total mass (Scoville and Solomon 1975; Gordon and Burton 1976). At the largest scales (> 100 pc), these clouds may form structures known as giant molecular associations (GMAs), which are complexes composed of many GMCs. Smaller (~ 10 pc) molecular clouds also exist, and are often found within these larger complexes.

The masses of molecular clouds range from small clouds of approximately ~ 100 $M_\odot$, to large GMCs containing as much as $\sim 10^7$ $M_\odot$, although the observed mass spectrum of molecular clouds implies that most of the molecular gas mass in the galaxy is contained within the largest GMCs. Small clouds are often found at high galactic latitudes (Magnani et al. 1985) and in the outer regions of the galactic disc (Brand and Wouterloot 1995; Heyer et al. 2001), **whereas GMCs are most commonly found within the spiral arms of the Galactic disc, as well as other regions of high density such as the central molecular zone (Oka et al. 2001); a large region of molecular gas near the centre of the Galaxy, and the Gould Belt; a partial ring of stars and gas inclined relative to the Galactic plane (André et al. 2010).**

1.1.1 Molecular cloud formation

The processes that give rise to the formation of molecular clouds are a matter of some debate. Several mechanisms have been proposed, which apply over different spatial and temporal scales, and may therefore dominate in different environments. All of these processes ultimately result in the generation of a compressive velocity field, raising the density of a region of the ISM substantially to form a molecular cloud.

Stellar feedback processes, such as expanding H II regions (Bania and Lyon 1980; Vazquez-Semadeni et al. 1995) and supernovae (McCray and Kafatos 1987; de Avillez and Mac Low 2001) may give rise to localised converging flows. The colliding gas in these flows then forms a turbulent, high-density region. As the density of the gas increases, molecular cooling in the ISM becomes important, allowing the region to form a molecular cloud. This process is thought to be important on scales of ~ 100 pc (Clark et al. 2012).

Gravitational instabilities driven by perturbations in the galactic disc may also play a role in the formation of molecular clouds (Goldreich and Lynden-Bell 1965; Julian and Toomre 1966). The dense gas contained within the spiral arms of the galaxy is more susceptible to these instabilities than the relatively sparse inter-arm regions. The gas contained within the spiral arms is shocked and compressed, triggering the formation of molecular clouds (Kim and Ostriker 2002, 2006). Dobbs et al. (2008) have argued that the compressions caused by these shocks may in fact be strong enough to form molecular clouds even in regions where the gas density is low.

Collisions between small clouds may also occur as the spiral arm density wave travels around the galactic disc. Clouds falling into the arm potential collide with each other, and amalgamate to form much larger clouds than those formed by localised converging flows. The collision rate between clouds is higher in regions of high density, and increased by the mutual gravitational attraction of massive clouds, allowing for the quick accumulation of mass (Casoli and Combes 1982; Kwan and Valdes 1983; Dobbs et al. 2008). Dobbs and Price (2008) have suggested that the presence of magnetic fields may act to suppress these collisions. Similar collisions have also been postulated to occur in high surface density galaxies with no spiral structure (Tasker and Tan 2009).

Other more complex mechanisms that have been proposed include magneto-Jeans instabilities (Lynden-Bell 1966; Elmegreen 1987; Gammie 1996; Kim and Ostriker 2001), in which magnetic tension acts against Coriolis forces in low-shear discs which otherwise help to suppress gravitational instabilities, and Parker instabilities (Mouschovias 1974; Mouschovias et al. 1974; Blitz and Thaddeus 1980), caused by the buckling of magnetic field lines in the ISM driven by the differential buoyancy of ISM material in the Galactic gravitational field, which results in the build up of dense gas in the Galactic mid-plane. However, due to their complexity and dependence on less well-constrained

properties of the ISM, such as the magnetic field strength, their relative importance is not clear.

1.1.2 Properties of molecular clouds

The internal properties of molecular clouds were first described by Larson (1981) in terms of several scaling relations. These relations have been subsequently confirmed by observational surveys (Solomon et al. 1987), and appear to be nearly universal amongst observed clouds. Larson's relations can be summarised as follows:

- The interiors of molecular clouds exhibit velocity fields which follow a dispersion relation of the form $\sigma_v \propto L^{0.38}$, where σ_v is the velocity dispersion and L is the size of the cloud. Larson noted the similarity of this behaviour to subsonic turbulence, which is described by the Kolmogorov law $\sigma_v \propto L^{1/3}$, and concluded that the steeper power law was consistent with a supersonic turbulent velocity field dissipating energy through shocks.

- Molecular clouds are gravitationally bound, and in approximate Virial equilibrium, such that $\sigma_v^2 \approx 2GM/L$, **where M is the mass of the cloud**. This is exact for polytropes of $n = 2$, and within factor of ~ 2 for most cloud shapes and density distributions.

- The previous two relations imply that smaller clouds must be more dense in order to remain gravitationally bound, such that their average density, expressed in terms of the number of H_2 molecules per cubic centimetre, $n(H_2)$, scales with the cloud size L as $n(H_2) \propto L^{-1.1}$. This implies that the column density of molecular clouds is almost independent of their size (Heyer et al. 2009).

1.2 Star formation in clusters

The number of multiple star systems in the galaxy is observed to be similar to the number of individual stars (Duquennoy and Mayor 1991). **In order to produce these systems, stars must form and evolve in close proximity to one another.** This requires either that stars form together in star-forming clusters, or that individual pre-stellar cores frequently become unstable to fragmentation and subsequently form multiple objects. Observations of molecular clouds in the Milky Way show that the former case is representative of the vast majority of star formation (Lada et al. 1991; Lada 1999), with an estimated 50-95% of all stars being formed within these clusters.

Star-forming clusters usually contain > 100 objects forming together within a region < 1 pc in size (Clarke et al. 2000). The shared environments and close proximities of

protostars in these clusters mean that they typically form and interact with each other on similar timescales. As such, the formation and evolution of protostars is heavily influenced by the properties of their parent clusters (Chapman et al. 1992; Bonnell et al. 1997; Bate et al. 2002b).

1.2.1 Star-forming cores

The interiors of molecular clouds are highly inhomogeneous, containing filaments, sheets and clumps with a wide range of sizes and morphologies (Blitz 1993; Wiseman and Ho 1996; Bally 1996; André et al. 2010; Hill et al. 2011; André et al. 2014). The densest of these structures may become self-gravitating and unstable to collapse. The resultant high-density regions are often referred to as 'cores'. Numerical models of star formation show that the turbulent fragmentation of these dense cores gives rise to hierarchical, filamentary structures (Bonnell et al. 1991; Bate et al. 1995; Truelove et al. 1998; Klessen et al. 1998; Klessen and Burkert 2000), similar to those seen in observations of nearby star-forming regions, such as the Serpens molecular cloud (Testi et al. 2000).

The formation and evolution of these dense cores is governed primarily by the turbulent motions of the molecular cloud interior. The supersonic turbulent velocity field of the molecular gas results in filamentary structure. Shocks and compressions form where the filaments interact, dissipating energy and allowing local regions to collapse while the cloud remains globally supported. The turbulence decays on a timescale similar to the dynamic timescale of cloud as a result of this dissipation (Mac Low et al. 1998). The converging gas flows produced by these compressions form high-density, star-forming cores. As such, the formation times and locations of these cores, as well as there resultant properties, are highly dependent on the dynamics of the cluster gas (Klessen and Burkert 2000; Bate et al. 2003). The subsequent gravitational collapse of these cores produces filaments which then fragment to form protostars (Boss and Bodenheimer 1979; Bastien 1983; Boss 1986; Bastien et al. 1991; Inutsuka and Miyama 1992).

1.2.2 The Jeans instability

In the case of a purely hydrodynamical system, the typical size of a region that will collapse to form a protostar is described by the Jeans length (Jeans 1902). **The Jeans length is defined by the minimum size of a pressure-supported sphere of gas embedded in uniform density medium which is stable against gravitational collapse. This can be derived by considering the time, t_s, taken for a sound wave to cross the sphere:**

$$t_s = \frac{R}{c_s}, \tag{1.1}$$

where R is the radius of the sphere and c_s is the sound speed of the gas. This can be compared with the gravitational free-fall time of the sphere, t_{ff}, (i.e. the time taken for the sphere to gravitationally collapse so that $R \rightarrow 0$), which is given by

$$t_{ff} = \frac{1}{\sqrt{G\rho}}, \tag{1.2}$$

where ρ is the gas density and G is the gravitational constant. The sphere will maintain a constant radius as long as any perturbations are restored by a pressure wave crossing the sphere. This can be expressed by the inequality $t_s < t_{ff}$. Therefore, the smallest sphere stable against perturbations in radius is described by $t_s = t_{ff}$, or equivalently

$$\frac{R}{c_s} = \frac{1}{\sqrt{G\rho}}. \tag{1.3}$$

This can be rearranged to give the standard expression for the Jeans length, λ_{Jeans}

$$\lambda_{\rm Jeans} = \frac{c_s}{\sqrt{G\rho}}. \tag{1.4}$$

The corresponding mass of this sphere is given by the Jeans mass, $M_{\rm J}$

$$M_{\rm Jeans} = \frac{4}{3}\pi\lambda_{\rm J}^3\rho. \tag{1.5}$$

Equations 1.2.2 and 1.2.2 represent the Jeans length and Jeans mass as originally derived by Jeans (1902). However, since the Jeans length is an expression of the pressure balance within a sphere of gas, there may be other types of Jeans lengths and Jeans masses corresponding to different sources of pressure, such as the magnetic Jeans mass and the turbulent Jeans mass. These quantities may vary, depending on the strength of the relevant pressure fields. In light of these additional quantities, the original Jeans mass is usually referred to as the thermal Jeans mass, as it is derived using the thermal pressure.

It should be noted that equations 1.2.2 and 1.2.2 apply only for the case of an isothermal gas. During the collapse of a fragment to form a protostar, the temperature of the sphere will increase due to compressional heating and radiative heating from the shock which forms where the accretion flow meets the protostellar surface. This will increase the corresponding Jeans mass. We shall return to this idea in our discussion of the dependence of the median stellar mass on cloud density in Chapter 4.

1.2.3 Core fragmentation & cluster formation

In contrast to the suggestion of Shu et al. (1987) that stars form in isolation due to perturbations of gravitationally unstable regions, the collapse of dense cores is triggered predominantly by external factors such as shocks **(1989MNRAS.239..361P1992Natur.359..207C)**. These shocks and compressions transform cores of approximately 1 M_{Jeans} into clumps containing multiple Jeans masses on time scales similar to the core dynamic time. This results in a highly inhomogeneous collapse, which occurs simultaneously in multiple regions.

The fragmentation of cores into several objects results in the creation of multiple protostars in close proximity to one another. The protostars then competitively accrete from the shared gas reservoir (Zinnecker 1982; Price and Podsiadlowski 1995; Bonnell et al. 1997). **Evidence of this has been found in observations of young stellar clusters, which find a correlation between the number of stars in a cluster and the mass of the most massive star contained within it (Weidner and Kroupa 2006), suggesting that the number of accreting objects affects their final masses. André et al. (2007) suggest that the spectrum of masses in young clusters may be determined by a combination of turbulent fragmentation in the pre stellar phase and subsequent growth of fragments via competitive accretion prior to the formation of protostars.** Competitive accretion from a common reservoir requires that the fragmentation process be relatively inefficient, such that a significant fraction of the core mass is not contained within the protostars (Bonnell et al. 2001). **This has been observed in pre-stellar systems and young stellar clusters, where the majority of the total mass is contained within the gas (Johnstone et al. 2000; Lada and Lada 2003; Johnstone et al. 2004; Bastian and Goodwin 2006).**

Fragments and newly formed protostars may also interact gravitationally with one another. Encounters can lead to the formation of unstable multiple systems which may decay, ejecting protostars and terminating their accretion (Klessen et al. 1998). Objects resembling T-Tauri stars found in X-ray observations of surroundings of star-forming regions (Neuhaeuser et al. 1995; Wichmann et al. 1997) may be candidates for these ejected objects. Dynamic encounters may also truncate accretion discs, reducing the final masses of protostars (Bonnell et al. 2003). Conversely, Bonnell et al. (1997) found that the increased gravitational potential of stable multiple systems may outweigh the increased competition for accretion of the gas reservoir, leading to higher protostellar masses than those accreting individually.

Following fragmentation of the core, the newly formed protostars fall together into their mutual potential well, forming a small stellar cluster (Bate et al. 2003). Similar structures have been observed in local star-forming regions such as the Ophiuchus-F (see Motte et al. 1998) and Taurus (see Herbig 1977; Gomez et al. 1993) regions. The initial accretion of mass by the protostars is rapid, due to acceleration of the gas to supersonic velocities

during infall, and replenishment by the further infall of gas. The rate at which the gas is replenished depends on both the protostellar gravity and the dynamics of the surrounding cluster. This leads to accretion rates which are highly non-uniform (Bonnell et al. 1997). The accretion of gas onto the protostars removes kinetic energy from the cluster, increasing its binding energy through a process known as mass loading. This increase in binding energy may also occur via gravitational drag on protostars as they move through the cluster medium, in a process known as gas drag, decelerating them and allowing gas to be accreted via the Bondi-Hoyle process (Bonnell et al. 1997). The result is a gravitationally bound cluster of protostars, accreting from a shared gas reservoir and interacting with each other via gravitational dynamics.

1.3 Predicting the properties of star clusters

Any complete theory of star formation must account not only for the properties and dynamics of individual stellar systems, but also for the distributions of stellar properties and the behaviour of these systems as part of larger ensembles. Many statistical properties must be explained, such as the star formation rate and efficiency, the relative numbers of binary and multiple systems as well as the structure and kinematics of the clusters in which star formation takes place. The advent of high resolution numerical models and large surveys has made it possible to study the properties of entire star-forming regions, whereas previous studies had been limited to much smaller systems.

1.3.1 Modelling star-forming clusters

When attempting to predict the properties of systems as complex as star clusters, a natural approach is to use numerical models. The majority of these calculations fall into two broad categories, based on their methods for generating the statistical populations of stars. The first method for generating stellar populations is to model the formation of stars in an ensemble of dense cores, and combine the resultant populations to create a larger sample (Delgado-Donate et al. 2004; Goodwin et al. 2004b, 2004a, 2004c, 2006; Stamatellos et al. 2007; Stamatellos and Whitworth 2009). This approach suffers from two major drawbacks, however. First, the initial mass distribution of cores must be specified. Although this may be chosen from a mass distribution based on observations of dense cores, the choice of sample will inevitably be somewhat arbitrary. Second, interactions between the cores and their surrounding environments are not modelled. These interactions include the growth of cores via accretion, and dynamic interactions between cores, both of which may significantly alter their properties.

An alternative method is to simulate an entire star-forming cloud in a single calculation. Increases in the computing power of modern high-performance computing (HPC) systems

have allowed such calculations to produce stellar populations large enough to study their statistical properties. This approach solves both of the issues with the ensemble method, as the cores are formed dynamically from large-scale motions in the parent molecular cloud, generating the distribution of core masses self-consistently and modelling the interactions between cores and their environments.

1.3.2 The initial mass function

Many early star formation calculations focused on reproducing the observed distributions of masses in star-forming clusters, commonly referred to as the initial mass function (IMF). Surveys of nearby star-forming regions have suggested that the IMF of young clusters is approximately constant, despite significant variations in their environmental conditions (Bastian et al. 2010). Salpeter's seminal paper on the distribution of stellar masses (Salpeter 1955) provided the first estimate of the form of the general IMF in Galactic star forming regions, expressing it as the power law

$$\xi(\log M) = \xi_0 M^{-1.35} \tag{1.6}$$

where ξ_0 is a normalisation factor related to the local stellar density. Modern observational studies have found that while this form provides a good approximation of the mass function at higher masses ($M > 1\ \mathrm{M}_\odot$), it over-estimates the number of brown dwarfs. Instead, a number of more complex mass functions have been proposed, which combine the Salpeter mass function at higher stellar masses with a function which decreases for lower masses. Commonly used parameterisations of this type are the Kroupa (2001) piecewise power-law IMF:

$$\xi(\log M) = \begin{cases} \xi_0 M^{0.7}, & \text{if } M \leq 0.08\ \mathrm{M}_\odot \\ \xi_0 M^{-0.3}, & \text{if } M \leq 0.5\ \mathrm{M}_\odot \\ \xi_0 M^{-1.3}, & \text{if } M > 0.5\ \mathrm{M}_\odot \end{cases} \tag{1.7}$$

and the Chabrier (2005) log-normal IMF:

$$\xi(\log M) = \begin{cases} \xi_0 \exp\left[-\frac{(\log M - \log 0.2)^2}{2\times 0.55^2}\right], & \text{if } M \leq 1\ \mathrm{M}_\odot \\ \xi_0 M^{-1.35}, & \text{if } M > 1\ \mathrm{M}_\odot \end{cases} \tag{1.8}$$

Bonnell et al. (1997) performed calculations of the formation of small stellar clusters beginning with protostars embedded within a gas reservoir, and found that the distribution of stellar masses within the clusters was primarily determined by the accretion histories of the protostars. The accretion histories of protostars were found to be dependent upon a number of factors, including their positions within the cluster potential, dynamic interactions with other protostars, and competitive accretion. Stars near the centre of the cluster potential were found to accrete at enhanced rates, allowing them to competitively accrete

more of the available cluster gas and obtain higher masses (see also Bonnell and Bate 2006). This coupled with the truncation of accretion discs or ejection of objects though dynamical interactions produced a distribution of protostellar masses within the cluster. Klessen et al. (1998) performed similar calculations, **and found that the fragmentation of Jeans unstable clumps into objects which subsequently evolve through accretion and dynamic interactions produced star clusters whose mass functions and multiplicities were qualitatively similar to observations of star clusters.** These calculations also confirmed the finding of Bonnell et al. (1997) that higher mass protostars formed predominantly near the centre of clusters due to the enhancement of accretion rates by the cluster potential.

1.3.3 Multiple systems

As mentioned in Section 1.2, the majority of stars form in clusters, with the number of multiple star systems being similar to the number of individual stars (Duquennoy and Mayor 1991). As such, many of the first calculations of star formation were motivated by the desire to reproduce the observed properties of binary and multiple systems. The possible ways in which the fragmentation of turbulent cores may give rise to observed binary properties were initially discussed by Pringle (1989b), Clarke and Pringle (1991), and McDonald and Clarke (1995).

Observations made by Duquennoy and Mayor (1991) using a range of techniques illustrated many of the basic properties of multiple systems. They found that separations ranged from a few solar radii to $\sim$ 10000 AU. The frequency of systems with low mass ratios was found to be higher than those with higher ratios, except for close binaries, which exhibited a flatter distribution of ratios. **More recent studies of multiple systems have confirmed these properties across a range of mass scales (Fischer and Marcy 1992; Patience et al. 2002; Basri and Reiners 2006; Mason et al. 2009; Raghavan et al. 2010).**

However, as these observations were of main-sequence stars, it was unclear how they might relate to the properties of pre-main-sequence systems. Mathieu (1992) and Reipurth and Zinnecker (1993) and Leinert et al. (1993) suggested that the properties of pre-main-sequence systems may be similar to those of main-sequence systems, implying that they are determined early in the star formation process. **However, later studies showed that the multiplicity of young clusters is often higher than those of older clusters (Duchêne 1999; Duchêne et al. 2004, 2007; Connelley et al. 2008; Tobin et al. 2016).**

Early calculations by Chapman et al. (1992) showed that multiple systems form naturally from the fragmentation of dense regions produced by compressive, radiative shocks that result from supersonic turbulence in molecular clouds. Subsequent calculations showed that the fragmentation of massive circumstellar discs which form around the first protostars also provides a significant source of multiple systems (Bonnell 1994; Bate and Bonnell 1994; Burkert et al. 1997).

Bonnell et al. (1997) examined the properties of the multiple systems formed in groups. They found that the dynamics of these small clusters resulted in binary systems composed of more massive stars, as less massive stars were more prone to ejections in dynamic encounters. Accretion was found to produce binaries with much smaller separations by removing angular momentum from multiple systems making them more stable (see also Bate 1997; Bate and Bonnell 1997). They also found that the mass ratios of systems were largely determined by their initial ratios, in agreement with the suggestion of Mathieu (1992), Reipurth and Zinnecker (1993) andLeinert et al. (1993) that these properties are determined early during the formation of systems. The formation of circumstellar and circumbinary discs was investigated by Bate and Bonnell (1997), and was found to depend on the ratio of the angular momentum of accreted material and that of the components of binary system and the total angular momentum of the system. The mass ratios and separations of systems were also found to depend on similar mechanisms.

1.3.4 Resolving the opacity limit

Early calculations of the formation of stellar groups and clusters used sink particles with large accretion radii (~ 100 AU) to model stars, inhibiting the formation of low-mass stars and brown dwarfs and obscuring the properties of most binaries and discs. Many recent calculations have continued to use sink particles of this size due to computational resource constraints. However, to fully investigate the properties of individual stars and multiple systems, the opacity limit for fragmentation (Low and Lynden-Bell 1976; Rees 1976) must be resolved. The opacity limit defines the minimum possible mass of fragments, and depends upon the metallicity and opacity of the gas. Below this limit, the gas becomes optically thick **to infrared radiation** at the densities required for a fragment to be unstable to gravitational collapse. This inhibits cooling of the fragment, providing thermal pressure support which prevents gravitational collapse.

The first simulations to resolve this limit were those of Bate et al. (2002a, 2002b, 2003). These calculations used a combination of hydrodynamics and gravitational dynamics with a barotropic equation of state, and produced clusters with properties broadly similar to observed systems, but which contained too many brown dwarfs, producing more brown dwarfs than stars. Jappsen et al. (2005) performed calculations using a piecewise polytropic equation of state, and suggested that the median stellar mass may be determined by the critical density at which the dominant mode of cooling switches from molecular cooling to thermal cooling. However, later calculations by Bate and Bonnell (2005) and Bonnell et al. (2006) using the same method as Bate et al. (2002a, 2002b, 2003) found instead that the characteristic (median) stellar mass of the clusters was linearly proportional to the thermal Jeans mass of the initial molecular cloud.

Further calculations performed by Bonnell et al. (2006) using an isothermal equation of

state confirmed this, and showed that the number of objects formed scaled approximately with the number of Jeans masses in the initial cloud. They also found that the 'knee' in stellar mass distribution, where the Salpeter power-law distribution for higher masses meets the log-normal form of the mass distribution for lower mass objects, was located approximately at the same mass as the initial thermal Jeans mass of cloud. This was also true in calculations performed by Bate (2009a). These calculations produced clusters whose binary properties, including the multiplicity as a function of primary mass, the frequency of very-low-mass (VLM) binaries, and distributions of separations, mass ratios and orbital orientations were in good agreement with observations, but which still contained too many brown dwarfs.

In addition to varying the initial thermal Jeans mass of the parent molecular clouds, several studies have investigated the effects of variations in other environmental factors on the statistical properties of star-forming clusters using calculations which resolved the opacity limit for fragmentation. Bate (2005) raised the opacity limit by lowering the density at which the gas becomes optically thick, and showed that raising the minimum fragment mass, as defined by opacity limit, did not affect distribution of stellar masses. Instead, median mass varied with thermal Jeans mass of initial cloud, as in the calculations of Bate et al. (2002a, 2002b, 2003), Bate and Bonnell (2005), and Bonnell et al. (2006) and Bate (2009a). Clark et al. (2008) varied the amount of kinetic energy initially contained within the molecular clouds. They found that the distribution of stellar masses may 'flatten', i.e. contain a more even distribution of masses, if the cloud becomes unbound. This increased parity of stellar masses suppressed the effects of competitive accretion, maintaining the shape of the distribution. Bate (2009b) also investigated the effects of the turbulent velocity field within molecular clouds, but varied the index of the turbulent velocity power spectrum from $P(k) \propto k^{-4}$ to $P(k) \propto k^{-6}$, where k is the wave number, biasing the velocity field in favour of large-scale motions. The properties of the resulting clusters were indistinguishable, suggesting that the properties of clusters are insensitive to the large scale structure of molecular clouds. More recent calculations performed by Bertelli Motta et al. (2016) and Liptai et al. (2017) yielded similar results.

1.4 Protostellar feedback in star formation

Many different forms of feedback have been shown to play a role in the star formation process. These include kinetic feedback processes, such as jets (Frank et al. 2014), winds (Lamers and Cassinelli 1999), and supernovae (Ostriker and McKee 1988), as well as radiative feedback processes in the form of photo-ionisation (Osterbrock and Ferland 2006), radiation pressure (Krumholz and Matzner 2009), and radiative heating (Offner et al. 2009; Bate 2009c)

Whilst often ignored on large scales due to the efficient cooling of low density gas,

radiative heating has been shown to be very important in the formation of low-mass stars. Several studies, most notably those of Bate (2009c, 2012) and Offner et al. (2009), have shown that the over-production of brown dwarfs can be overcome by including the effects of radiative feedback in calculations. The inclusion of radiative heating in these calculations inhibited fragmentation by providing additional thermal support, preventing the collapse of fragments which would otherwise have led to the production of low-mass objects. Bate (2012) confirmed this with the largest calculation to date to include radiative heating and resolve the opacity limit. Using a combination of hydrodynamics, radiative transfer and gravitational dynamics, the calculation produced a stellar population whose statistical properties, including the star to brown dwarf ratio, were in good agreement with observations.

In addition to suppressing the production of brown dwarfs, Bate (2009c) suggested that radiative heating may also weaken the dependence of the median stellar mass on the thermal Jeans mass of the initial molecular cloud, **by modifying the effective thermal Jeans mass of regions heated by accreting protostars.** This would provide a possible explanation for the apparent 'universality' of the observed IMF (Bastian et al. 2010). Results from two calculations that varied in initial density by a factor of 9 showed no statistically significant difference in the median stellar mass. However, as each calculation only produced populations of ~ 20 objects, the possibility of a dependence of the median mass on density that was too weak to be detected with such small numbers of stars remains. We shall return to this possibility in Chapter 4.

The invariance of the statistical properties of these clusters was further investigated in calculations performed by Bate (2014), which were similar to the calculations of Bate (2012), but varied the metallicity of the clouds, effectively varying the opacity of the gas. The statistical properties of the stellar populations were once again found to be indistinguishable. Bate did note that protostellar mergers were slightly more common at lower opacities, and that the calculations may have been slightly too dissipative. However, combining all of the calculations gave results in excellent agreement with observations, implying that radiative feedback may help to produce invariant statistical properties.

1.4.1 Modelling protostellar heating

Most hydrodynamical simulations of star-cluster formation have used sink particles to model protostars (Bate et al. 1995). In their simplest form, sink particles omit the effects of all physical processes that occur inside the accretion radius, $r_{\rm acc}$, on the surrounding calculation, barring gravitational forces. However, when mass accretes onto a protostar, its gravitational potential energy is converted into thermal energy, which is then radiated away. As the potential energy released scales inversely with the minimum radius, using sink particles with accretion radii much larger than the typical protostellar radius will

significantly underestimate the heating effect of mass accretion. Calculations resolving the formation of stellar cores performed by Bate (2010, 2011) and Tomida et al. (2010) have shown that radiative feedback from the formation of protostars can significantly effect the dynamics of the surrounding envelope, in some cases generating thermally driven outflows.

To include radiative feedback from inside the sink particle, there are two main sources of luminosity which must be accounted for: the intrinsic luminosity of the protostar, and the luminosity generated by the accretion of mass. The intrinsic luminosity of the protostar has been generally ignored in past studies, as for low-mass protostars accreting at high rates, it is expected to be small in comparison with the accretion luminosity (Offner et al. 2009; Hosokawa and Omukai 2009). Mass accretion onto a protostar generates luminosity in two ways. **The first is compressional and viscous heating, which occurs as the gas collapses or is channelled through an accretion disc and is radiated by the gas before it reaches the protostar.** The second is shock-heating which releases gravitational potential energy once the accretion flow meets the protostellar surface. A fraction of the gravitational potential energy may also be used to generate jets and outflows, or may be advected into the protostar to be released on longer timescales.

1.4.2 Previous studies including protostellar heating

Several different approaches have been taken in previous studies to model the effects of radiative feedback from accretion. Krumholz et al. (2007) and Offner et al. (2009) employed sink particles that emitted both the accretion luminosity and the luminosity of the central protostar in adaptive mesh refinement calculations. The accretion luminosities were calculated based on continuous accretion through a circumstellar accretion disc, and the luminosities of protostars were modelled using the one-zone protostellar evolution model developed by Nakano et al. (1995), Nakano et al. (2000), and Tan and McKee (2004). Urban et al. (2010) approximated the heating effect of protostellar accretion by setting the gas temperature based on the proximity of luminous sources (see Urban et al. 2009), whose luminosities were set by interpolating over the protostellar mass and accretion rate. **This was similar to the approach used by Smith et al. (2009) in larger scale calculations of massive star formation, which set the gas temperature in the vicinity of sink particles according to one-dimensional temperature profiles produced by the Monte Carlo radiative transfer models of Robitaille et al. (2006).** However, both of these methods used sink particle accretion radii much larger than the protostellar radius (30 AU for Krumholz et al. 2007, 16 – 128 AU for Offner et al. 2009; 150 AU for Urban et al. 2010), and consequently made broad assumptions about the dynamics in the interiors of the sink particles.

Bate (2009c, 2012) chose instead to use sink particles with much smaller accretion radii

(0.5 AU), and ignore the luminosity generated by material inside the sink. Using this method required few assumptions about the interior of the sink particle, and captured much more of the luminosity than is included when using larger ($\sim$ 100 AU) sink particles. However, the accretion luminosity was still underestimated by a large factor, $\approx r_{\rm acc}/R_*$, where R_* is the protostellar radius. Bate (2012) argued that, despite this, the luminosity generated by the resolved gas at small radii was sufficient to suppress most anomalous fragmentation.

Lomax et al. (2015) also employed much smaller sink particles ($\approx$ 0.2 AU), and modelled the radiative feedback generated inside sink particles using two different schemes, comparing the results. The first scheme, termed 'continuous radiative feedback', was based on continuous accretion through a circumstellar accretion disc. The second scheme modelled the protostellar accretion luminosity using 'episodic radiative feedback', and was based on 'episodes' of rapid accretion driven by instabilities in the circumstellar accretion disc, followed by quiescent periods of no accretion. Lomax et al. (2015) suggested that the episodic model more accurately modelled the effects of protostellar heating, predicting lower disc temperatures and lower luminosities than continuous models. However, the disc evolution models used to calculate the frequency of these periods of rapid accretion (Zhu et al. 2009, 2010) made a range of assumptions regarding the dynamics and structure of the circumstellar disc, making it unclear whether the episodic model provides a more accurate description of the accretion process than the continuous case. We examine this further in chapters 5 and 6.

1.5 Aside: magnetic fields

So far, we have described the properties of molecular clouds, and how they collapse to form stellar clusters, as well as the mechanisms which determine the properties of stellar populations, and the potential effects of protostellar feedback in these systems. However, one major component of the star formation process that we have omitted is the role of magnetic fields.

The importance of magnetic fields in star formation has long been a matter of debate. Early studies focused on the large-scale effects of magnetic fields on the collapse of molecular clouds. It was proposed that frozen-in magnetic fields in molecular clouds would provide support against gravitational collapse (Mestel and Spitzer 1956), thus explaining the low star formation efficiencies observed in Galactic star-forming regions (Mouschovias 1976; Shu et al. 1987). **Theories of this type are sometimes referred to as 'strong-field' models (Crutcher 2012). The basic premise of these models is that molecular clouds form with subcritical masses, such that $M < M_\Phi = \Phi/2/pi\sqrt{G}$, where M_Φ is the critical mass and Φ is the magnetic flux. In this case, the magnetic pressure is strong enough to prevent the gravitational collapse of the cloud. However, since the magnetic field**

is only frozen-in to the ionised gas and sit in the cloud, the neutral material may still collapse through the field, increasing the mass of the cloud cores and causing the gravitational field strength to increase faster than the magnetic field strength. This process is known as 'ambipolar' diffusion, and was thought to control the timescales on which star-forming clouds would collapse, thereby limiting the rate of star-formation in these regions (Strittmatter 1966).

This was later replaced by a more dynamic picture, with the exact role of magnetic fields becoming less clear. 'Weak-field' models were proposed, in which the magnetic field strength is much weaker, and therefore does not dominate the dynamics of clouds. Instead, it interacts with the turbulent dynamics of the cloud interior, producing intermittent effects (Mac Low et al. 1998; Padoan et al. 2004). At the same time, magnetic fields were also found to be responsible for a range of small scale phenomena, including jets (Payne and Blandford 1981; Lovelace et al. 1993), winds (Pringle 1989a), and outflows (Wardle and Koenigl 1993). Subsequent calculations investigated these mechanisms in detail, and found that magnetically driven outflows may be produced during both the first core (Tomisaka 2002; Machida et al. 2005; Banerjee and Pudritz 2006; Price et al. 2012) and second core (Banerjee and Pudritz 2006; Machida et al. 2006, 2008) phases of pre-stellar collapse.

Many recent studies have examined the effects of magnetic fields on the formation and evolution of circumstellar discs. These effects had been noted by some earlier studies, which found that magnetic fields may interact with disc material to produce effective magnetic viscosities (Tout and Pringle 1992), and disrupt the structure of the inner disc, funnelling accreted material along fields lines (Kenyon et al. 1996). However, modern numerical models of protostellar systems have experienced significant difficulties in producing rotationally supported Keplerian discs when including the effects of magnetic fields with similar strengths to those observed in molecular clouds (Allen et al. 2003; Price and Bate 2007; Hennebelle and Fromang 2008; Mellon and Li 2008). This has become known as the 'Magnetic Breaking Catastrophe'. Several authors have suggested that non-ideal magnetohydrodynamics (MHD) effects may provide a solution to this problem (Tsukamoto et al. 2015a; Wurster et al. 2016). Calculations have shown that non-ideal effects, such as **Ohmic resistance (Tsukamoto et al. 2015b), in which both ions and neutrals drift relative to the magnetic field, and the Hall effect (Wurster et al. 2016), which involves the drift of electrons along magnetic field lines to produce an electric field,** may reduce the impact of magnetic fields sufficiently to allow circumstellar discs to form (see also Wurster et al. 2017, 2018).

Despite the obvious importance of magnetic fields in the formation of stars, the precise nature of their impact is still somewhat unclear. For this reason, in the rest of this thesis, and in the calculations presented herein, we do not consider the effects of magnetic fields.

1.6 Motivations

As we have discussed, the effects of thermal feedback from protostars on the star formation process have been considered in several previous studies. However, these investigations have either resolved small scales but produced few objects, and have therefore relied upon artificial ensembles of dense cores to produce stellar populations, or have modelled the dynamics of entire star clusters without resolving the opacity limit.

In order to fully simulate the effects of protostellar heating on the dynamics of star-forming clusters, both of these regimes must be accounted for. In this thesis, we combine radiation hydrodynamical calculations of star formation, which resolve material down to the opacity limit, with methods for modelling the accretion luminosity and protostellar evolution. This allows us to accurately account for the effects of protostellar heating in calculations of star cluster formation, and, since the formation of individual objects is resolved, make predictions about the statistical properties of such clusters.

This thesis is structured as follows. Chapter 2 describes the fundamental basis of the Smoothed Particle Hydrodynamics (SPH) numerical method, as well as the method used to include the effects of radiative transfer in the calculations. In Chapter 3 we describe how protostars are modelled in our calculations using new methods to include the effects of protostellar feedback and evolution. Chapter 4 presents results from large-scale simulations of star-forming clusters with varying initial densities, and explores the dependence of the characteristic protostellar mass on the initial density, as well as the potential impact of protostellar heating. In Chapter 5, we investigate the effects of including the accretion luminosity generated inside sink particles in calculations of the collapse of Bonnor-Ebert spheres to form stars. We also present results from calculations of star formation in small stellar groups which include the accretion luminosity, and examine its effects on the evolution of the clusters. In Chapter 6, we investigate role of protostellar evolution in regulating protostellar heating by comparing the calculations presented in Chapter 5 with calculations which use the same initial conditions, but which also calculate the evolution of protostars using a live stellar evolution model. We also compare the stellar populations produced in the calculations with models of protostellar evolution, and demonstrate how they may be used to predict the properties of young stellar clusters. Chapter 7 presents our conclusions, and describes current and planned future efforts to further understand the impact of protostellar heating on the star formation process.

Chapter 2

Smoothed particle radiation hydrodynamics

Many astrophysical systems are hydrodynamical in nature. Indeed, the vast majority of the baryonic matter in the universe is found as either a neutral, partially ionised, or fully ionised gas. The macroscopic motions of these systems are governed by the equations of hydrodynamics

$$\frac{\mathrm{D}\rho}{\mathrm{D}t} = \rho\nabla\cdot\boldsymbol{v}, \tag{2.1}$$

$$\rho\frac{\mathrm{D}\boldsymbol{v}}{\mathrm{D}t} = -\nabla p, \tag{2.2}$$

$$\rho\frac{\mathrm{D}}{\mathrm{D}t}\left(\frac{u}{\rho}\right) = -p\nabla\cdot\boldsymbol{v}, \tag{2.3}$$

where $\mathbf{D}/\mathbf{D}t = \partial/\partial t + \mathbf{v}\cdot\nabla$ is the convective derivative. ρ is the fluid density, $\boldsymbol{v}$ is the fluid velocity, p is the specific fluid pressure, and u is the specific internal energy.

Smoothed particle hydrodynamics, commonly abbreviated as SPH, is a numerical method for approximating the above equations, in order to simulate the dynamics of fluids. Originally developed by Lucy (1977) and Gingold and Monaghan (1977) for modelling astrophysical systems, SPH now sees wide use across a number of different industries, including engineering, geophysics and computer animation (Monaghan 2005). SPH has a number of advantages which make it an excellent tool for studying astrophysical hydrodynamics problems. By using particles to model the fluid, many of the equations of fluid dynamics are formulated in an intuitive way, making analysis of complex systems much simpler for users. The method is also highly adaptive, varying the resolution naturally according to the local density, making it highly computationally efficient.

Since its inception, SPH has undergone many advances. **Numerical improvements, such as artificial viscosities (Morris and Monaghan 1997) and sink particles (Bate et**

al. 1995) have enabled larger and more accurate calculations; and additional physical mechanisms, including ideal (Price and Monaghan 2004b, 2004a; Price and Bate 2008) and non-ideal (Wurster et al. 2016) magnetic effects, radiative transfer (Whitehouse and Bate 2004; Whitehouse et al. 2005), ISM processes (Bate and Keto 2015), and dust-gas interactions (Lorén-Aguilar and Bate 2014, 2015), have increased their ability to simulate a wide range of physical systems.

In this chapter, we describe the fundamental elements of the SPH method as used to perform the calculations presented in this thesis. We also include details of the methods used to include radiative transfer in calculations. Section 2.1 introduces the concepts of the density estimate and smoothing kernels. In Section 2.2, we show how the density estimate and interpolation theory can be used to obtain the SPH equations of motion for a fluid. Section 2.3 describes the method used to calculate the artificial viscosity. In Section 2.4 we describe how radiative effects are included using flux-limited diffusion. Finally, in Section 2.5 we give details of the integration schemes used to solve the SPH equations of motion, and describe the features of the `sphNG` hydrodynamics code used to produce the calculations presented in this thesis.

2.1 Density & smoothing kernels

A fundamental concept in SPH is the calculation of the fluid density. Since SPH uses particles to model fluids, we require a method to derive the continuous properties of the fluid from the discrete properties of the particles. We will show that, once the density is computed, the rest of the fluid variables can be obtained via the same method.

2.1.1 Estimating the density

To calculate the density from a distribution of point mass particles, there are two main approaches. The first is to divide the calculation into cells, and estimate the density based upon the mass of the particles contained within each cell. This is the foundation of the Particle-In-Cell and Marker-In-Cell techniques. Combined with interpolation methods such as Cloud-In-Cell or Triangular-Shaped-Cloud, an accurate estimate of the density can be obtained. However, a fixed grid may suffer from too much or too little resolution when the particle distribution is clumped. Interpolating between the particles and the grid can also be slow and inconsistent.

Instead of sampling the mass distribution using a fixed grid, a local sample based on particles in the vicinity of the sampling point can be used. The most obvious approach is to sample the mass at a particle location, and include the mass of particles located within a sphere centred on the sample particle. The density estimate at a particle location, $\boldsymbol{r}$, is

then be given by

$$\rho(\boldsymbol{r}) = \frac{\sum_{b=1}^{N} m_b}{\frac{4}{3}\pi R^3}, \tag{2.4}$$

where m_b is the mass of the b-th particle, R is the sampling radius, and N is the total number of particles contained within the sphere with radius R. While a fixed 'sphere' size would encounter the same resolution problems as the fixed grid method, these are easily rectified by allowing the sampling radius to vary with the local particle or sample point density. A simple way of achieving this is to set the number of sample points, or 'neighbours', at a constant value. This ensures that the local resolution is always the same in both dense and sparse regions.

However, the density estimate produced by this method is very susceptible to noise, as small variations in the particle positions close to the boundary of the 'sphere' may change whether a particle is included in the mass sample or not, affecting the density. Instead, we would like the density at the sample particle to be sensitive to nearby changes in the particle distribution, but relatively insensitive to changes that are further away. A natural approach to this is to use a weighted sum such that the contribution of nearby particles to the mass sample is greater than those that are further away. The density then becomes

$$\rho(\boldsymbol{r}) = \sum_b m_b W(\boldsymbol{r} - \boldsymbol{r}_b, h), \tag{2.5}$$

where $\boldsymbol{r}_b$ is the position of the b-th neighbour particle, $W(\boldsymbol{r} - \boldsymbol{r}_b, h)$ is a weight function, known as the 'smoothing kernel', and h is a parameter that sets the characteristic scale of the function, known as the 'smoothing length'.

2.1.2 Kernel functions

It is clear that choosing the correct smoothing kernel is critical to achieving an accurate estimate of the density. There are several features which a suitable smoothing kernel requires in order to give physically sensible answers. Conservation of mass requires that W is normalised as

$$\int_V W(\boldsymbol{r}' - \boldsymbol{r}_b, h)\mathrm{d}V' = 1, \tag{2.6}$$

over the sample volume, V. In addition to this, the function should be positive, smooth and decrease monotonically with distance from the sample particle. It is typically symmetric with respect to the particle separation $\boldsymbol{r} - \boldsymbol{r}_b$. Finally, a function that is approximately flat at small radii is normally used to prevent the density estimate from being highly sensitive to small changes in the particle distribution close to the sample particle.

Given these constraints, an obvious choice for the smoothing kernel is a Gaussian of

the form:

$$W(\boldsymbol{r}-\boldsymbol{r}_b,h)=\frac{\sigma}{h^d}\exp\left(-\frac{(\boldsymbol{r}-\boldsymbol{r}_b)^2}{h^2}\right), \tag{2.7}$$

where $\sigma = [1/\pi^{1/2}, 1/\pi, 1/\pi^{3/2}]$ is a normalisation constant in [1, 2, 3] dimensions, and d is the number of dimensions. Using a Gaussian such as this for the smoothing kernel fulfils all of the requirements above, and gives an excellent estimate of the mass density at a particle location. However, as the extent of the Gaussian function is infinite, all particles in the calculation are included in equation 2.5. Since the value of the Gaussian weight function becomes small at large $\boldsymbol{r}$, including particles at large distances has a negligible effect on the density, but does so at a considerable computational cost of $O(N^2)$. A solution to this is to use an approximation to a Gaussian, for which the value beyond a limiting radius is zero. Such kernels are said to have 'compact support'. Using a function of this type does result in a more noisy density estimate, but also makes the calculation significantly more efficient. As such, kernels with compact support are widely used by modern SPH codes.

The most popular kernels with compact support are the Schoenberg B-spline functions (Monaghan and Lattanzio 1985; Monaghan 1985, 2005). These are generated using the Fourier transform

$$M_n(x,h)=\frac{1}{2\pi}\int_{-\infty}^{\infty}\left[\frac{\sin(kh/2)}{kh/2}\right]^n\cos(kx)\mathrm{d}k. \tag{2.8}$$

The minimum requirement for the smoothing kernel is that the first and second derivatives exist. Therefore the lowest-order B-spline that can be used is the $n = 4$ (cubic) spline, which is defined as the piecewise function

$$W(q)=\frac{\sigma}{h^d}\begin{cases}\frac{1}{4}(2-q)^3-(1-q)^3, & \text{if } 0\le q<1,\\ \frac{1}{4}(2-q)^3, & \text{if } 1\le q<2,\\ 0, & \text{otherwise .}\end{cases} \tag{2.9}$$

where $q = |\boldsymbol{r}-\boldsymbol{r}_b|/h$ is the particle separation in units of the smoothing length, and $\sigma = [2/3, 10/7\pi, 1/\pi]$ is a normalisation constant in [1, 2, 3] dimensions. Higher order functions provide better approximations to the Gaussian function, becoming more smooth and increasing the compact support radius. **While these kernels are useful for calculating higher-order derivatives, their larger compact support radii result in more particles being included in the density estimate, which increases the computational intensity of the calculation. We shall show in the following sections that the standard formulation of SPH involves only first and second order derivatives of the kernel function. Therefore, unless higher order derivatives are required to model additional processes, the lower order cubic spline is often used for computational efficiency.** Other types of kernel exist, and can be used to obtain an estimate of the density in a similar manner (e.g. Wendland kernels; see Dehnen and Aly 2012). However, as noted by Price (2012), investi-

gations into the effectiveness of these kernels have confirmed that Gaussian-like functions produce the most accurate density estimates.

2.1.3 Setting the smoothing length

To complete the calculation of the density, the smoothing length h must be specified. In the most basic formulation possible, h is set to constant value. However, using a constant value results in the same resolution problems that are associated with the particle/grid methods discussed at the beginning of this chapter. One of the key advantages of the SPH method is its adaptability and efficiency. This is primarily achieved by allowing the smoothing length to vary.

Early calculations used a global smoothing length, which varied according to the maximum density in the calculation (Gingold and Monaghan 1977). However, these calculations over-resolved regions of low density, making them inefficient. A more consistent approach is to vary the smoothing length of each particle according to the local number density. This allows the calculation to resolve the dense and sparse regions of the calculation evenly by ensuring that the 'number of neighbours' remains approximately constant. If the particles have equal masses, then the smoothing length is equivalently set by the mass density, and we obtain the following simultaneous equations

$$\rho(\boldsymbol{r}) = \sum_b m_b W(\boldsymbol{r} - \boldsymbol{r}_b, h); \qquad h(\boldsymbol{r}) = \eta \left(\frac{m}{\rho}\right)^{1/d}, \tag{2.10}$$

where η is the ratio of the smoothing length and the mean particle spacing. These equations can then be iteratively solved using root-finding methods to obtain the density and smoothing length for each particle in the calculation.

2.2 SPH fluid equations

As mentioned in the last section, the density estimate forms the fundamental basis of the SPH method. From it, it is possible to derive all of the equations necessary to model the motions of the particles in the calculation. We follow the Lagrangian approach taken by Price (2012) to derive the equations of motion for SPH, but they may also be derived directly from interpolation theory, as described by Monaghan (1992, 2005). The advantage of the Lagrangian approach is the intuitive way in which the density estimate leads to equations of motion. It also makes apparent the implicit conservation of quantities such as energy and momentum that is central to the method.

2.2.1 Lagrangian & Euler-Lagrange equations

We begin with a Lagrangian of the form $\mathcal{L} = T - V$, where T and V are the kinetic and potential energy terms. For a system of point mass particles, the kinetic energy is simply proportional to the velocities of the particles. If the particles represent a fluid with no external forces acting on it, then the potential energy is described by the internal (thermal) energy of each particle. The Lagrangian can therefore be expressed as

$$\mathcal{L} = \sum_b m_b \left(\frac{1}{2} v_b^2 - u_b \right), \tag{2.11}$$

where $\boldsymbol{v}_b$ and u_b are the particle velocities and internal (thermal) energies respectively. Assuming the action is minimised, we can apply the principle of least action to obtain the Euler-Lagrange equations

$$\frac{\mathrm{d}}{\mathrm{d}t} \left(\frac{\partial \mathcal{L}}{\partial \boldsymbol{v}_a} \right) - \frac{\partial \mathcal{L}}{\partial \boldsymbol{r}_a} = 0, \tag{2.12}$$

where $\boldsymbol{v}_a$ and $\boldsymbol{r}_a$ are the velocity and position of the a-th particle. Combining equations 2.11 and 2.12, we arrive at the following set of simultaneous equations

$$\frac{\partial \mathcal{L}}{\partial \boldsymbol{v}_a} = m_a \boldsymbol{v}_a; \qquad \frac{\partial \mathcal{L}}{\partial \boldsymbol{r}_a} = -\sum_b m_b \frac{\partial u_b}{\partial \rho_b}\bigg|_s \frac{\partial \rho_b}{\partial \boldsymbol{r}_a}, \tag{2.13}$$

where s is the entropy, **which is constant in the absence of dissipative effects.**

2.2.2 Equations of motion

Two sets of terms must be computed to fully describe the dynamics of the fluid. The first, $\partial u_b / \partial \rho_b|_s$, describes the changes in the internal energy due to variations in the density. This is simple to derive from the first law of thermodynamics

$$\mathrm{d}U = T\mathrm{d}S - P\mathrm{d}V, \tag{2.14}$$

where U, T, S, P and V are the internal energy, temperature, entropy, pressure and volume of the fluid. We can replace the volume term by considering the SPH estimate of the volume $V = m/\rho$, which implies that changes in the volume are described by $\mathrm{d}V = -m/\rho^2 \mathrm{d}\rho$. Substituting this into equation 2.14 and converting to the internal energy per unit mass, the expression becomes

$$\mathrm{d}u = T\mathrm{d}s + \frac{P}{\rho^2}\mathrm{d}\rho. \tag{2.15}$$

Therefore, if the entropy is constant, the change in the internal energy is

$$\frac{\partial u_b}{\partial \rho_b}\bigg|_s = \frac{P}{\rho^2}. \tag{2.16}$$

The second set of terms in the equations of motion, $\partial\rho_b/\partial\boldsymbol{r}_a$, describes the gradient in the density. Using our expression for the density estimate, the gradient at particle b with respect to the position of particle a is given by

$$\frac{\partial\rho_b}{\partial\boldsymbol{r}_a} = \frac{1}{\Omega_b}\sum_c m_c \frac{\partial W(\boldsymbol{r}_b - \boldsymbol{r}_c, h_b)}{\partial\boldsymbol{r}_a}(\delta_{ba} - \delta_{ca}), \tag{2.17}$$

where δ_{ab} is the Dirac delta function, and Ω_b is a term that accounts for the corresponding gradient in the smoothing length

$$\Omega_a \equiv 1 - \frac{\partial h_a}{\partial\rho_a}\sum_b m_b \frac{\partial W(\boldsymbol{r}_a - \boldsymbol{r}_b, h_a)}{\partial h_a}. \tag{2.18}$$

Combining 2.16 and 2.17 with 2.13 and rearranging slightly, we arrive at the Euler-Lagrange equations of motion (momentum equation) for SPH:

$$\frac{\mathrm{d}\boldsymbol{v}_a}{\mathrm{d}t} = -\sum_b m_b \left[\frac{P_a}{\Omega_a\rho_a^2}\frac{\partial W_{ab}(h_a)}{\partial\boldsymbol{r}_a} + \frac{P_b}{\Omega_b\rho_b^2}\frac{\partial W_{ab}(h_b)}{\partial\boldsymbol{r}_a}\right], \tag{2.19}$$

where we have used the abbreviation $W_{ab}(h_a) = W(\boldsymbol{r}_a - \boldsymbol{r}_b, h_a)$ for compactness. If the smoothing length is fixed, such that $\Omega = 1$, then this reduces to the standard form

$$\frac{\mathrm{d}\boldsymbol{v}_a}{\mathrm{d}t} = -\sum_b m_b \left(\frac{P_a}{\rho_a^2} + \frac{P_b}{\rho_b^2}\right)\nabla_a W_{ab}. \tag{2.20}$$

For simplicity, we assume $\Omega = 1$ for the remainder of this chapter. This allows us to write simpler equations, and does not significantly alter the derivations (Price 2012).

2.2.3 Energy evolution

In order to complete the description of the system, a method for evolving the internal energy of the fluid is also required. The evolution equation for the internal energy can be derived by using equations 2.5 and 2.16. Taking the time derivative of the density, we obtain

$$\frac{\mathrm{d}u_a}{\mathrm{d}t} = \frac{P_a}{\rho_a^2}\frac{\mathrm{d}\rho_a}{\mathrm{d}t}. \tag{2.21}$$

Substituting the SPH definition of density 2.5, this becomes

$$\frac{\mathrm{d}u_a}{\mathrm{d}t} = \frac{P_a}{\rho_a^2}\sum_b m_b(\boldsymbol{v}_a - \boldsymbol{v}_b)\cdot\nabla_a W_{ab}, \tag{2.22}$$

which describes the time evolution of the internal energy.

As noted by Price (2012), the internal energy is not the only possible choice of energy

parameter. The total energy and entropy may also be evolved. Since the equations for the system have been derived from the Lagrangian formulation, each of these approaches will produce identical results. They do however emphasise different aspects of the SPH formalism, specifically the conservation of energy and entropy.

2.2.4 Summary

Our full system of SPH fluid equations is as follows:

$$\rho(\boldsymbol{r}) = \sum_b m_b W(\boldsymbol{r} - \boldsymbol{r}_b, h); \qquad h(\boldsymbol{r}) = \eta \left(\frac{m}{\rho}\right)^{1/d}, \tag{2.23}$$

$$\frac{\mathrm{d}\boldsymbol{v}_a}{\mathrm{d}t} = -\sum_b m_b \left(\frac{P_a}{\rho_a^2} + \frac{P_b}{\rho_b^2}\right) \nabla_a W_{ab}, \tag{2.24}$$

$$\frac{\mathrm{d}u_a}{\mathrm{d}t} = \frac{P_a}{\rho_a^2} \sum_b m_b (\boldsymbol{v}_a - \boldsymbol{v}_b) \cdot \nabla_a W_{ab}. \tag{2.25}$$

These equations have been derived solely from the SPH density estimate combined with standard Lagrangian mechanics and thermodynamics, and completely describe the evolution of a fluid described by a system of SPH particles.

2.3 Artificial viscosity

The method that we have presented thus far has ignored the effects of dissipative processes on the dynamics of particles. While this approach is able to model smooth particle distributions with some accuracy, it produces unphysical results in regions with high density gradients, namely shocks. When viscosity is not included in SPH calculations, particles with high relative velocities are vulnerable to inter-penetration, which results in large pressure increases. As such, all modern SPH codes implement an artificial viscosity to resolve this. The name 'artificial viscosity' comes from the fact that, although they are generally formulated in a similar manner to real viscosities, these terms are included purely for numerical purposes, and do not directly reflect physical fluid processes.

Early Eulerian codes used explicit artificial viscosities, or implicit viscosities based on averaging (Richtmyer and Morton 1967). These methods suffered from a number of numerical problems however, such as smearing, discontinuities and vorticity decay. To solve these issues, switches based on local spatial derivatives were introduced, which gave much more accurate results. However, the gradients used for these switches have no obvious analogues in particle methods, making them difficult to implement. Instead, switches based on the relative velocities of particles were developed. The simplest prescrip-

tion of this type switches off the viscosity for particles moving apart, and on for particles approaching each other. While this method is effective for many calculations, it can give rise to anomalous edge pressures at natural boundaries (Morris and Monaghan 1997).

The standard formulation of the artificial viscosity in SPH is included as an extra term in the momentum equation as

$$\frac{\mathrm{d}\boldsymbol{v}_a}{\mathrm{d}t} = -\sum_b m_b \left(\frac{P_a}{\rho_a^2} + \frac{P_b}{\rho_b^2} + \Pi_{ab} \right) \nabla_a W_{ab}, \tag{2.26}$$

where

$$\Pi_{ab} = \begin{cases} -\frac{\alpha h \boldsymbol{v}_{ab} \cdot \boldsymbol{r}_{ab}}{\bar{\rho}_{ab} |\boldsymbol{r}_{ab}|^2} \left(\bar{c}_{ab} - 2\beta \frac{h \boldsymbol{v}_{ab} \cdot \boldsymbol{r}_{ab}}{|\boldsymbol{r}_{ab}|^2} \right), & \text{if } \boldsymbol{v}_{ab} \cdot \boldsymbol{r}_{ab} < 0, \\ 0, & \text{otherwise}, \end{cases} \tag{2.27}$$

where α and β are a dimensionless parameters, c is the sound speed, $\bar{c}_{ab} = \frac{1}{2}(c_a + c_b)$, and $\bar{\rho}_{ab} = \frac{1}{2}(\rho_a + \rho_b)$. The first term is based upon an approximation of the physical viscosity in a gas, whereas the second term generates an artificial pressure to prevent particle inter-penetration in shocks.

Morris and Monaghan (1997) proposed a method by which each particle is assigned its own viscosity parameter, α, which varies according to its environment. This allows the viscosity to increase as the particle enters a shock, and decrease once it has passed through. This mechanism is described by

$$\frac{\mathrm{d}\alpha}{\mathrm{d}t} = -\frac{\alpha - \alpha^*}{\tau} + S, \tag{2.28}$$

where α^* is the base value of α in the absence of shocks, τ is the characteristic decay time for α once the particle has exited a shock, and S is the source term which causes α to increase as the particle approaches a shock. The base viscosity parameter is usually set to $\alpha^* = 0.1$. Since the value of α typically reaches a peak value of ≈ 1 (see Morris and Monaghan 1997), this gives an order of magnitude decrease in the viscosity away from shocks while maintaining particle order. Theoretically, the values of τ and S vary according to the dynamics of each shock. Since the structure of each shock cannot be known, the characteristic timescale τ is instead set by

$$\tau = \frac{h}{C_1 c}, \tag{2.29}$$

where C_1 is a dimensionless parameter which controls the decay length relative to the smoothing length. It is typically set to $0.1 < C_1 < 0.2$, such that the viscosity decays over 2-5 smoothing lengths for an ideal gas. S is defined as

$$S = \max(-\nabla \cdot \boldsymbol{v}, 0), \tag{2.30}$$

so that the term becomes large near shocks.

2.4 Radiative transfer in SPH

Early SPH codes did not include radiative transfer, instead relying on the equation of state to directly set the gas temperature. Whilst such codes are well suited to simulating hydrodynamical processes, they can produce poor results when modelling systems in which radiative processes are important. In an astrophysical context, studies have shown that radiative heating is crucial to the star-formation process, where it helps to regulate the formation of low-mass objects. As such, a method for including radiative effects in SPH calculations is desirable. In this section, we describe the basics of radiative transfer and the flux-limited diffusion method, and how these processes can be included into the equations of SPH.

2.4.1 Radiation hydrodynamics & flux-limited diffusion

The effects of radiative processes in hydrodynamical systems can be modelled by modifying equations 2.1 - 2.3 to include terms to describe the properties of the radiation field and its interactions with the gas. In the co-moving frame, assuming local thermal equilibrium (LTE), the frequency-integrated equations describing the time-evolution of radiation hydrodynamics (RHD) are

$$\frac{\mathrm{D}\rho}{\mathrm{D}t} = \rho\nabla\cdot\boldsymbol{v}, \tag{2.31}$$

$$\rho\frac{\mathrm{D}\boldsymbol{v}}{\mathrm{D}t} = -\nabla p + \frac{\kappa\rho}{c}\boldsymbol{F}, \tag{2.32}$$

$$\rho\frac{\mathrm{D}}{\mathrm{D}t}\left(\frac{E}{\rho}\right) = -\nabla\cdot\boldsymbol{F} - \nabla\boldsymbol{v} : \mathbf{P} + 4\pi\kappa\rho B - c\kappa\rho E, \tag{2.33}$$

$$\rho\frac{\mathrm{D}}{\mathrm{D}t}\left(\frac{u}{\rho}\right) = -p\nabla\cdot\boldsymbol{v} - 4\pi\kappa\rho B + c\kappa\rho E, \tag{2.34}$$

$$\frac{\rho}{c^2}\frac{\mathrm{D}}{\mathrm{D}t}\frac{\boldsymbol{F}}{\rho} = -\nabla\cdot\mathbf{P} - \frac{\kappa\rho}{c}\boldsymbol{F}, \tag{2.35}$$

(Mihalas and Mihalas 1984), where ρ, e, $\boldsymbol{v}$ and p are the mass density, energy density, velocity and scalar isotropic pressure, and E, $\boldsymbol{F}$ and $\mathbf{P}$ represent the frequency-integrated radiation energy density, flux and pressure tensor. $B = (\sigma_{\mathrm{SB}}/\pi)T_{\mathrm{g}}^4$ is the frequency-integrated Planck function, where σ_{SB} is the Stefan-Boltzman constant, and κ is the **frequency-integrated** opacity.

Equations 2.31 - 2.35 are similar to equations 2.1 - 2.3, but include several new terms

to describe the interaction between the gas and the radiation field, as well as two additional equations to describe the evolution of the radiation field itself. Equation 2.31 remains unchanged from the hydrodynamical case. Equation 2.32 is the RHD equivalent of equation 2.2, and includes a new term on the right-hand side to describe the effect of the radiation pressure on the momentum of the gas. Equation 2.33 describes the evolution of the radiation energy, and includes terms which are related to the radiative flux and radiation pressure, as well as emission and absorption of radiation by the gas. Equation 2.34 describes the evolution of the internal energy of the gas, similar to equation 2.3, but also includes terms to model the emission and absorption of radiation, which match those in equation 2.33. Finally, equation 2.35 describes the evolution of the radiative flux according to the radiation pressure and its effect on the gas.

To close this set of equations, we must choose an equation of state. A common choice is the equation of state for an ideal gas $p = (\gamma - 1)u\rho$, where $u = e/\rho$ is the specific energy of the gas. In this case, the gas temperature is given by $T_{\rm gas} = (\gamma - 1)\mu u/\mathcal{R}_{\rm g} = u/c_V$, where μ is the **mean molecular weight**, $\mathcal{R}_{\rm g}$ is the gas constant, and c_V is the specific heat capacity of the gas. We can also define a radiation temperature, which is related to the radiation energy density by $E = 4\sigma_{\rm SB}T_{\rm rad}^4/c$.

There are several methods that can be used to transport the radiation. Codes using grid-based methods lend themselves well to Monte-Carlo or ray-tracing techniques, given the clear boundaries between cells. While these techniques can also be applied to SPH calculations, the methods for doing so are more complicated, often requiring the construction of grids to approximate the particle distribution (see Stamatellos and Whitworth 2005; Nayakshin et al. 2009).

Flux-limited diffusion (FLD) is a somewhat simpler approach, which models the transport of radiation as a diffusive process. Making this assumption results in a radiation transport model which is both simpler and less computationally expensive to calculate. However, it can produce poor results in regions of low density, or in regions containing sharp density contrasts (e.g. shadowed regions), where the assumption of a high optical depth does not apply. For many calculations of star formation, including those presented in this thesis, the assumption of diffusive radiative transfer is appropriate, provided that a flux limiter is used to calculate the flux correctly in optically thin regions.

Diffusion implies that the radiation field at every point is isotropic. The radiation pressure can therefore be written as $\mathbf{P} = 1/3E$. The corresponding flux is given by

$$\boldsymbol{F} = -\frac{c}{3\chi\rho}\nabla E, \tag{2.36}$$

where χ is the total opacity, i.e. the sum of the components from absorption, κ, and scattering, σ. In regions of high density, this is a good approximation of the true flux. However, in low density regions where $\chi\rho \to 0$, the flux $\boldsymbol{F} \to \infty$. In reality, the flux always

obeys the inequality $|\boldsymbol{F}| \leq cE$. To solve this issue, we introduce a function known as the 'flux-limiter'. In this case, the flux is given by

$$\boldsymbol{F} = -D\nabla E. \tag{2.37}$$

D is the diffusion constant

$$D = \frac{c\lambda}{\chi\rho}, \tag{2.38}$$

where $\lambda(E)$ is the flux-limiter. We can then write the radiation pressure as

$$\mathbf{P} = \mathbf{f}E, \tag{2.39}$$

where $\mathbf{f}$ is the Eddington tensor

$$\mathbf{f} = \frac{1}{2}(1-f)\mathbf{I} - \frac{1}{2}(3f-1)\hat{\boldsymbol{n}}\hat{\boldsymbol{n}}. \tag{2.40}$$

$\mathbf{I}$ is the identity tensor, $\hat{\boldsymbol{n}} = \nabla E/|\nabla E|$ is a unit vector indicating the direction of the radiation energy density gradient, and $f(E)$ is a dimensionless scalar related to the flux-limiter by

$$f = \lambda + \lambda^2 R^2, \tag{2.41}$$

where $R = |\nabla E|/(\chi\rho E)$. Finally, a choice for the function $\lambda(E)$ is required. A common choice is the Levermore and Pomraning (1981) limiter, expressed as a function of R

$$\lambda(R) = \frac{2+R}{6+3R+R^2}. \tag{2.42}$$

When the optical depth is low

$$\lim_{R\to\infty} \lambda(R) = \frac{1}{R}, \tag{2.43}$$

and when the optical depth is high

$$\lim_{R\to\infty} \lambda(R) = \frac{1}{3}, \tag{2.44}$$

such that $|\boldsymbol{F}| \to cE$ at low optical depths, and $|\boldsymbol{F}| \to c|\nabla E|/(3\chi\rho)$ at high optical depths, as required.

2.4.2 SPH equations for radiative transfer

To model the transport radiation in SPH using flux-limited diffusion, equations 2.31 - 2.35 must be expressed in terms of SPH variables. We follow the formulation of radiative transfer in SPH described by Whitehouse and Bate (2004) and Whitehouse et al. (2005). This uses a two-temperature method, in which energy is generated by doing work on the gas or radiation field, and transferred between the two according to their relative temperatures,

as well as the gas density and opacity. The gas and dust are assumed to be well-coupled, and their respective temperatures are assumed to be the same.

It is natural to use the specific energy of the gas $u = U/\rho$, and the specific energy of the radiation field $\xi = E/\rho$. Re-writing equations 2.32 - 2.34 in terms of the specific energies, we obtain

$$\frac{\mathrm{D}\boldsymbol{v}}{\mathrm{D}t} = -\frac{\nabla p}{\rho} + \frac{\chi}{c}\boldsymbol{F}, \tag{2.45}$$

$$\frac{\mathrm{D}\xi}{\mathrm{D}t} = -\frac{\nabla \cdot \boldsymbol{F}}{\rho} - \frac{\nabla \boldsymbol{v} : \mathbf{P}}{\rho} - ac\kappa\left[\frac{\rho\xi}{a} - \left(\frac{u}{c_v}\right)^4\right], \tag{2.46}$$

$$\frac{\mathrm{D}u}{\mathrm{D}t} = -\frac{p\nabla \cdot \boldsymbol{v}}{\rho} + ac\kappa\left[\frac{\rho\xi}{a} - \left(\frac{u}{c_v}\right)^4\right], \tag{2.47}$$

where $a = 4\sigma_{\mathrm{SB}}/c$.

From the previous section we have

$$\boldsymbol{F} = -\frac{c\lambda}{\chi\rho}\nabla E. \tag{2.48}$$

We can substitute this directly into the second term in equation 2.45, which describes the effect of the radiation pressure on the particle momentum.

$$\left(\frac{\mathrm{D}\boldsymbol{v}}{\mathrm{D}t}\right)_{\mathrm{radpress}} = \frac{\chi}{c}\boldsymbol{F} = -\frac{\lambda}{\rho}\nabla E. \tag{2.49}$$

Re-writing the radiation energy density in terms of the specific energy density and the SPH density estimate, we find

$$\left(\frac{\mathrm{D}\boldsymbol{v}}{\mathrm{D}t}\right)_{\mathrm{radpress}} = -\frac{\lambda_i}{\rho_i}\sum_{b=1}^{N} m_b\xi_b\nabla W_{ab}. \tag{2.50}$$

We can also substitute equation 2.48 into the first term on the right-hand-side of equation 2.33, which describes the flow of radiative flux, to obtain

$$\left(\frac{\mathrm{D}\xi}{\mathrm{D}t}\right)_{\mathrm{flux}} = -\frac{\nabla \cdot \boldsymbol{F}}{\rho} = \frac{1}{\rho}\nabla \cdot \left(\frac{c\lambda}{\kappa\rho}\nabla E\right). \tag{2.51}$$

Second-order spatial derivatives in SPH are highly sensitive to particle disorder (Price 2012). As such, it is preferable to reformulate this as a first-order derivative using a Taylor expansion. Following a similar procedure to that of Jubelgas et al. (2004), and again re-writing in terms of the specific energy density and the SPH density estimate, we arrive at the following

$$\left(\frac{\mathrm{D}\xi}{\mathrm{D}t}\right)_{\mathrm{flux}} = \sum_b \frac{m_b}{\rho_a\rho_b} bc(\rho_a\xi_a - \rho_b\xi_b)\frac{\nabla W_{ab}}{r_{ab}}, \tag{2.52}$$

where

$$b = \left[\frac{4 \frac{\lambda_a}{\kappa_a \rho_a} \frac{\lambda_b}{\kappa_b \rho_b}}{\left(\frac{\lambda_a}{\kappa_a \rho_a} + \frac{\lambda_b}{\kappa_b \rho_b} \right)} \right]. \tag{2.53}$$

The second term in equation 2.33 describes changes in the radiation energy due to the radiation pressure.

$$\left(\frac{\mathrm{D}\xi}{\mathrm{D}t} \right)_{\mathrm{radpress}} = -\frac{1}{\rho} \nabla \boldsymbol{v} : \mathbf{P}. \tag{2.54}$$

In the optically thick limit, $\mathbf{P}$ becomes isotropic, and equation 2.54 reduces to the one-dimensional form

$$\left(\frac{\mathrm{D}\xi}{\mathrm{D}t} \right)_{\mathrm{radpress}} = -(\nabla \cdot \boldsymbol{v})_a f_a \xi_a, \tag{2.55}$$

where the Eddington factor f_i is given by

$$f_a = \lambda_a + \lambda_a^2 \left[\frac{|\nabla(\rho_a \xi_a)|}{\kappa_a \rho_a^2 \xi_a} \right]^2. \tag{2.56}$$

The last terms on the right-hand-side of equations 2.46 and 2.47 describe the transfer of energy between the gas and the radiation field. They are proportional to $T_{\mathrm{rad}}^4 - T_{\mathrm{gas}}^4$ since $\xi = aT_{\mathrm{rad}}^4/\rho$ and $u = c_{\mathrm{v}} T_{\mathrm{gas}}$.

We therefore arrive at the following set of equations for the transport of radiation via flux-limited diffusion in SPH:

$$\frac{\mathrm{d}\boldsymbol{v}_a}{\mathrm{d}t} = -\sum_b m_b \left(\frac{p_a}{\rho_a^2} + \frac{p_b}{\rho_b^2} + \Pi_{ab} \right) \nabla W(r_{ab}, h_{ab}) - \frac{\lambda_a}{\rho_a} \sum_b m_b \xi_b \nabla W_{ab}, \tag{2.57}$$

$$\frac{\mathrm{d}\xi_a}{\mathrm{d}t} = \sum_b \frac{m_b}{\rho_a \rho_b} bc(\rho_a \xi_a - \rho_b \xi_b) \frac{\nabla W_{ab}}{r_{ab}} - (\nabla \cdot \boldsymbol{v})_a f_a \xi_a - ac\kappa \left[\frac{\rho \xi}{a} - \left(\frac{u_a}{c_{\mathrm{v}}} \right)^4 \right], \tag{2.58}$$

$$\frac{\mathrm{d}u_a}{\mathrm{d}t} = \frac{1}{2} \sum_b m_b \left(\frac{p_a}{\rho_a^2} + \frac{p_b}{\rho_b^2} + \Pi_{ab} \right) \nabla W_{ab} + ac\kappa \left[\frac{\rho \xi}{a} - \left(\frac{u_a}{c_{\mathrm{v}}} \right)^4 \right], \tag{2.59}$$

where we have included the artificial viscosity term, Π_{ab}.

2.5 Computational method

The equations described in the previous section completely determine the evolution of the gas and radiation field, and may be integrated using standard particle integration methods calculate the motions of the SPH particles. We briefly describe explicit and implicit methods for solving these equations below.

2.5.1 Explicit integration method

Equations 2.57 - 2.59 may be iterated over explicitly to obtain the evolution of the gas and radiation field. In order to do so, the integration time-step must be chosen appropriately. The Courant-Friedrichs-Lewy condition defines the minimum time-step required to resolve the local dynamics at a particle location. For hydrodynamics, the criteria are

$$\mathrm{d}t_{\mathrm{Courant},a} = \frac{\zeta h_a}{c_\mathrm{s} + h_a|\nabla\cdot\boldsymbol{v}|_a + 1.2(\alpha_\mathrm{v}c_\mathrm{s} + \beta_\mathrm{v}h_a|\nabla\cdot\boldsymbol{v}|_a)}, \tag{2.60}$$

$$\mathrm{d}t_{\mathrm{force},a} = \zeta\sqrt{\frac{h_a}{|\boldsymbol{a}_a|}}, \tag{2.61}$$

where $\zeta < 1$ is the Courant number (typically $\zeta \approx 0.3$), and $\boldsymbol{a}_a$ is the particle acceleration. In radiation hydrodynamics, we modify 2.60 such that the sound speed includes the contribution from the radiation pressure term. In this case, the sound speed is defined as $c_\mathrm{s} = [\max(\gamma, 4/3)P_\mathrm{tot}/\rho]^{1/2}$, where P_tot is the sum of the gas and radiation pressure magnitudes.

Separate time-step criteria are required for each of the terms in 2.58 and 2.59. The time-steps for the flux diffusion and radiation pressure terms in 2.58 are given by Whitehouse and Bate (2004)

$$\mathrm{d}t_{\mathrm{flux},a} = \zeta\frac{h_a^2\rho_a\kappa_a}{c\lambda_a}, \tag{2.62}$$

$$\mathrm{d}t_{\mathrm{radpress},a} = \zeta\frac{1}{f_a\rho_a\xi_a(\nabla\cdot\boldsymbol{v})_a}, \tag{2.63}$$

and the time-steps for the gas-radiation field interaction terms in 2.58 and 2.59 are given by

$$\mathrm{d}t_{\mathrm{int}\xi,a} = \zeta\frac{\xi_a}{ac\kappa_a|\rho_i\xi_a/a - (u_a/c_{\mathrm{v},a})^4|}, \tag{2.64}$$

$$\mathrm{d}t_{\mathrm{int}u,a} = \zeta\frac{u_a}{ac\kappa_a|\rho_a\xi_a/a - (u_a/c_{\mathrm{v},a})^4|}. \tag{2.65}$$

2.5.2 Implicit integration method

Although the time-step criteria described in the previous section allow the SPH equations of RHD to be calculated accurately, they are often impractical for larger or more complex calculations. The presence of the speed of light, c, in the denominator of equations 2.64 and 2.65 results in a radiation time-step which is typically much smaller than the hydrodynamical time-step.

To alleviate this issue, we use the implicit integration scheme developed by Whitehouse et al. (2005). The scheme uses a backwards Euler implicit method to solve equations 2.58

and 2.59. For a time-dependent variable A, the backwards Euler scheme states

$$A_a^{n+1} = A_a^n + \mathrm{d}t \left(\frac{\mathrm{d}A_a}{\mathrm{d}t} \right)^{n+1}, \tag{2.66}$$

where n is the current time-step. A Gauss-Seidel method is used to iterate towards a solution by arranging the implicit equations in the form

$$A_a^{n+1} = \frac{A_a^n - \mathrm{d}t \sum_b \sigma_{ab}(A_b^{n+1})}{1 - \mathrm{d}t \sum_b \sigma_{ab}}, \tag{2.67}$$

where σ_{ab} contains quantities other than A. This can then be iterated over to achieve convergence.

The implicit forms of equations 2.58 and 2.59 are given by

$$\begin{aligned} \xi_a^{n+1} = \xi_i^n + \mathrm{d}t \sum_b \frac{m_b}{\rho_a \rho_b} bc(\rho_a \xi_a^{n+1} - \rho_b \xi_b^{n+1}) \frac{\nabla W_{ab}}{r_{ab}} - \mathrm{d}t(\nabla \cdot \boldsymbol{v})_a f_a \xi_a^{n+1} s \\ - \mathrm{d}t ac\kappa_a \left[\frac{\rho_a \xi_a^{n+1}}{a} - \left(\frac{u_a^{n+1}}{c_{\mathrm{v},a}} \right)^4 \right], \end{aligned} \tag{2.68}$$

and

$$\begin{aligned} u_a^{n+1} = u_i^n + \mathrm{d}t \sum_b \frac{1}{2} m_b \boldsymbol{v}_{ab} \cdot \nabla W_{ab} \left[\frac{p_a^{n+1}}{\rho_a^2} + \frac{p_b^{n+1}}{\rho_b^2} + \Pi_{ab} \right] \\ + \mathrm{d}t ac\kappa_a \left[\frac{\rho_a \xi_a^{n+1}}{a} - \left(\frac{u_a^{n+1}}{c_{\mathrm{v},a}} \right)^4 \right], \end{aligned} \tag{2.69}$$

where b has the same definition as in equation 2.53. Note that we have indicated that the gas pressure p_a depends upon the internal energy u_a through the equation of state by using the notation p_a^n and p_a^{n+1} to denote the pressure at time-steps n and $n+1$.

These equations can be rearranged into form of equation 2.67, and solved for ξ_a^{n+1} and u_a^{n+1} using Gauss-Seidel iteration with all other variables fixed to obtain the evolution of the radiation field. Using an implicit integration scheme such as this allows us to use the much larger hydrodynamical time-step to evolve the SPH equations, resulting in a significant increase in computational speed (Whitehouse et al. 2005).

2.5.3 `sphNG` hydrodynamics code

To implement and evolve the equations we have described in the previous sections, we use the `sphNG` hydrodynamics code. The code was originally developed by Benz et al. (1990) and Benz (1990), and has been subsequently modified by several authors (Bate et al. 1995, Whitehouse et al. 2005, Whitehouse and Bate 2006) to improve and extend the numerical

method. It is also parallelised using both `OpenMP` and `MPI`.

A second-order Runge-Kutta-Fehlberg method (Fehlberg 1969) is used to integrate the SPH equations, with individual time-steps for each particle (Bate et al. 1995). The artificial viscosity prescription given by Morris and Monaghan (1997) is used, with α_v varying between 0.1 and 1 and $\beta_v = 2\alpha_v$, as described in Section 2.3. Gravitational forces are calculated using a hierarchical binary tree method (Benz 1988), which implements gravitational softening, as described by Price and Monaghan (2007).

The code uses an ideal gas equation of state $p = \rho T \mathcal{R}_g / \mu$, where T is the gas temperature, $\mathcal{R}_g$ is the gas constant and μ is the mean molecular weight of the gas, set to $\mu = 2.38$. Translational, rotational and vibrational degrees of freedom of molecular hydrogen are accounted for in the thermal evolution of the gas, as well as molecular dissociation of hydrogen and ionisation of both hydrogen and helium, with hydrogen and helium mass fractions of $X = 0.70$ and $Y = 0.28$. The contribution of metals to the equation of state is ignored.

To model the transport of radiation, two-temperature (gas and radiation) flux-limited diffusion is implemented, as described in Section 2.4. A grey opacity is used, set to maximum value of the interstellar grain opacity according to the tables of Pollack et al. (1985) for low temperatures, and the gas opacity according to the tables of Alexander (1975) at high temperatures.

Chapter 3

Simulating accreting protostars in SPH

The methods discussed in the previous chapter are adequate to describe the dynamics of the gas and dust found in star-forming clusters. However, to model the protostars that form, a different approach is required. There are many additional processes operating at stellar and sub-stellar scales which govern the formation and subsequent evolution of individual protostars. Resolving these processes, while still calculating the dynamics of the surrounding cluster, is an extremely computationally intensive task. As such, most calculations of star formation employ 'sub-grid' models to calculate the interactions between protostars and their environments. These are separate calculations coupled to the main numerical simulation which model specific processes or systems, and can be used to include more complex physics in calculations without needing to resolve them directly.

In this chapter, we present the sub-grid models used in our calculations to calculate the accretion luminosities and evolution of protostars. In the first section, we describe the concept of sink particles, and how they can be used to efficiently model protostars and their immediate surroundings. Then we describe our method for calculating the accretion luminosities of protostars which are modelled using sink particles. Finally, we demonstrate how the effects of protostellar evolution are included in our calculations using the `Lyon` stellar evolution code (Chabrier and Baraffe 1997; Baraffe et al. 1998).

3.1 Sink particles

Using radiation hydrodynamics with a realistic equation of state allows us to capture each phase of protostar formation (Larson 1969). However, as the first hydrostatic core collapses following the dissociation of molecular hydrogen, the time-step as defined by the

Courant-Friedrichs-Levy condition becomes very small, making the required calculation time unfeasibly long, particularly for larger calculations involving multiple protostars.

To alleviate this issue, the concept of sink particles was introduced (Bate et al. 1995). Sink particles, once inserted, replace all particles within a specified region with a single point mass particle. The region is usually defined as a sphere centred on the densest particle, with a radius, $r_{\rm acc}$, called the 'accretion radius'. The criteria that must be satisfied for the successful formation of a sink particle are as follows:

- The smoothing length, h_a, of the densest particle must be $h_a < \frac{1}{2} r_{\rm acc}$, such that the initial mass of the sink $m_{\rm sink} \approx N_{\rm neigh} m_a$, where m_a is the mass of the densest particle.

- The particles within $r_{\rm acc}$ must be gravitationally bound, i.e. $\beta_{\rm therm} < \frac{1}{2}$; $\beta_{\rm therm} + \beta_{\rm rot} < 1$; $\beta_{\rm tot} < 1$, where $\beta_{\rm therm}$ and $\beta_{\rm rot}$ are the ratios of thermal and rotational kinetic energy to gravitational potential energy of the particles within $r_{\rm acc}$, and $\beta_{\rm tot}$ is the ratio of all energies excluding the gravitational potential energy to gravitational potential energy.

- The divergence of the particle velocities $\nabla \cdot \boldsymbol{v} < 0$.

The initial mass of the sink particle is defined by the total mass of the gas particles contained within the accretion radius when the sink is inserted. Subsequent particles that pass within the accretion radius are accreted by the sink particle, and their masses added to the total sink mass.

Using sink particles to model protostars in calculations of star formation allows their macroscopic interactions to be calculated at very little computational cost, as the dynamics of accreted material (which would be otherwise be very computationally intensive to calculate) are ignored once it passes within the sink particle accretion radius.

The sink particles in our calculations provide no hydrodynamic pressure, and do not attempt to correct for the discontinuous pressure and viscous forces at the accretion radius, although several methods have been proposed for doing so (e.g. Bate et al. 1995; Hubber et al. 2013). They also do not emit material in the form of jets or winds, but they may emit radiation. The methods used to model this are discussed in the next section. Sink particles are permitted to merge if they pass within 0.015 AU of each other, as young protostars are expected to be larger than the Sun (e.g. Hosokawa and Omukai 2009).

3.2 Accretion luminosities

As mentioned in the previous section, sink particles in radiative calculations may emit radiation. There are three main sources of luminosity inside sink particles that are used to model protostellar systems. These are the accretion luminosity, generated as material collapses onto the central protostar; the disc luminosity, generated by viscous dissipation as material is transported through the circumstellar accretion disc; and the intrinsic luminosity of protostar itself.

To calculate the luminosity generated inside in each sink particle, we use a 'sub-grid' model **based on the continuous accretion of mass through a circumstellar accretion disc onto a central protostar.** As material collapses towards the protostar, it will begin to rotate with increasing angular velocity, due to the conservation of angular momentum. In the absence of dissipation, this would prevent the accretion of gas onto the protostar. Instead, accretion is facilitated by the transport of angular momentum from the inner regions of the disc to the outer regions by viscous torques. In general, the rate at which a protostar accretes mass via this method is much lower than the in-fall rate at larger radii.

To describe this process, we decompose the total sink mass into a 'protostellar mass' and a 'disc mass'. **This is shown in the schematic of the model setup in Fig. 3.1.** Mass from gas particles accreted by the sink particle is initially **added to the disc mass.** It is then allowed to accrete onto the central protostar from the disc at a rate given by

$$\dot{M}_* = \dot{M}_0 \left(\frac{M_\mathrm{D}}{M_{\mathrm{D},0}} \right), \tag{3.1}$$

where $\dot{M}_0$ is the initial accretion rate, M_D is the current mass of the disc, **and the initial mass of the disc, $M_{\mathbf{D},0}$, is the difference between the initial mass of the sink particles and the initial mass of the protostar, i.e. $M_{\mathbf{D},0} \equiv= M_{\mathbf{sink},0} - M_{*,0}$. In the absence of accretion by the sink particle, equation 3.1 results in the protostar accreting mass from the disc at an exponentially decreasing rate. There are two free parameters: the initial protostellar mass, $M_{*,0}$, and the initial accretion rate $\dot{M}_0$.**

Using this formulation to describe the protostellar accretion rate has several advantages. Fixing the initial accretion rate ensures that the initial conditions for each protostar are identical, irrespective of the size of the sink particle used, or the distribution of gas prior to its insertion. The dependence of accretion rate on the current disc mass and the initial conditions also allows accretion to be modelled without the need to specify a density profile for the disc. This is beneficial, as the structures of accretion discs may vary considerably between systems, and therefore using a fixed disc profile may produce inconsistent results. The storage of mass accreted by the sink particle in the disc mass prior to being accreted by the protostar produces a smoothly varying accretion rate, as large variations require changes in the disc mass of similar magnitude to the

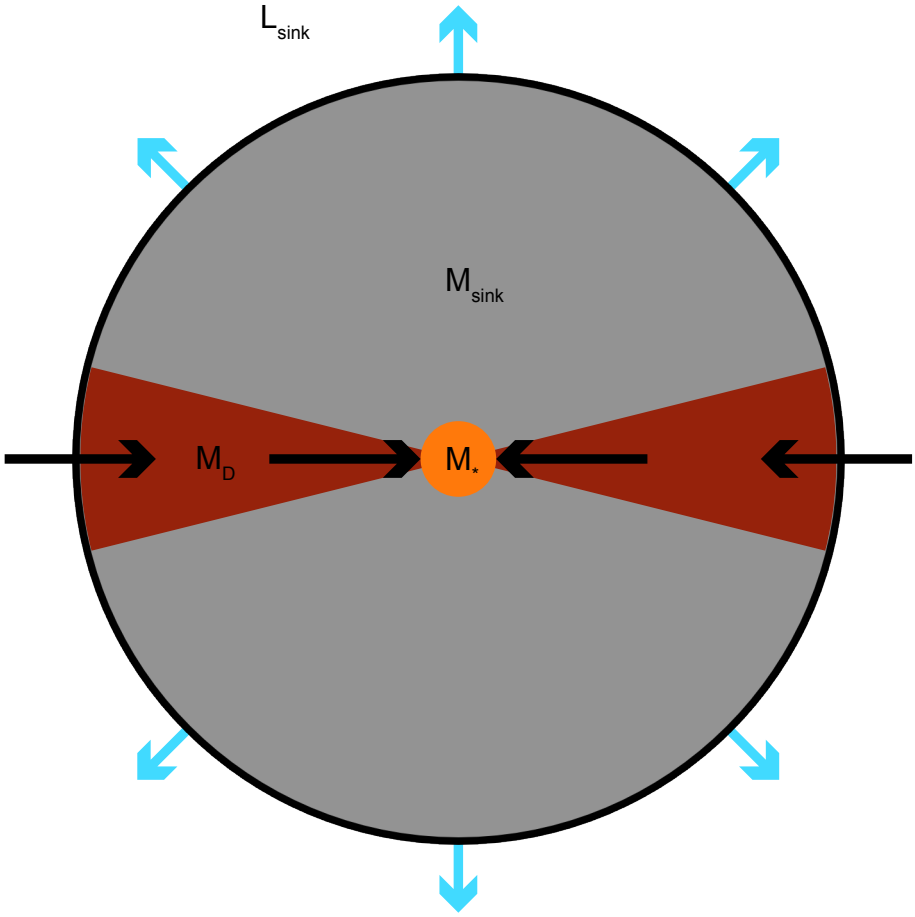

Figure 3.1: Schematic of the disc accretion algorithm components. Mass accreted by the sink particle (outer black arrows) is initially stored in the disc. The central protostar then accretes from the disc (inner black arrows) at a rate determined by equation 3.1. Luminosity generated via this process is radiated isotropically from the sink particle boundary (blue arrows).

disc mass itself. Finally, the linear dependence of the accretion rate of the disc mass results in the system to tending towards a steady state, with the protostellar accretion rate equal to the sink accretion rate, as the disc mass will naturally increase/decrease with the sink accretion rate until the the two accretion rates are equal.

Luminosity is generated via compressional and viscous heating in the circumstellar accretion disc, and through shock heating as the accretion flow meets the stellar surface. We can model both of these processes using the following equation

$$L_{\rm acc} = \epsilon \frac{G M_* \dot{M}_*}{R_*}, \tag{3.2}$$

where M_* is the protostellar mass, R_* is the protostellar radius and G is the gravitational constant. ϵ **is the efficiency factor for the conversion of potential energy to luminosity, which we set to 1 for simplicity.** This provides the maximum possible feedback. Some potential energy maybe converted to kinetic energy (e.g. jets), or thermal energy that is advected into the protostar to be released on longer timescales. In this case $\epsilon < 1$. For example, Offner et al. (2009) use $\epsilon = 0.75$. **The luminosity calculated by equation 3.2 is then radiated by the sink particle isotropically from the sink particle boundary. The method by which the radiation energy is delivered to surrounding SPH particles is described in the next section.**

To initialise the model, the sink particle's mass is split between the initial protostellar and disc masses. The protostellar mass is set to an initial value set by the model (see chapters 5 and 6). The remainder of the sink mass is then set equal to the initial disc mass. Previous calculations by Bate (2010) that resolved protostellar core formation showed that newly formed protostars undergo an initial phase of very rapid accretion ($\geq 10^{-3}$ M$_\odot$ yr^{-1}), lasting approximately 10 years, as the remnants of the first hydrostatic core are accreted. This is also true for calculations using sink particles to model protostars. During this time, the properties of the protostar and its surrounding material undergo rapid changes and a star with disc is a poor representation of the system. We therefore delay initialisation of the model **and ignore any emitted luminosity until 10 years after the sink particle forms.**

3.2.1 Adding the radiative feedback into the simulation

The protostellar luminosity determined from the above model must be radiated from the sink particle into the SPH simulation. This is done by including the source term $\rho\Gamma_*$ in the righthand side of equation 2.33, where Γ_* has units of erg s^{-1} g^{-1}. The source term for a particular SPH gas particle due to the radiative feedback from an individual sink particle is determined as follows:

First, the gas particles surrounding the sink particle are examined to determine which are directly exposed to the radiation emitted by the sink particle. This is implemented

by walking the tree structure that is also used to compute neighbouring particles and gravitational forces. A particle is determined to be exposed if no other gas particle 'blocks' the radiation from the sink particle. If there is another gas particle that is closer to the sink particle than the gas particle that is being examined, and the line segment from the sink particle's position to the position of the gas particle that is being examined intersects the smoothing sphere of the closer gas particle, then the gas particle is considered to be 'blocked'. The smoothing sphere of an SPH gas particle has a radius $r_{\rm W}h$, where h is the SPH smoothing length and $r_{\rm W}$ is the number of smoothing lengths required for the SPH kernel to drop to zero (i.e. for the standard cubic spline kernel $r_{\rm W} = 2$). An additional requirement for the particle to be blocked is that the distance between the two gas particles must be greater than the smoothing radius ($r_{\rm W}h$) of the intervening gas particle, otherwise both are considered to be potentially exposed.

Once a list of exposed particles has been constructed, the fraction of the sink particle's total luminosity that is distributed to each particle must be determined. This is done by calculating the solid angle subtended by the gas particle with smoothing length h_i with respect to the sink particle which we compute as

$$\Omega_i = 2\pi \left(1 - \cos(\sin^{-1}(\min(r_{\rm W}h_i, r)/r))\right), \tag{3.3}$$

where r is the distance between the sink particle and the gas particle. These values are then normalised such that the sum of the solid angles for all exposed particles is unity (i.e. all of the sink particle luminosity is distributed to the SPH particles). The source term for gas particle, i, is then given by

$$\Gamma_{*i} = \frac{L_*\Omega_i}{m_i \sum_i \Omega_i}, \tag{3.4}$$

where m_i is the mass of the gas particle.

This algorithm is sufficient for a calculation that uses global time steps for all particles. However, `sphNG` uses individual time steps such that particles have time-steps that may differ by powers of two (Bate et al. 1995). In this case, only those particles that are currently being evolved have their solid angles re-computed, and the sum of the solid angles over all exposed particles will not always equal unity. Furthermore, some particles with short time steps may be accreted between the time steps of exposed particles with longer time steps. To adjust for this, the amount of energy actually being added into the simulation over the time step of the exposed particle with the longest time step is calculated, and if this energy is slightly too large or small this deficit or excess is corrected over the subsequent period of time equal to the length of the time step of the exposed particle with the longest time step.

The above method of distributing the radiant energy to surrounding SPH gas particles essentially assumes that the surrounding particles are optically thick and the radiation is absorbed close to the protostar. This will be the case for rapidly accreting, young protostars. If a sink particle is not surrounded by optically thick gas, the radiant energy emitted by

the sink particle is still added into the radiation hydrodynamical simulation, but it will then propagate to larger distances as prescribed by flux-limited diffusion with all the usual limitations of that approximation (in particular, it will propagate diffusively rather than along rays).

The method also assumes that the luminosity is emitted isotropically. For the case of a central protostar surrounded by a circumstellar accretion disc this is reasonable, as the solid angle subtended by the disc is small. The anisotropic case is more complex, requiring the angular momentum axis of the material within the sink particle to be calculated. This is difficult to compute, as the viscous forces produced by material inside the sink accretion radius are not modelled, affecting the transport of angular momentum across the sink particle boundary. It is therefore simpler, and arguably more accurate, to use the isotropic approximation.

3.3 Modelling protostellar evolution

In addition to the accretion and disc luminosities, the intrinsic luminosity of the protostar contributes to the total luminosity of the protostellar system. This luminosity depends upon the surface temperature of the protostar and the protostellar radius. The accretion luminosity described in the previous section also depends upon the protostellar mass-radius ratio. As such, to consistently calculate the luminosity of the protostellar system it is necessary to model the evolution of the protostellar structure.

3.3.1 Lyon stellar evolution code

To calculate the structure and evolution of protostars in our calculations, we use the Lyon stellar evolution code, originally developed at the Gottingen Observatory (Langer et al. 1989; Baraffe and El Eid 1991), and subsequently modified (Chabrier and Baraffe 1997; Baraffe et al. 1998, 2009, 2012). The code solves the one-dimensional implicit equations of stellar structure, which can be written as

$$\frac{\mathrm{d}P}{\mathrm{d}M_r} = -\frac{GM_r}{4\pi r^4}, \tag{3.5}$$

$$\frac{\mathrm{d}r}{\mathrm{d}M_r} = \frac{1}{4\pi r^2 \rho}, \tag{3.6}$$

$$\frac{\mathrm{d}L_r}{\mathrm{d}M_r} = E_{\mathrm{nuc}} - c_P \frac{\mathrm{d}T}{\mathrm{d}t} + \frac{\delta}{\rho}\frac{\mathrm{d}P}{\mathrm{d}t}, \tag{3.7}$$

$$\frac{\mathrm{d}T}{\mathrm{d}M_r} = -\frac{GM_r T}{4\pi r^4 P}\nabla, \tag{3.8}$$

(Bodenheimer et al. 2007) where ρ and P are the density and scalar pressure, M_r is the mass contained within radius r, $L_r = 4\pi r^2 F_r$, where F_r is the net outward energy flux at radius r, $E_{\rm nuc} = {\rm d}L_r/{\rm d}M_r$ is the nuclear energy generation rate per unit mass, T is the temperature, c_P is the specific heat at constant pressure, and $\delta = -(\partial \ln \rho / \partial \ln T)_P$. ∇ is a term which describes the transport of energy in the stellar interior. If energy transport is via radiation then

$$\nabla = \nabla_{\rm rad} = \frac{3}{16\pi G a c} \frac{\kappa_{\rm R} L_r P}{M_r T^4} = \left(\frac{\partial \ln T}{\partial \ln P} \right)_{\rm rad}, \tag{3.9}$$

where $\kappa_{\rm R}$ is the Rosseland mean opacity and $a = 4\sigma_{\rm SB}/c$. Equations 3.5 - 3.8 are solved using the Henyey method (Kippenhahn and Weigert 1990). Convection is described by the mixing-length theory, using a mixing length equal to the pressure scale height. The Livermore opacities (Rogers and Iglesias 1992) are used for regions with temperatures $T > 10000$ K, and the Alexander and Ferguson (1994) opacities used for lower temperatures. The helium fraction is set to $Y = 0.275$.

To describe the thermodynamics of the stellar interior, the Saumon-Chabrier equation of state (Saumon 1990; Chabrier 1990; Saumon and Chabrier 1991, 1992) is used. This is a pure hydrogen and helium equation of state based on the additive volume law between the pure components (H and He), which has been specifically designed to describe the interiors of low-mass stars, brown dwarfs and giant planets. Energy is generated initially by gravitational contraction, and then by thermonuclear fusion in the protostellar core, once the core temperature is sufficiently high. The primary energy generation is deuterium burning via the PPI chain. The burning of light elements, specifically Li, Be and B, is also included. The rates at which these reactions take place are based on those of Caughlan and Fowler (1988).

The protostellar atmosphere is simulated using the *NextGen* non-grey atmosphere models for low-mass stars at finite metallicities (Allard et al. 1997). The boundary conditions for the internal structure equations are set by the temperature and density at the interface between the atmosphere and the stellar interior. These are found by generating a 2D-spline of the atmosphere temperature-density profile for a given metallicity. The atmosphere/interior interface is chosen to be at an optical depth of $\tau = 100$. All atmosphere models are adiabatic at this depth, allowing them to match with the interior adiabat, and the corresponding photospheric radius, $R_{\rm ph} < 0.01 R_*$, is such that the Stefan-Boltzmann equation $T^4 = L_*/4\pi\sigma_{\rm SB} R_*^2$ holds.

3.3.2 Protostellar accretion

The accretion of mass is treated using the method developed by Hartmann et al. (1997). The method uses a simplified, one-dimensional model, which assumes that accretion affects only a small area of the stellar surface and therefore most of the surface may radiate freely.

The stellar interior is assumed to be convective, regardless of whether deuterium-burning is taking place.

Convective stars are approximately isentropic, such that they may be approximated by an $n = 3/2$ polytrope, with total energy given by

$$E_{\rm T} = U + V = -U = -\frac{3}{7}\frac{GM_*^2}{R_*}, \tag{3.10}$$

where M_*, R_*, U and V are the stellar mass, radius, internal energy and gravitational potential energy, respectively. When a gas element is accreted by the star, it adds a gravitational potential energy per unit mass of $-GM_*/R_*$ and an internal energy of $\epsilon GM_*/R_*$ to the star, where $\epsilon < 1$ describes the efficiency of the conversion of gravitational potential energy to luminosity by the accretion flow. This is set to 1 by the disc-accretion algorithm (see Section 3.2) For the star to retain a polytropic configuration, the balance of energy requires

$$\frac{\rm d}{{\rm d}t}\left(-\frac{3}{7}\frac{GM_*^2}{R_*}\right) = \dot{M}\frac{GM_*}{R_*}(\epsilon - 1) - \frac{{\rm d}E_{\rm surf}}{{\rm d}t} + L_{\rm D}, \tag{3.11}$$

where $\dot{M}$ is the mass accretion rate, ${\rm d}E_{\rm surf}/{\rm d}t$ is the rate of radiative energy loss from the stellar surface, and $L_{\rm D}$ is the deuterium fusion luminosity.

In the case of boundary accretion from a circumstellar disc, the accretion affects only a small fraction of the stellar surface. The surface energy loss can therefore be split into two terms:

$$\frac{{\rm d}E_{\rm surf}}{{\rm d}t} = 4\pi R_*^2[\delta F_{\rm acc} + (1-\delta)\sigma_{\rm SB}T_{\rm eff}^4]. \tag{3.12}$$

Accretion occurs over a fraction δ of the stellar surface. $F_{\rm acc}$ is the radiative flux averaged over the accreting region $F_{\rm acc}$. The rest of the stellar surface radiates with a temperature $T_{\rm eff}$. **In the limit where $\delta \to 0$, the most of the stellar surface radiates freely, such that the stellar luminosity can be written as**

$$L_{\rm phot} = 4\pi R_*^2(1-\delta)\sigma_{\rm SB}T_{\rm eff}^4 \simeq 4\pi R_*^2\sigma_{\rm SB}T_{\rm eff}^4. \tag{3.13}$$

This assumes that radiative transfer of energy between the accreting region and the stellar photosphere is negligible.

We combine the expression for the thermal energy gain with the expression for the radiative energy loss over the accreting surface to obtain

$$\dot{M}\frac{GM_*}{R_*}\alpha \equiv \dot{M}\frac{GM_*}{R_*}\epsilon - 4\pi R_*^2\delta F_{\rm acc}, \tag{3.14}$$

where α is the fraction of the accretion energy advected as thermal energy into the protostellar interior. The boundary of the accreting surface is assumed to be where the accreted material is in near hydrostatic equilibrium with the stellar surface.

Equation 3.10 may now be re-written as

$$L_{\rm phot} = -\frac{3}{7}\frac{GM_*^2}{R_*}\left[\left(\frac{1}{3} - \frac{7\alpha}{3}\right)\frac{\dot{M}}{M_*} + \frac{\dot{R}}{R_*}\right] + L_{\rm D}, \tag{3.15}$$

which describes the evolution of the protostellar structure according to the internal energy balance. In the case where $\dot{M} = 0$ and $L_{\rm D} = 0$, **the only source of energy generation is the gravitational contraction of the star, and equation 3.15 reduces to the standard result:**

$$L_{\rm phot} = -\frac{3}{7}\frac{GM_*^2}{R_*}\frac{\dot{R}}{R}. \tag{3.16}$$

This is used to evolve the structure of the protostar according to the accretion rate, $\dot{M}$, calculated by the disc-accretion algorithm. The new intrinsic protostellar luminosity is then combined with the accretion luminosity calculated using equation 3.2 to obtain the total luminosity of the protostellar system, which is included in the SPH calculation using the method described in Section 3.2.1.

Chapter 4

The dependence of stellar properties on initial cloud density

In Chapter 1, we described previous investigations into the dependence of the properties of stellar clusters on the environmental conditions in which they form. Several of these studies showed that the inclusion of radiative feedback and the use of a realistic equation of state prevents the over-production of low-mass objects, and may suppress variations in cluster properties due to changes in their initial conditions. Bate (2009c) showed that it may also result in a median stellar mass which depends only weakly on initial density. However, these calculations were small and produced only a few protostars, making weak variations in the median stellar mass difficult to detect statistically.

In this chapter, we simulate the formation of star clusters from the collapse of turbulent, molecular clouds, which differ in their initial densities but are otherwise identical. **Such differences in density may arise due to compressions in the ISM driven by spiral arm induced collisions between clouds (Dobbs et al. 2008), gravitational instabilities (Kim and Ostriker 2006), or stellar feedback (de Avillez and Mac Low 2001; Clark et al. 2012) (see Section 1.1.1), and manifest in observations as gravitationally bound regions of enhanced density.** We use initial conditions similar to those of Bate (2009c), but simulate clouds that are ten times more massive than the original calculations, and equivalent in mass to those of Bate (2012). The increased scale of these new calculations allows us to test the predictions of Bate (2009c) using a more thorough statistical analysis than was previously possible.

Section 4.1 describes our numerical method, and the initial conditions for each of the calculations. In Section 4.2, we present the results of the three cluster calculations, including an analysis of the cluster density and temperature structures, mass functions and multiple system properties. In Section 4.3, we discuss the results in the context of previous calculations, and compare them to recent observations of stellar populations.

Table 4.1: The initial properties of the molecular clouds which vary in initial density by a factor of 100. The gas spheres each contain 500 $M_\odot$ of gas, but vary in radius such that their initial densities vary by factors of 10 over a total range of 2 orders of magnitude. The initial temperatures of the spheres are 10.3 K, and they all begin with a turbulent velocity field defined by the power law $P \propto k^{-4}$.

Cloud Radius (pc)	Cloud Mass ($M_\odot$)	Mean Density (g cm^{-3})	Temperature (K)
0.188	500	1.2×10^{-19}	10.3
0.404	500	1.2×10^{-20}	10.3
0.870	500	1.2×10^{-21}	10.3

Our conclusions are then presented in Section 4.4.

4.1 Computational method

To model the gas and protostars, we used the `sphNG` code, described in Chapter 2. **The calculations were performed using the DiRAC Complexity supercomputer using 32 nodes and a total of 512 cores. The approximate wall-time of each calculation was** ~ 36 **months.** The calculations include hydrodynamical and gravitational forces, as well as radiative transfer. Protostars are modelled using sink particles, as described in Chapter 3, with accretion radii of 0.5 AU.

The sink particles used in these calculations do not emit radiation. By omitting radiation from inside sink particles, the protostellar luminosities are underestimated by a factor of $\approx R_{\rm acc}/R_*$. Bate (2012) discussed of the potential effects of this and concluded that **using** $R_{\rm acc} = 0.5$ **AU provided sufficient protostellar luminosity to suppress the majority of the anomalous fragmentation that occurs without radiative transfer, and gave a star to brown-dwarf ratio that was in good agreement with observed values.** We take the same approach, and discuss the implications for our results in Section 4.3.

4.1.1 Initial conditions

We simulate three turbulent, uniform density gas clouds, using the same initial conditions as Bate (2012), but varying the initial densities by factors of 10, 1, and 0.1 (i.e. over a range of a factor of 100). This is achieved by constructing uniform spheres containing 500 $M_\odot$ of gas, with radii of 0.188 pc, 0.404 pc and 0.870 pc. The initial mean densities of the sphere are therefore 1.2×10^{-19} g cm^{-3}, 1.2×10^{-20} g cm^{-3} and 1.2×10^{-21} g cm^{-3}, corresponding to number densities of $\sim 3 \times 10^4$ cm^{-3}, $\sim 3 \times 10^3$ cm^{-3} and ~ 300 cm^{-3} respectively. **These properties are summarised in Table 4.1.** The initial temperatures of the spheres are set at 10.3 K. While real molecular clouds of different densities may be expected to have somewhat different temperatures (e.g. due to different levels of extinction), in this study we wish to vary only one parameter at a time so we do not vary the initial temperature.

An initial 'supersonic', turbulent velocity field is applied to each cloud, in the manner described by Ostriker et al. (2001) and Bate et al. (2003). To do this, a divergence-free, random Gaussian field is generated with a power spectrum of $P \propto k^{-4}$, where k is the wavenumber, giving a velocity dispersion which varies with distance λ as $\sigma(\lambda) \propto \lambda^{-1/2}$ in three dimensions, in agreement with the Larson scaling relations for molecular clouds (Larson 1981). The field is generated on a 128^3 grid and the velocities interpolated from the grid. The field is normalised such that the total kinetic energy was equal to the gravitational potential energy of the sphere. The molecular clouds have free boundaries. However, to provide a boundary for the radiation field, all SPH particles with a density less than 10^{-21} g cm^{-3} have both their gas and radiation temperatures set to 10 K. The initial free-fall times of the clouds are 1.90×10^{12} s (6.0×10^4 yr), 6.00×10^{12} s (1.90×10^5 yr) and 1.90×10^{13} s (6.0×10^5 yr).

The random seed used to realise the velocity field used in these calculations differs from that used in the calculation by Bate (2012). If the statistical properties of stars and brown dwarfs depend only on global quantities, the results should be unaffected by a change in the random seed. Since we reproduce the same initial conditions as the 0.404 pc case in Bate (2012), by using different random seeds we are able to test this hypothesis.

4.1.2 Resolution

To correctly model fragmentation down to the opacity limit, the local Jeans mass must be resolved (Bate and Burkert 1997; Truelove et al. 1997; Whitworth 1998; Boss et al. 2000; Hubber et al. 2006). As in Bate (2012, 2014), we use 3.5×10^7 particles to model the 500 $M_\odot$ clouds, giving a mass resolution of 1.4×10^{-5} $M_\odot$ per particle (7×10^4 particles per $M_\odot$), **which allows us to resolve the minimum Jeans mass of ~ 1 M_J.**

4.2 Results

We present results from the three radiation hydrodynamical simulations of star-cluster formation, varying in initial density by up to a factor of 100. The calculations were run for 1.20 initial cloud free-fall times, by which time the 0.188 pc, 0.404 pc and 0.870 pc clouds had produced 474, 233 and 87 stars and brown dwarfs, with total stellar masses of 91.2 $M_\odot$, 43.2 $M_\odot$ and 13.2 $M_\odot$, respectively.

We follow a similar analysis to that of Bate (2012) and Bate (2014). However, we focus our discussion on the final state of each cluster and their statistical properties. In Section 4.2.1, we describe the density and temperature structure of each cluster. In Section 4.2.2, we examine the stellar mass distributions of the clusters, and compare them to analytical

models and previous results. Sections 4.2.3, 4.2.4 and 4.2.5 give details of the multiple systems produced in each calculation, comparing the multiplicities, separation distributions and mass distributions. We omit more detailed aspects of the multiple system properties, such as orbit orientations and eccentricities, as well as the time evolution and kinematic properties of the clusters.

4.2.1 Density & temperature distributions

Fig. 4.1 shows the gas column-density and mass-weighted temperature distributions at the end of each of the calculations. In all cases the initial 'turbulent' velocity field results in filamentary structure. Dense cores form in regions where filaments meet, as shocks dissipate the turbulent energy initially supporting the cloud, allowing local regions of the cloud to collapse (see Bonnell et al. 2003, Gómez and Vázquez-Semadeni 2014). These cores become the primary sites of star formation in the cloud, heating the surrounding regions as gas falls into the potential well of the core and is accreted by the protostars within.

The higher the initial density of the molecular cloud, the greater the initial number of Jeans masses contained within it. This leaves the gas more unstable to fragmentation. The effect is clear in the high-density 0.188 pc calculation, as large regions undergo rapid fragmentation, resulting in a single star-forming core that encompasses much of the cluster. The lower density of the 0.404 pc and 0.870 pc calculations gives rise to more dispersed regions of star formation, as the initial Jeans length is larger and the distance between regions unstable to collapse is increased. The level of instability to collapse is also reflected in the star formation rates and star formation efficiencies of the clusters, which increase with higher initial cloud density. The mean star formation rates are 1.26×10^{-3} $M_\odot$ yr^{-1}, 0.19×10^{-3} $M_\odot$ yr^{-1}, and 0.02×10^{-3} $M_\odot$ yr^{-1} for the 0.188 pc, 0.404 pc and 0.870pc clouds, respectively. **The corresponding star formation efficiencies per free-fall time are 15%, 7% and 2% for the 0.188 pc, 0.404 pc and 0.870 pc clouds, respectively.**

As the temperature of a region heated by an embedded source increases with luminosity and decreases with distance from the source, regions where star formation is more heavily concentrated are heated to higher temperatures. The higher gas density in these regions also increases the optical depth, trapping radiation emitted by the accreting protostars and heating the star-forming core. The high star formation rate and short distances between protostars in the 0.188 pc calculation result in a large heated region approximately 0.2 pc in diameter with temperatures of $\approx 20 - 50$ K. The 0.404 pc and 0.870 pc calculations also contain heated regions. However, at these lower densities, the cores become more isolated and the heated regions are smaller.

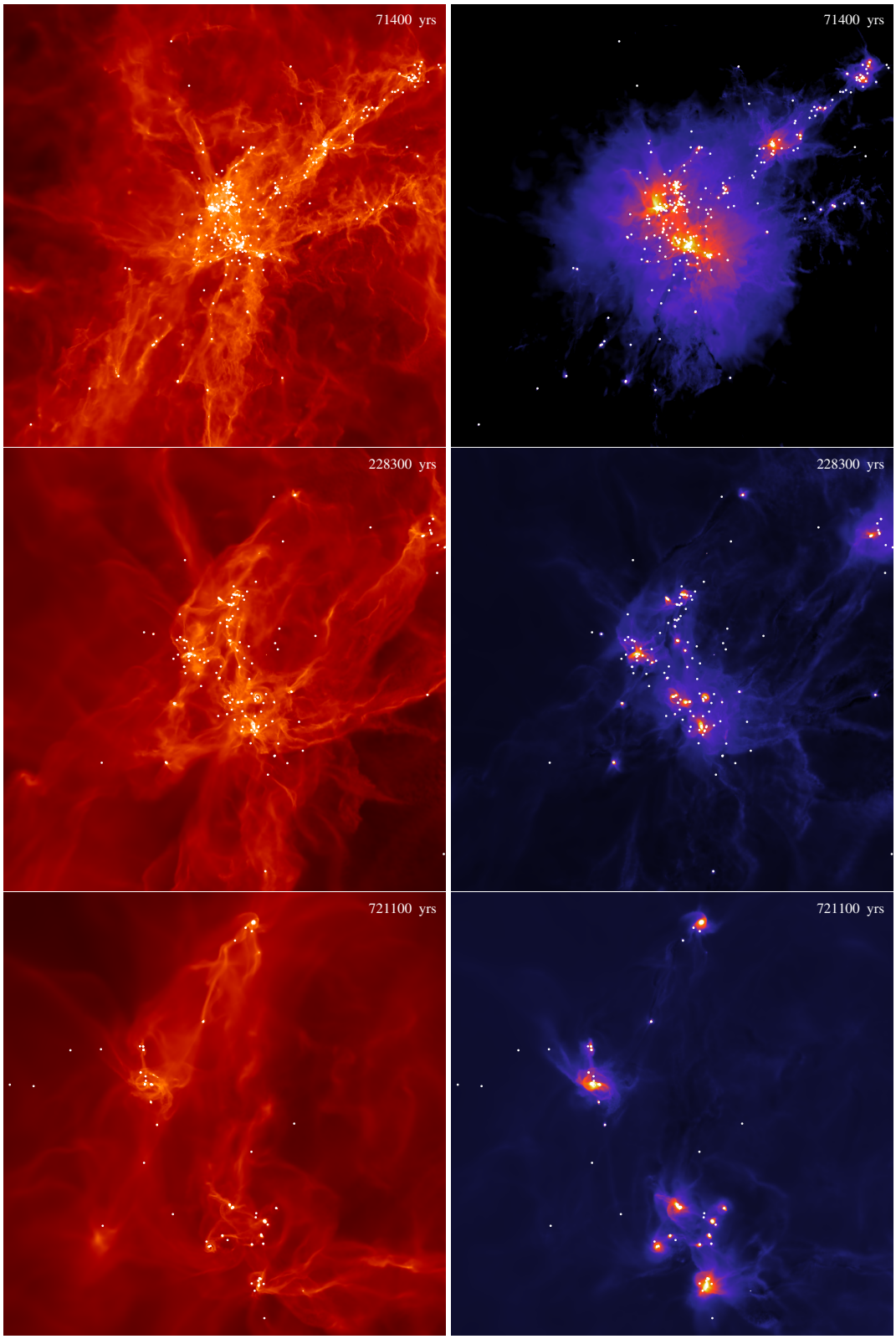

Figure 4.1: The gas column density (left column) and mass-weighted temperature (right column) in the each of the cluster calculations at time $t = 1.2\ t_{\rm ff}$. The top, middle and bottom rows show the clouds with initial radii of 0.188 pc, 0.404 pc and 0.870 pc, respectively. The colour scales show column densities on a logarithmic scale between 0.01 g cm^{-2} and 100 g cm^{-2}, and temperatures on a logarithmic scale between 9 K and 50 K. Each panel is 0.4 pc (82333 AU) across, with the time in years is displayed in the top-right corner. White dots indicate the locations of stars and brown dwarfs. The dissipation of energy via shocks allows local regions of the clouds to undergo gravitational collapse, producing dense, star-forming cores. Increasing the mean density of the cloud has the effect of producing a more centrally concentrated distribution of cores in the clusters.

4.2.2 The initial mass function

Fig. 4.2 shows the differential mass functions at the end of each of the three calculations. We compare each with the parameterisation of the observed Galactic IMF by Chabrier (2005). **The median stellar masses of the clouds are** 0.01 $\mathbf{M_\odot}$ **for the 0.188 pc calculation,** 0.18 $\mathbf{M_\odot}$ **for the 0.404 pc calculation, and** 0.24 $\mathbf{M_\odot}$ **for the 0.870 pc calculation. These are substantially lower than the initial thermal Jeans masses of the clouds, which are** 0.32 $\mathbf{M_\odot}$**,** 1 $\mathbf{M_\odot}$ **and** 3.16 $\mathbf{M_\odot}$ **for the 0.188 pc, 0.404 pc, and 0.870 pc calculations, respectively. This reflects the fact that objects typically form in regions where the gas density is significantly higher than the initial mean density of the cloud. The numbers of objects formed in each of the calculations are also lower than the number of thermal Jeans masses initially contained within the cloud, which are 1582, 500 and 158 for the 0.188 pc, 0.404 pc, and 0.870 pc calculations, respectively. This is in part due to the fact that star formation has not ceased the end of the calculations, and therefore the number of objects would be expected to increase further with time. However, the number of objects is likely to remain lower than the number of thermal Jeans masses due to the inclusion of radiative transfer, which raises the temperature of the gas and increases the effective Jeans mass. We discuss this mechanism in detail in Section 4.3.**

It is clear that increasing the initial density of the cloud results in the production of more low-mass stars and fewer intermediate-mass stars, whereas the converse is true for decreasing density. This results in a shift in the characteristic (median) stellar mass between each of the calculations. **If a relationship of the form** $M_\mathrm{c} \propto \rho^{-n}$ **is assumed, then these shifts imply exponents of 0.27 between the highest density and intermediate density calculations, 0.12 between the lowest density and intermediate density calculations, and 0.19 between the highest and lowest density calculations. The arithmetic mean of these exponents is 0.19.** The mass function also becomes noticeably 'broader' as the initial density of the cloud decreases. This is reflected in an increase in the standard deviations of the distributions, which are 0.469 dex for the 0.188 pc calculation, 0.543 dex for the 0.404 pc calculation, and 0.594 dex for the 0.870 pc calculation. As such, although the results of the 0.404 pc calculation are in good agreement with the parameterisation by Chabrier (2005), the IMFs produced by increasing or decreasing the initial cloud density from the 0.404 pc case differ significantly, with the 0.188 pc calculation producing too many low-mass stars and brown dwarfs, and the 0.870 pc calculation producing too many intermediate-mass stars.

Fig. 4.3 shows the cumulative mass function for each of the calculations. Again, we plot the parameterisation by Chabrier (2005) and also include the result from Bate (2012) for comparison. The overproduction of low-mass objects in the 0.188 pc calculation is even more apparent here, with stars of mass $\leq$ 0.1 $\mathrm{M_\odot}$ making up 48% of the produced population, compared with 36% in the 0.404 pc calculation. Also evident is the excess of intermediate-mass objects in the 0.870 pc calculation, with 24% of the stellar population

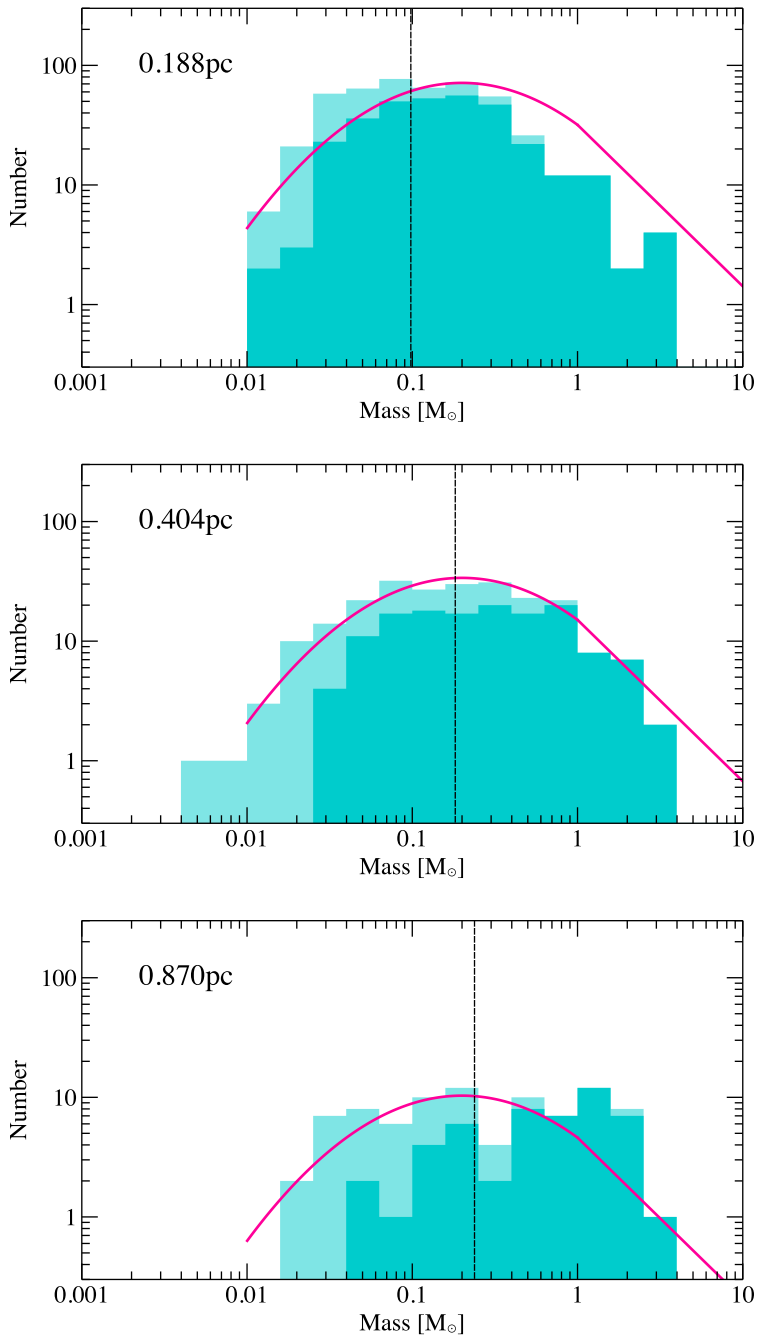

Figure 4.2: The distribution of stellar and brown dwarf masses in the each of the cluster calculations at time $t = 1.2\ t_{\rm ff}$. The dark shaded areas represent objects that have are still accreting when the calculations were stopped (defined as accreting at a rate if less than 10^{-7} M$_\odot$ yr^{-1}), and the light shaded areas show those that have stopped accreting. **The median masses of the distributions are shown by the black dashed lines.** We also plot the parameterisation of the observed Galactic IMF by Chabrier (2005) in magenta for comparison. There is a weak, but clear dependence of the shape of the IMFs on the mean cloud density. Increasing the mean density of the cloud appears to increase the relative number of low-mass stars produced, and decrease the number of intermediate-mass stars. Decreasing the cloud mean density has the inverse effect.

having a mass ≥ 1.0 M$_\odot$, compared with 7% in the 0.404 pc calculation and 10% in the Chabrier IMF. This qualitative observation is confirmed by running Kolmogorov-Smirnov tests between the pairs of distributions, which give probabilities of 1×10^{-6} and 9×10^{-5} of the 0.188 pc and 0.870 pc populations, respectively, being drawn from the same underlying distribution as the 0.404 pc population. The probability that the 0.188 pc and 0.870 pc populations are drawn from the same underlying distribution is only 2×10^{-9}.

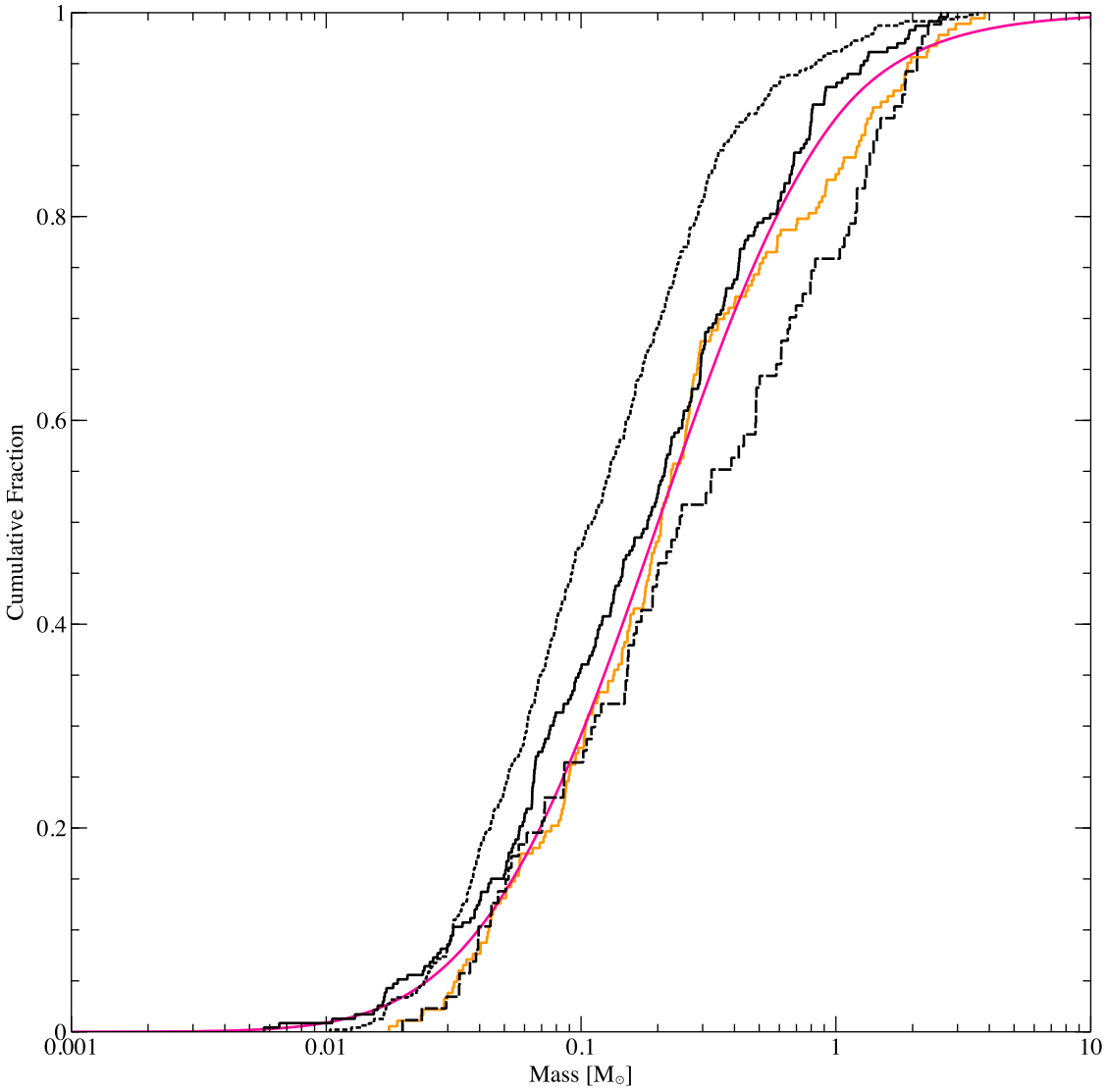

Figure 4.3: The cumulative distribution of stellar and brown dwarf masses in the each of the calculations at time $t = 1.2\ t_{\rm ff}$. Results from the 0.188 pc calculation are shown by the dotted line, the 0.404 pc results by the solid line, and the 0.870 pc results by the dashed line. We also plot the Chabrier (2005) parameterisation of the IMF in magenta and the results of Bate (2012) in orange for comparison. Here the differences between the mass distributions produced by the calculations are clear. The results of the 0.404 pc calculation are in good agreement with both the Chabrier (2005) and Bate (2012) mass functions, however there is an excess of low-mass objects formed in the 0.188 pc calculation, and an excess of intermediate-mass stars in the 0.870 pc calculation.

We also note that the results of our 0.404 pc calculation and those of the previous 0.404 pc calculation by Bate (2012) are statistically indistinguishable, with a 0.149 probability of

being drawn from the same underlying distribution according to a Kolmogorov-Smirnov test. This shows that the mass functions are insensitive to the particular random realisation of the initial velocity field, as we use different seeds to those used in the previous calculation.

It should be noted here that the 'IMFs' plotted here are actually protostellar mass functions (PMFs; see McKee and Offner 2010 Offner and McKee 2011). As shown by the dark-shaded areas in Fig. 4.2, a number of objects are still accreting (defined as having an accretion rate $\geq 10^{-7}$ $M_\odot$ yr^{-1}) by the end of the calculations. Bate (2012) found that the distributions of stellar properties evolved such that data taken at any instant of time was representative of the same underlying distribution. Stopping the calculations at 1.2 t_{ff} therefore does not affect that statistical analysis presented here, as the forms of the distributions are expected to remain constant throughout the duration of the simulation. Therefore, for the remainder of this thesis, we refer to the distribution of masses in each cluster as 'IMFs' and compare them to observed IMFs, as current methods are unable to accurately determine the PMFs of clusters observationally.

4.2.3 Multiplicity as a function of primary mass

To quantify the relative abundance of multiple systems in each calculation, we use the multiplicity fraction as in Bate (2009c) and Bate (2012), defined as a function of stellar mass by

$$f = \frac{B + T + Q}{S + B + T + Q} \tag{4.1}$$

where S, B, T and Q are the numbers of single stars, binaries, triples and quadruples with primary masses in the same mass range. As discussed in Bate (2012), this method is relatively insensitive to observational incompleteness and subsequent dynamical evolution.

We use the same algorithm to detect multiple systems as in Bate (2009c) and Bate (2012), details of which can be found in the former paper. Ambiguities arise when classifying the components of multiples systems, as some binary systems may be part of a triple or quadruple system, and similarly some triple systems may be part of a quadruple system. In this thesis, unless otherwise stated, we do not count multiples that are components of higher order systems separately (e.g. a binary system with a third wide companion would only contribute to the number of triples, and not to the number of binaries). We also choose to ignore systems of higher order than quadruples, as such systems are usually dynamically unstable and are therefore unlikely to remain if the calculations were evolved for longer.

Bate (2012) provided a detailed discussion of the formation and evolution of multiple systems in radiation hydro-dynamical calculations. In the interest of brevity we do not repeat it here, and instead focus on the effects of initial cloud density on the final states of

the simulated clusters. The total multiplicities for each of the calculations are 0.31, 0.34 and 0.33 for the 0.188 pc, 0.404 pc and 0.870 pc clouds respectively, each with 1σ uncertainties of ±5%. We therefore conclude that there is no significant variation in the overall multiplicity with initial cloud density.

Fig. 4.4 shows the multiplicity fraction as a function of primary mass for each of the calculations, and compares them with values obtained from various observational surveys (see caption for details). The solid line gives the continuous multiplicity fraction calculated using a lognormal moving average, with the associated 1σ and 2σ confidence limits shown by the dotted lines, and observations are shown by the squares with error bars. The multiplicity in each calculation increases steadily with primary mass, in agreement with observations of field stars by Mason et al. (2009) (massive stars), Patience et al. (2002) (intermediate-mass stars), Raghavan et al. (2010) (solar-type stars), Fischer and Marcy (1992) (M-dwarfs) and Basri and Reiners (2006) (very-low-mass stars and brown dwarfs).

However, whilst the multiplicities of the simulated clusters agree with the values observed for lower stellar masses, all of the calculations exhibit multiplicities higher than observed for solar-type stars. **Observations have shown that the multiplicity of young stars is often higher than the field value (Ghez et al. 1993; Simon et al. 1995; Duchêne 1999; Duchêne et al. 2004, 2007; Connelley et al. 2008; Tobin et al. 2016)**. Given the young age of the stars formed in the calculations, this provides a plausible explanation for the high values for solar-type stars. It is likely that, as the stellar population ages, some systems will decay through dynamic interactions, reducing the multiplicity.

4.2.4 Separation distributions of multiples

Fig. 4.5 shows the distributions of semi-major axes of all multiples systems with stellar primaries (i.e. $M \geq 0.1$ M$_\odot$) in each of the three calculations. Due to the low numbers of VLM systems produced by each of the calculations (19, 2 and 0 in the 0.188 pc, 0.404 pc and 0.870 pc calculations, respectively), we do not discuss their statistical properties. We compare with results from surveys of M-dwarfs by Janson et al. (2012), shown by the solid line, and solar-type stars by Raghavan et al. (2010), shown by the dotted line. It should be noted here that, although binaries are not assumed to merge until they reach a separation of 0.015 AU, the accretion radii of sink particles in the calculations are significantly larger (0.5 AU), preventing us from accurately modelling any interactions between the stars and gas within this radius, which may be important in the formation of closely-bound systems (Bate et al. 2002a). There is no obvious difference between each of the distributions, with each calculation's median separation in the range 10 – 100 AU, similar to observed stellar systems.

Fig. 4.6 displays the cumulative separation distributions for all systems (i.e. both stellar and VLM systems). We note a slight deficit of systems with separations > 100 AU in the

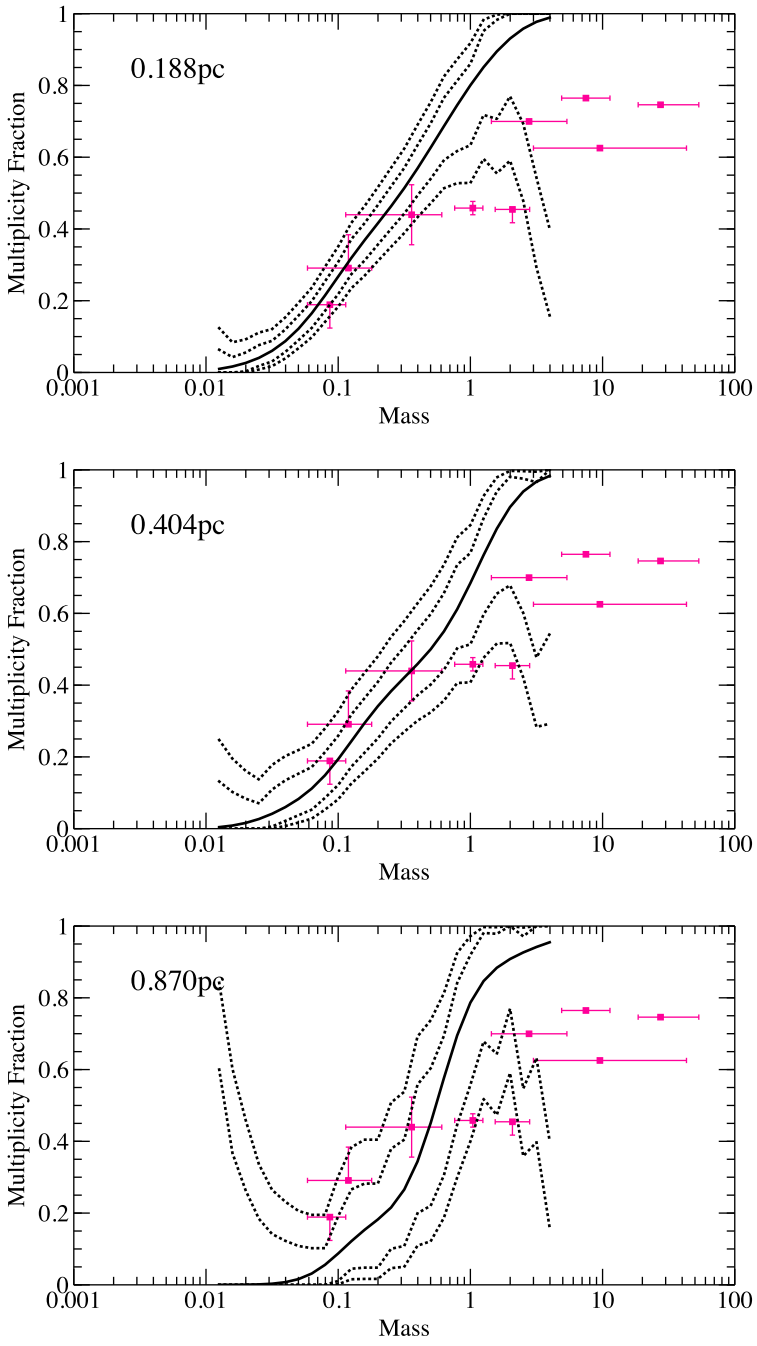

Figure 4.4: The multiplicity fraction as a function of primary mass in the each of the calculations at time $t = 1.2\ t_{\rm ff}$. The solid line shows the multiplicity fraction, calculated using a moving lognormal average, with the dotted lines representing the 1σ and 2σ confidence intervals around the solid line. Filled squares with error bars show the observed multiplicity fractions from surveys by Close et al. (2003), Basri and Reiners (2006), Fischer and Marcy (1992), Raghavan et al. (2010), Duquennoy and Mayor (1991), Kouwenhoven et al. (2007), Rizzuto et al. (2013), and Preibisch et al. (1999) and Mason et al. (1998). Each of the calculations produces and increasing multiplicity with primary mass, in qualitative agreement with observations. There is, however, an increased multiplicity for solar-type stars across all of the calculations when compared to observations by Raghavan et al. (2010). This may be due to the young age of the stellar population.

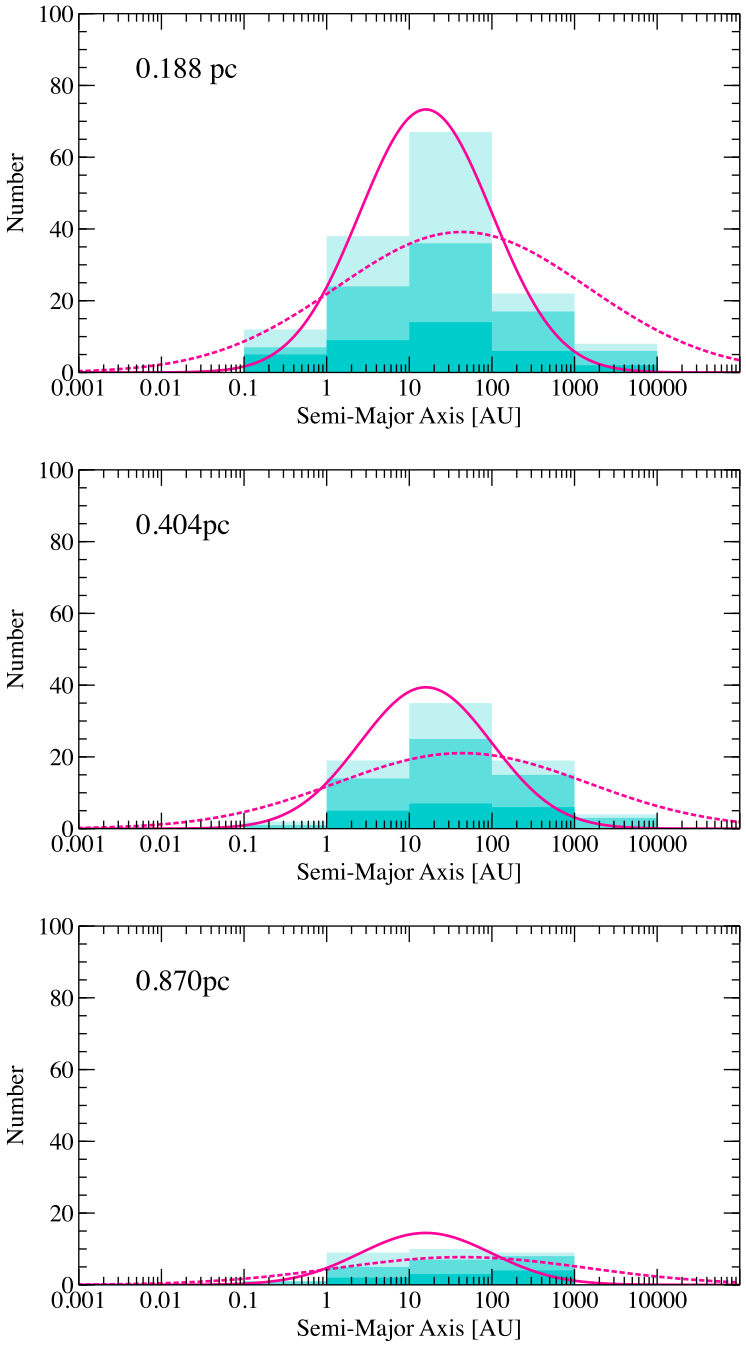

Figure 4.5: The distribution of semi-major axes in multiple systems with stellar primaries ($M_1 > 0.1\,M_\odot$) in the each of the cluster calculations at time $t = 1.2\,t_{\rm ff}$. The light shaded areas show the semi-major axes of binaries; the medium shaded areas show the semi-major axes from triples (two from each triple); and the dark shaded areas show the semi-major axes from quadruple systems. We also plot M-dwarf separation distribution from the M-dwarf survey of Janson et al. (2012) (solid line), as well as the solar-type separation distribution from Raghavan et al. (2010) (dotted line) in magenta for comparison. There is no significant difference between the distributions, and all are in reasonable agreement with the parameterisations shown. As noted in Bate (2014), the results are expected to match the Janson et al. distribution better, as the the simulated systems are primarily low-mass.

0.188 pc calculation, which comprise ~ 20% of the total number of multiple systems, compared with ~ 30% of the total number of systems in the 0.404 pc and 0.870 pc calculations. This may be due to the dynamical disruption of systems with wide separations, as observed in star-forming regions in Orion (Petr et al. 1998; Scally et al. 1999). Kolmogorov-Smirnov tests performed on the distributions find that the 0.188 pc distribution is different from the 0.404 pc calculation at the 2σ level. Tests between the other calculations' distributions find them to be statistically indistinguishable. The distributions of binary, triple and quadruple systems in all of the calculations are similar, although the numbers of systems are small. There is a noticeable lack of close-binaries with separations less than 0.5 AU in all of the calculations. This is likely due to the lack of dissipative effects caused by the size of the sink particle accretion radii.

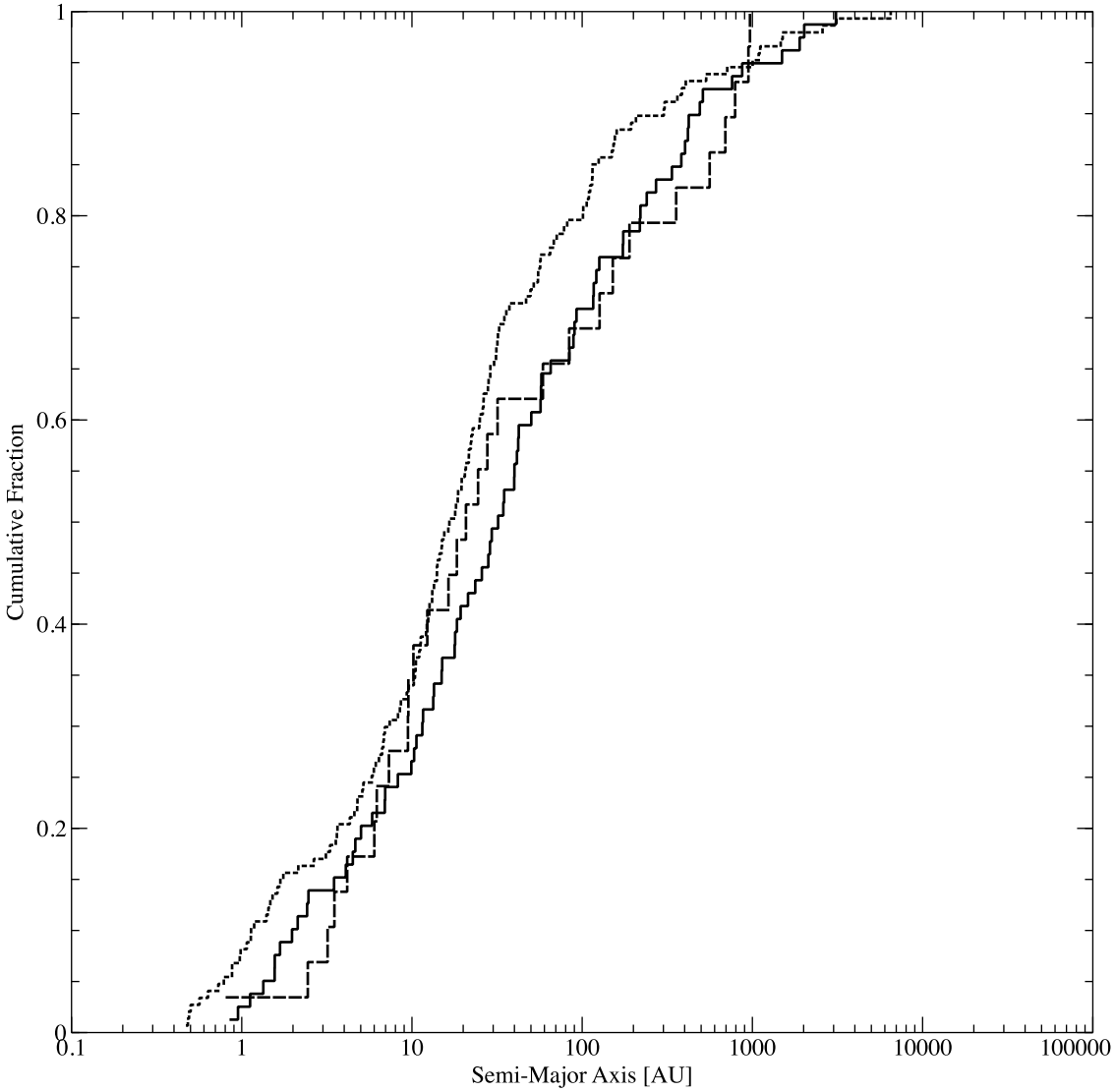

Figure 4.6: The cumulative distribution of semi-major axes for all multiple systems in the each of the cluster calculations at time $t = 1.2\ t_{\rm ff}$. Results from the 0.188 pc calculation are shown by the dotted line, the 0.404 pc results by the solid line, and the 0.870 pc results by the dashed line. We include all orbits from binary, triple and quadruple systems. Kolmogrov-Smirnov tests performed on the distributions show that they are statistically indistinguishable.

4.2.5 Mass-ratio distributions of multiples

Fig. 4.7 shows the distribution of mass-ratios of systems with stellar primaries (i.e. $M \geq 0.1$ $M_{\odot}$) in each calculation. We consider only binary systems here, but include binary components of higher-order multiples. We also plot mass ratio distribution of solar-type binaries from Raghavan et al. (2010) for comparison. Once again, the distributions are similar, with no clear peak value except in the case of the 0.188 pc, which produces a large number of systems with mass ratios in the 0.6-0.7 range compared to the other calculations. There is also an absence of systems with ratios less than 0.1 across all of the distributions. This is consistent with the expectations of a 'brown dwarf desert' noted by Raghavan et al. (2010).

Fig. 4.8 shows the cumulative distribution of binary mass ratios in each calculation (including VLM binaries). Despite the excess in the number of systems in the 0.6-0.7 range in the 0.188 pc calculation, Kolmogorov-Smirnov tests show that all three of the distributions are statistically indistinguishable from each other. Overall, the distributions are similar to those presented in Bate (2012, 2014), and are in good agreement with the Janson et al. (2012) and Raghavan et al. (2010) results. As with the previous section, we do not discuss the properties of VLM systems, as too few were produced.

4.3 Discussion

With the three calculations presented in this chapter, we have investigated the effects of changing the initial density of a star-forming molecular cloud on the properties of the resultant stellar populations. Having simulated clouds varying in initial density by two orders of magnitude, we have found evidence of a dependence of the chacteristic stellar mass on the initial cloud density of approximately as $M_{\rm c} \propto \rho^{-1/5}$, but no significant change in the multiple system properties. We now compare these results to previous theoretical studies and observational surveys.

4.3.1 The dependence of the IMF on density

Several authors have put forward theories to explain the apparent universality of the IMF. Each of these theories differs from the others in its predictions about the dependencies of the characteristic stellar mass which, along with the mass spread, defines the IMF. In particular, they all predict a different scaling of the characteristic mass with molecular cloud density. With the results presented in this chapter, we are now in a position to compare these predictions.

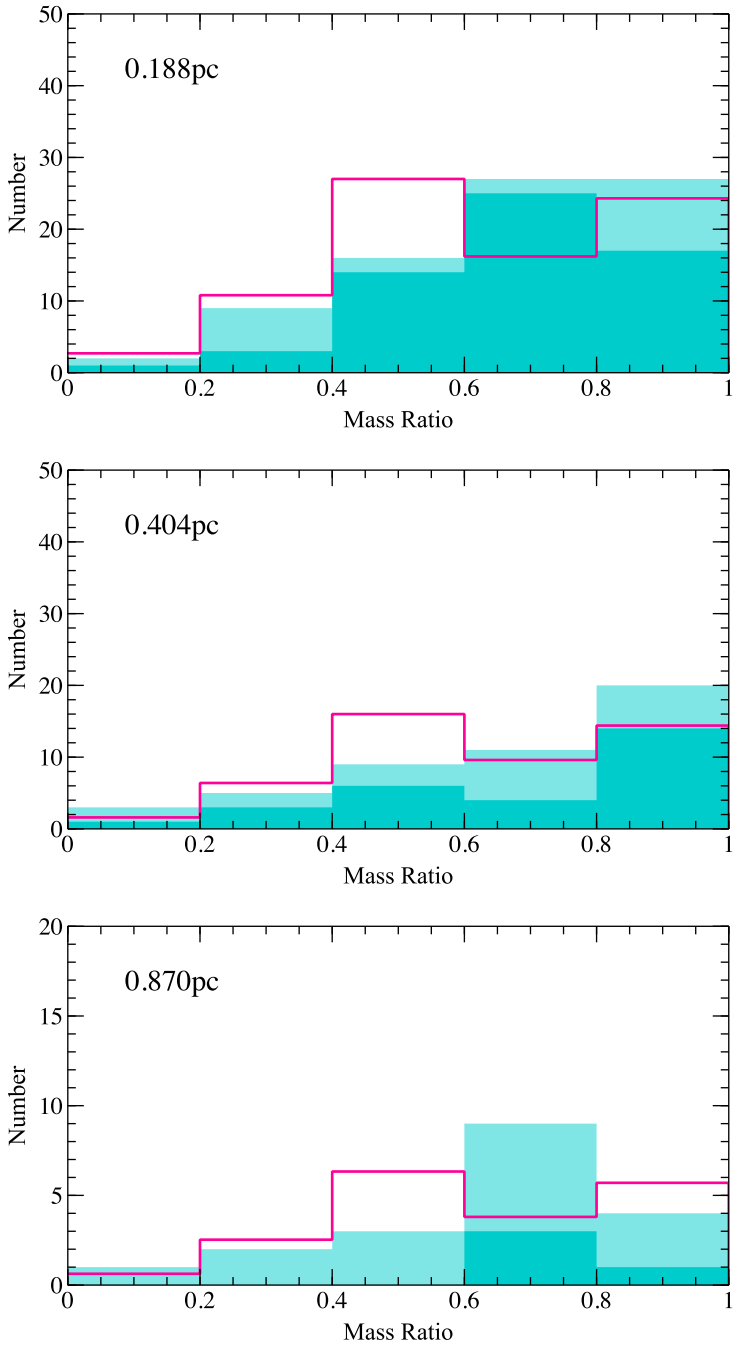

Figure 4.7: The distribution of mass ratios of stellar pairs in the each of the cluster calculations at time $t = 1.2\ t_{\rm ff}$. The light shaded areas show the ratios of systems with stellar primaries in the mass range $M_1 > 0.5\ M_\odot$, and the dark shaded areas show the ratios of systems with stellar primaries in the mass range $M_1 = 0.1 - 0.5\ M_\odot$. We include the ratios of binaries and binary components of higher-order systems. We also plot the results of Raghavan et al. (2010) in magenta for comparison. The 0.870 pc calculation produces an excess of systems in the 0.6-0.7 range, but there are otherwise no clear differences between the distributions, which are in good agreement with the observations.

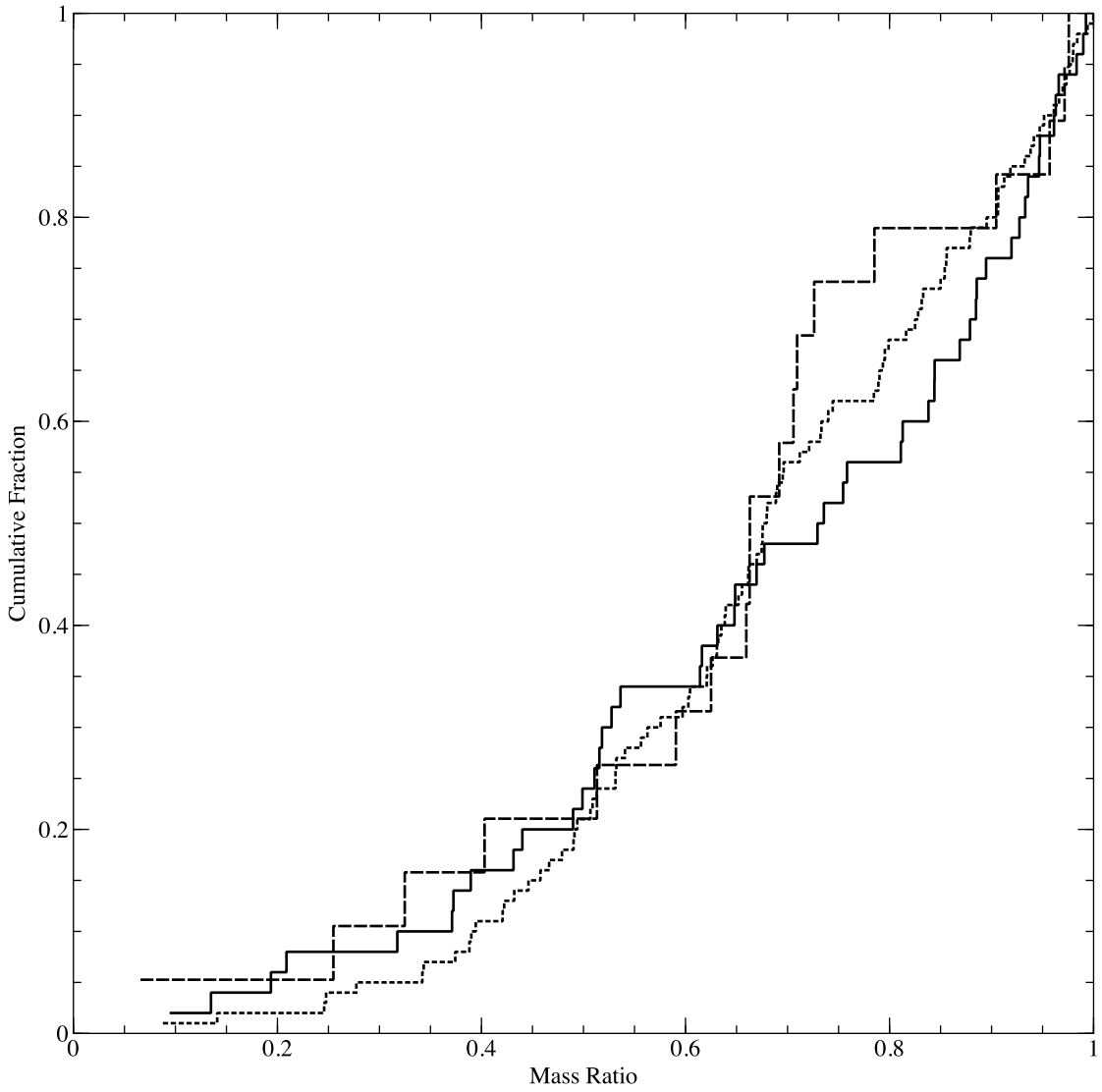

Figure 4.8: The cumulative distribution of mass ratios in multiple systems in the each of the cluster calculations at time $t = 1.2\ t_{\rm ff}$. Results from the 0.188 pc calculation are shown by the dotted line, the 0.404 pc results by the solid line, and the 0.870 pc results by the dashed line. We include the ratios of binaries and binary components of higher-order systems. An excess of systems in the $0.7 - 0.9$ range in the 0.870 pc calculation is evident, but the distributions are otherwise in good agreement with each other. Kolmogorov-Smirnov tests performed on the distributions show there are no statistically significant differences between the distributions.

4.3.1.1 Jeans mass

When attempting to predict the characteristic (median) mass of the IMF, the thermal Jeans mass is a natural starting point (Larson 1998, Larson 2005). The Jeans length and associated Jeans mass for a gas cloud of uniform temperature and density can be written as

$$\lambda_{\rm Jeans} = \frac{c_{\rm s}}{\sqrt{G\rho}}, \tag{4.2}$$

$$M_{\rm Jeans} = \frac{4}{3}\pi\lambda_{\rm Jeans}^3\rho, \tag{4.3}$$

where c_s is the gas sound speed, and ρ is the gas density. Combining equations 4.2 and 4.3 gives the following form for the Jeans mass

$$M_{\rm Jeans} \propto \frac{c_{\rm s}^3}{\sqrt{\rho}}. \tag{4.4}$$

For a molecular cloud of total mass M, the gas will be divided up into $\sim M/M_{\rm Jeans}$ objects. In the absence of other effects, these gravitationally bound structures will tend to collapse to form protostars with masses equal to $M_{\rm Jeans}$. However, density perturbations, competitive accretion and dynamical interactions between protostars in the same cluster ensure that some stars are able to accrete more material than others, broadening the distribution of masses to create an IMF (Bonnell et al. 1997). From this simple analysis it seems clear that the median mass of the IMF should scale with cloud density according to the Jeans mass, which, from equation 4.4, depends on density as $M_{\rm Jeans} \propto \rho^{-1/2}$.

Numerical calculations of star formation in molecular clouds confirm a linear dependence of the characteristic stellar mass on the global Jeans mass when using a barotropic gas equation of state. Bate and Bonnell (2005) compared two hydrodynamical simulations of star formation which used identical initial conditions, but which varied in initial density by a factor of 9 (factor of 3 in $M_{\rm Jeans}$), and found that the median mass of the cluster populations varied by a factor of 3 between the calculations. Subsequent calculations by Bonnell et al. (2006) confirmed this scaling, and found that the 'knee' of the IMF, i.e. the mass at which the form of the IMF transitions from a flat slope to a steeper slope of the type described by Salpeter (1955), was located at the approximate mass scale of the initial Jeans mass of the cloud.

Calculations performed by Jappsen et al. (2005) using a piecewise polytropic equation of state found that the median mass was dependent on the critical number density, $n_{\rm c}$, at which the dominant form of cooling was assumed to switch from molecular line cooling to thermal cooling, as $M_{\rm c} \propto n_{\rm c}^{-1/2}$. This led them to suggest that the balance between heating and cooling processes, which depend on fundamental physics and chemical abundances and can therefore be derived from universal quantities and constants, determined the characteristic stellar mass, a view supported by Bonnell et al. (2006).

Elmegreen et al. (2008) expanded upon this idea, considering star formation in three distinct environments: dense star-forming cores, the ambient interstellar medium (ISM), and ionising clusters. In dense cores, which most closely resemble the calculations presented in this chapter, Elmegreen et al. proposed that molecular cooling resulted in a Jeans mass with a dependence on the particle number density of $M_{\rm Jeans} \propto n^{1/4}$ at the grain-gas coupling point. This relative insensitivity of the Jeans mass to environmental conditions would then give rise to an approximately constant median stellar mass.

4.3.1.2 The role of radiative feedback

The first paper to propose radiative heating from protostars as a method of generating a universal IMF was Bate (2009c). Similar to a theory put forward by Nayakshin (2006) to explain the apparent top-heavy IMF of stars observed near Sgr A* in the central region of the Galaxy, Bate suggested that radiative feedback from newly-formed, accreting protostars would heat surrounding gas, suppressing fragmentation and increasing the reservoir of gas available for accretion. This would explain the increased characteristic mass observed in the radiative calculation when compared with previous barotropic calculations, and provide a mechanism for the star formation process to regulate itself.

Results from radiative hydrodynamical calculations of star formation in 50 $M_\odot$ clusters by Bate (2009c) showed that the inclusion of radiative transfer weakened the dependency of the median stellar mass on the initial cloud density sufficiently to make any variation undetectable with the small number statistics provided by the numerical calculations. In order to explain this behaviour, **Bate proposed a simplified analytical model based on a spherically symmetric gas cloud of uniform density in which the centre has collapsed to form a protostar which then accretes from the surrounding cloud.** To test the predictions made by Bate (2009c), it is beneficial to review the arguments made in that paper. We provide a brief summary of the main points, but encourage interested readers to refer to Bate (2009c) for a more complete treatment.

Bate (2009c) begins by considering the case of gas that is optically thin to infrared radiation and well-coupled to the dust. The gas opacity is assumed to be independent of frequency for simplicity. As mentioned in Bate (2009c), the result including a wavelength dependent opacity is simple enough to derive, but complicates matters and does not change the conclusions significantly. Making these assumptions, the gas temperature, T, at a distance, r, from a spherically symmetric protostar of luminosity, L_* is obtained from

$$L_* = 4\pi r^2 \sigma_{\rm SB} T^4, \tag{4.5}$$

where $\sigma_{\rm SB}$ is the Stefan-Boltzmann constant.

It is possible to express the Jeans length $\lambda_{\rm Jeans}$ as the distance at which the sound speed

of the gas is equal to the escape velocity of the mass enclosed by a sphere of the same radius. This is written as

$$c_{\rm s}^2 = \frac{\mathcal{R}_{\rm g}}{\mu} T = \frac{GM}{\lambda_{\rm Jeans}}, \tag{4.6}$$

where $c_{\rm s}$ is the gas sound speed, $\mathcal{R}_{\rm g}$ is the gas constant, **and μ is the mean molecular weight.**

By combining equations 4.3, 4.5 and 4.6, we obtain expressions for the 'effective' Jeans mass, $M_{\rm eff}$, and Jeans length, $\lambda_{\rm eff}$ for a sphere of gas internally heated by a protostar embedded at its centre:

$$M_{\rm eff} = \rho^{-1/5} L_*^{3/10} \frac{4\pi}{3} \left(\frac{3\mathcal{R}_{\rm g}}{4\pi\mu G} \right)^{6/5} (4\pi\sigma_{\rm SB})^{-3/10}, \tag{4.7}$$

$$\lambda_{\rm eff} = \rho^{-2/5} L_*^{1/10} \frac{4\pi}{3} \left(\frac{3\mathcal{R}_{\rm g}}{4\pi\mu G} \right)^{2/5} (4\pi\sigma_{\rm SB})^{-1/10}. \tag{4.8}$$

From these two equations, we see that the effect of the heating from the protostellar luminosity is to modify the thermal Jeans mass, creating an 'effective Jeans mass' which depends only weakly on the gas density, with the form $M_{\rm eff} \propto \rho^{-1/5}$. There is also a dependence on the protostellar luminosity, of the form $M_{\rm eff} \propto L_*^{3/10}$. This will depend on both the properties of the accretion flow, and the structure of the protostar itself.

Bate (2009c) considered the luminosity of a 0.1 $\rm M_\odot$ protostar with a radius of 2 $\rm R_\odot$, accreting at a rate of 1×10^{-5} $\rm M_\odot$ $\rm yr^{-1}$, taken from the typical sink particle accretion rates in the calculations, and obtained a protostellar luminosity of 150 $\rm L_\odot$. Assuming an initial mean density of 1.2×10^{-19} g $\rm cm^{-3}$ and substituting into equation 4.7, Bate derived a characteristic mass of ≈ 0.5 $\rm M_\odot$.

As with the calculations in this chapter, the simulations of small stellar clusters performed by Bate (2009c) did not include radiative feedback from inside the sink accretion radius. Using an accretion radius of $R_{\rm acc} = 0.5$ AU, and assuming an approximate protostellar radius of $R_* = 2$ $\rm R_\odot$, the protostellar luminosity is underestimated by a factor of $R_{\rm acc}/R_* \sim 50$. Assuming equation 4.7 holds, this implies that the effective Jeans mass in the calculations maybe underestimated by up to a factor of ≈ 3. This order-of-magnitude calculation assumes that the protostellar luminosity is independent of the mean cloud density. In reality, the luminosity depends upon the mass accretion rate, which will depend on the density of surrounding material, and the protostellar mass-radius relation, which will depend on the entropy content of the protostar. Therefore, to obtain a more accurate expression for the effective Jeans mass, an expression for the protostellar luminosity in terms of the mass accretion rate and protostellar mass-radius ratio is required.

The dominant source of luminosity for newly formed protostars is the conversion of gravitational potential energy via the accretion of mass. The luminosity generated by this

process is given by

$$L_* = \epsilon \frac{GM_*}{R_*} \dot{M}, \tag{4.9}$$

where ϵ is the efficiency of energy conversion, M_* and R_* are the protostellar mass and radius, and $\dot{M}$ is the mass accretion rate. If we assume that the time-scale for the accretion of the surrounding gas cloud is $\approx \lambda_{\rm eff}/c_{\rm s}$, where $c_{\rm s}$ is the sound speed at radius $\lambda_{\rm eff}$ from the central protostar, we obtain an approximate accretion rate of

$$\dot{M} \sim \frac{M_{\rm eff} c_{\rm s}}{\lambda_{\rm eff}} = \frac{4\pi\rho\lambda_{\rm eff}^2}{3} \left(\frac{\mathcal{R}_{\rm g}}{\mu} T \right)^{1/2}. \tag{4.10}$$

Following the same steps as before, this gives an effective Jeans mass of

$$M_{\rm eff} \propto \left(\frac{M_*}{R_*} \right)^{3/7} \rho^{-1/14}. \tag{4.11}$$

The dependence on density is now much weaker, and there is a dependence on the ratio between protostellar mass and radius, which comes from the conversion of gravitational potential energy to luminosity as the protostar accretes. The effect of this second term is difficult to predict, as it will likely depend on the accretion rate as well as the entropy content of the protostar.

One final point of consideration is the effect of higher optical depths. Bate (2009c) briefly considered the case where the gas is optically thick to infrared radiation, which results in the transport of radiation becoming diffusive, finding an effective Jeans mass of

$$M_{\rm eff} \propto \rho^{-1/3} L_*^{1/3}. \tag{4.12}$$

The density dependence here is stronger than in the optically thin case, as is the luminosity dependence. Bate (2009c) did not discuss this case any further, suggesting that the conditions under which it applies (mean number densities $\geq 10^8$ cm^{-3}; temperatures ≥ 30 K) are very different to those in local star forming regions.

4.3.1.3 The potential impact of protostellar evolution

Krumholz (2011) attempted to extend the analysis of Bate (2009c) by including the effects of protostellar evolution in order to more accurately determine the accretion luminosity. Similar to Bate (2009c), Krumholz proposed that deviations from isothermality are the mechanism by which the characteristic mass scale of the IMF is defined. By relating accretion luminosity to the structure of protostars, Krumholz aimed to link the mechanism by which non-isothermal regions are created to fundamental physics, which would then provide an explanation for the universality of the IMF. Again, we review the main arguments of Krumholz (2011) for the purpose of comparison with the previous study by Bate (2009c)

and with the results of the calculations presented here.

Similar to Bate (2009c), Krumholz begins by considering the minimum mass able to gravitationally collapse to form a new protostar. Krumholz chooses the Bonnor-Ebert mass, which is approximately equal to the Jeans mass, and defined by

$$M_{\rm BE} = 1.18\sqrt{\left(\frac{k_{\rm B}T_{\rm e}}{\mu_{\rm H_2} m_{\rm H} G}\right)^3 \frac{1}{\rho_{\rm e}}}, \tag{4.13}$$

where $T_{\rm e}$ and $\rho_{\rm e}$ are the gas temperature and density at the edge of the sphere containing $M_{\rm BE}$. A fraction of this mass will be lost via outflows and jets, such that the final stellar mass will be $M_* = \epsilon_{\rm M} M_{\rm BE}$, where $\epsilon_{\rm M}$ is the fraction of collapsed mass accreted by the protostar.

To estimate the value of the characteristic mass, the temperature profile of the sphere must be calculated. So long as protostellar heating remains the dominant form of heating, the temperature of the sphere will depend upon the luminosity of the protostar.

As before, this requires an estimate of the accretion rate and mass to radius ratio of the protostar. Krumholz assumes an accretion rate $\dot{M} \approx \epsilon_{\rm M} M_{\rm BE}/t_{\rm dyn}$, based on the dynamic time of the sphere $t_{\rm dyn} \approx 1/\sqrt{G\bar{\rho}} = \sqrt{(3-k_\rho)/(3G\rho_{\rm e})}$ which, when combined with equation 4.9, results in a protostellar luminosity of

$$L_* = \epsilon_{\rm L}\epsilon_{\rm M}\sqrt{\frac{3G\rho_{\rm e}}{3-k_\rho}} M_{\rm BE}\psi, \tag{4.14}$$

where k_ρ is defined by the sphere's density profile as $\rho = \rho_{\rm e}(r/R)^{-k_\rho}$, and ψ is defined as $\psi \equiv GM_*/R_*$. **Note we have used $\epsilon_{\rm L} \equiv \epsilon$ to distinguish between $\epsilon_{\rm L}$, the efficiency of conversion of gravitational potential energy to luminosity, and $\epsilon_{\rm M}$, the fraction of collapsed mass accreted by the protostar.**

In order to derive the protostellar mass to radius relation, Krumholz considers the collapse of a prestellar core to form an $n = 3/2$ polytrope supported by deuterium burning. Solving the equations of stellar structure, the following relationship between the protostellar mass and radius can be written

$$\psi = \left(\frac{T_{\rm n}}{4\Theta_{\rm c}^3}\right)\frac{E_{\rm G}}{\mu_{\rm i} m_{\rm H}}, \tag{4.15}$$

where $T_{\rm n}$ is a normalisation constant, $\mu_{\rm i}$ is the mean molecular weight of ionised gas, $E_{\rm G} = 0.66$MeV is the Gamow energy and $\Theta_{\rm c}$ is related to the core temperature by $T_{\rm c} \approx E_G/(4k_{\rm B}\Theta_c^3)$.

By combining equations 4.13, 4.14 and 4.15, and assuming that Θ_c is independent of

protostellar mass, Krumholz obtains the following expression for the characteristic mass

$$M_* = m_{\rm H} \left(\frac{1.18^{64} 2^{69} 5^{21}}{3^{17} \pi^7} \right) \left(\frac{T_{\rm n}^4 \epsilon_{\rm L}^4 \epsilon_{\rm M}^{13}}{\mu_{\rm H_2}^{16} \mu_{\rm i}^4} \right)^{1/9} \left(\frac{\alpha_{\rm e}^{16}}{\alpha_{\rm G}^{25}} \right)^{1/18} \Theta_{\rm c}^{-4/3} \left(\frac{P}{P_{\rm P}} \right)^{-1/18} \tag{4.16}$$

where $\alpha_{\rm e}$ is the electromagnetic fine structure constant, $\alpha_{\rm G} = G m_{\rm H}^2 / (\hbar c) = 5.91 \times 10^{-39}$ is the gravitational fine structure constant for two protons and $P_{\rm P} = c^7 / (\hbar G^2) = 4.63 \times 10^{114}$ dyn cm^{-2} is the Planck pressure.

As Krumholz (2011) notes, the predicted characteristic mass depends largely on fundamental constants and dimensionless variables that describe either the geometry of the accretion flow, structure of the protostar or properties of the gas, and are of order unity. The only explicit dependence on the system's initial conditions is a very weak dependence on the interstellar pressure. Krumholz cites this as the reason behind the apparently universal form of the observed IMF, as variations in the interstellar pressure over a range of reasonable values produce results that would be indistinguishable observationally.

However, Krumholz relies upon the assumption that, following the second-stage collapse of a hydrostatic core, the resultant protostar is supported by thermal pressure generated by deuterium burning, in order to link the internal structure of the protostar to fundamental physical constants and processes. In fact, deuterium burning is not expected to begin until later in the protostar's lifetime (Chabrier et al. 2000), by which time most star formation in the vicinity will have ceased. Instead, protostars are supported by thermal pressure generated via gravitational contraction during the period immediately following their formation, which results in internal structures that are heavily dependant on their accretion histories and thermodynamic content (Hartmann et al. 1997; Tout et al. 1999; Baraffe et al. 2002). As such, although this simplified model highlights the importance of protostellar evolution in correctly modelling protostellar accretion luminosity and determining the form of the IMF, its predictions should be treated with caution.

4.3.1.4 Comparison between analytic and numerical results

The numerical calculations presented in this chapter produce stellar mass functions whose characteristic masses scale with density as $M_{\rm c} \propto \rho^{-1/5}$. This scaling with density is much weaker than that expected from a simple Jeans mass argument, or from the basic semi-analytic turbulent models of the origin of the IMF. Instead, the numerical scaling is in agreement with the simple optically thin description (equation 4.7) given by Bate (2009c).

However, the calculations performed for this chapter use sink particles with accretion radii much larger than typical protostellar radii and they do not emit radiation that would be generated from within the accretion radii. This leads to less radiative heating than would be produced in reality, and means that the radiative heating that is produced may not scale

in the same way as if the protostars were modelled accurately. Generally speaking, more radiative heating would be expected to decrease the amount of fragmentation and increase the characteristic stellar mass. However, if accretion is episodic this may not necessarily be the case. Lomax et al. (2015) considered fragmentation of low-mass pre-stellar cores and found that with continuous radiative feedback brown dwarfs were under-produced and multiple star properties were in poor agreement with observations. However, when they treated the feedback as being episodic they obtained more realistic stellar properties that were similar to those obtained without including radiative feedback at all.

Because of the incomplete protostellar heating, the disagreement between our results and the predictions of the more advanced treatments of Bate (2009c) (equation 4.11) and Krumholz (2011) (equation 4.16) is perhaps unsurprising. These models make estimates for the luminosities of the protostars that depend on assumptions about the rate of mass accretion during protostar formation, and on knowledge of the protostellar structure to calculate the accretion luminosity of protostars, neither of which are resolved by our calculations. As such, we are unable to rule out either of these more advanced theories based on the results of these calculations alone.

4.3.2 Comparison with observations

As with previous calculations of this scale (Bate 2012, 2014), the number of stars and brown dwarfs produced by each of the three clusters presented is sufficient for us to make comparisons between the distributions of properties in the simulated clusters and those found in observational surveys.

It is now widely accepted that the number of stars produced in star-forming regions is higher than the number of brown dwarfs (Chabrier 2003; Greissl et al. 2007; Luhman 2007; Andersen et al. 2008). The results of our calculations are in agreement with this, with brown dwarfs making up 42%, 31%, 24% of the stellar populations in the 0.188 pc, 0.404 pc, and 0.870 pc calculations respectively. We also find that the median mass does vary with initial cloud density, albeit more weakly than would be expected from the simplest Jeans-mass arguments. While many past observations have suggested that the median stellar mass is approximately constant (Bastian et al. 2010), there is some evidence for variation with environmental conditions.

Low-density star-forming regions, such as the nearby Taurus-Auriga cloud complex, have been observed to contain an apparent excess of solar-type stars when compared to common parameterisations of the IMF (Luhman et al. 2003). Of the calculations presented in this chapter, the low-density 0.870 pc calculation is the most comparable. As in Taurus-Auriga, we find an excess of intermediate-mass stars (see Fig. 4.2) in the cluster. Goodwin et al. (2004a) suggested this excess may be due to dynamic interactions between small groups of protostars in star-forming cores early in the formation process. Ejections of

brown dwarfs and low-mass stars would deplete the mass of the core by a negligible amount, leaving the remaining objects with a larger proportion of the gas reservoir from which to accrete, increasing their final masses. Star formation in our low-density 0.870 pc calculation does occur in small isolated groups (see Fig. 4.1), and these systems evolve through dynamic ejections in a manner similar to that proposed by Goodwin et al. (2004a).

Observations have also found evidence of bottom-heavy mass distributions in the inner regions of early-type galaxies, with median masses that decrease with increased velocity dispersions (Treu et al. 2010; Spiniello et al. 2012; Conroy and van Dokkum 2012; Lagattuta et al. 2017). Conroy and van Dokkum (2012) suggest several explanations for this, including increased pressure in the interstellar medium, and high star formation rates. Direct comparisons with our calculations are difficult because the initial conditions for the stellar populations in the inner regions of early-type galaxies are not known. However, if these stars were predominantly produced from high-density molecular gas, the fact that we obtain lower characteristic stellar masses in regions of high density may help explain the origin of such a bottom-heavy mass function.

4.4 Conclusions

In this chapter, we have presented results from three radiation hydrodynamical calculations of star formation in clusters that resolve masses down to the opacity limit for fragmentation. Each of the calculations began with the same basic initial conditions, except that the mean density was varied by up to a factor of 100 between the clouds by changing their initial radii. The calculations produced 474, 233 and 87 stars and brown dwarfs, which we modelled using sink particles with accretion radii of 0.5 AU. The large number of objects formed allowed us to examine the statistical properties of the clusters and compare them to observational surveys of nearby star-forming regions, as well as previous analytical theories.

Our conclusions for how stellar properties in star-forming clusters depend on the initial cloud density are as follows:

1. We find that including the effects of radiative feedback in the calculations produces clusters whose median stellar masses exhibit a weaker dependency on the initial cloud density than the thermal Jeans mass, confirming the results of previous calculations by Bate (2009c).

2. We observe a dependency of the characteristic (median) stellar mass on density approximately of the form $M_{\rm c} \propto \rho^{-1/5}$, in contrast to similar, but much smaller, calculations performed by Bate (2009c), which found no significant variation in the median mass between calculations of different initial densities. The dependency of

the median mass on initial density that we find is consistent with the basic treatment of the optically thin case proposed by Bate (2009c) ($M_c \propto \rho^{-1/5}$).

3. The $M_c \propto \rho^{-1/5}$ scaling is much stronger than that predicted by the extended models of Bate (2009c) and Krumholz (2011) which attempt to take the luminosity of accreting protostars into account. However, our numerical calculations use sink particles that exclude the luminosity that would be generated from within the 0.5 AU accretion radii.

4. The multiple system properties of the clusters display little variation and are generally in good agreement with the properties observed for Galactic stellar populations. All of our calculations exhibit multiplicities higher than those observed for solar-type field stars. This is consistent with surveys of young stars in nearby star-forming regions (see Ghez et al. 1993, Simon et al. 1995, Duchêne 1999, Duchêne et al. 2004, Duchêne et al. 2007). We also find possible evidence for a weak dependence of the number of wide binaries/multiples on density, which is consistent with wide systems being preferentially disrupted, although the effect is not statistically robust.

5. The lowest density calculation (0.870 pc) exhibits comparable structures to those observed in the Taurus-Auriga star-forming region, and produces a similar stellar mass distribution with an excess of solar-type stars. This suggests that the apparently top-heavy IMF observed in Taurus-Auriga may be due to the region's low density.

6. If the characteristic stellar mass does decrease with increasing cloud density, this may help to explain the bottom-heavy stellar mass functions that have been inferred from observations of the inner regions of early-type galaxies.

Chapter 5

Accretion feedback in SPH models of star formation

In the last chapter, we found that including radiative feedback in calculations of stellar cluster formation had a significant impact upon the scaling of the median stellar mass with the initial cloud density, by modifying the effective thermal Jeans mass. The protostellar luminosity is central to this mechanism, heating the sphere of gas surrounding the protostar and increasing the size of the region stable against gravitational collapse. However, as mentioned in the previous chapter, using sink particles with accretion radii larger than the protostellar radius that do not emit radiation underestimates the protostellar luminosity by a factor of $\approx R_{\rm acc}/R_{*}$. In order to fully simulate the effects of radiative feedback on the median stellar mass, this missing luminosity must be included.

Previous efforts to include protostellar heating in calculations of star formation have possessed significant limitations. As mentioned in Chapter 1, many have used sink particles much larger than the protostellar radius ($\sim 10 - 100$ AU) (Krumholz et al. 2007; Offner et al. 2009; Urban et al. 2010), requiring complex models to describe the structure of their interiors. Others have used smaller sink particles (~ 1 AU) (Stamatellos et al. 2011, 2012), allowing them to better capture the dynamics of inner disc material. However, even these calculations have used complex models to describe the accretion of material onto protostars. In this chapter, we present results from small cluster calculations which model the accretion luminosities of protostars using the disc-accretion algorithm presented in Chapter 3. This method has advantages over previous attempts, combining small sink particles with a simple linear model of viscous disc accretion onto a central protostar, which enables us to include the majority of the radiative feedback produced by protostars whilst making relatively few assumptions.

Section 5.1 describes our numerical method, and the initial conditions used for each of the calculations. In Section 5.2, we examine the effects of including radiative feedback from

sink particles in simulations of the formation of single protostellar systems. We compare the results of calculations using the disc-accretion algorithm to calculate sink luminosities with those using a range of constant sink luminosities. We also compare calculations using the disc-accretion algorithm with different sink accretion radii. In Section 5.3, we analyse the effects of the extra feedback on simulations of the formation of small stellar clusters, using similar initial conditions to those used by Bate (2009c). Section 5.4 compares our results to those of previous calculations which included radiative feedback from sink particles, as well as observations of radiative feedback. Our conclusions are given in Section 5.5.

5.1 Computational method

To model the gas and protostars, we use the `sphNG` code, as described in Chapter 2. The calculations include hydrodynamics, gravitational forces, and radiative transfer. **The calculations were performed using the University of Exeter Isca supercomputer. The Bonnor-Ebert sphere calculations used 1 node and a total of 16 cores, with an approximate wall-time of ~ 5 days. The cluster calculations used 4 nodes and a total of 64 cores, with an approximate wall-time of ~ 1 month.** Protostars are modelled using sink particles, as described in Chapter 3. **We vary their accretion radii in order to the investigate any possible dependence of the feedback method on sink particle size.** The sink particles have accretion radii of 0.05 AU, 0.5 AU, 5 AU and 50 AU in the calculations presented in Section 5.2, and accretion radii of 0.5 AU and 5 AU in the calculations presented in Section 5.3.

Unlike the calculations in the previous chapter, the sink particles used in these calculations emit radiation. The sink luminosities are set using the disc-accretion algorithm described in Chapter 3, apart from those in Section 5.2.1, which are set at constant values of 0.1 $L_\odot$, 1 $L_\odot$ and 10 $L_\odot$. The disc-accretion algorithm begins with an initial object of mass 1 M_J and radius 2 $R_\odot$ for each new protostar (Larson 1969), which is initialised after the 10 year pre-collapse period used by the disc accretion algorithm (see Chapter 3). The initial accretion rate used by the disc-accretion algorithm is 10^{-5} $M_\odot$ yr^{-1}. Previous calculations have shown that this is a typical value for newly formed protostars (Bate 2010, 2011), and for young protostars in clusters (Bate and Bonnell 2005; Bate 2009a, 2009c).

The mass of the protostar is allowed to evolve according to the calculated accretion rate. We keep the protostellar radius constant throughout the calculations. This is a reasonable approximation for low-mass protostars ($M_* \lesssim 1$ $M_\odot$) accreting at rates of $\dot{M}_* \approx 10^{-6}$-$10^{-5}$ $M_\odot$ yr^{-1}, as shown by the accreting stellar models of Hosokawa and Omukai (2009). We choose to ignore the protostar's intrinsic luminosity, as the accretion luminosity dominates over the intrinsic luminosity when the protostars are undergoing significant accretion (Offner et al. 2009; Hosokawa and Omukai 2009). Fixing the protostellar radius ignores the

effects of accretion on the structure of the protostar, as well as any subsequent effects on the accretion luminosity through its dependence on the protostellar radius (see Chapter 2). A more complicated protostellar evolutionary model may be used to compute the intrinsic luminosity and the variations in the protostellar radius. However, our aim here is to determine the predominant effects of including the luminosity that was missing in the past radiation hydrodynamical SPH models of low-mass star formation. We investigate the effects of including a protostellar evolutionary model in combination with the feedback algorithm in Chapter 6.

5.1.1 Initial conditions

In the calculations presented in Section 5.2, we simulate Bonnor-Ebert spheres containing 5 $M_\odot$ of gas, with a uniform initial temperature of 10 K. The spheres have a radius of 0.126 pc, and a centre-to-edge density ratio of 14:1, such that the ratio of thermal energy to gravitational potential energy is $\alpha_{\rm therm} = 0.4$. The spheres are set in solid body rotation with an angular velocity of 8.02×10^{-14} rad s^{-1}, such that the ratio of rotational kinetic energy to gravitational potential energy is $\beta = 0.001$. The initial free-fall times of the spheres, based on their mean density, are 1.05×10^{13} s (3.31×10^5 yrs).

For the calculations presented in Section 5.3, we simulate turbulent, uniform density gas clouds, using the same initial conditions as Bate (2009c). We construct uniform spheres containing 50 $M_\odot$ with uniform initial temperatures of 10.3 K. The spheres have a radius of 0.188 pc and an initial mean density of 1.2×10^{-19} g cm^{-3}. An initial 'supersonic', turbulent velocity field is applied to each of the clouds, in the same manner as described in Chapter 4. The boundary conditions for the clouds and radiation field are the same as for the calculations in previous chapter. The initial free-fall times of the clouds are 6.02×10^{12} s (1.91×10^5 yrs).

5.1.2 Resolution

The same criteria for modelling fragmentation down to the opacity limit that applied to the calculations in the previous chapter also apply to the calculations presented here. We use 1×10^6 particles to model the 5 $M_\odot$ Bonnor-Ebert spheres, and 3.5×10^6 particles to model the 50 $M_\odot$ clouds, giving mass resolutions of 1×10^{-6} $M_\odot$ per particle (2×10^5 particles per $M_\odot$) for the Bonnor-Ebert spheres and 1.4×10^{-5} $M_\odot$ per particle (7×10^4 particles per $M_\odot$) for the turbulent clouds.

5.2 Results: Bonnor-Ebert spheres

In this section, we present results from radiation hydrodynamical calculations of star formation from the collapse of a single, rotating, Bonnort-Ebert sphere. We examine the effects of including sink particles with constant luminosities of 0.1 $L_\odot$, 1 $L_\odot$ and 10 $L_\odot$ (Section 5.2.1), as well as those with luminosities calculated by the disc-accretion algorithm (Section 5.2.2) using sink particles with accretion radii of $r_{\rm acc}$ = 0.5 AU. We also compare the results of disc-accretion calculations using accretion radii of 0.05 AU, 0.5 AU, 5 AU and 50 AU (Section 5.2.3).

The initial phase of cloud collapse is approximately isothermal, due the efficiency of radiative cooling at low densities. This initial phase lasts until the maximum density in the simulation reaches $\sim 10^{-13}$ g cm^{-3}, at which point the collapse becomes approximately adiabatic, forming a hydrostatic 'first core' (see Larson 1969). **Once the temperature reaches $\approx$ 2000K, molecular hydrogen begins to dissociate, absorbing energy and lowering the opacity, which allows the first core to cool and gravitationally collapse. A sink particle is then inserted once the maximum density of the core reaches 10^{-5} g cm^3. During this second phase, the core rapidly collapses to form a protostar, with a free-fall time of $\sim$ 1 yr.**

5.2.1 Constant luminosities

Fig.s 5.1 and 5.2 show the evolution of the gas column density in the Bonnor-Ebert sphere calculations using sink particles that have constant luminosities. The impact of including the sink luminosity varies between the calculations. In each of the calculations, once the sink is inserted, it begins to heat the surrounding disc material. If the heating is significant, the resultant increase in pressure may cause the disc to expand. **Fig.s 5.3 and 5.3 show the gas temperature in the calculations.** In the 0.1 $L_\odot$ and 1 $L_\odot$ calculations, the heating effect is small, enabling the disc to radiate the additional energy away with little change in its radius. As such, the results are highly similar to the no-feedback case. The heating effect of the 10 $L_\odot$ sink, however, is strong enough to overcome the weak binding energy of the disc around the newly-formed protostar. This causes the surrounding material to expand dramatically, temporarily destroying the disc and driving a large outflow. The expanding gas eventually cools and re-collapses, forming a disc of similar size and mass to the disc formed in the no-feedback calculation. This process can be unstable to fragmentation if the sink particle becomes displaced from the outflow's centre of mass and has a low mass relative to the outflow mass. In this case, the dynamics of the collapse are dominated by the gas mass, forming a new object at the outflow's centre of mass.

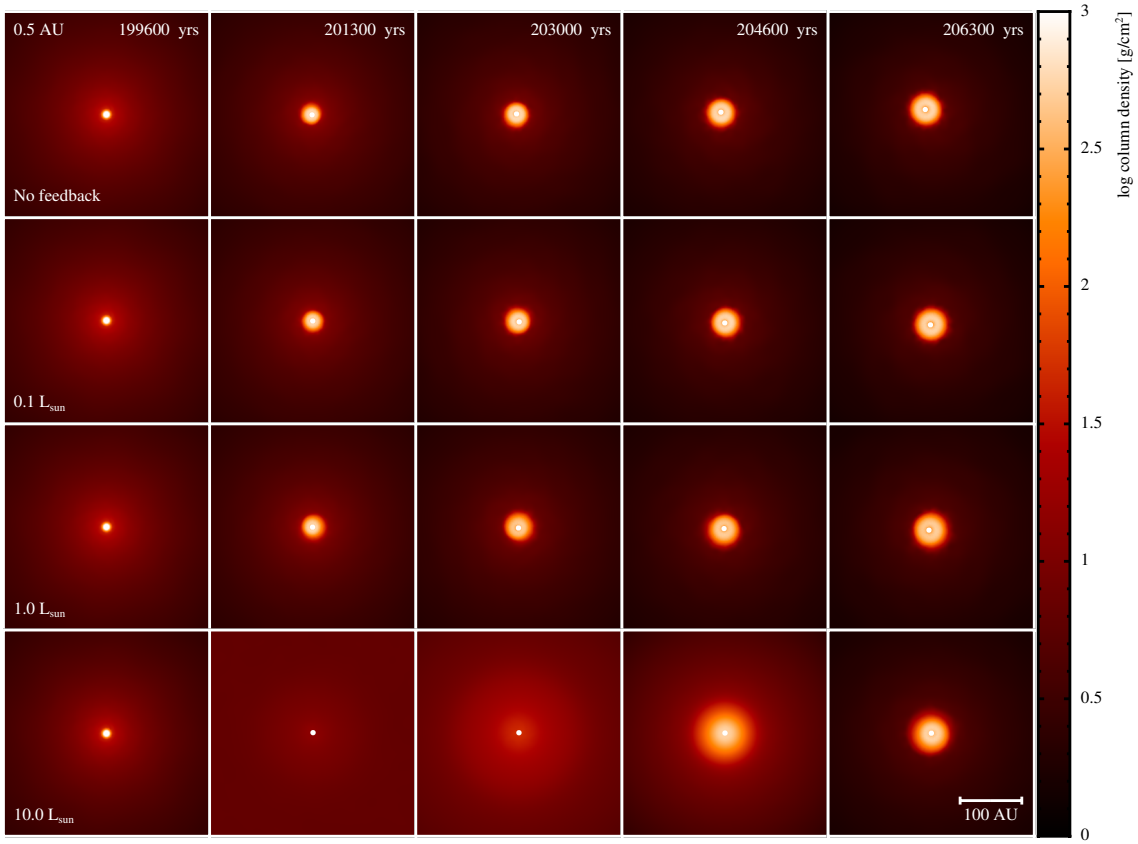

Figure 5.1: The time evolution of the gas column density in each of the Bonnor-Ebert sphere calculations using sink particles with accretion radii of 0.5 AU and constant luminosities. The luminosities used in the calculations are given in the first panel of each row. We also plot results from a calculation using a sink particle with no luminosity for comparison (top row). The panels display the calculations at times separated by intervals of 1,657 yrs, which corresponds to 1/200th of the initial cloud free-fall time. The colour scale shows column densities on a logarithmic scale between 1 g cm^{-2} and 1000 g cm^{-2}, **viewed parallel to the cloud's rotation axis.** The length scale is shown in the bottom-right of the plot. The constant luminosity of the sink particle has little effect on the system for luminosities of 0.1 $L_\odot$ and 1 $L_\odot$. However, using a luminosity of 10 $L_\odot$ rapidly heats the inner disc, driving an expansion that temporarily destroys the disc.

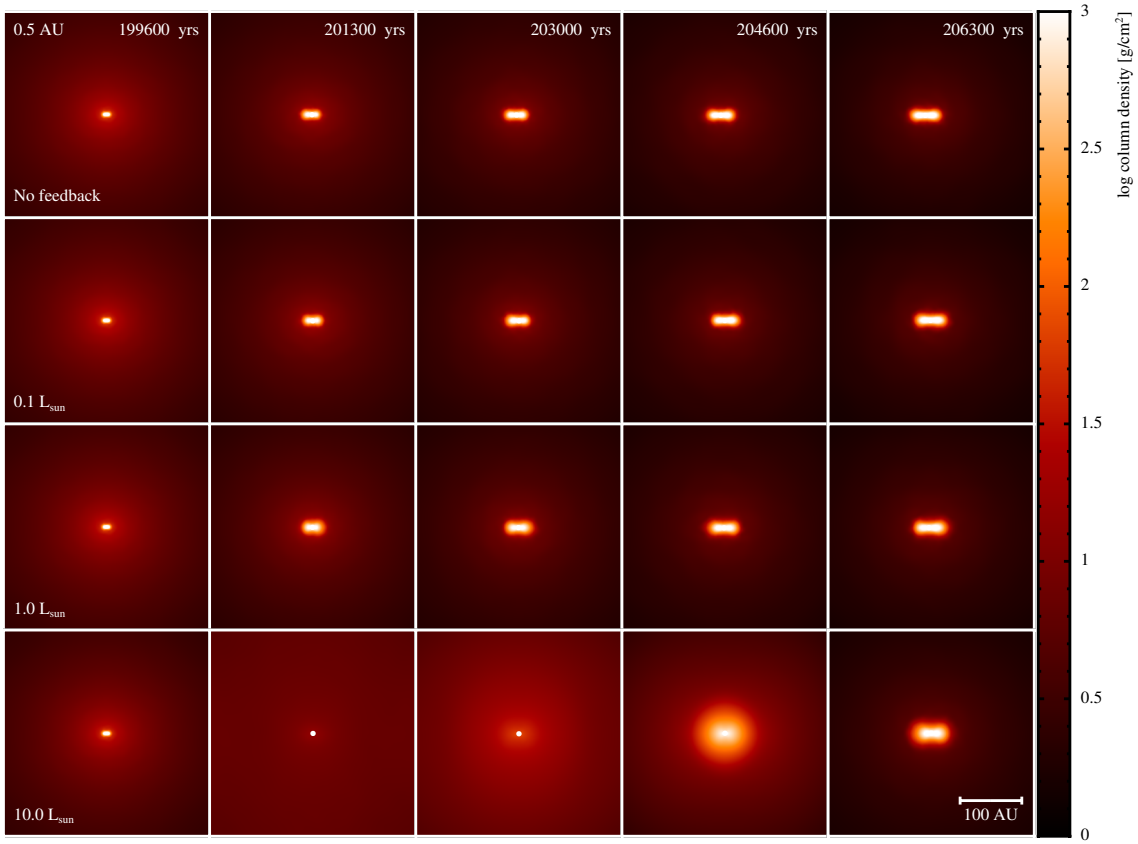

Figure 5.2: The time evolution of the gas column density in each of the Bonnor-Ebert sphere calculations using sink particles with accretion radii of 0.5 AU and constant luminosities. The luminosities used in the calculations are given in the first panel of each row. We also plot results from a calculation using a sink particle with no luminosity for comparison (top row). The panels display the calculations at times separated by intervals of 1,657 yrs, which corresponds to 1/200th of the initial cloud free-fall time. The colour scale shows column densities on a logarithmic scale between 1 g cm^{-2} and 1000 g cm^{-2}, **viewed perpendicular to the cloud's rotation axis.** The length scale is shown in the bottom-right of the plot. The destruction of the circumstellar disc in the 10 L$_{\odot}$ calculation due to the rapid heating of material close to the sink particle is clear in the second and third panels of the bottom row.

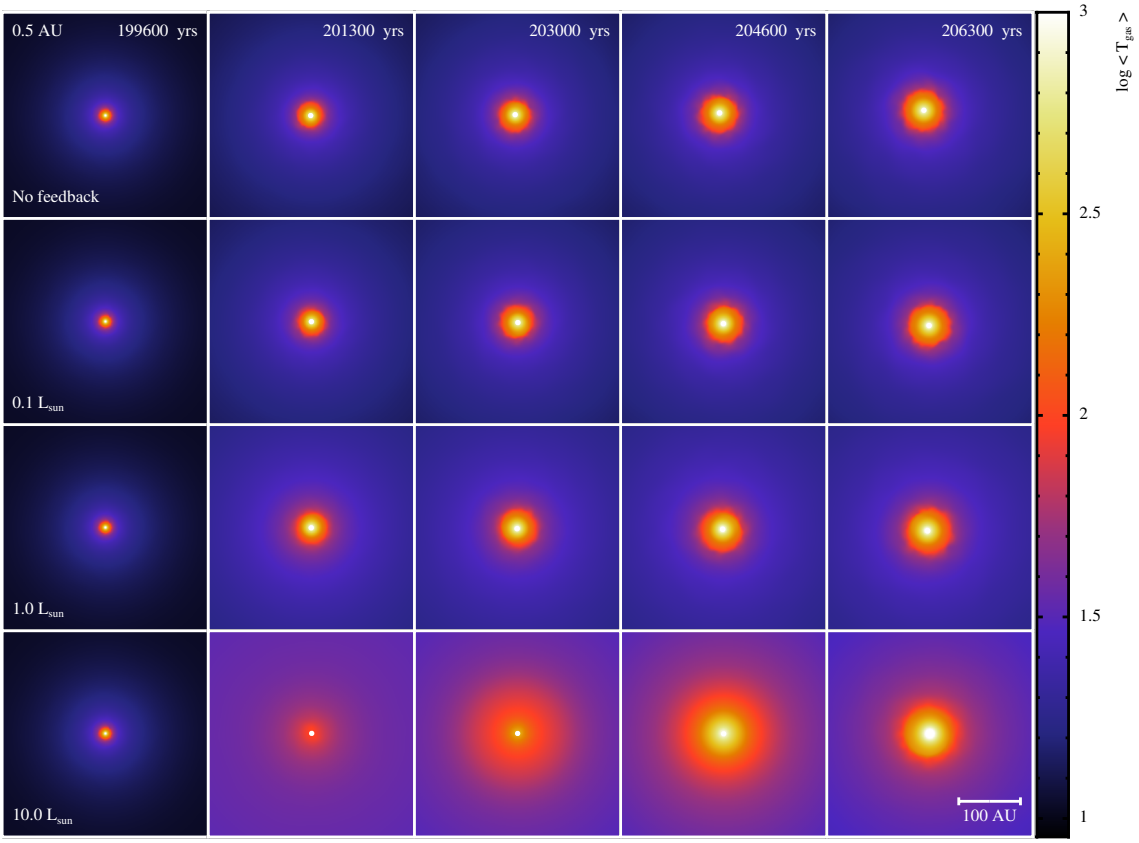

Figure 5.3: The time evolution of the mass-weighted gas temperature in each of the Bonnor-Ebert sphere calculations using sink particles with accretion radii of 0.5 AU and constant luminosities. The luminosities used in the calculations are given in the first panel of each row. We also plot results from a calculation using a sink particle with no luminosity for comparison (top row). The panels display the calculations at times separated by intervals of 1,657 yrs, which corresponds to 1/200th of the initial cloud free-fall time. The colour scale shows column densities on a logarithmic scale between 1 g cm^{-2} and 1000 g cm^{-2}, **viewed parallel to the cloud's rotation axis.** The length scale is shown in the bottom-right of the plot. The sink particles with luminosities of 0.1 $L_{\odot}$ and 1 $L_{\odot}$ produce gas temperatures which are almost identical to the no-feedback case. However, using a higher luminosity of 10 $L_{\odot}$ produces gas temperatures which are significantly higher, both in the disc and in the surrounding medium.

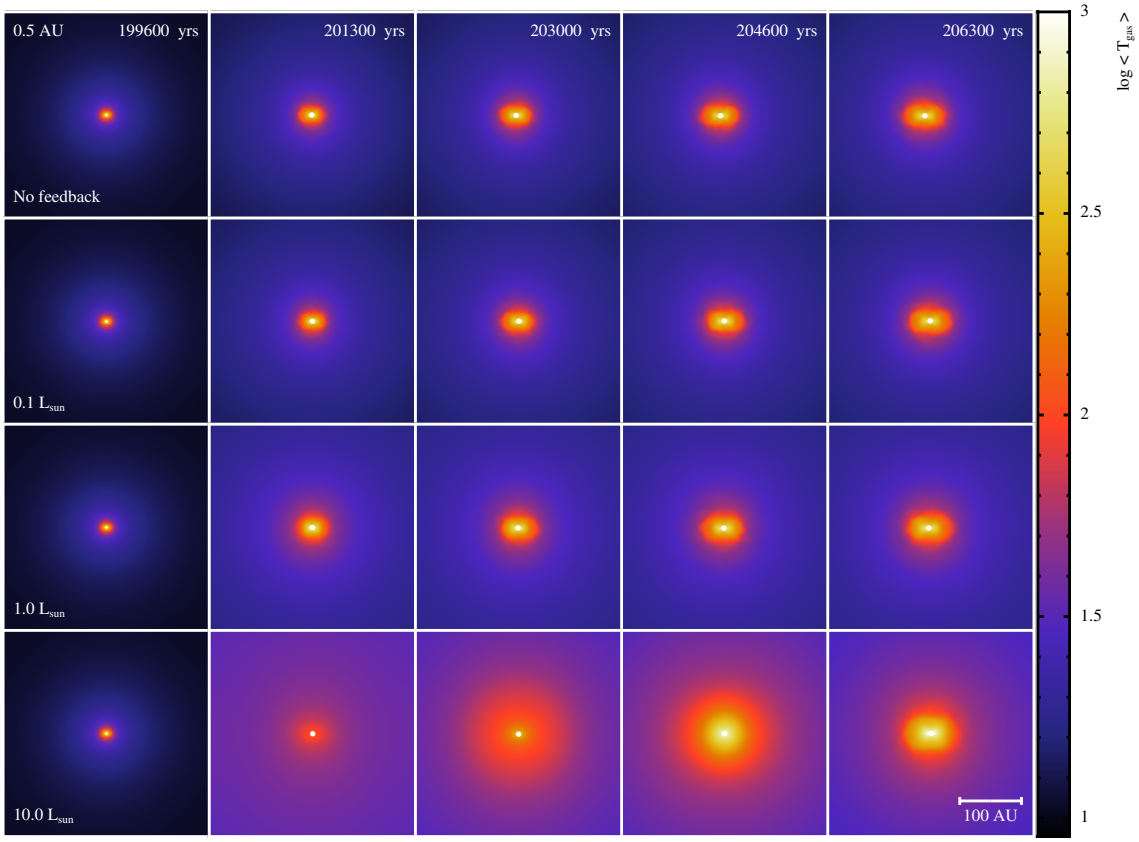

Figure 5.4: The time evolution of the mass-weighted gas temperature in each of the Bonnor-Ebert sphere calculations using sink particles with accretion radii of 0.5 AU and constant luminosities. The luminosities used in the calculations are given in the first panel of each row. We also plot results from a calculation using a sink particle with no luminosity for comparison (top row). The panels display the calculations at times separated by intervals of 1,657 yrs, which corresponds to 1/200th of the initial cloud free-fall time. The colour scale shows column densities on a logarithmic scale between 1 g cm^{-2} and 1000 g cm^{-2}, **viewed perpendicular to the cloud's rotation axis.** The length scale is shown in the bottom-right of the plot. The strong heating effect of the sink particle with a constant luminosity of 10 $L_{\odot}$ is evident, producing higher temperatures and a more isotropic temperature profile.

5.2.2 Disc-accretion feedback model

Fig.s 5.5 and 5.6 show snapshots of the gas column density and temperature in a Bonnor-Ebert sphere calculation using 0.5 AU sink particles with luminosities calculated by the disc-accretion algorithm, compared to a calculation which uses a sink particle with no luminosity. Similar to the calculations using constant sink luminosities, once a sink particle is inserted, the additional luminosity heats the inner region of the surrounding disc, causing it to expand. However, unlike the 10 $L_\odot$ calculation in Section 5.2.1, the expansion of the disc is steady, and there is no subsequent re-collapse.

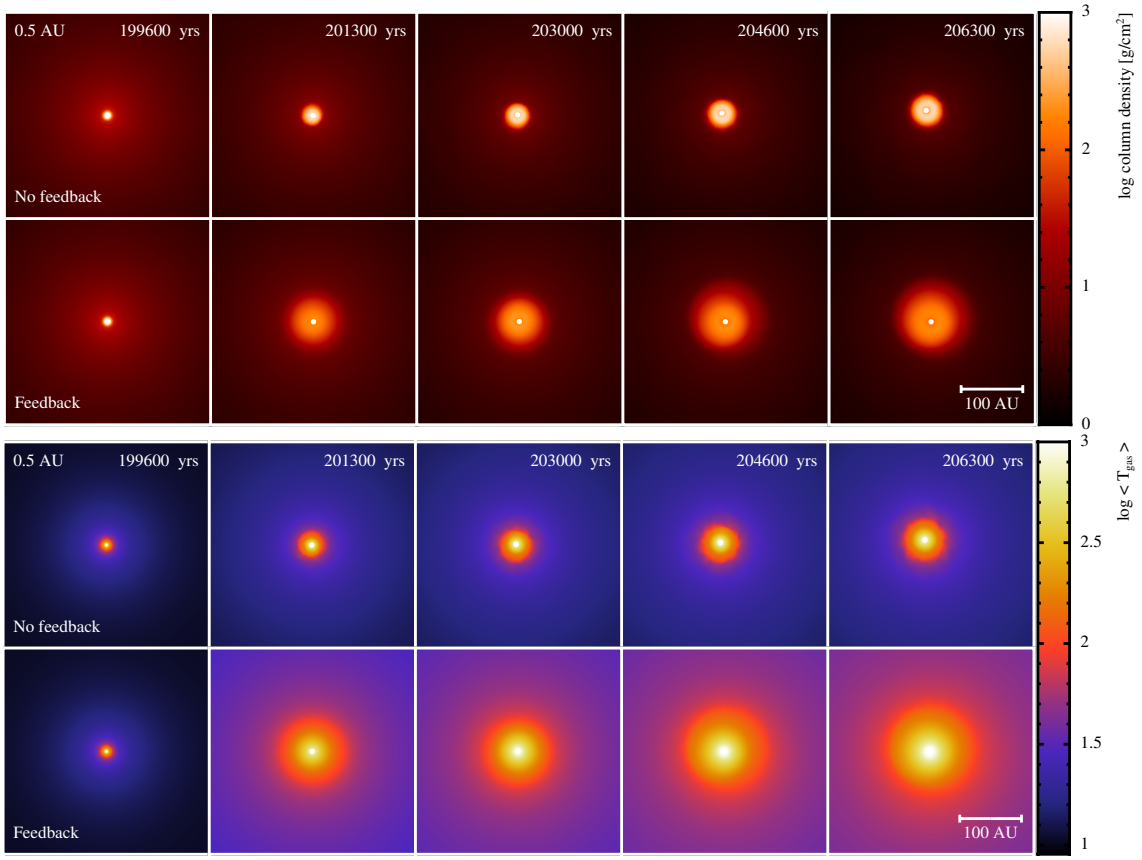

Figure 5.5: The time evolution of the gas column density and mass-weighted temperature in the Bonnor-Ebert sphere calculations using sink particles with accretion radii of 0.5 AU without feedback (top row of each sub-panel) and with luminosities set by the disc-accretion algorithm (bottom row of each sub-panel). The panels display the calculations at times separated by intervals of 1,657 yrs, which corresponds to 1/200th of the initial cloud free-fall time. The colour scales show column densities on a logarithmic scale between 1 g cm^{-2} and 1000 g cm^{-2}, viewed parallel to the cloud's rotation axis, and temperatures on a logarithmic scale between 9 K and 1000 K. The length scale is shown in the bottom-right of each plot. The increasing luminosity of the sink particle heats the disc, causing it to expand steadily throughout the calculation. The result is a much larger and hotter disc than in the calculation that does not include sink particle feedback.

Fig. 5.7 shows the time evolution of the sink particle masses and luminosity in the calculation with feedback. The initial luminosity of the sink is low, beginning at ~ 0.01 $L_\odot$, but it reaches ≈ 2 $L_\odot$ after 500 years. From the calculations using constant sink luminosities, it is clear that this is in the luminosity regime that does not significantly disrupt the disc structure. As such, the initial expansion of the disc following the insertion of the sink

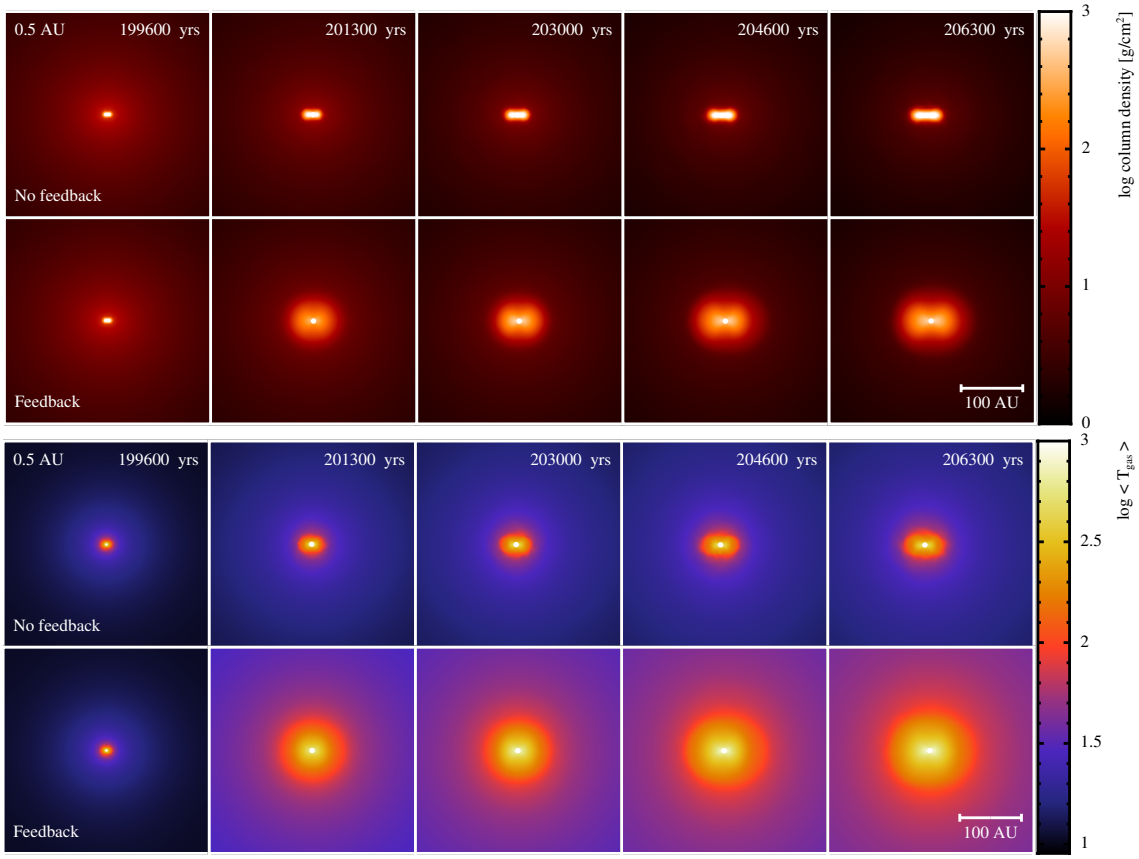

Figure 5.6: The time evolution of the gas column density and mass-weighted temperature in the Bonnor-Ebert sphere calculations using sink particles with accretion radii of 0.5 AU without feedback (top row of each sub-panel) and with luminosities set by the disc-accretion algorithm (bottom row of each sub-panel). The panels display the calculations at times separated by intervals of 1,657 yrs, which corresponds to 1/200th of the initial cloud free-fall time. The colour scales show column densities on a logarithmic scale between 1 g cm^{-2} and 1000 g cm^{-2}, viewed parallel to the cloud's rotation axis, and temperatures on a logarithmic scale between 9 K and 1000 K. The length scale is shown in the bottom-right of each plot. The heating effect of the sink particle causes a significant expansion of the disc perpendicular to the rotation axis, due to the increase in thermal pressure. This results in a more diffuse disc structure than in the no-feedback case.

particle is small. The luminosity steadily increases throughout the calculation, reaching a maximum value of ~ 60 $L_{\odot}$ by the end of the calculation. This is substantially higher than the 10 $L_{\odot}$ case presented in the previous section. **However, as the luminosity increases slowly from an initially low value and the sink particle mass grows with time, the disc temperature remains low enough ($\gtrsim 1000$ K) that the sound speed (~ 200 m s^{-1}) never exceeds the escape velocity of the sink particle ($\sim 10^5$ m s^{-1}), and no thermally-driven expansion occurs**. Instead, as the disc temperature continues to rise, it steadily expands but remains in hydrostatic equilibrium. The result is a disc that is approximately twice as large and noticeably more diffuse than in the no-feedback calculation, with a typical gas density of ~ 100 g cm^{-2}, compared to a typical gas surface density of ~ 500 g cm^{-2} in the no feedback calculation. The disc is also substantially hotter, with a large portion of the disc exhibiting temperatures in excess of 500 K, compared to typical temperatures of 200 K in the no-feedback calculations.

In addition to its impact upon the surrounding disc structure, the inclusion of sink feedback also affects the evolution of the sink particle mass. The accretion rate of the sink particle with radiative feedback is lower than the sink particle with no luminosity for the first ~ 4000 yrs of the calculation. This results a sink mass which is ≈ 0.03 $M_{\odot}$ lower in the feedback case than in the non-feedback case by the end of the calculations (0.24 $M_{\odot}$ versus 0.27 $M_{\odot}$, respectively). During the same period, the growth rate of the protostellar mass is marginally lower than the sink accretion rate, causing the disc mass to increase slowly. Eventually however, the disc mass reaches an approximately constant value of 0.09 $M_{\odot}$, indicating that a steady-state has been reached, with the sink accretion rate equal to the protostellar accretion rate. The protostellar mass provides the dominant contribution of the total sink mass ≈ 4000 yrs after the sink particle is inserted. When the calculation is stopped, the protostellar mass is ~ 0.15 $M_{\odot}$, which is 2/3 of the total sink mass of 0.24 $M_{\odot}$.

5.2.3 Dependence on sink particle radius

Fig.s 5.8 and 5.9 show the gas column density in calculations using the disc-accretion algorithm to calculate the luminosities of sink particles with a range of accretion radii. While the calculations using accretion radii of 0.05 AU and 0.5 AU produce circumstellar discs approximately 100 AU in diameter, the 5 AU calculation produces a disc only 30 AU in diameter, and the 50 AU calculation does not form a resolved disc. We also see that the 0.05 AU sink particle produces a thermally-driven **expansion** after being inserted (second and third panels in the top row of Fig.s 5.8 and 5.9).

The main differences between the calculations using sink particles of different sizes come about from the fact that sink particles bind material inside the accretion radius once accreted and do not let it out again. As we saw in sections 5.2.1 and 5.2.2, the radiative feedback can cause a thermally-driven disc expansion, which may significantly alter the

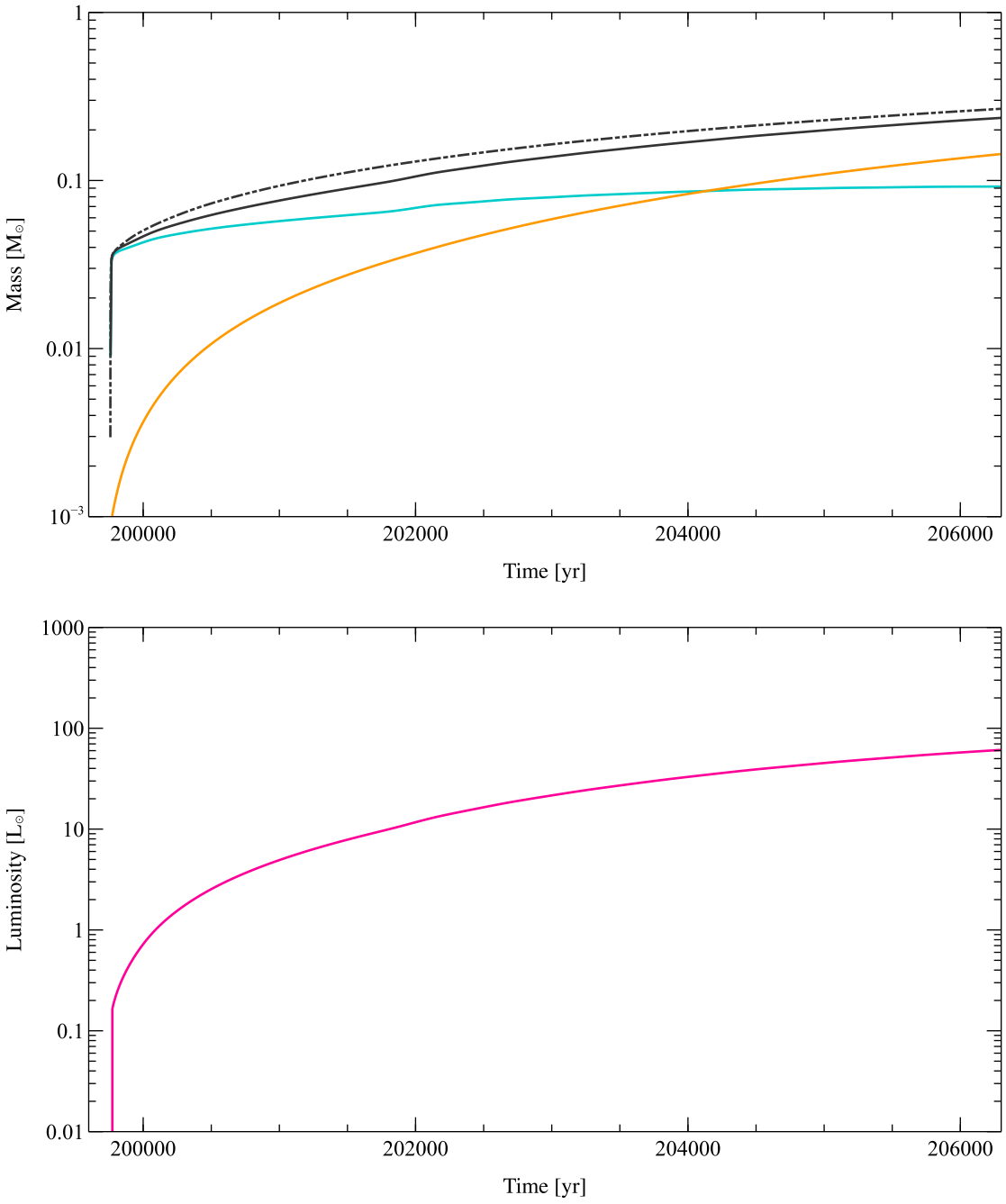

Figure 5.7: The evolution of the sink particle, protostellar and disc masses, and sink luminosities in the Bonnor-Ebert sphere calculations, using sink particles with accretion radii of 0.5 AU without feedback and with luminosities set by the disc-accretion algorithm. In the top plot, the total sink particle masses are shown in black, and the disc and protostellar masses are shown in blue and orange respectively. In the bottom plot, the sink luminosity is shown in magenta. Values for the feedback calculation are shown with solid lines, and values for the no-feedback calculation are shown with dot-dot-dashed lines. Including feedback reduces the mass accretion rate of the sink particle, resulting in a slightly lower sink mass compared to the no-feedback calculation at the same time. The luminosity continues to increase for the duration of the calculation, due to the growth of the stellar mass via accretion.

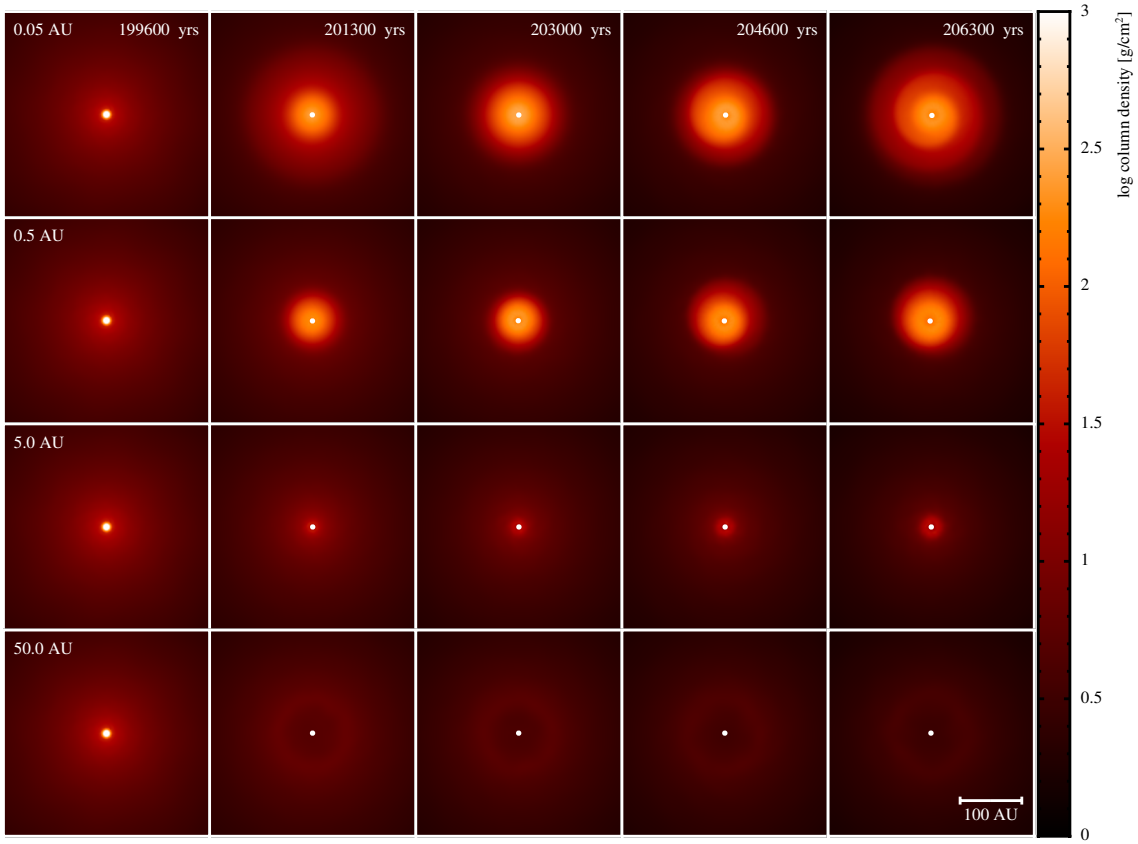

Figure 5.8: The time evolution of the gas column density in the Bonnor-Ebert sphere calculations, using sink particles with luminosities set by the disc-accretion algorithm and a range of accretion radii. The accretion radii used in the calculations are given in the first panel of each row. The panels display the calculations at times separated by intervals of 1,657 yrs, which corresponds to 1/200th of the initial cloud free-fall time. The colour scale shows column densities on a logarithmic scale between 1 g cm^{-2} and 1000 g cm^{-2}, viewed parallel to the cloud's rotation axis. The length scale is shown in the bottom-right of the plot. Using a larger accretion radius binds more material inside the sink particle, preventing it from escaping. In the case of the 0.05 AU sink, this gas expands, increasing the disc radius, whereas the 5 AU and 50 AU sinks encompass the majority of the disc material, such that little or no disc is formed.

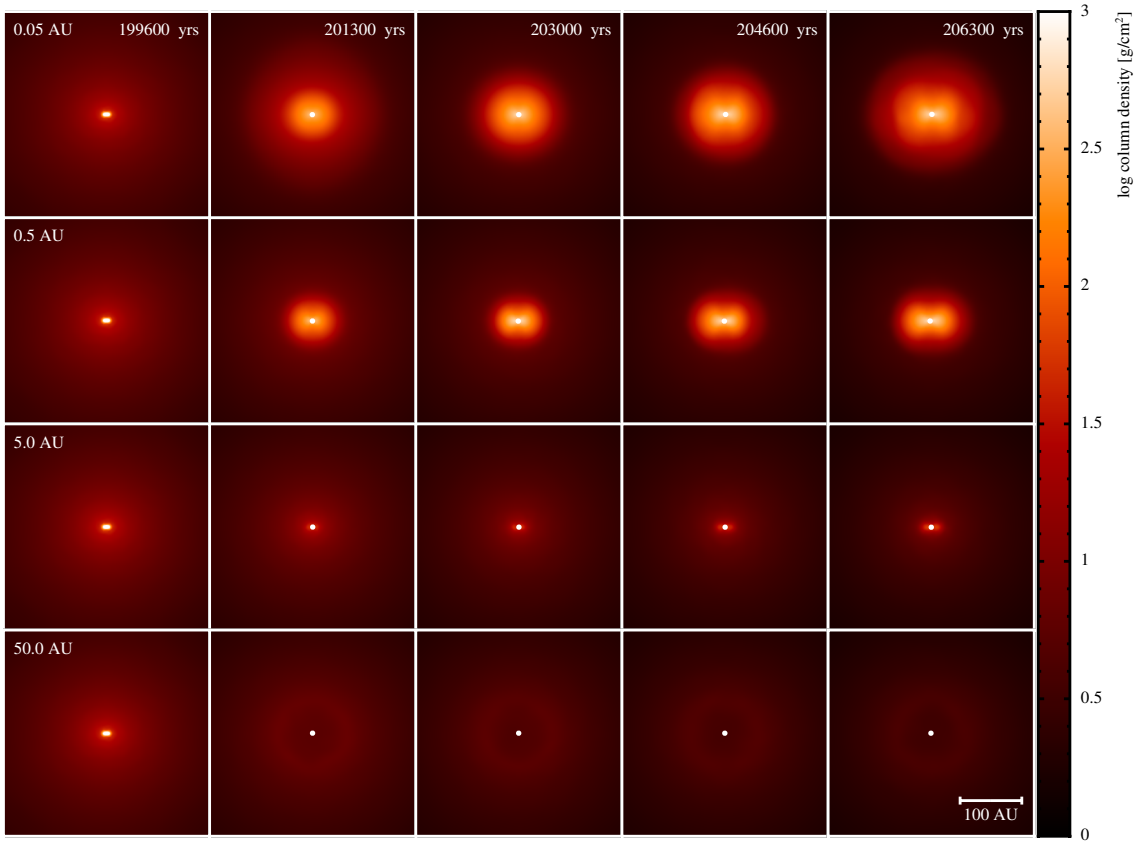

Figure 5.9: The time evolution of the gas column density in the Bonnor-Ebert sphere calculations, using sink particles with luminosities set by the disc-accretion algorithm and a range of accretion radii. The accretion radii used in the calculations are given in the first panel of each row. The panels display the calculations at times separated by intervals of 1,657 yrs, which corresponds to 1/200th of the initial cloud free-fall time. The colour scale shows column densities on a logarithmic scale between 1 g cm^{-2} and 1000 g cm^{-2}, viewed parallel to the cloud's rotation axis. The length scale is shown in the bottom-right of the plot. In the 0.05 AU calculation, the gas expands perpendicular to the disc plane, resulting in a more diffuse disc when compared to the 0.5 AU calculation. The 5 AU and 50 AU calculations produce little to no disc, due to the binding of material within the sinks.

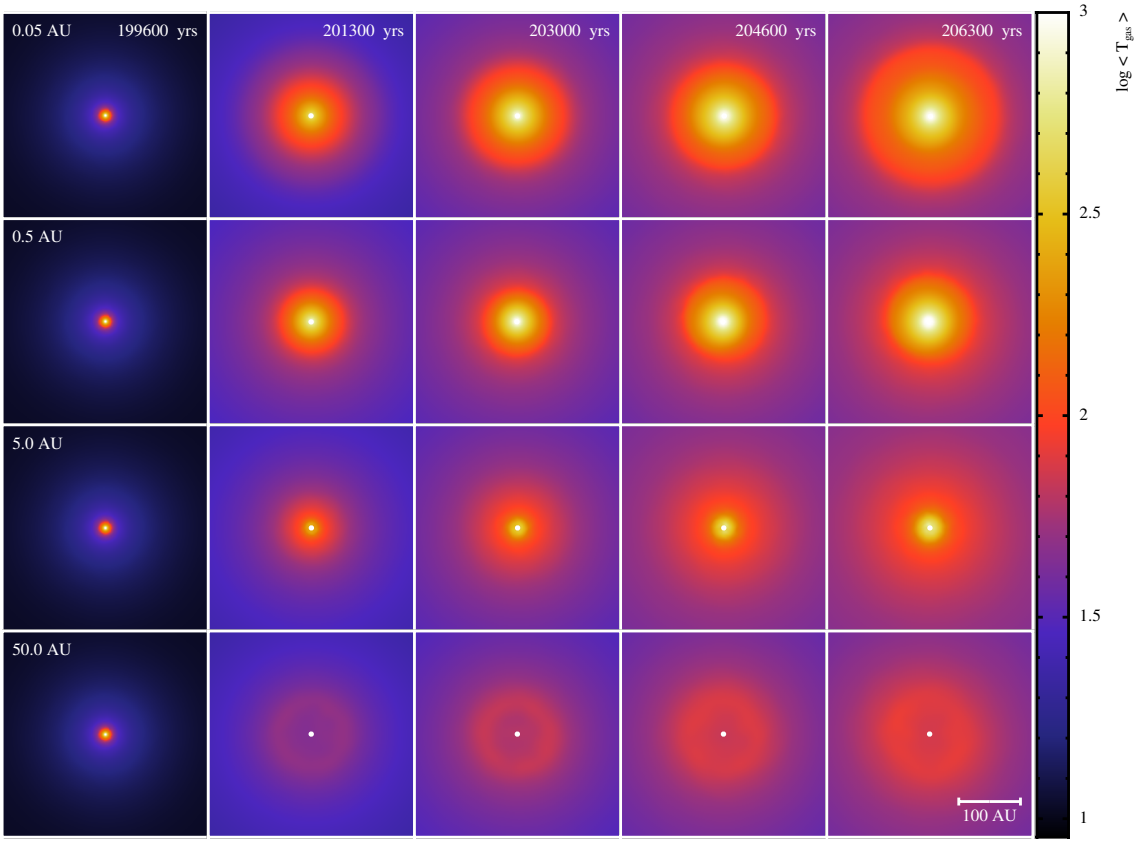

Figure 5.10: The time evolution of the mass-weighted gas temperature in the Bonnor-Ebert sphere calculations, using sink particles with luminosities set by the disc-accretion algorithm and a range of accretion radii. The accretion radii used in the calculations are given in the first panel of each row. The panels display the calculations at times separated by intervals of 1,657 yrs, which corresponds to 1/200th of the initial cloud free-fall time. The colour scale shows column densities on a logarithmic scale between 1 g cm^{-2} and 1000 g cm^{-2}, viewed parallel to the cloud's rotation axis. The length scale is shown in the bottom-right of the plot. The expansion of hot material from the inner disc raises the temperature of disc significantly in the 0.05 AU calculation. This effect is reduced wen using larger sink particles, as material in the inner disc is not resolved

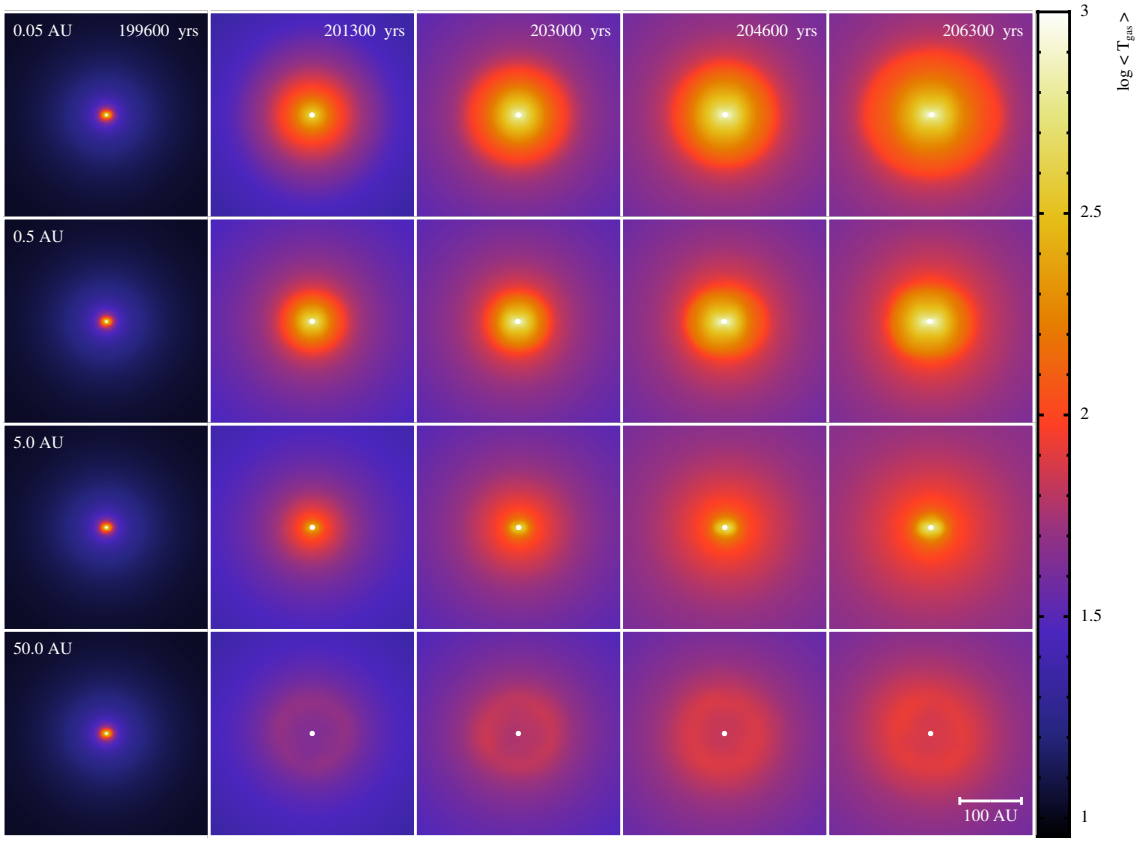

Figure 5.11: The time evolution of the mass-weighted gas temperature in the Bonnor-Ebert sphere calculations, using sink particles with luminosities set by the disc-accretion algorithm and a range of accretion radii. The accretion radii used in the calculations are given in the first panel of each row. The panels display the calculations at times separated by intervals of 1,657 yrs, which corresponds to 1/200th of the initial cloud free-fall time. The colour scale shows column densities on a logarithmic scale between 1 g cm^{-2} and 1000 g cm^{-2}, viewed parallel to the cloud's rotation axis. The length scale is shown in the bottom-right of the plot. Material at small radii expands in the 0.05 AU calculation due to the heating effect of the sink particle, producing a hot, diffuse region surrounding the disc. Again, this is effect is suppressed in the calculations using larger sink particles, as the inner disc is not resolved.

structure and dynamics of the surrounding disc. When the accretion radius is small, gas close to the sink particle is not bound within the sink particle. It is therefore able to expand when heated (see Bate 2010, 2011). However, when the accretion radius is large, this mass is bound within the sink particle, and no expansion is possible. This behaviour is clear in Fig.s 5.10 and 5.11, which show the mass-weighted gas temperature in each of the calculations. Furthermore, if the sink accretion radius is large enough, it may encompass the entire first core, and much of the material that forms a disc when using smaller sink particles. In this case, most of the gas surrounding the newly-formed protostar is either accreted immediately by the sink particle, or shortly after its formation, and no disc is resolved. This is particularly evident in the 50 AU calculation.

5.2.4 Summary

The calculations presented here illustrate several key points about radiative feedback from sink particles, and its effects on protostellar systems. Firstly, due to the low binding energy of newly-formed sink particles and their surrounding discs, the discs are susceptible to becoming unbound and expanding due to excess thermal pressure. This primarily occurs if the luminosity of the sink particle is large at early times. We have shown that this problem may be avoided by increasing the luminosity with time from an initially small value using the disc-accretion algorithm. This produces a stable disc while still allowing the sink particle to generate large luminosities a few thousand years after sink particle insertion. We have also found that there is some variation in the results when using sink particles with different accretion radii. These variations mainly come about from the trapping of gas at small radii when using large sink particles, which is free to expand when larger accretion radii are used. This effect is not caused by the sink feedback mechanism; it is simply a consequence of the increased resolution when using smaller sink particles.

5.3 Results: small stellar clusters

In this section, we present results from four radiation hydrodynamical simulations that produce small clusters of stars. We compare the effects of including radiative feedback from sink particles with accretion radii of 0.5 AU and 5 AU with calculations that do not include sink feedback. Each of the calculations were run until they reached 1.40 initial cloud free-fall times. A total of 5 and 15 objects were formed by the feedback and no-feedback calculations, respectively, using accretion radii of 0.5 AU, and 7 and 20 objects were formed by the feedback and no-feedback calculations respectively, using accretion radii of 5 AU. In each of the no-feedback calculations, one sink merger occurred, at times of 252,600 yrs and 263,200 yrs in the 0.5 AU and 5 AU calculations, respectively.

Section 5.3.1 describes the time evolution of the clouds, including the formation of

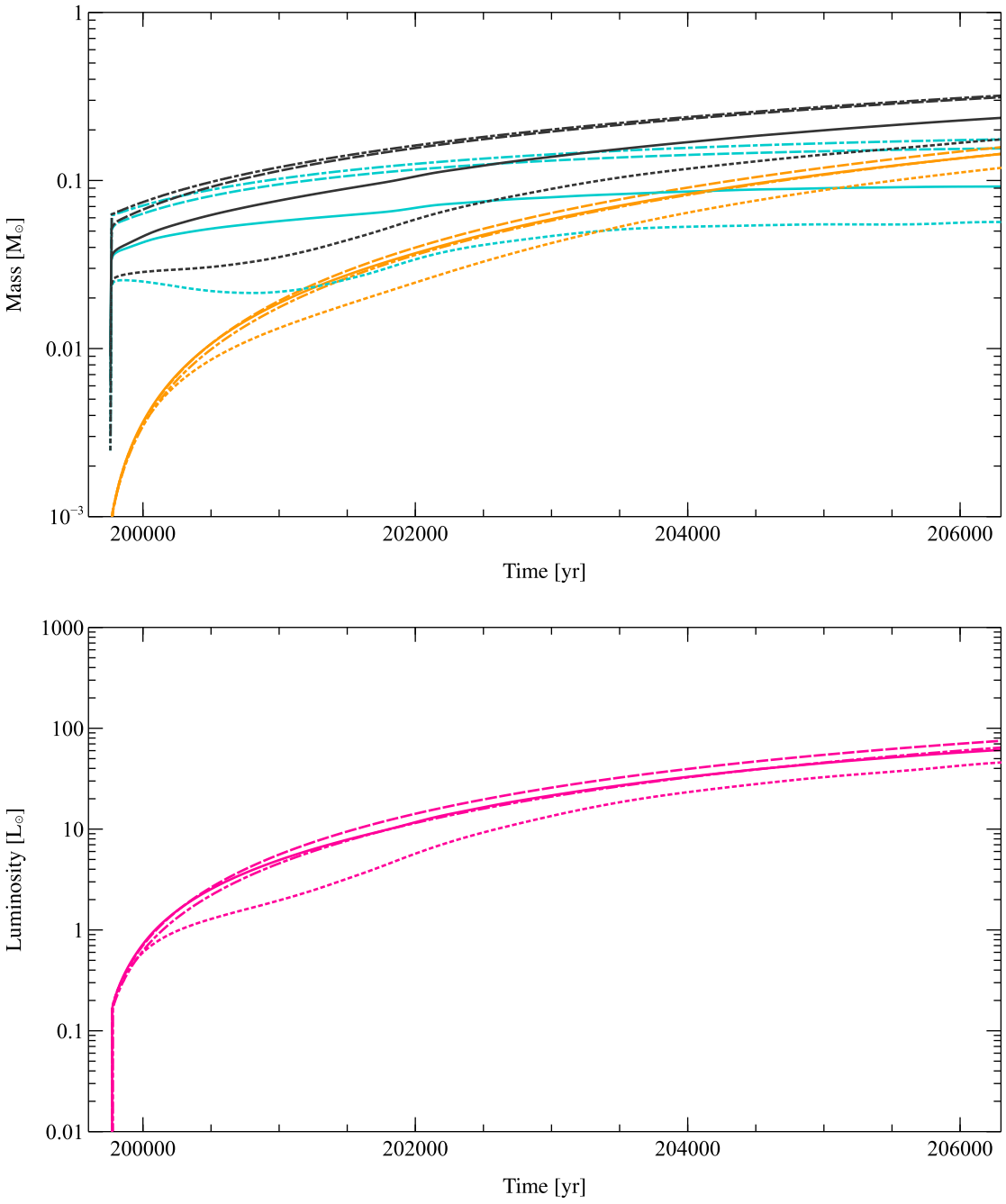

Figure 5.12: The evolution of the sink particle, protostellar, and disc masses and luminosity in the Bonnor-Ebert sphere calculations, using sink particles with luminosities set by the disc-accretion algorithm and a range of accretion radii. In the top plot, the total sink particle masses are shown in black, and the disc and protostellar masses are shown in blue and orange respectively. In the bottom plot, the sink luminosity is shown in magenta. Values for the 0.05 AU, 0.5 AU, 5 AU and 50 AU calculations are shown by the dotted, solid, dashed, and dot-dashed lines respectively. Larger sink particles encompass more material and have higher initial masses. The protostellar feedback heats material in the inner disc, which remains bound within larger sink particles, but expands as an outflow when using smaller sink particles, reducing their accretion rates. The lower accretion rate also reduces the protostellar luminosity.

objects and their impact on the surrounding cloud structure. In Section 5.3.2, we examine the distribution of masses in each cluster, and compare the results from the calculations including sink feedback to those ignoring feedback in order to probe its effects on the statistical properties of clusters.

5.3.1 The evolution of the clouds

Figs. 5.13 and 5.14 show the evolution of the gas density and temperature in the main star-forming core during each of the cluster calculations. Protostars also form in other regions of the cloud, but we only show a single dense core here for clarity. In each of the clusters, the initial 'turbulent' velocity field results in a filamentary structure. Where flows of gas collide, the turbulent energy is dissipated by shocks forming filaments. The interactions of these filaments produce dense cores that can collapse to produce stars, often at the intersections of filaments. Star formation occurs primarily in these cores, which heat the surrounding region as gas falls into the gravitational potential and is accreted by newly formed protostars.

Including radiative feedback from sink particles results in significantly different evolution of the clusters. Once the first protostars form, the feedback generated by accretion raises the temperature of the surrounding gas. This results in a diffuse density structure that is less prone to fragmentation. Contrastingly, in the calculations that do not include sink feedback, the gas is much cooler and therefore more unstable to collapse. This leads to the fragmentation of several massive discs that form around the first protostars.

Fig. 5.15, which shows the formation time and final mass of each star and brown dwarf in the cluster calculations, reflects this. The formation times of the first four objects are almost identical in both the feedback and no-feedback calculations. However, as the calculations progress, those that do not include feedback from sink particles begin to rapidly form more objects due to fragmentation of the gas. This is particularly true for the 5 AU no-feedback calculation, which produces many more objects than the 0.5 AU no-feedback calculation due to the lack of heating from material being resolved at small radii. However, in the calculations including sink feedback, the accretion luminosity dominates, and is calculated regardless of the accretion radius. This results in highly similar temperature distributions, and therefore similar fragmentation in both calculations.

Fig. 5.16 shows the evolution of the total stellar mass (that is, the combined mass of the sink particles) and total number of objects in each of the calculations. The difference in the rate of fragmentation between the calculations is even more obvious here. The total mass and number of objects are similar across all of the calculations for the first $\sim 20,000$ years. However, in the calculations including sink feedback, once the luminosity from the first protostars begins to heat the gas, the rate of star-formation becomes heavily suppressed, reducing the number of objects formed by a factor of $1/2$ to $2/3$, depending

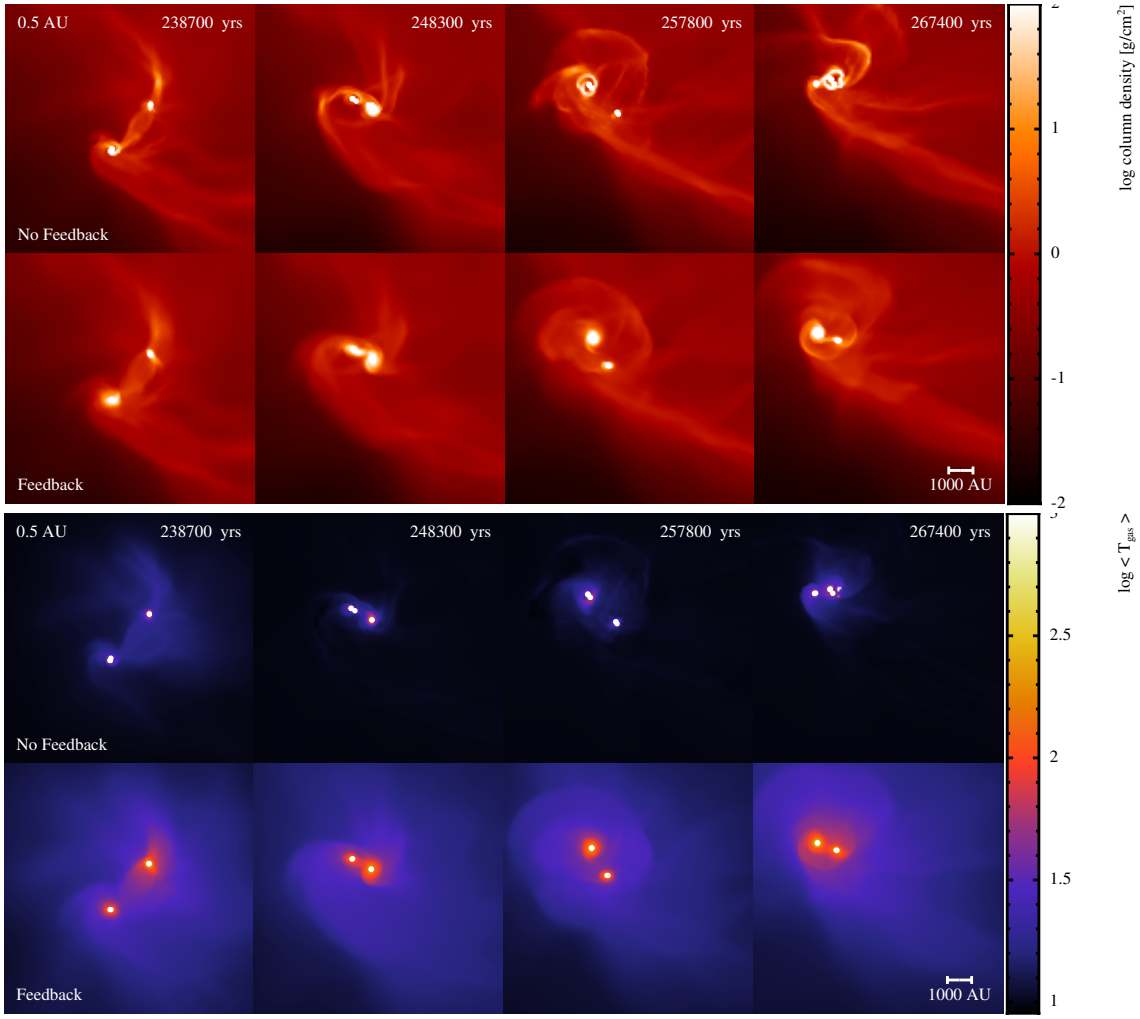

Figure 5.13: The time evolution of the gas column density and mass-weighted temperature in the cluster calculations using 0.5 AU sink particles without feedback and with luminosities set by the disc-accretion algorithm. The panels display the calculations at times separated by intervals of 9,549 yrs, which corresponds to 1/20th of the initial cloud free-fall time. The colour scales show column densities on a logarithmic scale between 0.01 g cm^{-2} and 100 g cm^{-2}, and temperatures on a logarithmic scale between 9 K and 1000 K. The length scale is shown in the bottom-right of each set of panels. Including radiative feedback from sinks results in higher temperatures and a more diffuse structure than in the calculation not including sink feedback, and inhibits fragmentation.

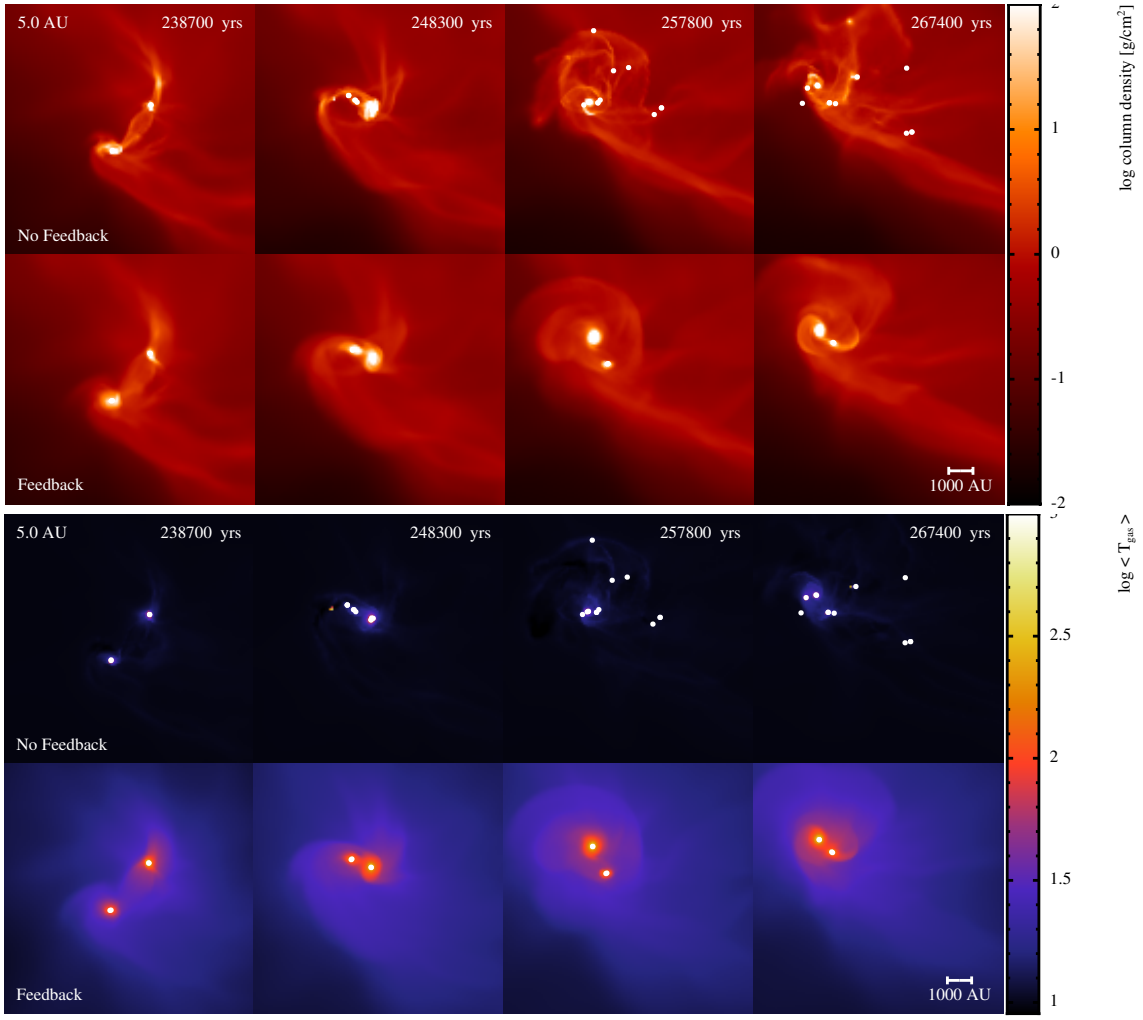

Figure 5.14: The time evolution of the gas column density and mass-weighted temperature in the cluster calculations using 5 AU sink particles without feedback and with luminosities set by the disc-accretion algorithm. The panels display the calculations at times separated by intervals of 9,549 yrs, which corresponds to 1/20th of the initial cloud free-fall time. The colour scales show column densities on a logarithmic scale between 0.01 g cm^{-2} and 100 g cm^{-2}, and temperatures on a logarithmic scale between 9 K and 1000 K. The length scale is shown in the bottom-right of each set of panels. Including radiative feedback from sinks once again results in higher temperatures and more diffuse structures than in the calculation not including sink feedback. The inhibition of fragmentation is even more evident, with the no feedback calculation producing many more objects than the calculation including feedback.

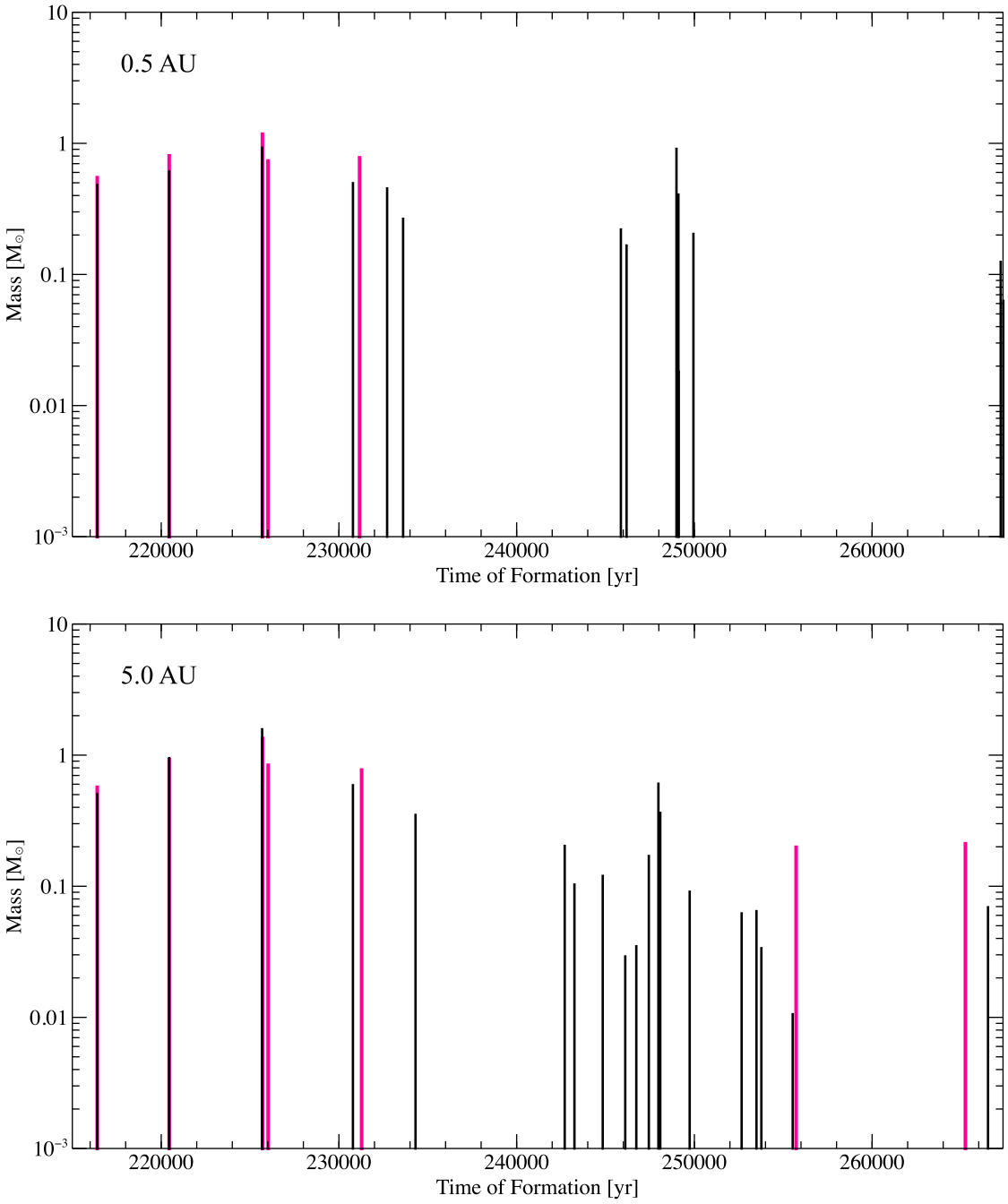

Figure 5.15: The mass and formation time of each star and brown dwarf in the cluster calculations using 0.5 AU (top) and 5 AU (bottom) sink particles without feedback and with luminosities set by the disc-accretion algorithm. Objects formed in the calculations including radiative feedback from sink particles are shown in magenta, and objects formed in the calculations without feedback from sinks are shown in black. A similar number of objects are produced by both the feedback and no-feedback calculations early in the star-formation process. Once the feedback from the first protostars begins to heat the gas however, the gas becomes more stable against fragmentation, and fewer objects are produced than in the calculations not including feedback from sinks.

on the accretion radii, by the end of the calculations. The total stellar mass is also reduced by $\approx 40\%$ by the end of the calculations when including feedback, due to the additional support against collapse provided by the extra thermal pressure generated from the extra luminosity, which decreases the average protostellar accretion rate. This is similar to the findings of Bate (2012) when comparing calculations using a barotropic equation of state with calculations using radiative transfer but without luminous sink particles. Note that there is very little dependence of the total stellar mass on whether 0.5 or 5 AU sink particles are used; what little difference there is can be attributed to the fact that the latter includes mass lying between 0.5 and 5 AU of a sink particle, while with the smaller accretion radii this mass is still part of the hydrodynamical simulation and so is not counted.

Plotting the number of objects against the total stellar mass illustrates how the distribution of mass changes throughout the duration of the calculations. Whilst in the calculations that do not include sink feedback the number of objects increases steadily with the total stellar mass, in the feedback calculations, after an initial period of star formation, the number of objects remains almost constant as the stellar mass increases. This reflects the lack of fragmentation in the calculations including sink feedback. The result is that the first protostars to form are able to accrete from the available gas reservoir with little competition from other nearby objects. As such, they account for a larger proportion of the total stellar mass. They are also able to attain higher masses than their counterparts in the calculations that do not include sink feedback, despite the lower total stellar mass in the feedback calculations.

Importantly, when feedback from the sink particles is included, there is very little dependence of the results on whether 0.5 AU or 5 AU sink particles are used. In Fig. 5.16, the evolution of the total stellar mass is very similar (and the small difference can be attributed to the difference in the way mass between 0.5 AU and 5 AU is treated). The numbers of protostars formed and the times at which they form are also almost identical. This lack of dependence on sink particle radius is exactly what we would hope for from a 'sub-grid' model. By contrast, when only including radiative feedback from resolved gas, although reducing the sink particle accretion radius does result in less fragmentation, the number of protostars formed in the calculation using 0.5 AU is still a long way from converging to the result obtained with sink particle feedback (twice as many protostars are formed).

Fig. 5.17 shows the evolution of the sink masses and luminosities in each of the calculations including feedback. The masses of the sink particles increase rapidly during the period shortly after their formation, as they accrete the remains of the first hydrostatic cores. Following this period of rapid accretion, the masses continue to increase at lower rates that are relatively stable. There is a spike at approximately 238,000 years in the mass accretion rates of two sink particles. Comparing with Fig. 5.13 and Fig. 5.14, we see that this is due to a dynamical interaction between two protostellar discs that removes angular

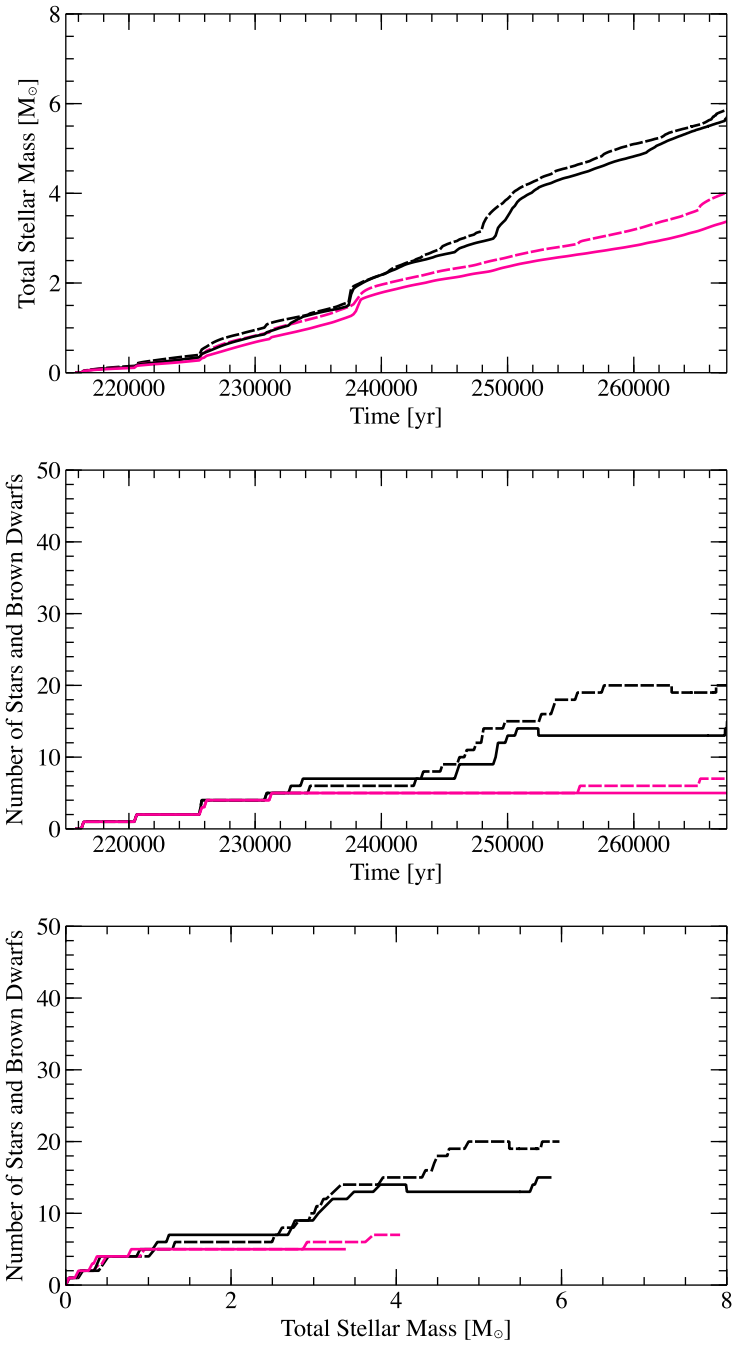

Figure 5.16: The evolution of the total stellar mass and total number of objects in the cluster calculations using 0.5 AU and 5 AU sink particles without feedback and with luminosities set by the disc-accretion algorithm. The values for the calculations including sink feedback are shown in magenta, and the calculations that do not include feedback are shown in black. The solid lines show the calculations using a sink accretion radius of 0.5 AU, and the dashed lines show the calculations using 5 AU. Including radiative feedback from sinks results in a lower star-formation rate, and a low number of objects produced. The total stellar mass is also distributed between fewer objects than in the calculations that do not include sink feedback.

momentum from the disc material, increasing the accretion rates.

Whilst the masses increase at a reasonably steady rate for the majority of the calculations, the luminosities of the sinks are more variable. After the initial phase of rapid accretion, there is a general increase in the luminosities, reflecting the increasing mass of the protostars. However, within this trend there is significant variation. The spike in the accretion rate of two sink particles due to the dynamic interaction of their discs is noticeable, leading the higher mass particle to temporarily reach 500 $L_\odot$. At the end of the calculations, the luminosities of the first five protostars to form exhibit a spread of approximately one order of magnitude, compared to the masses, which only vary by a factor of ~ 2. These variations are primarily caused by changes in the protostellar accretion rates. This is clear from the third panel of the figure, which shows that the luminosities of several sink particles decrease despite their masses increasing. Changes in the accretion rates are largely due to dynamics and filamentary structures in the cluster gas, which are produced by the turbulent velocity field and/or dynamical encounters.

5.3.2 The protostellar mass function

Fig. 5.18 shows the cumulative protostellar mass function at the end of each of the calculations ($t = 1.40\ t_{\rm ff}$). We do not plot the differential mass functions, as too few objects were produced. It is clear that including feedback from sink particles has a significant impact on the distribution of masses formed in the groups. The additional thermal pressure provided by the sink particle luminosities inhibits fragmentation, leading to a lower number of low-mass objects. With fewer objects to compete with, protostars that form are able to accrete a larger fraction of the available gas reservoir, resulting in a higher final mass. This increases the median mass of the cluster, from 0.41 $M_\odot$ to 0.77 $M_\odot$ in the 0.5 AU calculations, and from 0.12 $M_\odot$ to 0.77 $M_\odot$ in the 5 AU calculations.

The median masses and the overall mass distributions of the calculations using sink particle feedback but different accretion radii are very similar. This reflects the ability of the disc-accretion feedback method to correctly account for the luminosity lost when using different sink particle accretion radii, as found in the previous section. By contrast, in the no feedback cases, the median stellar masses for the calculations without sink particle feedback differ by more than a factor of three when the accretion radius is changed from 0.5 to 5 AU. Using an accretion radius of 5 AU results in a significant reduction in the temperature of the surrounding gas, compared to the 0.5 AU calculation, as shown in Fig. 5.13 and Fig. 5.14. This makes the gas much more unstable to fragmentation, increasing the number of low-mass objects in the cluster relative to the 0.5 AU calculation.

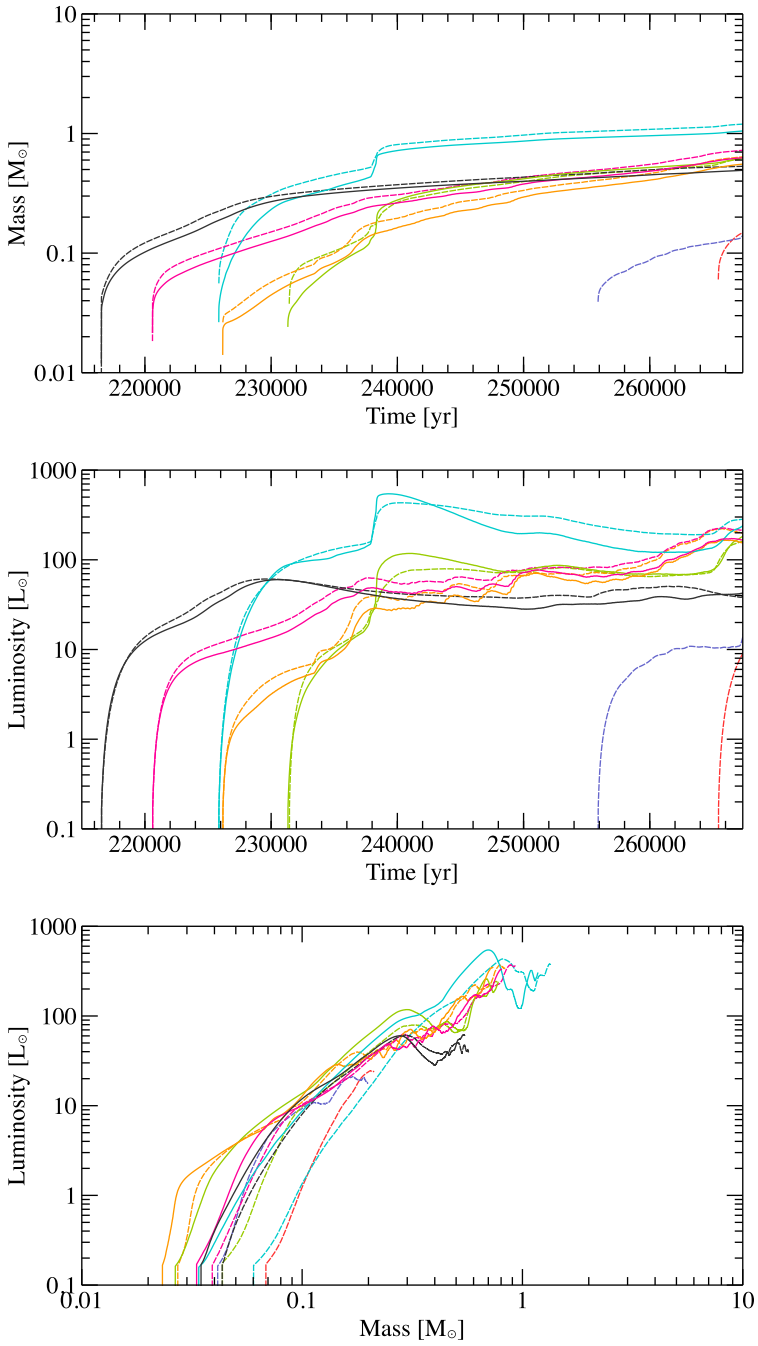

Figure 5.17: The evolution of the masses and luminosities of sink particles in the cluster calculations using 0.5 AU and 5 AU sink particles with luminosities set by the disc-accretion algorithm. Each colour denotes a different sink particle. The results of the 0.5 AU calculations are shown by the solid lines, and the 5 AU calculations are shown by the dashed lines. Once formed, the masses of the protostars increase steadily as the calculations progress. The protostellar luminosities increase as the masses increase. However, there is also considerable spread in luminosities of sink particles with similar masses, due to variations in the accretion rates.

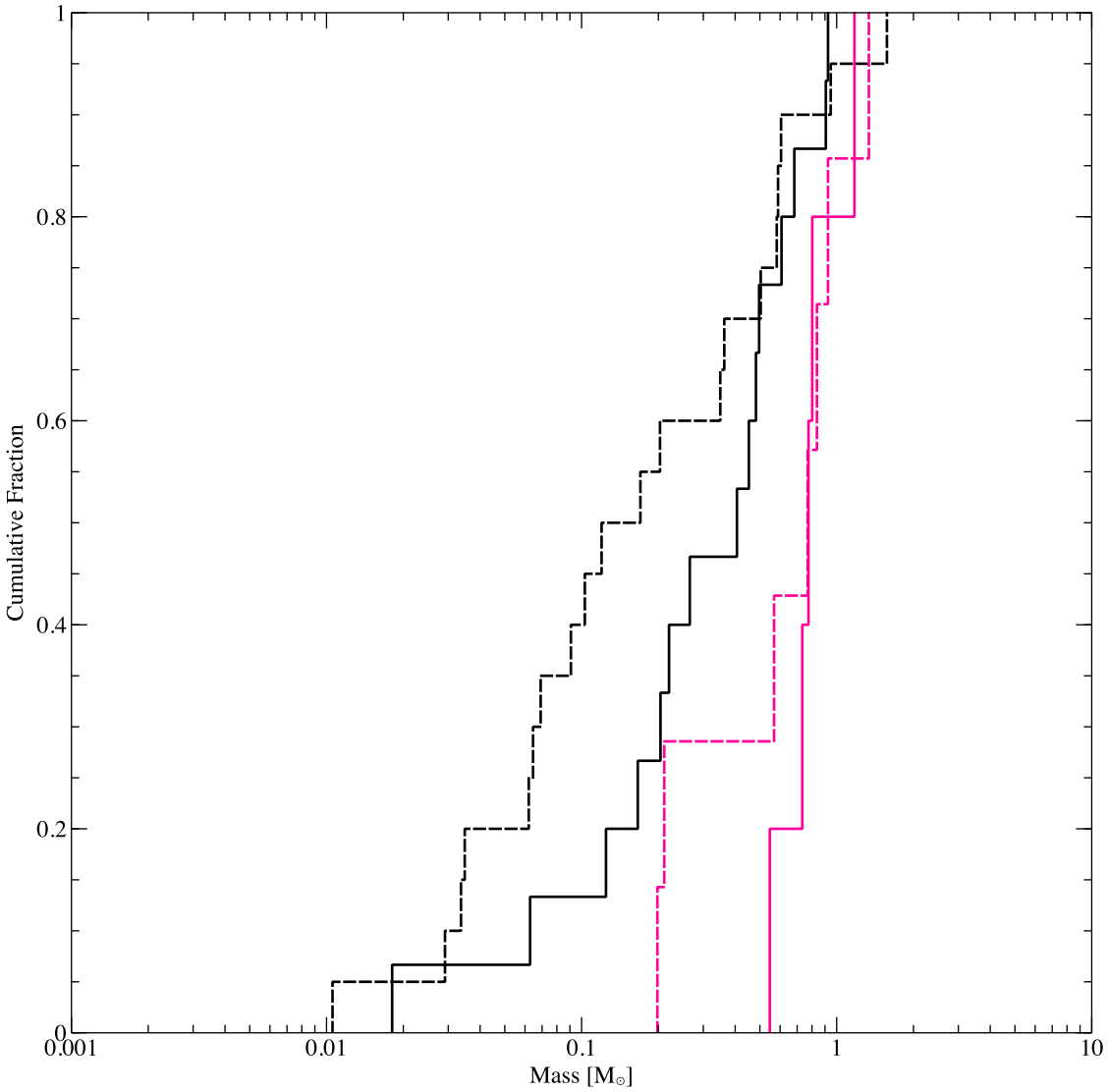

Figure 5.18: The cumulative distribution of stellar and brown dwarf masses in the cluster calculations using 0.5 AU and 5 AU sink particles without feedback and with luminosities set by the disc-accretion algorithm. The values for the calculations including sink feedback are shown in magenta, and the calculations that do not include feedback are shown in black. The solid lines show the calculations using a sink accretion radius of 0.5 AU, and the dashed lines show the calculations using 5 AU. Including radiative feedback from sink particles increases the median mass of the clusters. It also decreases the difference between the distributions in the calculations using accretion radii of 0.5 AU and 5 AU.

5.4 Discussion

The results of our calculations show that including radiative feedback from sink particles in simulations of star-formation significantly affects both the dynamics of the cluster gas and the distribution of protostellar masses produced. In this section, we consider our results in the context of previous simulations of star formation, examining the implications for the protostellar mass function and luminosity evolution. We also compare our results to observations of protostellar heating within molecular clouds.

5.4.1 Protostellar mass function

Including feedback from sink particles has a significant impact on the distribution of protostellar masses in star-forming cores. The reduced level of fragmentation increases the median stellar mass, as fewer objects means less competition for accretion, enabling the protostars that do form to accrete more of the gas reservoir and attain higher masses.

Our results follow similar patterns to those found by Bate (2009c) and Bate (2012) when comparing calculations including radiative transfer with those using a barotropic equation of state. The initial phase of star-formation in each dense core does not depend greatly on whether radiative transfer or a barotropic equation of state is used, or on whether or not sink particle feedback is included. However, once the first few protostars have formed, the additional heating begins to inhibit fragmentation and slow the rate of star formation. Bate (2012) performed small radiation hydrodynamical star formation calculations very similar to those we present here, using 5 AU, 0.5 AU, and 0.05 AU non-luminous sink particles that produced 15, 11, and 8 protostars, respectively. He also performed a barotropic version of the calculation that produced 48 protostars. Based on these results, he argued that using radiative transfer with 0.5 AU sink particles feedback was sufficient to capture most of the effects of radiative feedback. However, while this may be true, our results with radiative feedback from sink particles show that the additional luminosity can produce roughly a factor of two reduction in the number of protostars and increase the median stellar mass. Therefore, it does need to be accounted for.

We may also consider the typical size of regions that collapse to form protostars. The mass of these regions should be approximately the same as the typical protostellar mass, which can be identified with the median mass of the cluster. In an isothermal system, this is described by the typical Jeans length which depends solely on the density. However, the luminosity from an embedded protostar will heat the surrounding gas, increasing the size of the region required to overcome the thermal pressure of the gas. Bate (2009c) described this as the 'effective Jeans length', and identified the corresponding 'effective Jeans mass'. By considering simple analytical arguments, Bate (2009c) predicted that the median mass should scale as $M_C \propto \rho^{-1/5} L_*^{3/10}$ where ρ is the density of the gas, and L_* is the protostellar

luminosity. As the accretion luminosity scales as $L \propto 1/R_*$, our no-feedback calculations using sink particles with accretion radii of 0.5 AU and 5 AU underestimate the luminosity by factors of 50 and 500 respectively for a typical protostellar radius of 2 $R_\odot$ (Larson 1969). Thus, the analytical model of Bate (2009c) predicts that this should result in a shift in the median mass by factors of 3.2 and 6.5 respectively. Given the small numbers of protostars formed, this is in good agreement with our results (using 0.5 AU sink particles, the median mass increased from 0.41 to 0.77 $M_\odot$, a factor of 1.9, and using 5 AU sink particles, the median mass increased from 0.12 to 0.77 $M_\odot$, a factor of 6.4).

We also find that the mass distributions produced by the calculations including sink particle feedback are almost independent of whether accretion radii of 0.5 AU or 5 AU are used. This agrees with the assertion of Offner et al. (2009) that the protostellar luminosity becomes the dominant source of heating once the first protostars have formed, as it implies that the primary source of heating is included, regardless of the sink particle accretion radius.

The median masses of the clusters in the feedback calculations are higher than typically observed in local star-forming regions (Bastian et al. 2010) and in the canonical Galactic stellar initial mass function (Chabrier 2005). This was also true of calculations performed by Bate (2009c), which used similar initial conditions to those we use in this chapter, and those of Offner et al. (2009). The star formation in our calculations and in these earlier calculations occurred in small protostellar groups. Jones and Bate (2018) (see Chapter 4 found that low-density molecular clouds form stars in well separated groups, similar to the groups that form in the calculations of Bate (2009c) and Offner et al. (2009). These low-density clusters were also found to exhibit higher than expected median stellar masses. Goodwin et al. (2004a) suggested that this may be caused by ejections of low-mass objects from the groups, which decrease the number of accreting objects whilst depleting the mass of the group by a negligible amount. In fact, our calculations suggest that it is in fact due to a lack of dynamical interactions, due to the small numbers of stars within each group. With fewer dynamical interactions and ejections, most objects are able to accrete to higher masses without having their growth terminated prematurely, raising the median mass. The implication is that to obtain the typical Galactic stellar mass function with a lower median stellar mass, stars must form in groups that are large enough and dynamically interactive enough to fully populate the low-mass end of the mass function. It is also possible that the feedback from first protostars in the group may inhibit fragmentation long enough to allow them to accrete a substantial amount of mass before any new protostars form. Once new objects do form, the larger masses of the existing protostars allows them to competitively accrete within the small group, attaining a higher mass than would otherwise be expected. Simulations of star formation in massive protostellar cores performed by Krumholz et al. (2007) displayed similar behaviour, with the feedback from the first protostar to form inhibiting fragmentation in the group, allowing it to accrete the majority of the available mass.

A possibility mechanism for lowering the median stellar mass is that disc accretion is episodic rather than continuous. Lomax et al. (2015) considered the effects of no feedback, constant feedback and episodic feedback for protostars formed in an ensemble of star-forming cores. As in our calculations, they found that continuous feedback heavily suppressed fragmentation, causing low-mass objects to be underproduced, resulting in a higher median mass. However, when including episodic feedback from protostars, this issue was resolved. In the episodic case, they varied protostellar luminosities from ~ 0.1 $L_\odot$ during quiescent periods to ~ 100 $L_\odot$ during outbursts. Due to the short timescales over which outbursts occurred, the distributions of protostellar masses in these calculations were highly similar to the calculations that did not include protostellar feedback. The primary issue with this solution however, is that the characteristics of episodic accretion are poorly understood. **It is also possible that the conversion of gravitational potential energy to luminosity is much less efficient than assumed in our calculations. As mentioned in Section 5.1, previous calculations, such as those of Offner et al. (2009), have used values of $\epsilon < 1$, implying that a significant fraction of the accretion energy is carried away by jets/outflows. If sufficient energy is removed from the system in this manner, then the heating effect of accreting protostars may be reduced enough to allow brown dwarfs to form via disc fragmentation. Future calculations using a range of values of ϵ would be needed to ascertain whether such a mechanism is realistic.**

5.4.2 Protostellar evolution

Fig. 5.15 indicates that there is no correlation between the final masses and the formation time of protostars, in contrast to simple predictions (e.g Shu 1977). Instead the final protostellar masses are determined by their accretion histories, which are largely governed through competitive accretion, in agreement with the results of Bonnell et al. (1997, 2001), Klessen et al. (1998), Klessen (2001), and (Bate and Bonnell 2005).

The average luminosities of the protostars increase with final mass, in agreement with the findings of Urban et al. (2010). However, there is significant spread among the luminosities of protostars with similar masses, as seen in Fig. 5.17. This suggests that the luminosities of protostars depend not only on their mass, but also on variations in their accretion rates due to the dynamics of their environments. During the formation of the first protostars, the accretion rates and luminosities increase smoothly. However, once more objects form, the increased frequency of dynamic interactions causes variations in the accretion rates, which give rise to variations in the accretion luminosities. **Such variations in the luminosities of objects with similar masses may help to explain the so-called 'luminosity problem', where young stars exhibit much lower accretion luminosities than would be expected if they had grown via continuous accretion.**

The luminosities typically differ by less than an order of magnitude after the initial

growth phase ($M_* \gtrsim 0.1$ M$_\odot$). Prior to this the luminosities may increase by up to two orders of magnitude as the surrounding remnants of their preceding first hydrostatic cores are accreted. This is in broad agreement with the results of Offner et al. (2009), who found that accretion rates were smoother once feedback was introduced. However, the sink particle accretion radii used in those calculations were 30 – 250 times larger than the smallest radius used here. This suggests that the dynamics driving these luminosity variations on 100-1000 yrs timescales have similar effects at ≈ 1 AU and ≈ 100 AU scales. Contrastingly, Urban et al. (2010) found that their protostellar accretion rates were highly variable. The reason for this is unclear. It is possible that their method for calculating protostellar luminosities, via interpolation over the protostellar mass and accretion rate, may not fully resolve the self-regulating effect of the luminosity on the accretion flow, and may therefore over-estimate its variability. The typical size of these luminosity variations is much smaller than those employed in episodic models of accretion feedback, such as those of Lomax et al. (2015) which vary by three orders of magnitude. If such episodic accretion does occur, it must come from some type of disc instability that is not captured by the physical processes modelled in our simulations.

5.4.3 Comparison with observations

Observational studies of young stellar objects (YSOs) have found substantial evidence of protostellar heating in low-mass star-forming regions. van Kempen et al. (2009a, 2009b) conducted observations using APEX-CHAMP to map high-J CO lines around ∼ 30 nearby sources in order to trace the distribution of warm gas. van Kempen et al. (2010) subsequently performed spectroscopy using Herschel/PACS to study the spectra of these sources. Combining these data sets, both Visser et al. (2012) and Yıldız et al. (2012) confirmed that these studies indicated the presence of heated regions of ≈ 100 K extending out to ∼ 1000 AU in the vicinity of embedded low-mass protostars. These findings were corroborated by Sicilia-Aguilar et al. (2013), using multi-wavelength Herschel observations to create temperature maps of the Corona Australis star-forming region. The temperature distributions in our calculations including protostellar feedback (see Figs. 5.13 and 5.14) are remarkably similar to those of Sicilia-Aguilar et al. (2013), with heated regions of ∼ 30 – 100 K extending for several thousand AU around the newly formed protostars.

Hatchell et al. (2013) used James Clerk Maxwell Telescope (JCMT) SCUBA-2 observations to map the heating from young stars and protostars in the NGC 1333 star-forming region. They also detected elevated temperatures upwards of 20 K in the vicinity of embedded protostars, and argued that this heating effect would lead to an increase in the typical mass of the next generation of protostars as we find in our simulations.

The protostars in both our calculations and in the observations of Sicilia-Aguilar et al. (2013) and Hatchell et al. (2013) form in small groups approximately 0.1 pc across. Similar

structures have been observed in the nearby Taurus-Auriga region (Luhman et al. 2003), which also exhibit a median stellar mass that is higher than expected. Goodwin et al. (2004a) have suggested that the formation of stars in groups such as this may lead to increased masses, as low-mass objects are often dynamically ejected, leaving fewer objects to compete for accretion of the gas reservoir. **Luhman et al. (2016) observed low-mass objects in the IC 348 ad NGC 1333 star-forming regions, and identified several potential candidates for these ejected brown dwarfs.** However, the lack of brown dwarfs in our calculations suggests that this is not the case, as ejections would increase the number of objects that have their accretion terminated before reaching higher masses. Instead, it seems more probable that inhibition of fragmentation via protostellar heating, combined with a lack of dynamics ejections is responsible for the increased median mass of stars in these regions.

5.5 Conclusions

In this chapter, we have presented results from calculations of star formation in small clusters to investigate the effects of including sink feedback on the formation of stellar clusters and their properties.

We find that including sink feedback has a significant effect on the star formation process and the evolution of star-forming clusters. Our conclusions are as follows:

1. The additional heating from newly formed protostars in calculations including radiative feedback from sink particles suppresses fragmentation even further than in calculations that include radiative transfer and use small sink particles that do not emit radiation. This reduces the star formation rate after the formation of the first protostars, resulting in a lower total number of objects formed and total stellar mass at the end of the calculations.

2. The reduced number of objects allows the protostars to attain higher final masses than in calculations with no sink particle feedback. The final protostellar masses are a function of their accretion histories, rather than simply depending on their formation times.

3. The average protostellar luminosities are found to not only to depend on the protostellar mass, but also to depend strongly on the mass accretion rate, causing an order of magnitude spread in the luminosities of protostars with similar masses. The luminosity variations of protostars are largely due to changes in the accretion rate driven by the dynamics of the cluster gas.

4. Including feedback from sink particles raises the median mass of protostars in the calculations. The magnitude of the effect is in agreement with the scaling predicted by the simple analytical model proposed by Bate (2009c). We also find that the stellar

mass distributions obtained from calculations that include radiative feedback from sink particles are insensitive to the choice of sink particle accretion radii (varied between 0.5 and 5 AU). This implies that protostellar heating from accretion is the dominant form of heating in star-forming clusters, as asserted by Offner et al. (2009).

5. The median masses of the clusters in feedback calculations are higher than typically observed, due to a lack of brown dwarfs. This provides an alternative explanation for the high median mass of similar groups observed in the Taurus-Auriga region from that given by Goodwin et al. (2004a). They proposed that low-mass objects were preferentially ejected, leaving behind higher-mass stars. Instead, the higher median mass may be due to a *lack* of dynamical interactions and ejections in small groups of protostars so that brown dwarfs are underproduced.

6. The temperature distributions in the calculations including radiative feedback from sink particles are similar to those observed in Galactic star-forming regions, such as the Perseus (Hatchell et al. 2013) and Corona Australis (Sicilia-Aguilar et al. 2013) regions.

Chapter 6

Feedback including the effects of protostellar evolution

Over the last two chapters, we have illustrated the role that radiative heating plays in determining the masses of protostars formed in clusters, and shown how treating the luminosity generated by the accretion of mass onto protostars may dramatically alter the evolution of these clusters. However, so far we have ignored the evolution of the protostars themselves. Along with the accretion luminosity, the evolution of protostars contributes to the total protostellar heating effect in two ways. First, it contributes directly via the intrinsic luminosity of the protostar radiated from the protostellar surface. Although this is expected to be small compared to the accretion luminosity for protostars accreting at high rates (Hosokawa and Omukai 2009), at lower accretion rates and higher stellar masses it may contribute a significant proportion of the total luminosity of the system (Offner et al. 2009). Second, variations in the protostellar structure affect the amount of gravitational energy converted to radiation energy by the accretion flow. More specifically, the accretion luminosity depends on the ratio of the protostellar mass and protostellar radius (see Chapter 3). Since the protostellar radius will vary with time, even when none of the accretion energy is advected into the protostellar interior (Baraffe et al. 2009), the evolution of the protostellar structure must be modelled in order to consistently calculate the accretion luminosity.

In this chapter, we investigate the effects of modelling the evolution of protostars, in addition to the accretion luminosity, in SPH calculations of star formation in small stellar clusters. We use the `Lyon` one-dimensional stellar evolution code to calculate the structures and luminosities of the protostars, and combine this with our disc-accretion algorithm for modelling the accretion luminosity. This allows us to completely describe the mechanisms responsible for protostellar heating, including the evolution of the protostellar radius via the advection of entropy into the protostar, and the intrinsic protostellar luminosity.

Section 6.1 describes our numerical method, as well as the parameters and initial conditions used for each of the calculations. In Section 6.2, we examine the effects of including protostellar evolution in calculations of the formation of small stellar clusters. We do so by comparing the results of these calculations with those of the cluster calculations presented in the previous chapter, which did not model the evolution of protostars. We then compare results from several calculations including protostellar evolution, using different initial accretion rates to calculate the accretion luminosities, and advecting different fractions of the accretion energy into the protostars. In Section 6.3, we discuss the results of our calculations in the context of other calculations of star formation which include accretion feedback and protostellar evolution. We also examine the distributions of protostellar properties produced by the calculations, and compare them to those produced by models of stellar evolution. Our conclusions are listed in Section 6.4.

6.1 Computational method

As in the previous two chapters, we used the `sphNG` code to model the gas and protostars, using the methods described in Chapters 2 and 3. **The calculations were performed using the University of Exeter Isca supercomputer. They used 4 nodes and a total of 64 cores, with an approximate wall-time of ~ 1 month.** The calculations include hydrodynamics, gravitational forces, and radiative transfer. Protostars are modelled using sink particles, as described in Chapter 3, which have accretion radii of 0.5 AU.

All of the calculations model the accretion luminosity using the disc-accretion algorithm, in the same manner as the calculations presented in Chapter 5. They also model the evolution of protostars using the `Lyon` stellar evolution code, as described in Chapter 3. The stellar evolution model begins with an initial object of mass 1 M_J and radius 1.3 $R_\odot$ for each new protostar, which is initialised after the 10 year pre-collapse period used by the disc accretion algorithm (see Chapter 3).

Since the initial accretion rate is a free parameter of the disc accretion model, we vary its value to investigate its effects on the level of feedback and the evolution of the protostars. The initial accretion rates used in the calculations are 10^{-5} $M_\odot$ yr^{-1} and 10^{-6} $M_\odot$ yr^{-1}. The stellar evolution model also requires a specification for the value of $\alpha < 1$, the fraction of the accretion energy advected into the protostellar interior. This will depend in general upon the properties of the accretion flow, as well as the properties of the stellar interior. It's value however, is poorly constrained. As such, we vary its value as well in order to assess its impact on the evolution of the protostars. The parameters used for each of the calculations are summarised in Table 6.1.

Table 6.1: The run parameters of the calculations which calculate accretion luminosities and model protostellar evolution. We also include the 0.5 AU calculations from Chapter 5 one of which calculated the accretion luminosity, but did not model protostellar evolution, and one which did not include protostellar feedback, for comparison. Two of the new calculations differ from the FB05 in the initial accretion rate used by the disc algorithm, which is an order of magnitude lower. One calculation also uses a higher value of $\alpha = 0.05$ than the other calculations which include protostellar evolution, which use $\alpha = 0.01$.

Calculation	Acc. Radius (AU)	Acc. Rate ($M_\odot$ yrs^{-1})	α
noFB05	0.5	–	–
FB05	0.5	10^{-5}	–
FB05+PE5001	0.5	10^{-5}	0.01
FB05+PE6001	0.5	10^{-6}	0.01
FB05+PE6005	0.5	10^{-6}	0.05

6.1.1 Initial conditions

We simulate turbulent, uniform density gas clouds, using the same initial conditions as the cluster calculations presented in Chapter 5. The clouds have masses of 50 $M_\odot$ and radii of 0.188 pc, with initial mean densities of 1.2×10^{-19} g cm^{-3}. They have uniform initial temperatures of 10.3 K. The initial free-fall times of the clouds are 6.02×10^{12} s (1.91×10^5 yrs).

6.2 Results

We present results from three radiation hydrodynamical simulations of the formation of a small stellar clusters, similar to the cluster calculations in the previous chapter. However, while those calculations did not model the evolution of the protostellar structure, and instead fixed the protostellar radius at 2 $R_\odot$, the calculations presented here model protostellar evolution using a live stellar model, as described in Chapter 3.

First, we compare the results of the FB05+PE5001 calculation with those from the noFB05 and FB05 calculations presented in the previous chapter to assess the impact of protostellar evolution on the star formation process. Next, we investigate the dependence of the effects of protostellar evolution on the initial accretion rate used by the disc accretion algorithm, as well as the fraction of the accretion energy that is advected into the protostar, by comparing the results of the FB05+PE5001, FB05+PE6001 and FB05+PE6005 calculations. Finally, we examine the evolution of the distributions of protostellar properties in the FB05+PE5001, FB05+PE6001 and FB05+PE6005 calculations, and compare them to results from static models of protostellar evolution.

The calculations were run until they reached 1.25 initial cloud free-fall times. The FB05+PE5001, FB05+PE6001 and FB05+PE6005 calculations produced a total of 5, 7, and 7 objects, respectively. The results of the FB05+PE5001 calculations are compared with the

noFB05 and FB05 calculations from Chapter 5 at 1.25 initial cloud free-fall times, which produced 15 and 5 objects, respectively.

6.2.1 The effects of protostellar evolution

Fig. 6.1 shows the evolution of the gas density and temperature in the main star-forming core of the FB05 and FB05+PE5001 calculations. Again, stars also form in other regions of the cluster, but we only show the largest core for clarity. As with the calculations in the previous chapters, the turbulent velocity field of the molecular cloud results in a filamentary structure. Where gas flows collide, dense cores are formed, which gravitationally collapse and fragment to form stars. The majority of star formation occurs in these cores, which heat the surrounding region as gas falls into the gravitational potential and is accreted by the embedded protostars.

The evolution of the clusters in each of the calculations is similar. The first protostars form in a similar manner to those in the noFB05 calculation. After these first protostars form, the radiative feedback generated via the accretion of mass raises the temperature of the surrounding gas, resulting in a diffuse cloud structure and suppressing further fragmentation. This behaviour is reflected in Fig. 6.2, which shows the formation time and final mass of each star and brown dwarf in noFB05, FB05 and FB05+PE5001 calculations. As in the previous chapter, the formation times and final masses of the first protostars are approximately the same across all of the calculations. However, as the calculations progress, both calculations including accretion feedback produce fewer objects than the noFB05 calculation, due to the additional thermal pressure provided by the accretion luminosities of the protostars.

Fig. 6.3 shows the evolution of the total stellar mass (i.e. the combined mass of the sink particles) and the total number of objects in each of the calculations, which reflect the evolution of the distribution of mass in the clusters. The total numbers of objects formed in the FB05 and FB05+PE5001 calculations are identical, and the star-formation rates are also similar. During the formation of the first protostars, the numbers of objects formed and total masses of the FB05 and FB05+PE5001 calculations are very similar to the noFB05 calculation. However, once the first protostars begin to accrete, the radiative heating generated raises the temperature of the cluster gas, supporting it against collapse. This results in fewer objects being formed by the FB05 and FB05+PE5001 calculations and a lower total stellar mass in each calculation.

Despite the similarities in the evolutions of the FB05 and FB05+PE5001 calculations, there are some minor differences evident in the fragmentation and total stellar masses of the clouds. Fig. 6.1 (third column) shows that fragmentation of a circumstellar disc occurs in the FB05+PE5001 calculation, but not in the FB05 calculation. Fig. 6.2 also shows that the collapse of some fragments to form protostars occurs later in the FB05+PE5001

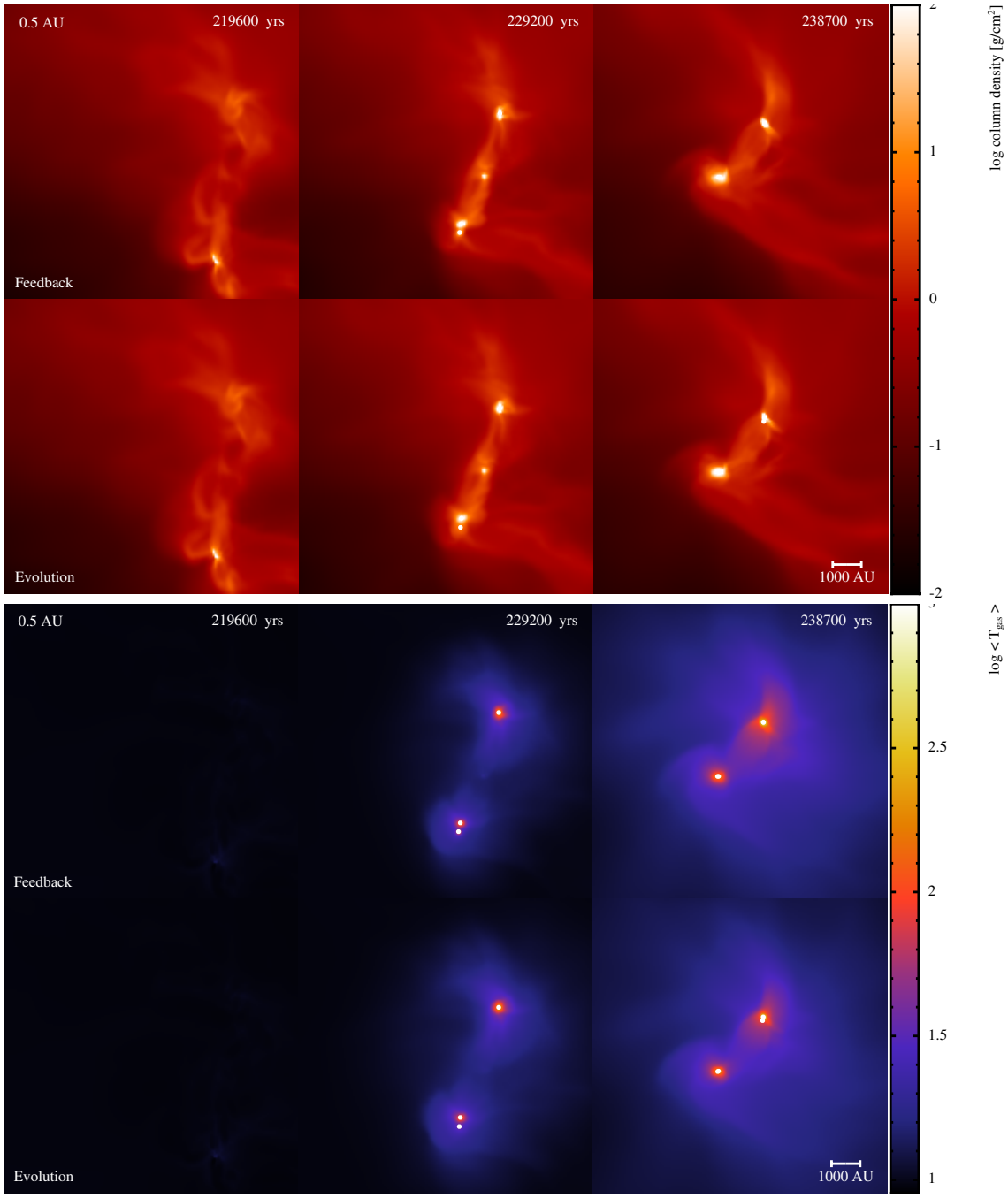

Figure 6.1: The time evolution of the gas column density and mass-weighted temperature in the FB05 and FB05+PE5001 calculations. The panels display the calculations at times separated by intervals of 9,549 yrs, which corresponds to 1/20th of the initial cloud free-fall time. The colour scales show column densities on a logarithmic scale between 0.01 g cm^{-2} and 100 g cm^{-2}, and temperatures on a logarithmic scale between 9 K and 1000 K. The length scale is shown in the bottom-right of each set of panels. Including the effects of protostellar evolution results in similar dynamics to the calculation which does not evolve the structure of the protostars.

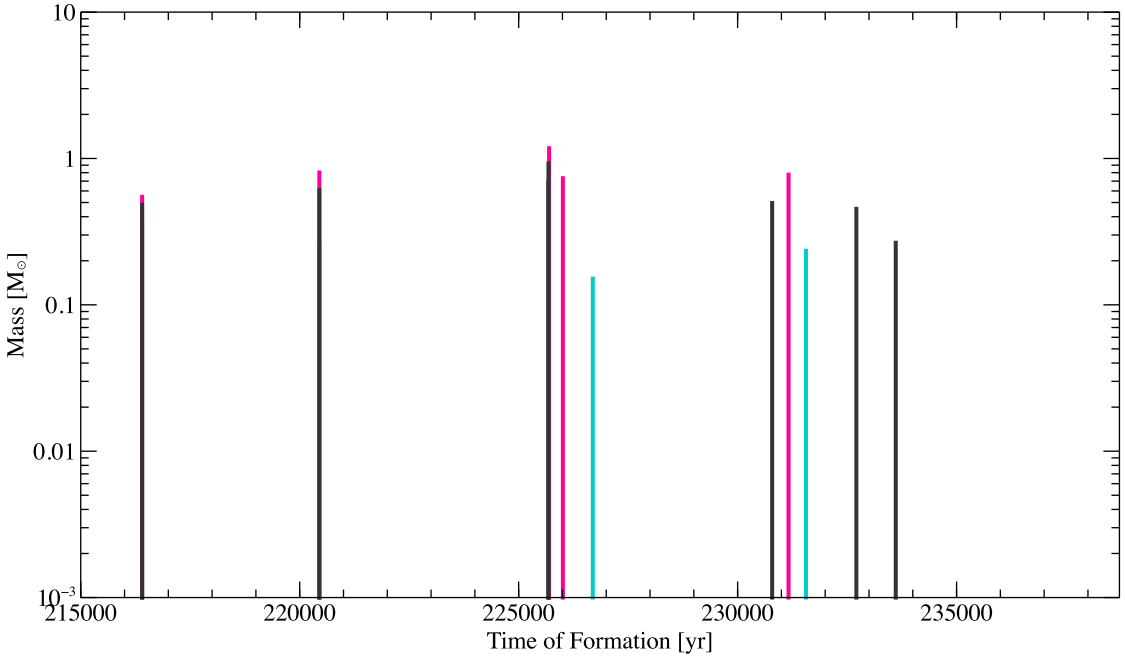

Figure 6.2: The mass and formation time of each star and brown dwarf in the noFB05, FB05 and FB05+PE5001 calculations. Objects formed in the noFB05 calculation are shown in black, objects formed in the FB05 calculation are shown in magenta, and objects formed in the FB05+PE5001 calculation are shown in cyan. Similar numbers of objects are formed in each of the calculations initially. In the calculations including accretion feedback, the subsequent heating from these first protostars inhibits fragmentation, and fewer objects are produced than in the calculation including no feedback. The increase in accretion luminosity in the FB05+PE5001 calculation, due to the smaller radii of protostars, results in the formation of some objects at later times than in the calculation which only includes accretion feedback.

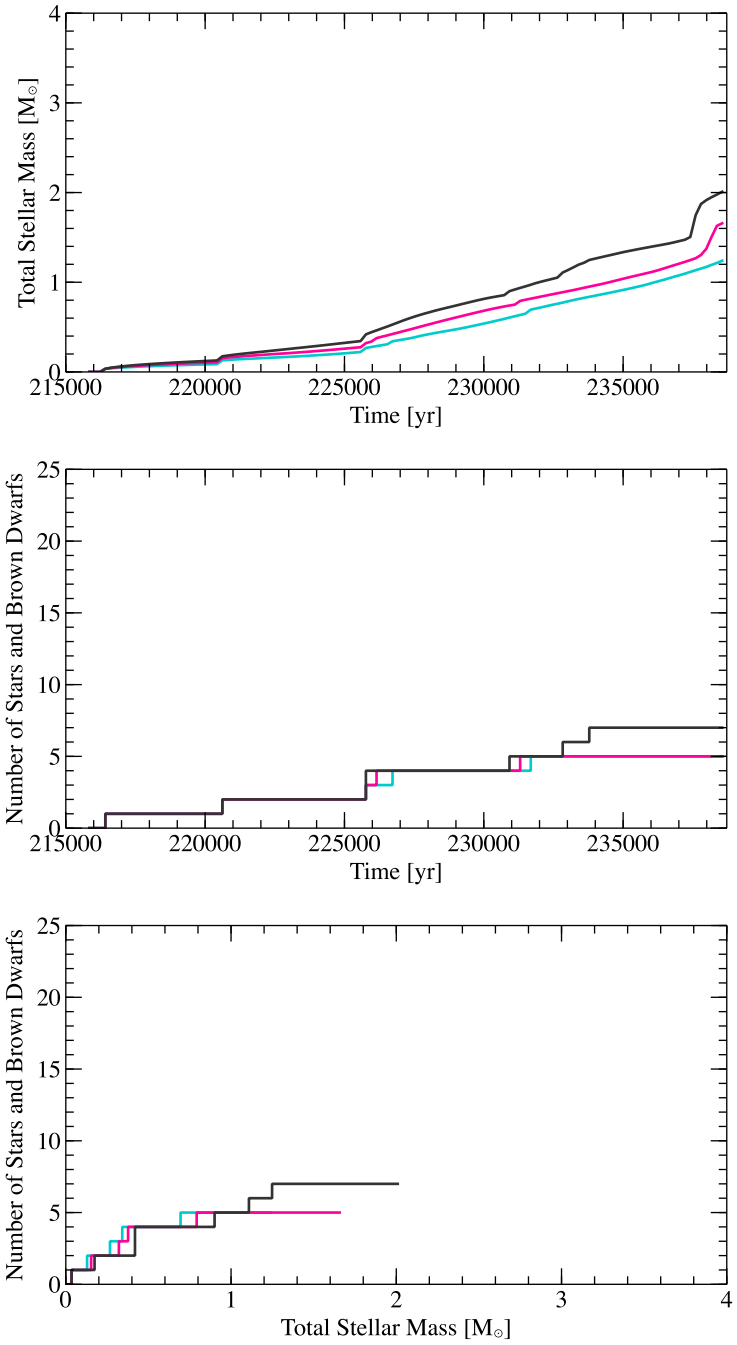

Figure 6.3: The evolution of the total stellar mass and total number of objects in the noFB05, FB05 and FB05+PE5001 calculations. The noFB05 calculation is shown by the black line, the FB05 calculation is shown by the magenta line, and the FB05+PE5001 calculation is shown by the cyan line. Including protostellar evolution results in a lower star-formation rate, due to the increased heating from the smaller protostars, which supports the cluster gas against gravitational collapse and reduces the protostellar accretion rates.

calculation than in the FB05 calculation. Finally, Fig. 6.3 shows that the FB05+PE5001 calculation forms stars at a lower rate than the FB05 calculation, such that by the end of the calculations, the total stellar mass is $\sim$ 25% lower than in the FB05 calculation, and $\sim$ 40% lower than in the noFB05 calculation.

Since the thermodynamics of the cluster are largely determined by protostellar heating, once the effects of the accretion luminosity are included, these differences in the fragmentary behaviour and total accretion rates of the clusters imply differences in the luminosities of the sink particles in the calculations. We plot these, along with the corresponding sink masses in Fig. 6.4. As the middle panel of Fig. 6.4 shows, the luminosities of the sink particles in the FB05+PE5001 calculation are initially higher than in the FB05 calculation. They are also noticeably more variable in the FB05+PE5001 calculation. Since the only difference between the FB05 and FB05+PE5001 calculations is the inclusion of a live stellar model, the cause of the increased sink luminosities in the FB05+PE5001 calculation must be the evolution of the protostars. We plot the evolution of the protostellar masses, radii and luminosities for each of the protostars in the FB05+PE5001 calculation in Fig. 6.5.

It is clear from the figure that the protostars undergo a rapid contraction of their radii following their formation, from their initial radii of 1.3 $R_\odot$ to ~ 0.3 $R_\odot$ over a period of ~ 200 yrs. As the protostellar luminosity depends upon the surface area of the protostar available to radiate, there is also a corresponding decrease in the luminosities of the protostars during the same period, from ~ 0.01 $L_\odot$ to ~ 0.001 $L_\odot$. Such contractions occur when the protostar is able to cool efficiently, with the speed of the collapse depends on both the rate of cooling, and the rate of advection of accretion energy into the protostellar interior (Baraffe et al. 2009). Since the protostellar model used in the FB05+PE5001 calculation assumes that the protostar is surrounded by a vacuum, radiative cooling from the surface of the protostar is highly efficient. However, the collapse timescale is significantly shorter than the expected Kelvin-Helmholz timescale, which is ~ 3000 yrs for a 1 M_J object with a radius of 1 $R_\odot$ and a luminosity of 0.01 $L_\odot$, implying that the contraction cannot be purely due to thermal cooling.

The contraction occurs as the protostars continue to gain mass through accretion. It is therefore possible that the gravitational potential energy added to the star by the accreted mass is not matched by the thermal energy input into the stellar interior. This is particularly likely if the fraction of the accretion energy advected into the protostellar interior, α, is a small, as in our calculations. In this case, accretion increases the gravitational binding energy of the protostar at a faster rate than its internal energy, which will cause it to contract due to the lack of thermal pressure support. The implication of this is that, in order to maintain a constant protostellar radius, accreting protostars must absorb sufficient thermal energy from the accreted mass to offset the increase in their binding energy, as well as replenish the energy lost through surface cooling. We discuss this further in Section 6.3.

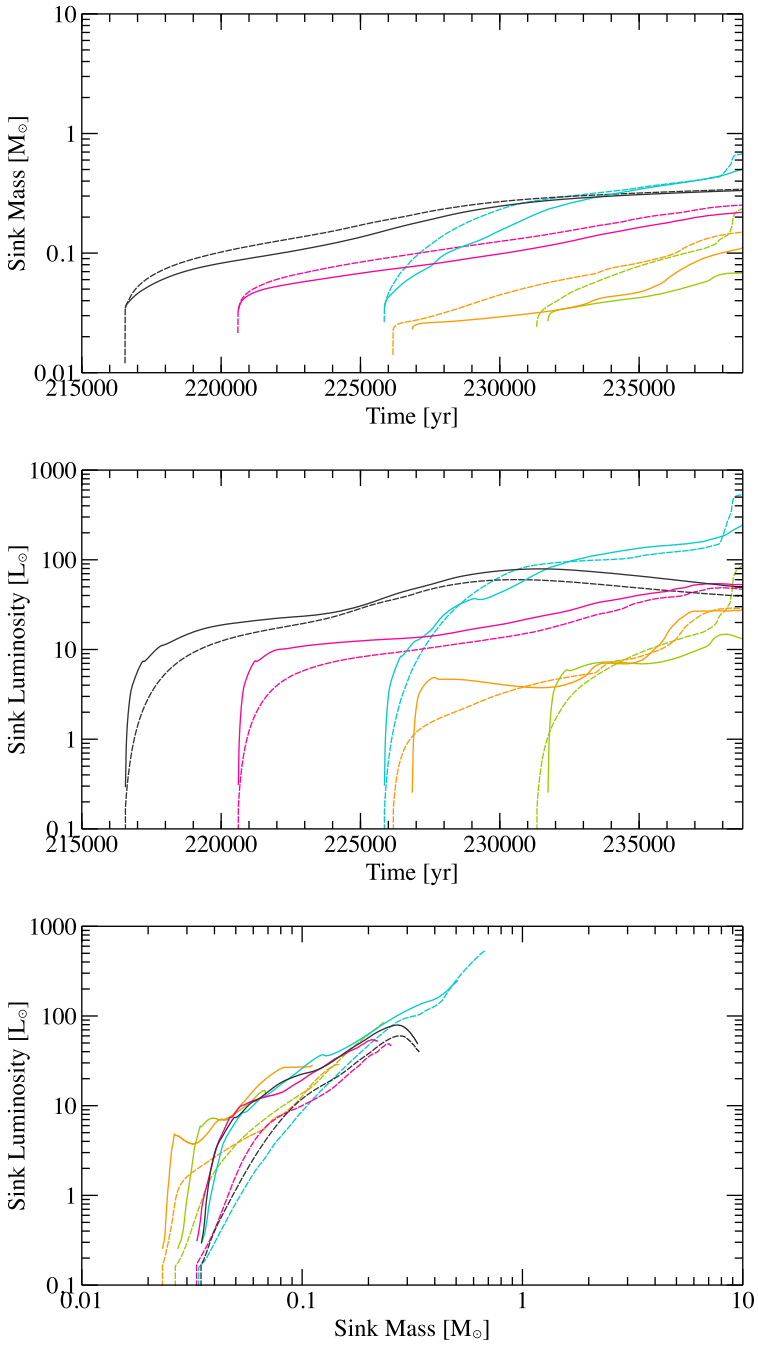

Figure 6.4: The evolution of the sink masses and luminosities in the FB05 and FB05+PE5001 calculations. Objects in the calculation which only includes accretion feedback are shown by the dashed lines, and objects in calculation also including protostellar evolution are shown by the solid lines. Each colour denotes a different sink particle. The results of both calculations are similar. The sink masses in the calculation including protostellar evolution increase at lower rate, due to the increased accretion luminosity of the smaller protostar. Rapid contraction of the protostars following their formation also causes a sharp initial rise in the sink accretion luminosities.

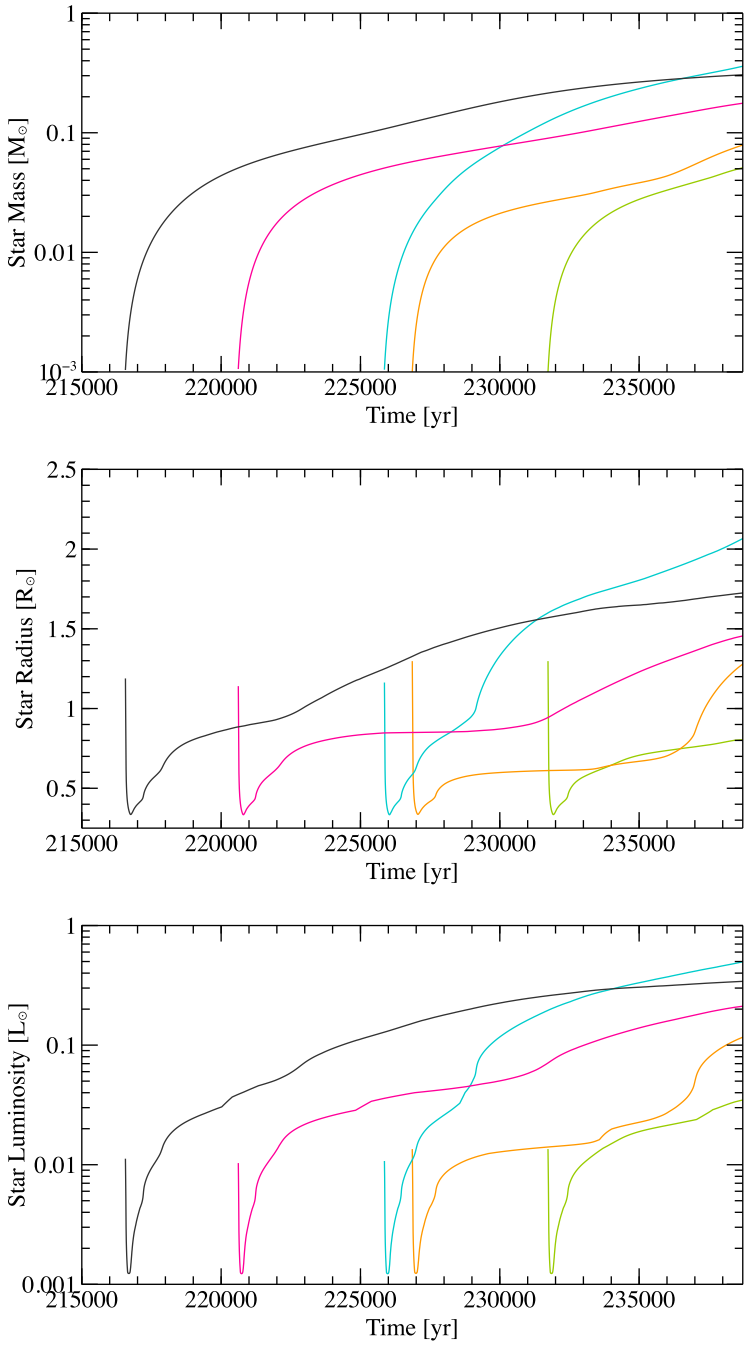

Figure 6.5: The evolution of the protostellar masses, radii and luminosities in the FB05+PE5001 calculation. Each colour denotes a different sink particle. While the protostellar masses steadily increase with time, the protostellar radii and luminosities decrease sharply after formation. This is caused by efficient surface cooling of the protostars, **as well as the increase in the gravitational binding energy of the protostars due to the accretion of mass.**

As the accretion luminosity of the sink particle depends inversely on the protostellar radius (see Chapter 3), this initial contraction produces a much higher accretion luminosity in the FB05+PE5001 calculation than in the FB05 calculation, as seen in Fig. 6.4. When such large luminosities (~ 10 $L_\odot$) are produced while the sink mass is low, they may drive thermal outflows due to the low gravitational binding energy of the sink and surrounding gas. This behaviour was seen in the Bonnor-Ebert sphere calculations presented in Chapter 5. The bottom panel of Fig. 6.4 suggests that this may occur in the FB05+PE5001 calculation, with luminosities which are much higher than in the FB05 calculation at sink masses of < 0.1 $M_\odot$. These outflows can significantly disrupt the structure and dynamics of surrounding gas, expelling material from the circumstellar disc and resulting in a highly variable sink accretion rate. This may account for both the lower sink masses and more variable luminosities seen in the FB05+PE5001 calculation. It may also give rise to the differences in the fragmentation of the clusters, as the outflows can disrupt circumstellar discs, causing them to fragment.

Once the contraction phase ends, the protostellar radius begins to increase due to the advection of energy from the accretion flow into the protostellar interior. However, as can be seen in Fig. 6.5, the radii of the protostars in the FB05+PE5001 calculation remain below 2 $R_\odot$, the value used by the FB05 calculation. As such, the sink luminosities remain marginally higher for the entire duration of the FB05+PE5001 calculation. The additional heating raises the temperatures of the gas reservoirs from which the protostars form and accrete, supporting them against gravitational collapse. This delays the collapse of fragments to form protostars and lowers their accretion rates, resulting in the later formation times of some objects in Fig. 6.2, and the lower total stellar mass seen in Fig. 6.3.

6.2.2 Varying the initial accretion rate and advection fraction

The FB05+PE5001 calculation examined in the previous section used an initial accretion rate of 10^{-5} $M_\odot$ yr^{-1} and $\alpha = 0.01$. Both of these parameters affect the evolution of the protostellar structure, and consequently the accretion feedback, but are weakly constrained. It is therefore important to examine the effects of varying these parameters on the results we have presented thus far. To do this, we compare the results of the FB05+PE5001, FB05+PE6001, and FB05+PE6005 calculations, which use different initial accretion rates, and different values of α.

Fig. 6.6 shows the evolution of the sink masses and luminosities in the FB05+PE5001, FB05+PE6001, and FB05+PE6005 calculations. The sink masses in the FB05+PE6001, and FB05+PE6005 calculations are noticeably higher than in the FB05+PE5001 calculation. This is caused by the lower accretion luminosities of the sinks, which allow the sinks to accrete mass at a high rate by producing lower temperatures in the surrounding gas. The lower luminosities of the protostars in the FB05+PE6001, and FB05+PE6005 calculations also

result in smoother evolution of both the sink luminosities and masses, with less variability than those in the FB05+PE5001 calculation, as they do not heat the surrounding gas strongly enough to drive the thermal outflows present in the FB05+PE5001 calculation.

The luminosities of the sinks in the FB05+PE6001 and FB05+PE6005 calculations increase less rapidly with sink mass than in the FB05+PE5001 calculation, due to the slower growth of the protostellar mass. They also display a spread of luminosities for given mass which is much greater than in the FB05+PE5001 calculation. The greater spread is due to an increased dependence of the accretion rate on the local gas dynamics, caused by the weaker heating effect of the lower accretion luminosities. At higher luminosities, the thermodynamics of the gas, which regulates the sink accretion rate, is dominated by the heating effect of accreting protostars, giving rise to the narrow spread observed in the FB05+PE5001 calculation. However, at lower luminosities, the accretion rate evolves primarily due to the dynamics of the cluster gas, rather than the heating effects of the protostellar radiation field. This may then lead to a wider range of luminosities for a given mass due to variations in the immediate environments of the protostars.

The sink luminosities in the FB05+PE6005 calculation are lower than in the FB05+PE6001 calculation. This is a result of the inflated radii of the protostars, caused by their increased entropy content. We plot the protostellar radii, along with the protostellar masses and intrinsic protostellar luminosities in Fig. 6.8. The top panel of the figure suggests that the evolution of the protostellar masses is dominated by **the value of** $\dot{M}_0$. The masses are significantly higher in the FB05+PE5001 calculation than in the FB05+PE6001 and FB05+PE6005 calculations, which exhibit almost identical results, regardless of the value of α. In all of the calculations, the growth of the stellar masses is smooth; an effect caused by the disc accretion algorithm. Since the accretion rate set by the algorithm depends upon the mass of the disc, any significant variation in the protostellar accretion rate requires a large change in the disc mass. Since the disc mass is large compared to the mass gained through accretion on the typical timescale of variations in the sink accretion rate, any variations in the sink accretion rates are 'smoothed' by the disc algorithm. **This is behaviour is clear from Fig. ??, which shows the evolution of the disc masses and protostellar accretion rates in the FB05+PE5001, FB05+PE6001 and FB05+PE6005 calculations.**

The protostellar radii and luminosities are much more variable. In each of the calculations, the radii and intrinsic luminosities of the protostars decrease rapidly following their formation. As mentioned in the previous section, this is due to the boundary conditions of the protostellar evolution model, which allow, the protostars cool to rapidly upon forming, causing them to contract, and decreasing their luminosities. **The increase in the gravitational binding energies of the protostars due to the accretion of mass also contributes to this collapse, as only a small fraction of the accretion energy is advected into the protostellar interior. Comparing the two calculations using the lower initial accretion rate with the calculation using the higher accretion rate, it is clear that the**

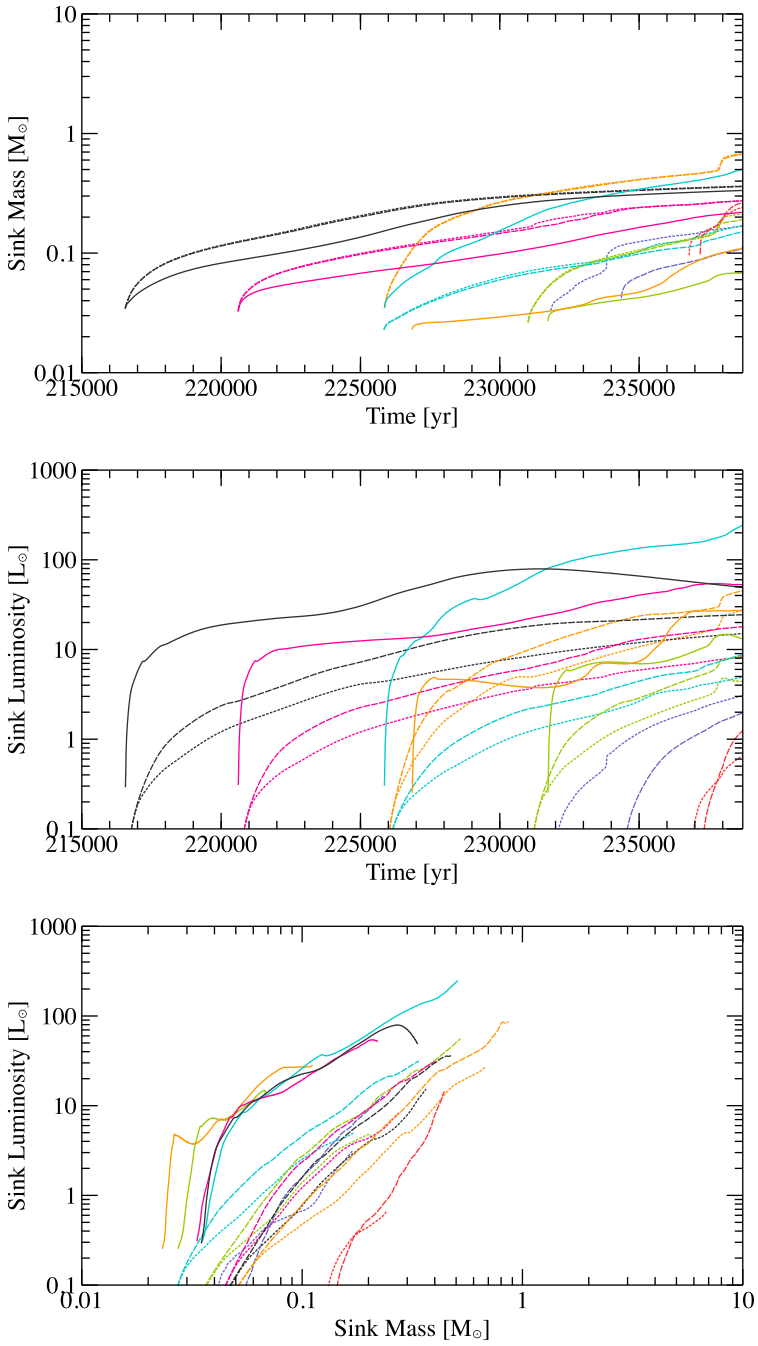

Figure 6.6: The evolution of the sink masses and luminosities in the FB05+PE5001, FB05+PE6001 and FB05+PE6005 calculations. Objects in the FB05+PE5001 calculation are shown by the solid lines, objects in the FB05+PE6001 are shown by the dashed lines, and objects in the FB05+PE6005 are shown by the dotted lines. Each colour denotes a different sink particle. Decreasing the initial accretion rate to 10^{-6} $M_\odot$ yrs^{-1} results in lower sink luminosities, reducing the heating effect on the surrounding gas and allowing the sinks to attain higher masses. Increasing α from 0.01 to 0.05 also reduces the sink luminosities, **due to the increased protostellar radii caused by the advection of energy into the protostellar interior.**

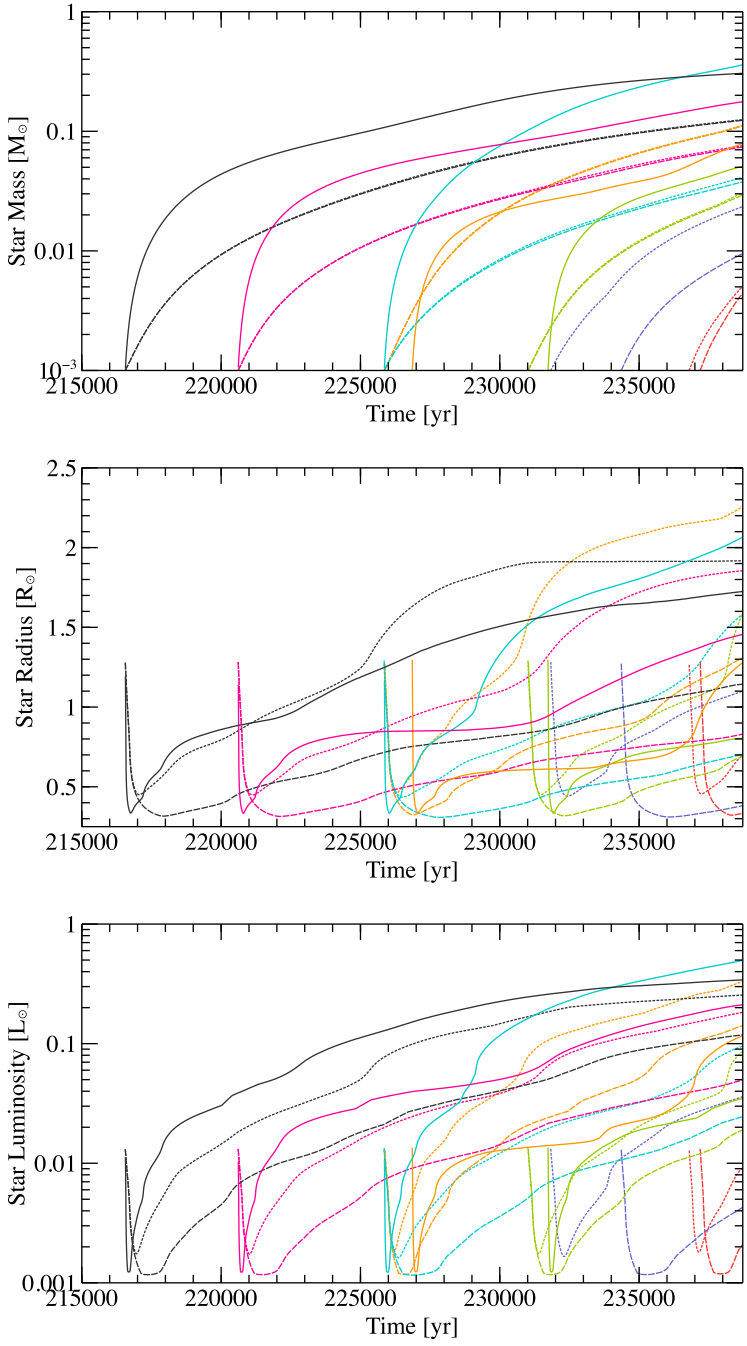

Figure 6.7: The evolution of the protostellar masses, radii and luminosities in the FB05+PE5001, FB05+PE6001 and FB05+PE6005 calculations. Objects in the FB05+PE5001 calculation are shown by the solid lines, objects in the FB05+PE6001 calculation are shown by the dashed lines, and objects in the FB05+PE6005 calculation are shown by the dotted lines. Each colour denotes a different sink particle. Increasing α from 0.01 to 0.05 does not significantly affect the protostellar masses, but does increase the protostellar radii and luminosities, **due to the increased thermal pressure support in the protostellar interior caused by advecting a greater fraction of the accretion energy into the protostellar interior.** Using a lower initial accretion rate of 10^{-6} $M_{\odot}$ yrs^{-1} results in lower protostellar masses, as well as lower protostellar radii and luminosities, **again due to the lower amount of energy advected into the interiors of the protostars.**

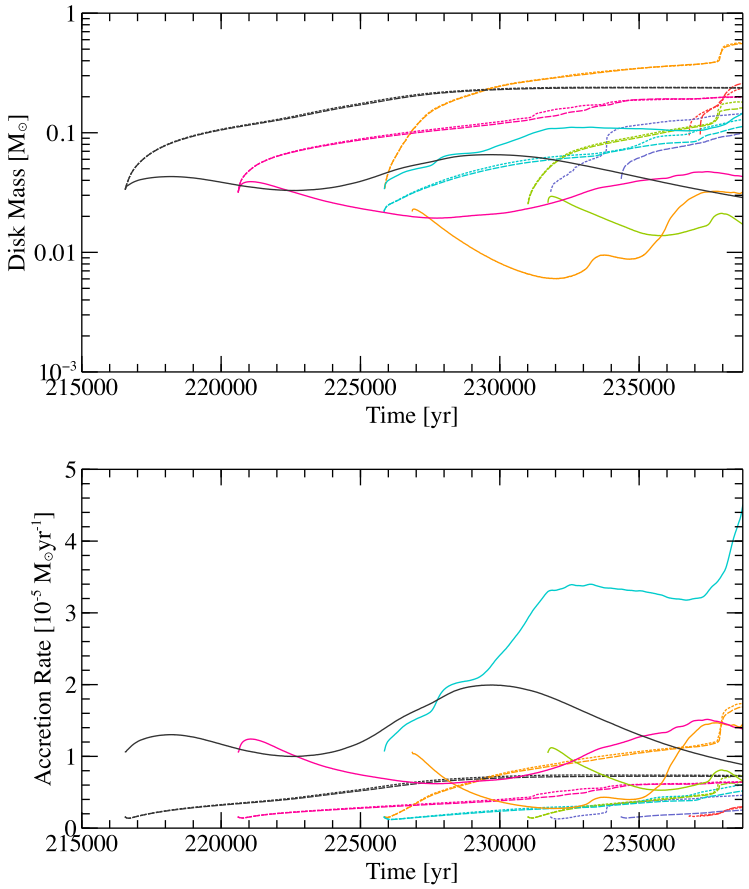

Figure 6.8: The evolution of the disc masses and protostellar accretion rates in the FB05+PE5001, FB05+PE6001 and FB05+PE6005 calculations. Objects in the FB05+PE5001 calculation are shown by the solid lines, objects in the FB05+PE6001 calculation are shown by the dashed lines, and objects in the FB05+PE6005 calculation are shown by the dotted lines. Each colour denotes a different sink particle. Using a lower initial accretion rate of 10^{-6} $M_{\odot}$ yr^{-1} results lower accretion rates and correspondingly higher disc masses, when compared with the calculation using a higher initial accretion rate of 10^{-5} $M_{\odot}$ yr^{-1}. This is due to the way in which the accretion rate is defined, such that a lower normalisation will require a higher disc mass to produce the same accretion rate (see Chapter 3. The disc masses and accretion rates are also more variable when using the higher initial accretion rate. This may be caused by changes in the dynamics of the gas driven by the higher level of radiative feedback.

contraction is more rapid when the accretion rate is higher, due to the greater rate at which gravitational potential energy is added to the protostar. It is also clear from the comparison between the FB05+PE6001 and FB05+PE6005 calculations that increasing the value of α, and therefore advocating more energy into the protostellar interior, reduces the magnitude of the contraction, due to the increased thermal pressure support which counteracts the additional gravitational potential energy. Advecting more energy into the protostellar interior, either by increasing the accretion rate or the value of α, also increases the final radius of protostars. This can be seen in the FB05+PE5001 and FB05+PE6005 calculations, both of which exhibit larger protostellar radii than the FB05+PE6001 calculation.

Comparing all three calculations, the protostellar radii are generally largest in the FB05+PE6005 calculation, and lowest in the FB05+PE6001 calculation. This implies that the advection of entropy is the primary factor which determines the protostellar structure, and that the accretion rate has only a small effect on the radius of the protostar. Baraffe et al. (2009) found similar results when performing calculations simulating a range of continuous and episodic accretion scenarios. The luminosities of the protostars in the FB05+PE5001 and FB05+PE6005 calculations are broadly comparable, despite the larger radii of protostars in the FB05+PE6005 calculation. This is because the increased gravitational binding energy of the more massive protostars in the FB05+PE5001 calculation produces higher surface temperatures at smaller protostellar radii.

6.2.3 Protostellar evolution

In addition to examining the global evolution of the clusters and the sink particles they contain, evolving the protostars using a live stellar evolution model permits us to study the properties of the protostars themselves. Since our calculations simulate the formation of clusters of protostars, we may also examine the statistical distributions of these properties.

In Fig. 6.9, we plot the evolution of the protostellar radii with mass in each of the calculations. At very low masses, during the initial contraction phase of the protostars, the protostellar radii evolve very similarly in all of the calculations. However, as the protostellar mass increases, using $\alpha = 0.05$ produces significantly larger radii for a given mass than the calculations using $\alpha = 0.01$. The results of the FB05+PE5001 and FB05+PE6001 calculations are similar, despite an order of magnitude difference in the initial protostellar accretion rate. This reflects the sensitivity of the protostellar structure to the value of α, and relative insensitivity to the accretion rate.

The spread of radii at a given mass increases significantly with mass across all of the calculations. This may be due to the increasingly variable accretion histories of protostars as the cluster evolves. The early accretion phases of protostars are dominated by the accretion of their surrounding first cores, which have similar structures, whereas later in

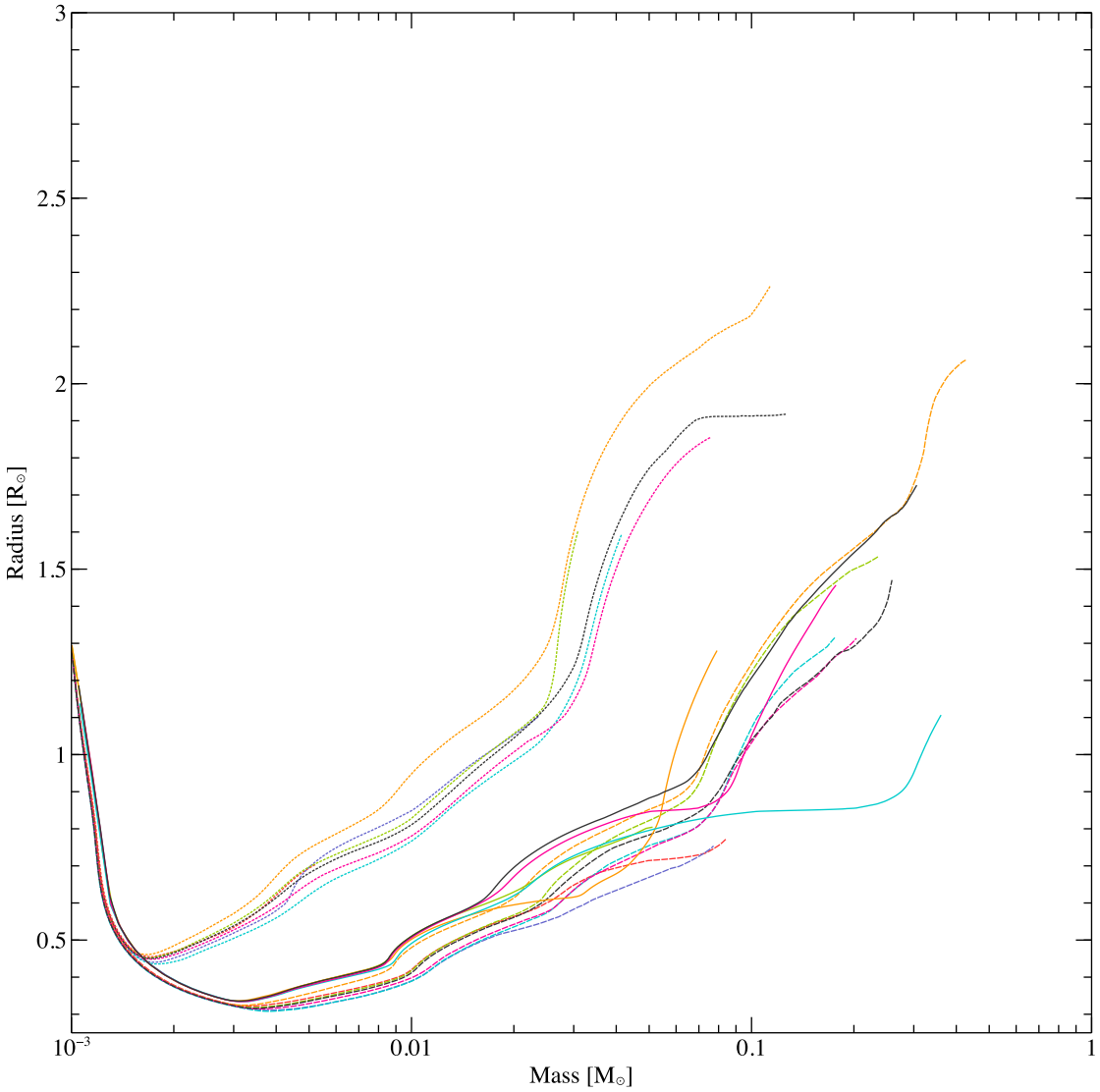

Figure 6.9: The evolution of the protostellar radii with mass in the FB05+PE5001, FB05+PE6001 and FB05+PE6005 calculations. Objects in the FB05+PE5001 calculation are shown by the solid lines, objects in the FB05+PE6001 calculation are shown by the dashed lines, and objects in the FB05+PE6005 calculation are shown by the dotted lines. Each colour denotes a different sink particle. The radii of the protostars evolve similarly in the FB05+PE5001 and FB05+PE6001 calculations. Using $\alpha = 0.05$ increases the radii for a given mass in the FB05+PE6005 calculation, **due to the increased thermal content of the protostars**, but does not significantly alter the forms of the evolutionary tracks, which remain similar to the calculations using $\alpha = 0.01$.

the lifetime of the cluster, protostellar accretion rates are likely to be determined by the dynamics of cluster, giving rise to a range of protostellar structures. The gradient of the radius evolution with mass appears to remain constant, even when changing the value of α. This may have implications for some proposed theories of the universal IMF. We discuss this point further in the next section.

We may also derive the effective surface temperatures of the protostars from the protostellar radii and luminosities using the Stefan-Boltzmann law $L = 4\pi R_*^2 \sigma_{\rm SB} T_{\rm eff}^4$, and use them to plot a Hertzsprung-Russell (HR) diagram for the protostars in each cluster. The HR diagrams for each of the clusters are shown in Fig. 6.10. We also plot isochrones from fixed-mass evolution models of pre-main-sequence stars constructed by Baraffe et al. (2015) for comparison.

The effects of varying α are once again clear in the HR diagrams of each of the clusters. The evolutionary tracks of the protostars in the FB05+PE5001 and FB05+PE6001 calculations are similar, despite the difference in the initial accretion rates, whereas the protostars in the $\alpha = 0.05$ calculation are more luminous at a given surface temperature, due to their enlarged radii. Comparing with the isochrones of Baraffe et al. (2015), we see that the evolutionary tracks of protostars in the FB05+PE5001 and FB05+PE6001 calculations are broadly similar to the 1 Myr isochrone, despite only having ages of ~ 0.01 Myr. Increasing α to 0.05 results in apparently younger protostars when compared to the isochrones, despite having similar ages and masses.

6.3 Discussion

Our calculations show that including the effects of protostellar evolution in addition to modelling the accretion luminosity produces similar results to calculations which include the accretion luminosity, but do not evolve the protostars. However, these effects, as well as the properties of the protostars themselves, are dependent upon both the initial accretion rate used by the disc accretion algorithm and the proportion of the accretion energy that is advected into the protostellar interior, α. We now discuss these results in the context of other calculations which model protostellar feedback, and compare the properties of the protostars with results from models of protostellar evolution.

6.3.1 Comparison with fixed stellar model calculations

The similarity of the gas density and temperature distributions, as well as the number of protostars, in the FB05 and FB05+PE5001 calculations indicates that our analysis of the impact of including accretion feedback in the previous chapter still holds for the calculations presented here, and is relatively unaffected by the inclusion of a live stellar

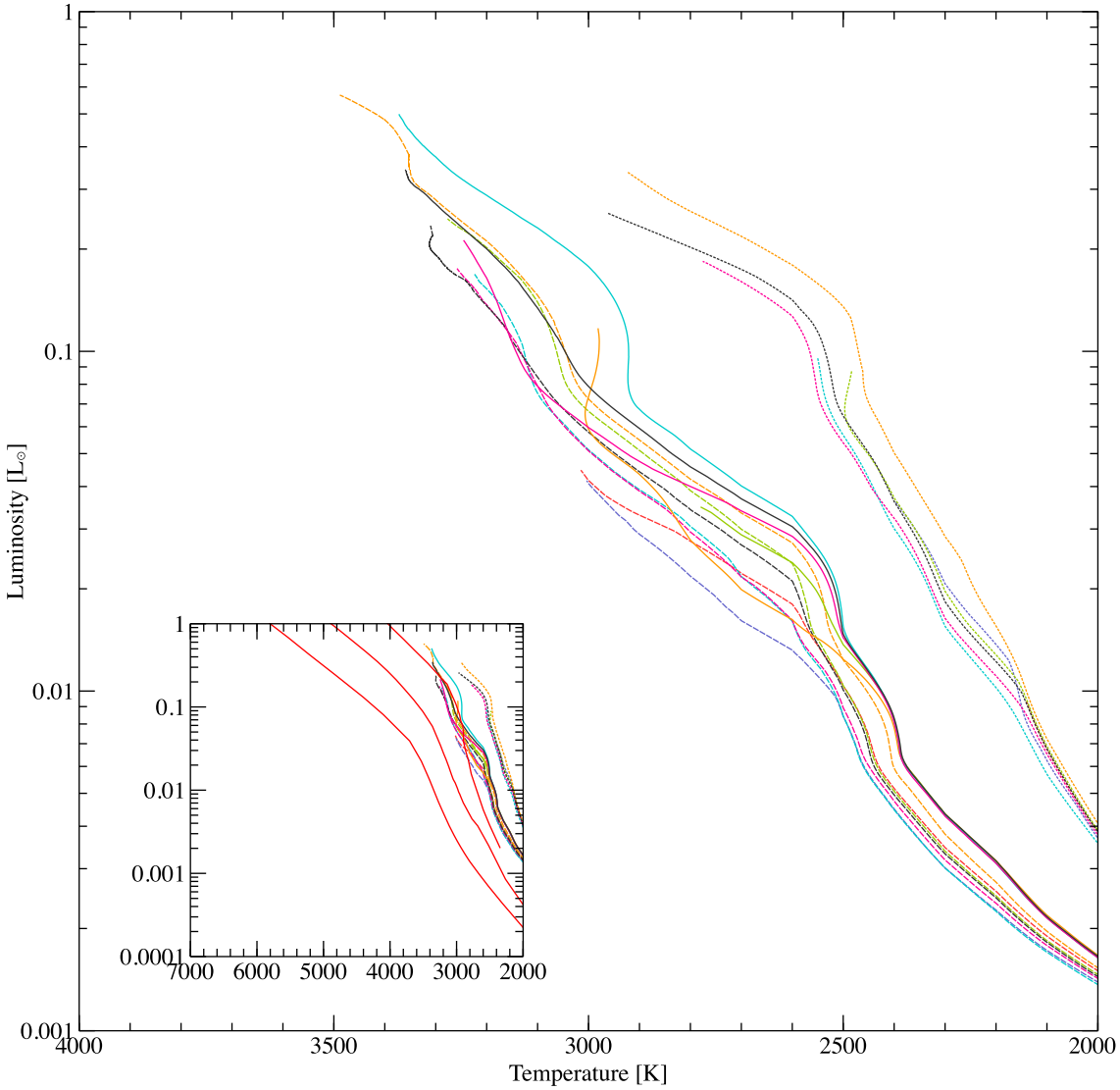

Figure 6.10: The evolution of the protostellar luminosities with effective temperature in the FB05+PE5001, FB05+PE6001 and FB05+PE6005 calculations. Objects in the FB05+PE5001 calculation are shown by the solid lines, objects in the FB05+PE6001 calculation are shown by the dashed lines, and objects in the FB05+PE6005 calculation are shown by the dotted lines. Each colour denotes a different sink particle. The evolutions of the surface temperatures and luminosities of the protostars are also similar for the FB05+PE5001 and FB05+PE6001 calculations. Using $\alpha = 0.05$ increases the luminosities for a given surface temperature, **due to the increased protostellar radii**, but once again does not significantly alter the form of the relationship between the surface temperature and the luminosity, which remain similar to the calculations using $\alpha = 0.01$. In the bottom-left of the figure, we plot the results against 1 Myr, 10 Myr and 100 Myr isochrones obtained from stellar evolution models of pre-main-sequence stars produced by Baraffe et al. (2015). Increasing the value of α decreases the apparent age of the protostars by increasing the protostellar radius for a given mass, **as suggested by Baraffe et al. (2012).**

evolution model. The differences between the calculations are primarily due to the initial behaviour of the protostellar model. The smaller initial protostellar radius produces a higher accretion luminosity initially, and the subsequent contraction of the protostar amplifies this effect.

Calculations performed by Larson (1969) and Bate (2010, 2011) showed that newly formed protostars which are embedded within a dense gaseous envelope of similar temperature do not experience a significant contraction, as the surface cooling of the protostar is inhibited by the hot, dense surrounding gas. Instead, they grow steadily in mass and size from an initial object of approximately 1 M_J in mass and 2 $R_\odot$ in radius. This suggests that altering the boundary conditions of the stellar model, such that the protostar is unable to cool efficiently, may help to prevent it from rapidly contracting after its formation.

However, in Section 6.2.1 we also noted that the initial contraction of the protostars occurs over a much shorter timescale than the Kelvin-Helmholz timescale, implying that the contraction is not solely due to the surface cooling of the protostar, and may also depend upon the increase in the gravitational binding energy caused by the accretion of mass. In this case, in order for the protostar to maintain a constant radius whilst accreting, sufficient thermal energy must be advected into the protostellar interior to counteract the increase in the gravitational potential energy. The comparison between the results of the FB05+PE6001 and FB05+PE6005 calculations appear to support this hypothesis, as the increased value of α reduces the magnitude of the contractions in the radii of protostars in the FB05+PE6005 calculation. These results suggest however, that the value of α required to prevent this contraction is much larger than the values typically used by models ($\alpha < 0.1$). Hosokawa et al. (2011) and Baraffe et al. (2017) have argued for a value of α which varies with the protostellar accretion rate, which may help to counteract the large increases in the protostellar binding energy at high accretion rates, provided a large enough fraction of the accretion energy is advected into the protostellar interior.

Since our results show that the dynamics of the clusters are insensitive to all but the largest changes (i.e. order of magnitude) in the protostellar radii, and given that the accretion feedback calculations use a fixed protostellar radius of 2 $R_\odot$, any subsequent growth of the protostellar radii from 2 $R_\odot$ to $\sim$ 3 $R_\odot$ is unlikely to significantly alter the results of the calculations. As such, it seems probable that, by using an initial protostellar seed of similar size and mass to that used in the accretion feedback calculations, reducing the surface cooling rate by modifying the boundary conditions of the stellar model, and increasing the value of α such that accretion does not cause the protostar to rapidly contract, the differences between the feedback and evolution calculations would become negligible.

6.3.2 Dependence on model parameters

One caveat to the above discussion is the dependence of the results on the specification of the initial protostellar accretion rate. Using a higher initial accretion rate results in higher accretion luminosities, and lower sink masses, due to the stronger heating effect of the accretion feedback. While some of these values begin to converge by the end of the calculations, the evolution of the sink luminosities with mass shows that the luminosities of sinks in the FB05+PE5001 calculation remain approximately one order of magnitude higher than those in the FB05+PE6001 and FB05+PE6005 calculations at a given mass. There is also an increase in the spread of luminosities at a given mass when using a lower initial accretion rate of 10^{-6} $M_\odot$ yr^{-1}. This may reflect the decreased importance of the accretion feedback in determining the evolution of the cluster when using the lower initial accretion rate. Offner et al. (2009) found that the total luminosity of clusters was dominated by the protostars with the highest accretion rates. Our results imply that accretion rates of $\sim 10^{-5}$ $M_\odot$ yr^{-1} or higher are required to have a strong impact on cluster the dynamics.

Examining the magnitudes of the sink luminosities, we find that the luminosities of sinks in the calculations using the lower initial accretion rate of $\sim 10^{-5}$ $M_\odot$ yr^{-1} stay predominantly below 10 $L_\odot$. Comparing with the results from the Bonnor-Ebert calculations in Chapter 5, it is clear that these low luminosities do not alter the temperature of surrounding gas significantly compared to calculations that do not include accretion feedback. Similar results were found by Lomax et al. (2015) in calculations simulating accreting protostars using an episodic accretion model. The low average luminosities of the protostars, due to the short duration of the rapid accretion 'episodes' and the lack of accretion during quiescent periods, were found to produce clusters with temperature distributions which were highly similar to calculations that did not include accretion feedback from protostars. In the absence of an episodic accretion model, such as the magneto-rotational-instability (MRI) driven disc model of Lomax et al. (2015), initial accretion rates as low as 10^{-6} $M_\odot$ yr^{-1} appear unlikely. Several numerical studies have shown that protostars may accrete at rates as high as 10^{-4} $M_\odot$ yr^{-1} during their initial growth phase (Offner et al. 2009; Bate 2010, 2011), guaranteeing that the protostellar heating will have a significant impact on the dynamics of the cluster.

While sensitive to the value of $\dot{M}_)$, the evolution of the sinks is relatively unaffected by the value of α. This is despite significant variation in the protostellar properties, which depend heavily on α. Comparing the evolutions of the sink and protostellar properties, the sink luminosities do not appear vary significantly with changes to the protostellar radii, despite an order of magnitude contraction in the radii of all protostars shortly after formation. The sink particle masses are similar unaffected. This indicates that the large-scale dynamics of the surrounding clusters are not strongly affected by variations in the protostellar structure, at least on short timescales. The most likely cause of this is the relatively small magnitude of changes in the protostellar properties when compared to

changes in the cluster environment. While the protostellar radii vary by a maximum of one order of magnitude during the course of the calculation, the accretion rates of sink particles may vary over several orders of magnitude, and over shorter timescales.

Variations in the protostellar luminosities also have little impact on the evolution of the sink particles. While they may vary over larger ranges than the protostellar radius, and can provide more heating than viscous dissipation or compression (Offner et al. 2009), the protostellar luminosities are much lower than the accretion luminosities when using an initial accretion rate of 10^{-5} $M_\odot$ yr^{-1}, and therefore impact minimally on the heating of the cluster. They may contribute as much as $1 - 10\%$ of the total sink luminosity when using the lower initial accretion rate of 10^{-6} $M_\odot$ yr^{-1}, however the total luminosity is much lower, and becomes less relevant in determining the dynamics of the cluster. This accounts for the insensitivity of the protostellar mass to variations in α, as the accretion luminosity is much larger than the protostellar luminosity, and therefore sets the temperature of the surrounding gas, which regulates the sink mass accretion rate. The effects of variations in the protostellar properties may become even more muted if the boundary conditions of the protostellar model are modified such that the initial phase of contraction is avoided, or if the value of α is significantly increased, such that the radii only vary by a factor of ~ 2 from their initial value.

Although the dynamics of the cluster are largely insensitive to the value of α chosen, and depend more heavily on the initial accretion rate set by the disc accretion algorithm, the converse is true of the properties of the protostars. The protostellar radii at a given mass are similar in the both of the calculations using $\alpha = 0.01$, but increase significantly when using $\alpha = 0.05$. This indicates that the protostellar mass-radius ratio is determined primarily by α, and is insensitive to the value of $\dot{M}_0$. It is possible that this may not reflect the behaviour of systems with much higher accretion rates, however it is likely that at these higher accretion rates, the assumptions about the convective structure of the protostar made by the stellar model will not hold, requiring additional physics to describe the significant radiative zone that will develop in the protostellar interior (Hartmann et al. 1997).

While the magnitude of the protostellar radius at a given protostellar mass increases for larger values of α, the evolution of the radius with increasing mass is approximately the same for both the $\alpha = 0.01$ and $\alpha = 0.05$ calculations. This has potential implications for the analytical theories of the IMF proposed by Bate (2009c) and Krumholz (2011), discussed in Chapter 4. Both theories make reference to the protostellar structure as a means to derive a median stellar mass which depends only weakly on the properties of the molecular cloud. Bate (2009b) did not consider the internal structure of the protostar, instead postulating that the median stellar mass should depend on the mass-radius ratio of the protostar, as well as the density of the gas, with a scaling of $M_c \propto \left(\frac{M_*}{R_*}\right)^{3/7} \rho^{-1/14}$. Krumholz (2011) attempted to describe the structure of the protostellar interior, linking it to fundamental constants

describing the rates of energy generation processes in the protostellar core, which resulted in a median stellar mass which depends only on the pressure of the ISM, with a scaling of $M_{\rm c} \propto P_{\rm ISM}^{-1/18}$. The approximately constant form of the mass-radius relationship provides some, albeit circumstantial, support for these theories as a means for obtaining a universal median stellar mass. However, to test such weak scalings, a much larger statistical sample of protostars than was produced by the calculations presented here is required (Jones and Bate 2018; see also Chapter 4).

6.3.3 Comparison with stellar evolution models

By deriving effective surface temperatures for the protostars using the Stefan-Boltzmann law, we are able to model the evolution of distributions of properties of the protostars formed in the cluster calculations. Many stellar evolution models do not treat accretion, and instead produce isochrones for a range of masses (Baraffe et al. 2015). Those that have included the effects of protostellar accretion have employed a variety of methods to describe its behaviour. Many earlier models used constant accretion rates (Hartmann et al. 1997; Tout et al. 1999) or rates which varied in time according to analytical prescriptions (Baraffe et al. 2009). More complex models have used accretion data from hydrodynamics simulations of circumstellar discs and pre stellar cores (Baraffe et al. 2012, 2017). By including a live stellar model in a radiation hydrodynamics calculation of star-cluster formation, we can consistently model the accretion rates of protostars due to the dynamics of the parent molecular cloud, and calculate their effects on the structure and properties of protostars.

We find that the evolution of protostars on the HR diagram in the FB05+PE5001 and FB05+PE6001 calculations is similar, despite an order of magnitude difference in the initial accretion rates. Tout et al. (1999) found that accretion delayed the formation of a radiative core, causing protostars to appear older. They therefore suggested that the positions of protostars on the HR diagram depend upon their accretion histories, which may vary significantly. Baraffe et al. (2009) further suggested that the observed luminosity spread of young clusters may result from variations in the accretion histories of protostars due to episodic accretion. The insensitivity of our calculations to the initial accretion rate appears to contradict this.

Hosokawa et al. (2011) have suggested that variations in the accretion histories of protostars alone cannot account for the observed spread of luminosities. Instead, they suggest that a much larger spread is produced by varying the amount of accretion energy advected into the protostellar interiors. The large difference between the luminosities of protostars in our calculations using different values of α supports this. Baraffe et al. (2009) found that using $\alpha = 0$, a scenario known as 'cold accretion', caused the protostars to contract rapidly, due to the large increase in the thermal timescale of the protostar relative

to the accretion timescale, caused by the increased gravitational potential. This resulted in smaller protostellar radii and luminosities for a given mass. Allowing a non-zero amount of accretion energy to be advected into the protostar resulted in a less drastic contraction, due to the pressure support from the additional entropy in the protostellar interior. This is in broad agreement with the results of our calculations and suggests that a population of protostars accreting with different values of α may produce a spread of luminosities at a given surface temperature on the HR diagram.

Baraffe et al. (2012) suggest that protostars accreting at low rates may be expected to absorb very little accretion energy through advection, but that those accreting at higher rates may absorb a more substantial proportion through 'hot accretion'. Baraffe et al. (2017) implemented a version of this in coupled calculations of a one-dimensional stellar evolution model and a two-dimensional hydrodynamics calculation of a circumstellar accretion disc, developed by Vorobyov and Basu (2010) and Vorobyov et al. (2013). The calculations used a value of α which varied according to the protostellar accretion rate calculated by the hydrodynamical disc model, such that at low accretion rates ($< 10^{-5}$ $M_\odot$ yr^{-1}), no energy was advected into the protostellar interior ($\alpha = 0$), and at high accretion rates ($\geq 10^{-5}$ $M_\odot$ yr^{-1}), a significant fraction of the accretion energy was advected ($\alpha = 0.2$). With this model, they were able to reproduce a luminosity spread in good agreement with observation at ages of 1-10 Myr. It therefore seems plausible that populations of coeval stars accreting at different rates may produce a spread of luminosities.

Comparing the results of our calculations with the isochrones produced by Baraffe et al. (2015), we find that the calculations using $\alpha = 0.01$ are in broad agreement with the 1 Myr isochrone, whereas the evolutionary tracks of the protostars in the $\alpha = 0.05$ calculation appear significantly younger, due to their larger radii and luminosities for a given temperature. This agrees with the observation of Baraffe et al. (2009) that protostars which accrete mass through cold accretion ($\alpha = 0$) appear older than those that advect a fraction of the accretion energy into the protostellar interior ($\alpha > 0$). Baraffe et al. (2012) suggest that this variation in the properties of protostars with α implies that predictable evolutionary tracks for protostars are unlikely, and that the individual accretion histories of protostars determine their places on the HR diagram. As such, caution should be used when inferring the ages of protostars from static isochrones.

6.4 Conclusions

In this chapter, we have presented results from calculations of star formation in small clusters which model both the accretion luminosity of protostars as well as their evolution. We find that the calculations produce similar clusters to calculations that model the accretion luminosity but do not model the evolution of protostars. However, we find that the relative importance of the accretion and protostellar feedback processes is dependent on

the accretion rate of the protostars. We also find that the properties and evolutions of the protostars themselves depend strongly on the fraction of the accretion energy advected into the protostellar interior.

Our detailed conclusions are as follows.

1. Including the evolution of protostars in calculations does not significantly affect the global evolution of the clusters. The luminosities of the sinks in the evolution calculation are higher due to the initial size of the protostellar model, and its subsequent contraction due to the atmospheric boundary conditions. This results in lower star formation rate, and delays the collapse of some fragments to form protostars. Using an initial protostellar model with a larger radius, as well as reducing the efficiency of surface cooling of the protostars should render the differences between the two calculations negligible.

2. The initial accretion rate used by the disc accretion algorithm significantly alters the impact of the accretion luminosity on the dynamics of the cluster. Using a lower rate of 10^{-6} $M_{\odot}$ yr^{-1} reduces the heating effect sufficiently such that the accretion rates of sinks are no longer set predominantly by the thermodynamics of accretion, and instead vary according to the local dynamics of the molecular cloud, resulting in a larger spread of luminosities for a given mass.

3. Variations in the protostellar radii and intrinsic luminosities do not significantly affect the evolution of the clusters, as they are small compared to the magnitude of the accretion luminosities and the potential magnitude of variations in the accretion rate. This may not be true for lower accretion rates, however the total luminosity of such systems is sufficiently low that any variations have little impact on the surrounding cluster.

4. The evolution of the protostellar radius with mass is not significantly affected by the accretion rate, but does strongly depend upon the value of α, with larger values of α increasing the protostellar radius for a given mass. The form of the mass-radius relation is insensitive to both the accretion rate and the amount of energy advected into the protostar. This may support the analytical theories of the IMF proposed by Bate (2009c) and Krumholz (2011), although much larger statistical samples would be needed to test this.

5. The evolution of protostars on the HR diagram does not depend upon the accretion rate, but is dependent on the value of α. This contradicts the findings of Tout et al. (1999). Increasing the fraction of energy advected into the protostars results in higher luminosities at a given temperature. This supports the suggestions of Hosokawa et al. (2011) and Baraffe et al. (2017) that the observed luminosity spread in clusters is generated by protostars accreting at different rates, with different values of α.

Protostars accreting with higher values of α also appear younger when compared with static isochrones produced by Baraffe et al. (2015). This supports the assertion of Baraffe et al. (2017) that inferring ages of young stars from static isochrones may be unreliable.

Chapter 7

Conclusions

In the introduction, we stated that the construction of a complete and comprehensive theory of star formation has been a long standing goal of theoretical astrophysics. During the course of this thesis, we have explored a major component of the star formation process: that of protostellar heating. We have shown that thermal feedback from accreting protostars can have a dramatic impact upon the fragmentation of clusters, as well as the distributions of properties in young stellar populations. We have also found that protostellar evolution is inextricably linked to this process, both regulating and depending upon the effects of protostellar feedback. In this chapter, we present a summary of our findings, and discuss the possibilities for the methods developed here to investigate new problems in the future.

7.1 Summary

We investigated the effects of protostellar heating on the properties of stars by performing radiative smoothed particle hydrodynamics simulations of star formation in clusters. As part of this investigation, we introduced new methods to calculate the accretion luminosity generated by protostars and to model their evolution. We found that the heating effect of accreting protostars has a significant impact on the evolution of star-forming clusters, and may help to regulate the distribution of stellar masses by inhibiting the fragmentation of molecular clouds. We also showed that calculations of this type produce clusters of stars whose statistical properties are in good agreement with observations, and can be used to study the evolution of these properties in detail.

In chapters 1 and 2, we explored the basic elements of the star formation process, reviewed previous studies of star formation, and described the methods used to simulate radiative hydrodynamical processes using the `sphNG` smoothed particle hydrodynamics code.

Chapter 3 presented our method for simulating protostars in the calculations. We described the sink particle approximation used to represent protostars, and the rules governing their formation and interactions with the SPH calculation. We then explained how an algorithm based on the accretion of material through a circumstellar disc onto a central object can be used to calculate the luminosity generated inside sink particles by accreting protostellar systems, and described the method by which this luminosity was included in the SPH calculations. Finally, we gave a description of the `Lyon` stellar evolution code, which we used to model the evolution of protostars, and described how the model interfaces with the feedback algorithm to simulate the growth of the protostar via mass accretion.

We began our study of the effects of radiative feedback on the star formation process in Chapter 4, in which we investigated the dependence of stellar properties on the initial density of molecular clouds. We presented results from three radiative hydrodynamical calculations of star formation in clusters which resolved fragmentation down to the opacity limit. The calculations simulated three turbulent molecular clouds with identical initial conditions apart from their initial densities, which varied by a factor of up to 100. The clouds began with total masses of 500 $M_\odot$, and produced 474, 233 and 87 stars and brown dwarfs, which were modelled using sink particles with accretion radii of 0.5 AU. The feedback generated by accreting protostars inside the sink accretion radius was not modelled.

The calculations showed that, while the multiple system properties of the clusters did not depend upon the initial densities of the clouds, the median stellar mass did exhibit a dependence on the initial cloud density, of the form $M_C \propto \rho^{-1/5}$. We compared this result with analytical theories of the characteristic stellar mass proposed by Bate (2009c) and Krumholz (2011), and found that the results of our calculations were in agreement with the simple Bate model, which was based on a modified thermal Jeans mass in the optically thin limit. We discussed the implications of this for the role of protostellar heating in determining the median mass in clusters, and concluded that it may provide a mechanism for producing a near universal median stellar mass. We also noted similarities between the results of the low-density calculation and the population of young stars in the Taurus-Auriga star-forming region, and between the results of the high-density calculation and the stellar populations of early-type galaxies, suggesting that a scaling of the median stellar mass with density may explain the properties of these systems.

In Chapter 5, we expanded upon the discussion of Chapter 4 by investigating the impact of the protostellar accretion luminosity on star formation in small clusters. We presented results from four radiative hydrodynamical calculations of star formation in clusters, two of which used the disc-accretion algorithm described in Chapter 3 to calculate the accretion luminosity generated inside sink particles, and two of which did not. Once again, we simulated four turbulent molecular clouds with identical initial conditions. The clouds began with total masses of 50 $M_\odot$, and produced between 5 and 20 stars and brown dwarfs,

which were modelled using sink particles with accretion radii of 0.5 AU and 5.0 AU.

We found that the heating provided by the accretion luminosities of the protostars significantly affected the evolution of the clusters. The additional luminosity raised the temperature of the molecular cloud, suppressing fragmentation even further than in the radiative calculations which did not model the accretion luminosities. This resulted in fewer objects being produced, as well as a lower total stellar mass in the clusters at a given time. The lower number of objects in the clusters allowed the protostars to attain higher masses, increasing the median stellar mass. We found that the magnitude of this increase in the median stellar mass was in agreement with the scaling predicted by the analytical model proposed by Bate (2009c). The distribution of stellar masses in each of the calculations which included the accretion luminosities was insensitive to the sink particle accretion radius used, implying that the heating from protostellar accretion dominates the thermodynamics of star-forming clusters. We also noted the similarities between the temperature distributions produced by the calculations including the accretion luminosities and observations of Galactic star-forming regions such as the Perseus and Corona Australis regions.

Finally, in Chapter 6, we examined how the evolution of protostars may alter the effects of protostellar heating in star-forming clusters. We presented results from three radiative hydrodynamical calculations of star formation in clusters, which calculated the accretion luminosities of protostars using the disc-accretion algorithm, and also modelled the evolution of the protostars using the Lyon stellar evolution code. The calculations varied in the initial accretion rates used by the disc-accretion algorithm, as well as the fractions of the accretion energy advected into the protostars by the stellar evolution model. We used identical initial conditions to those used in the calculations presented in Chapter 5 to enable a comparison between the calculations. The calculations produced 5, 7 and 7 objects, respectively, which were modelled using sink particles with accretion radii of 0.5 AU.

Comparing the calculations to those of Chapter 5, we found that modelling protostellar evolution did not significantly affect the evolution of star-forming clusters. All of the protostars experienced an initial phase of rapid contraction, due to the efficiency of radiative cooling from the protostellar surfaces. This led to a large increase in the accretion luminosities of the sink particles, driving thermal outflows which affected the fragmentation of discs in some cases and heating the cluster, which lowered the accretion rates and final masses of sink particles. We concluded that using different boundary conditions for the protostellar model, and beginning with a larger initial protostellar radius, would likely reduce differences between the calculations which modelled protostellar evolution and those that did not. Varying the initial accretion rate used by the disc accretion model, as well as the fraction of the accretion energy advected into the protostellar interior, we found that the effects of the accretion luminosity were dependent on the accretion rate

used, but were insensitive to the advection fraction, α. The converse was found to be true for the properties of the protostars themselves, which were insensitive to changes in the initial accretion rate, but depended strongly on the value of α. Increasing the advection fraction increased the radii of protostars for a given protostellar mass, but did not alter the gradient of the relationship. We suggested that this approximately constant form of the mass-radius relationship for protostars provide tentative support for the advanced analytical theories of the IMF proposed by Bate (2009c) and Krumholz (2011). Finally, we showed that increasing the value of α caused protostars to appear younger on the Hertzsprung-Russell diagram when compared with static isochrones. We suggest that this may help to explain the observed spreads of luminosities in young stellar clusters.

7.2 Future work

During the course of this exploration into the effects of protostellar heating on star formation, we have discussed several major problems which are areas of active research in the star formation community. We have also shown that large scale numerical simulations are powerful tools for investigating these problems. With the new methods we have introduced in this thesis, we hope to be able to progress the theoretical understanding of several key issues, which we detail below.

7.2.1 The apparent universality of the initial stellar mass function

As we discussed in Chapters 4 and 5, observations of nearby star-forming regions show that the median stellar mass of young stellar clusters is approximately constant, despite variations in the environmental conditions in which these clusters form (Bastian et al. 2010). The calculations presented in Chapter 4 showed that including the effects of radiative transfer in calculations of star formation produces stellar populations whose median masses depend more weakly on the initial density of the molecular cloud than the standard scaling of the thermal Jeans mass. However, while this result is promising, it indicates a dependence on initial conditions which is not supported by the majority of observations.

A key limitation of these calculations was the lack of a method to calculate the accretion luminosity generated inside the accretion radii of sink particles. Analytical theories of the IMF proposed by Bate (2009c) and Krumholz (2011) suggest that the protostellar luminosity is critical in determining the effective thermal Jeans mass of star-forming molecular clouds. We therefore performed calculations which included the accretion luminosity generated inside sink particles, and found that the accretion feedback significantly impacted fragmentation, and increased the median stellar mass in agreement with the optically thin model proposed by Bate (2009c).

This result implies that protostellar heating may be the primary mechanism by which the median stellar mass of clusters is determined, by modifying the effective thermal Jeans mass of the cloud. However, as the calculations in Chapter 4 showed, large populations of stars are required to detect such weak variations in the statistical properties of clusters. In light of this, we are currently running calculations using identical initial conditions to those used by the calculations in Chapter 4, but which also include the accretion luminosities of protostars, using the disc-accretion algorithm described in Chapter 3. These large scale calculations should enable us to probe the effects of accretion feedback on the statistical properties of star-forming clusters, and assess whether the impact is sufficient to produce a universal median stellar mass. Unfortunately, the projected time taken to complete these calculations is approximately one year, preventing them from being included in this thesis.

7.2.2 The luminosity problem for young protostars

A somewhat related issue to the effect of the accretion luminosity on stellar masses is the so-called 'Luminosity Problem'. First described by Kenyon et al. (1990), the Luminosity Problem relates to the inferred accretion rates from observations of the luminosities of young protostars. Kenyon et al. (1990) noted that the luminosities of some protostars were observed to be much lower than would be expected from their masses and ages if they had accreted their current masses at a continuous rate. This effect has since been observed in many Galactic star-forming regions (Evans et al. 2009; Dunham et al. 2013).

Several solutions to this problem have been proposed, the most popular of which is the 'Episodic Accretion' model. The model suggests that protostars do not accrete mass continuously, but instead accrete large amounts of material in short-lived ($\sim$ 100 yr) 'episodes' at very rapid rates, followed by long ($\sim 10^4$ yr) quiescent periods in which no accretion occurs. Lomax et al. (2015) performed radiative hydrodynamical calculations of star formation which modelled the protostellar feedback using an episodic accretion model based on magneto-rotational-instabilities in the circumstellar accretion disc. They found that episodic feedback produced clusters whose multiple system properties were in better agreement with observations than calculations which modelled protostellar feedback using continuous accretion. They also found that continuous feedback calculations produced too few brown dwarfs in comparison with observed stellar mass functions, **a result which the continuous feedback models presented in Chapter 5 appear to confirm for small stellar clusters.**

However, the calculations of Lomax et al. (2015) modelled populations of stars formed from an ensemble of dense cores, whose properties were set according to observed distributions of core properties. As such, they omitted larger scale effects arising from the interactions of the cores with their environments, as discussed in Chapter 1. Modelling the formation of a star cluster using a single calculation which includes the luminosities gen-

erated by accreting protostars would provide a more consistent approach, enabling us to examine the assertions of Lomax et al. (2015) regarding the results of continuous feedback. It would also produce a stellar population large enough to compare with observational surveys, and verify the inferred accretion rates of young protostars. It is our intention to use the cluster calculations described above to address this problem.

7.2.3 Predicting luminosity spreads in young clusters

The calculations presented in Chapter 6 demonstrated the potential for using large-scale cluster calculations to investigate the evolution of protostellar properties in star-forming clusters. Using a range of model parameters, we compared the properties of protostars produced by the calculations with isochrones generated from static models of protostellar evolution, and found that they were in broad agreement. We did however note a dependence of the protostellar properties on α, the fraction of accretion energy advected into the stellar interior, used by the stellar model. Higher values of α produced protostars with larger radii and consequently higher luminosities than lower values for a given effective surface temperature. This had the effect of making the protostars appear younger when compared with static isochrones.

Observations of young clusters in star-forming regions display a range of luminosities for protostars with similar surface temperatures (Hillenbrand 2009). This is often interpreted as a spread of ages of protostars in the clusters. However, several authors have suggested that such spreads in luminosities may also occur in populations of coeval stars, due to variations in the accretion histories (Tout et al. 1999; Baraffe et al. 2009) and advection fractions (Hosokawa et al. 2011; Baraffe et al. 2012, 2017). The results of our calculations appear to support this hypothesis.

Large-scale cluster calculations of the type presented in this thesis could be used to predict the spreads of protostellar luminosities in these systems using stellar evolution models, as we have shown. In addition to producing large statistical samples, cluster calculations model the accretion rates of protostars consistently, whereas stellar evolution calculations must rely either on analytical functions (Tout et al. 1999; Baraffe et al. 2009) or simplified hydrodynamical models (Hosokawa et al. 2011; Baraffe et al. 2017) to calculate the accretion rate.

Using the implementation presented here, it is also possible to investigate the effects of varying α. Baraffe et al. (2017) performed calculations using a value of α which varied based on the accretion rate, and found that this did indeed produce a stellar population with a luminosity spread, although the distribution exhibited a distinct bimodality, possibly due to the use of two fixed values of α to model the advection of energy into the protostellar interior. Similar, or more advanced, methods could be used in future cluster calculations to replicate the spreads of luminosities in young star-forming clusters.

Bibliography

Alexander, D. R. 1975. 'Low-Temperature Rosseland Opacity Tables.' ApJS 29 (August): 363.

Alexander, D. R., and J. W. Ferguson. 1994. 'Low-temperature Rosseland opacities.' ApJ 437 (December): 879–891.

Allard, F., P. H. Hauschildt, D. R. Alexander, and S. Starrfield. 1997. 'Model Atmospheres of Very Low Mass Stars and Brown Dwarfs.' ARA&A 35:137–177.

Allen, A., F. Shu, Z.-Y. Li, M. Choi, and H.-W. Chuang. 2003. 'Collapse of Magnetized, Rotating, Toroidal Clouds.' In *IAU Symposium,* vol. 221. IAU Symposium.

Andersen, M., M. R. Meyer, J. Greissl, and A. Aversa. 2008. 'Evidence for a Turnover in the Initial Mass Function of Low-Mass Stars and Substellar Objects: Analysis from an Ensemble of Young Clusters.' ApJL 683, L183 (August): L183.

André, P., A. Belloche, F. Motte, and N. Peretto. 2007. 'The initial conditions of star formation in the Ophiuchus main cloud: Kinematics of the protocluster condensations.' A&A 472 (September): 519–535.

André, P., et al. 2010. 'From filamentary clouds to prestellar cores to the stellar IMF: Initial highlights from the Herschel Gould Belt Survey.' A&A 518, L102 (July): L102.

André, P., et al. 2014. 'From Filamentary Networks to Dense Cores in Molecular Clouds: Toward a New Paradigm for Star Formation.' *Protostars and Planets VI:*27–51.

Bally, J. 1996. 'Filaments in creation's heart.' Nature 382 (July): 114–115.

Banerjee, R., and R. E. Pudritz. 2006. 'Outflows and Jets from Collapsing Magnetized Cloud Cores.' ApJ 641 (April): 949–960.

Bania, T. M., and J. G. Lyon. 1980. 'OB stars and the structure of the interstellar medium - Cloud formation and effects of different equations of state.' ApJ 239 (July): 173–192.

Baraffe, I., G. Chabrier, F. Allard, and P. H. Hauschildt. 1998. 'Evolutionary models for solar metallicity low-mass stars: mass-magnitude relationships and color-magnitude diagrams.' A&A 337 (September): 403–412.

———. 2002. 'Evolutionary models for low-mass stars and brown dwarfs: Uncertainties and limits at very young ages.' A&A 382 (February): 563–572.

Baraffe, I., G. Chabrier, and J. Gallardo. 2009. 'Episodic Accretion at Early Stages of Evolution of Low-Mass Stars and Brown Dwarfs: A Solution for the Observed Luminosity Spread in H-R Diagrams?' ApJL 702 (September): L27–L31.

Baraffe, I., and M. F. El Eid. 1991. 'Evolution of massive stars with variable initial compositions.' A&A 245 (May): 548–560.

Baraffe, I., V. G. Elbakyan, E. I. Vorobyov, and G. Chabrier. 2017. 'Self-consistent evolution of accreting low-mass stars and brown dwarfs.' A&A 597, A19 (January): A19.

Baraffe, I., D. Homeier, F. Allard, and G. Chabrier. 2015. 'New evolutionary models for pre-main sequence and main sequence low-mass stars down to the hydrogen-burning limit.' A&A 577, A42 (May): A42.

Baraffe, I., E. Vorobyov, and G. Chabrier. 2012. 'Observed Luminosity Spread in Young Clusters and FU Ori Stars: A Unified Picture.' ApJ 756, 118 (September): 118.

Basri, G., and A. Reiners. 2006. 'A Survey for Spectroscopic Binaries among Very Low Mass Stars.' AJ 132 (August): 663–675.

Bastian, N., K. R. Covey, and M. R. Meyer. 2010. 'A Universal Stellar Initial Mass Function? A Critical Look at Variations.' ARA&A 48 (September): 339–389.

Bastian, N., and S. P. Goodwin. 2006. 'Evidence for the strong effect of gas removal on the internal dynamics of young stellar clusters.' MNRAS 369 (June): L9–L13.

Bastien, P. 1983. 'Gravitational collapse and fragmentation of isothermal, non-rotating, cylindrical clouds.' A&A 119 (March): 109–116.

Bastien, P., J.-P. Arcoragi, W. Benz, I. Bonnell, and H. Martel. 1991. 'Fragmentation of elongated cylindrical clouds. I - Isothermal clouds.' ApJ 378 (September): 255–265.

Bate, M. R. 1997. 'Accretion during binary star formation - I. Ballistic accretion.' MNRAS 285 (February): 16–32.

———. 2005. 'The dependence of the initial mass function on metallicity and the opacity limit for fragmentation.' MNRAS 363 (October): 363–378.

———. 2009a. 'Stellar, brown dwarf and multiple star properties from hydrodynamical simulations of star cluster formation.' MNRAS 392 (January): 590–616.

———. 2009b. 'The dependence of star formation on initial conditions and molecular cloud structure.' MNRAS 397 (July): 232–248.

———. 2009c. 'The importance of radiative feedback for the stellar initial mass function.' MNRAS 392 (February): 1363–1380.

———. 2010. 'Collapse of a molecular cloud core to stellar densities: the radiative impact of stellar core formation on the circumstellar disc.' MNRAS 404 (May): L79–L83.

———. 2011. 'Collapse of a molecular cloud core to stellar densities: the formation and evolution of pre-stellar discs.' MNRAS 417 (November): 2036–2056.

———. 2012. 'Stellar, brown dwarf and multiple star properties from a radiation hydrodynamical simulation of star cluster formation.' MNRAS 419 (February): 3115–3146.

———. 2014. 'The statistical properties of stars and their dependence on metallicity: the effects of opacity.' MNRAS 442 (July): 285–313.

Bate, M. R., and I. A. Bonnell. 1994. 'Accretion and Binary Star Formation.' In *American Astronomical Society Meeting Abstracts*, 26:1521. Bulletin of the American Astronomical Society. December.

———. 1997. 'Accretion during binary star formation - II. Gaseous accretion and disc formation.' MNRAS 285 (February): 33–48.

———. 2005. 'The origin of the initial mass function and its dependence on the mean Jeans mass in molecular clouds.' MNRAS 356 (February): 1201–1221.

Bate, M. R., I. A. Bonnell, and V. Bromm. 2002a. 'The formation mechanism of brown dwarfs.' MNRAS 332 (May): L65–L68.

———. 2002b. 'The formation of close binary systems by dynamical interactions and orbital decay.' MNRAS 336 (November): 705–713.

———. 2003. 'The formation of a star cluster: predicting the properties of stars and brown dwarfs.' MNRAS 339 (March): 577–599.

Bate, M. R., I. A. Bonnell, and N. M. Price. 1995. 'Modelling accretion in protobinary systems.' MNRAS 277 (November): 362–376.

Bate, M. R., and A. Burkert. 1997. 'Resolution requirements for smoothed particle hydrodynamics calculations with self-gravity.' MNRAS 288 (July): 1060–1072.

Bate, M. R., and E. R. Keto. 2015. 'Combining radiative transfer and diffuse interstellar medium physics to model star formation.' MNRAS 449 (May): 2643–2667.

Benz, W. 1988. 'Applications of smooth particle hydrodynamics (SPH) to astrophysical problems.' *Computer Physics Communications* 48:97–105.

———. 1990. 'Smooth Particle Hydrodynamics - a Review.' In *Numerical Modelling of Nonlinear Stellar Pulsations Problems and Prospects*, edited by J. R. Buchler, 269.

Benz, W., R. L. Bowers, A. G. W. Cameron, and W. H. . Press. 1990. 'Dynamic mass exchange in doubly degenerate binaries. I - 0.9 and 1.2 solar mass stars.' ApJ 348 (January): 647–667.

Bertelli Motta, C., P. C. Clark, S. C. O. Glover, R. S. Klessen, and A. Pasquali. 2016. 'The IMF as a function of supersonic turbulence.' MNRAS 462 (November): 4171–4182.

Blair, G. N., N. J. Evans II, P. A. Vanden Bout, and W. L. Peters III. 1978. 'The energetics of molecular clouds. II - The S140 molecular cloud.' ApJ 219 (February): 896.

Blitz, L. 1993. 'Giant molecular clouds.' In *Protostars and Planets III*, edited by E. H. Levy and J. I. Lunine, 125–161.

Blitz, L., and P. Thaddeus. 1980. 'Giant molecular complexes and OB associations. I - The Rosette molecular complex.' ApJ 241 (October): 676–696.

Bonnell, I. A. 1994. 'A New Binary Formation Mechanism.' MNRAS 269 (August).

Bonnell, I. A., and M. R. Bate. 2006. 'Star formation through gravitational collapse and competitive accretion.' MNRAS 370 (July): 488–494.

Bonnell, I. A., M. R. Bate, C. J. Clarke, and J. E. Pringle. 1997. 'Accretion and the stellar mass spectrum in small clusters.' MNRAS 285 (February): 201–208.

———. 2001. 'Competitive accretion in embedded stellar clusters.' MNRAS 323 (May): 785–794.

Bonnell, I. A., M. R. Bate, and S. G. Vine. 2003. 'The hierarchical formation of a stellar cluster.' MNRAS 343 (August): 413–418.

Bonnell, I. A., C. J. Clarke, and M. R. Bate. 2006. 'The Jeans mass and the origin of the knee in the IMF.' MNRAS 368 (May): 1296–1300.

Bonnell, I., H. Martel, P. Bastien, J.-P. Arcoragi, and W. Benz. 1991. 'Fragmentation of elongated cylindrical clouds. III - Formation of binary and multiple systems.' ApJ 377 (August): 553–558.

Boss, A. P. 1986. 'Protostellar formation in rotating interstellar clouds. V - Nonisothermal collapse and fragmentation.' ApJS 62 (November): 519–552.

Boss, A. P., and P. Bodenheimer. 1979. 'Fragmentation in a rotating protostar - A comparison of two three-dimensional computer codes.' ApJ 234 (November): 289–295.

Boss, A. P., R. T. Fisher, R. I. Klein, and C. F. McKee. 2000. 'The Jeans Condition and Collapsing Molecular Cloud Cores: Filaments or Binaries?' ApJ 528 (January): 325–335.

Brand, J., and J. G. A. Wouterloot. 1995. 'IRAS sources beyond the solar circle. V. Properties of far-outer Galaxy molecular clouds.' A&A 303 (November): 851.

Burkert, A., M. R. Bate, and P. Bodenheimer. 1997. 'Protostellar fragmentation in a power-law density distribution.' MNRAS 289 (August): 497–504.

Casoli, F., and F. Combes. 1982. 'Can giant molecular clouds form in spiral arms.' A&A 110 (June): 287–294.

Caughlan, G. R., and W. A. Fowler. 1988. 'Thermonuclear Reaction Rates V.' *Atomic Data and Nuclear Data Tables* 40:283.

Chabrier, G. 1990. 'An equation of state for fully ionized hydrogen.' *Journal de Physique* 51 (August).

———. 2003. 'Galactic Stellar and Substellar Initial Mass Function.' PASP 115 (July): 763–795.

———. 2005. 'The Initial Mass Function: From Salpeter 1955 to 2005.' In *The Initial Mass Function 50 Years Later*, edited by E. Corbelli, F. Palla, and H. Zinnecker, 327:41. Astrophysics and Space Science Library. January.

Chabrier, G., and I. Baraffe. 1997. 'Structure and evolution of low-mass stars.' A&A 327 (November): 1039–1053.

Chabrier, G., I. Baraffe, F. Allard, and P. Hauschildt. 2000. 'Deuterium Burning in Substellar Objects.' ApJL 542 (October): L119–L122.

Chapman, S., et al. 1992. 'The formation of binary and multiple star systems.' Nature 359 (September): 207–210.

Clark, P. C., I. A. Bonnell, and R. S. Klessen. 2008. 'The star formation efficiency and its relation to variations in the initial mass function.' MNRAS 386 (May): 3–10.

Clark, P. C., S. C. O. Glover, R. S. Klessen, and I. A. Bonnell. 2012. 'How long does it take to form a molecular cloud?' MNRAS 424 (August): 2599–2613.

Clarke, C. J., I. A. Bonnell, and L. A. Hillenbrand. 2000. 'The Formation of Stellar Clusters.' *Protostars and Planets IV* (May): 151.

Clarke, C. J., and J. E. Pringle. 1991. 'The role of discs in the formation of binary and multiple star systems.' MNRAS 249 (April): 588–595.

Close, L. M., N. Siegler, M. Freed, and B. Biller. 2003. 'Detection of Nine M8.0-L0.5 Binaries: The Very Low Mass Binary Population and Its Implications for Brown Dwarf and Very Low Mass Star Formation.' ApJ 587 (April): 407–422.

Connelley, M. S., B. Reipurth, and A. T. Tokunaga. 2008. 'The Evolution of the Multiplicity of Embedded Protostars. II. Binary Separation Distribution and Analysis.' AJ 135 (June): 2526–2536.

Conroy, C., and P. G. van Dokkum. 2012. 'The Stellar Initial Mass Function in Early-type Galaxies From Absorption Line Spectroscopy. II. Results.' ApJ 760, 71 (November): 71.

Crutcher, R. M. 2012. 'Magnetic Fields in Molecular Clouds.' ARA&A 50 (September): 29–63.

de Avillez, M. A., and M.-M. Mac Low. 2001. 'Modelling the Formation of HI Clouds in the Galactic Halo.' In *American Astronomical Society Meeting Abstracts #198*, 33:875. Bulletin of the American Astronomical Society. May.

Dehnen, W., and H. Aly. 2012. 'Improving convergence in smoothed particle hydrodynamics simulations without pairing instability.' MNRAS 425 (September): 1068–1082.

Delgado-Donate, E. J., C. J. Clarke, M. R. Bate, and S. T. Hodgkin. 2004. 'On the properties of young multiple stars.' MNRAS 351 (June): 617–629.

Dobbs, C. L., S. C. O. Glover, P. C. Clark, and R. S. Klessen. 2008. 'The ISM in spiral galaxies: can cooling in spiral shocks produce molecular clouds?' MNRAS 389 (September): 1097–1110.

Dobbs, C. L., and D. J. Price. 2008. 'Magnetic fields and the dynamics of spiral galaxies.' MNRAS 383 (January): 497–512.

Duchêne, G. 1999. 'Binary fraction in low-mass star forming regions: a reexamination of the possible excesses and implications.' A&A 341 (January): 547–552.

Duchêne, G., J. Bouvier, S. Bontemps, P. André, and F. Motte. 2004. 'Multiple protostellar systems. I. A deep near infrared survey of Taurus and Ophiuchus protostellar objects.' A&A 427 (November): 651–665.

Duchêne, G., et al. 2007. 'Multiple protostellar systems. II. A high resolution near-infrared imaging survey in nearby star-forming regions.' A&A 476 (December): 229–242.

Dunham, M. M., et al. 2013. 'The Luminosities of Protostars in the Spitzer c2d and Gould Belt Legacy Clouds.' AJ 145, 94 (April): 94.

Duquennoy, A., and M. Mayor. 1991. 'Multiplicity among solar-type stars in the solar neighbourhood. II - Distribution of the orbital elements in an unbiased sample.' A&A 248 (August): 485–524.

Elmegreen, B. G. 1987. 'Supercloud formation by nonaxisymmetric gravitational instabilities in sheared magnetic galaxy disks.' ApJ 312 (January): 626–639.

Elmegreen, B. G., R. S. Klessen, and C. D. Wilson. 2008. 'On the Constancy of the Characteristic Mass of Young Stars.' ApJ 681, 365-374 (July): 365–374.

Evans, N. J., II, et al. 2009. 'The Spitzer c2d Legacy Results: Star-Formation Rates and Efficiencies; Evolution and Lifetimes.' ApJS 181 (April): 321–350.

Fehlberg, E. 1969. 'Low-Order Classical Runge-Kutta Formulas with Stepsize Control and Their Application to Some Heat Transfer Problems.' *NASA Technical Report R-315.*

Fischer, D. A., and G. W. Marcy. 1992. 'Multiplicity among M dwarfs.' ApJ 396 (September): 178–194.

Frank, A., et al. 2014. 'Jets and Outflows from Star to Cloud: Observations Confront Theory.' *Protostars and Planets VI:*451–474.

Fukui, Y., and A. Kawamura. 2010. 'Molecular Clouds in Nearby Galaxies.' ARA&A 48 (September): 547–580.

Gammie, C. F. 1996. 'Linear Theory of Magnetized, Viscous, Self-gravitating Gas Disks.' ApJ 462 (May): 725.

Ghez, A. M., G. Neugebauer, and K. Matthews. 1993. 'The multiplicity of T Tauri stars in the star forming regions Taurus-Auriga and Ophiuchus-Scorpius: A 2.2 micron speckle imaging survey.' AJ 106 (November): 2005–2023.

Gingold, R. A., and J. J. Monaghan. 1977. 'Smoothed particle hydrodynamics - Theory and application to non-spherical stars.' MNRAS 181 (November): 375–389.

Goldreich, P., and D. Lynden-Bell. 1965. 'I. Gravitational stability of uniformly rotating disks.' MNRAS 130:97.

Gómez, G. C., and E. Vázquez-Semadeni. 2014. 'Filaments in Simulations of Molecular Cloud Formation.' ApJ 791, 124 (August): 124.

Gomez, M., L. Hartmann, S. J. Kenyon, and R. Hewett. 1993. 'On the spatial distribution of pre-main-sequence stars in Taurus.' AJ 105 (May): 1927–1937.

Goodwin, S. P., A. P. Whitworth, and D. Ward-Thompson. 2004a. 'An explanation for the unusual IMF in Taurus.' A&A 419 (May): 543–547.

———. 2004b. 'Simulating star formation in molecular cloud cores. I. The influence of low levels of turbulence on fragmentation and multiplicity.' A&A 414 (February): 633–650.

———. 2004c. 'Simulating star formation in molecular cores. II. The effects of different levels of turbulence.' A&A 423 (August): 169–182.

———. 2006. 'Star formation in molecular cores. III. The effect of the turbulent power spectrum.' A&A 452 (June): 487–492.

Gordon, M. A., and W. B. Burton. 1976. 'Carbon monoxide in the Galaxy. I - The radial distribution of CO, H2, and nucleons.' ApJ 208 (September): 346–353.

Gould, R. J., and E. E. Salpeter. 1963. 'The Interstellar Abundance of the Hydrogen Molecule. I. Basic Processes.' ApJ 138 (August): 393.

Greissl, J., et al. 2007. 'Hubble Space Telescope NICMOS Observations of NGC 1333: The Ratio of Stars to Substellar Objects.' AJ 133 (April): 1321–1330.

Hartmann, L., P. Cassen, and S. J. Kenyon. 1997. 'Disk Accretion and the Stellar Birthline.' ApJ 475 (February): 770–785.

Hatchell, J., et al. 2013. 'The JCMT Gould Belt Survey: SCUBA-2 observations of radiative feedback in NGC 1333.' MNRAS 429 (February): L10–L14.

Hennebelle, P., and S. Fromang. 2008. 'Magnetic processes in a collapsing dense core. I. Accretion and ejection.' A&A 477 (January): 9–24.

Herbig, G. H. 1977. 'Radial velocities and spectral types of T Tauri stars.' ApJ 214 (June): 747–758.

Heyer, M. H., J. M. Carpenter, and R. L. Snell. 2001. 'The Equilibrium State of Molecular Regions in the Outer Galaxy.' ApJ 551 (April): 852–866.

Heyer, M., C. Krawczyk, J. Duval, and J. M. Jackson. 2009. 'Re-Examining Larson's Scaling Relationships in Galactic Molecular Clouds.' ApJ 699 (July): 1092–1103.

Hill, T., et al. 2011. 'Filaments and ridges in Vela C revealed by Herschel: from low-mass to high-mass star-forming sites.' A&A 533, A94 (September): A94.

Hillenbrand, L. A. 2009. 'Age-related observations of low mass pre-main and young main sequence stars.' In *The Ages of Stars,* edited by E. E. Mamajek, D. R. Soderblom, and R. F. G. Wyse, 258:81–94. IAU Symposium. June.

Hosokawa, T., S. S. R. Offner, and M. R. Krumholz. 2011. 'On the Reliability of Stellar Ages and Age Spreads Inferred from Pre-main-sequence Evolutionary Models.' ApJ 738, 140 (September): 140.

Hosokawa, T., and K. Omukai. 2009. 'Evolution of Massive Protostars with High Accretion Rates.' ApJ 691 (January): 823–846.

Hubber, D. A., S. P. Goodwin, and A. P. Whitworth. 2006. 'Resolution requirements for simulating gravitational fragmentation using SPH.' A&A 450 (May): 881–886.

Hubber, D. A., S. Walch, and A. P. Whitworth. 2013. 'An improved sink particle algorithm for SPH simulations.' MNRAS 430 (April): 3261–3275.

Inutsuka, S.-I., and S. M. Miyama. 1992. 'Self-similar solutions and the stability of collapsing isothermal filaments.' ApJ 388 (April): 392–399.

Janson, M., et al. 2012. 'The AstraLux Large M-dwarf Multiplicity Survey.' ApJ 754, 44 (July): 44.

Jappsen, A.-K., R. S. Klessen, R. B. Larson, Y. Li, and M.-M. Mac Low. 2005. 'The stellar mass spectrum from non-isothermal gravoturbulent fragmentation.' A&A 435 (May): 611–623.

Jeans, J. H. 1902. 'The Stability of a Spherical Nebula.' *Philosophical Transactions of the Royal Society of London Series A* 199:1–53.

Johnstone, D., J. Di Francesco, and H. Kirk. 2004. 'An Extinction Threshold for Protostellar Cores in Ophiuchus.' ApJL 611 (August): L45–L48.

Johnstone, D., et al. 2000. 'Large-Area Mapping at 850 Microns. II. Analysis of the Clump Distribution in the ρ Ophiuchi Molecular Cloud.' ApJ 545 (December): 327–339.

Jones, M. O., and M. R. Bate. 2018. 'The dependence of stellar properties on initial cloud density.' MNRAS (May).

Jubelgas, M., V. Springel, and K. Dolag. 2004. 'Thermal conduction in cosmological SPH simulations.' MNRAS 351 (June): 423–435.

Julian, W. H., and A. Toomre. 1966. 'Non-Axisymmetric Responses of Differentially Rotating Disks of Stars.' ApJ 146 (December): 810.

Kennicutt, R. C., Jr. 1989. 'The star formation law in galactic disks.' ApJ 344 (September): 685–703.

———. 1998. 'The Global Schmidt Law in Star-forming Galaxies.' ApJ 498 (May): 541–552.

Kenyon, S. J., L. W. Hartmann, K. M. Strom, and S. E. Strom. 1990. 'An IRAS survey of the Taurus-Auriga molecular cloud.' AJ 99 (March): 869–887.

Kenyon, S. J., I. Yi, and L. Hartmann. 1996. 'A Magnetic Accretion Disk Model for the Infrared Excesses of T Tauri Stars.' ApJ 462 (May): 439.

Kim, W.-T., and E. C. Ostriker. 2001. 'Amplification, Saturation, and Q Thresholds for Runaway: Growth of Self-Gravitating Structures in Models of Magnetized Galactic Gas Disks.' ApJ 559 (September): 70–95.

———. 2002. 'Formation and Fragmentation of Gaseous Spurs in Spiral Galaxies.' ApJ 570 (May): 132–151.

———. 2006. 'Formation of Spiral-Arm Spurs and Bound Clouds in Vertically Stratified Galactic Gas Disks.' ApJ 646 (July): 213–231.

Kippenhahn, R., and A. Weigert. 1990. *Stellar Structure and Evolution,* 192.

Klessen, R. S. 2001. 'The Formation of Stellar Clusters: Mass Spectra from Turbulent Molecular Cloud Fragmentation.' ApJ 556 (August): 837–846.

Klessen, R. S., and A. Burkert. 2000. 'The Formation of Stellar Clusters: Gaussian Cloud Conditions. I.' ApJS 128 (May): 287–319.

Klessen, R. S., A. Burkert, and M. R. Bate. 1998. 'Fragmentation of Molecular Clouds: The Initial Phase of a Stellar Cluster.' ApJL 501 (July): L205–L208.

Kouwenhoven, M. B. N., A. G. A. Brown, S. F. Portegies Zwart, and L. Kaper. 2007. 'The primordial binary population. II.. Recovering the binary population for intermediate mass stars in Scorpius OB2.' A&A 474 (October): 77–104.

Kroupa, P. 2001. 'On the variation of the initial mass function.' MNRAS 322 (April): 231–246.

Krumholz, M. R. 2011. 'On the Origin of Stellar Masses.' ApJ 743, 110 (December): 110.

Krumholz, M. R., R. I. Klein, and C. F. McKee. 2007. 'Radiation-Hydrodynamic Simulations of Collapse and Fragmentation in Massive Protostellar Cores.' ApJ 656 (February): 959–979.

Krumholz, M. R., and C. D. Matzner. 2009. 'The Dynamics of Radiation-pressure-dominated H II Regions.' ApJ 703 (October): 1352–1362.

Kwan, J., and F. Valdes. 1983. 'Spiral gravitational potentials and the mass growth of molecular clouds.' ApJ 271 (August): 604–610.

Lada, C. J. 1976. 'Detailed observations of the M17 molecular cloud complex.' ApJS 32 (October): 603–629.

Lada, C. J., and E. A. Lada. 2003. 'Embedded Clusters in Molecular Clouds.' ARA&A 41:57–115.

Lada, E. A. 1999. 'The Role of Embedded Clusters in Star Formation.' In *NATO Advanced Science Institutes (ASI) Series C,* edited by C. J. Lada and N. D. Kylafis, 540:441. NATO Advanced Science Institutes (ASI) Series C.

Lada, E. A., D. L. Depoy, N. J. Evans II, and I. Gatley. 1991. 'A 2.2 micron survey in the L1630 molecular cloud.' ApJ 371 (April): 171–182.

Lagattuta, D. J., et al. 2017. 'Evidence of a Bottom-heavy Initial Mass Function in Massive Early-type Galaxies from Near-infrared Metal Lines.' ApJ 846, 166 (September): 166.

Lamers, H. J. G. L. M., and J. P. Cassinelli. 1999. *Introduction to Stellar Winds,* 452. June.

Langer, N., M. F. El Eid, and I. Baraffe. 1989. 'Blue supergiant supernova progenitors.' A&A 224 (October): L17–L20.

Larson, R. B. 1969. 'Numerical calculations of the dynamics of collapsing proto-star.' MNRAS 145:271.

———. 1981. 'Turbulence and star formation in molecular clouds.' MNRAS 194 (March): 809–826.

———. 1998. 'Early star formation and the evolution of the stellar initial mass function in galaxies.' MNRAS 301 (December): 569–581.

———. 2005. 'Thermal physics, cloud geometry and the stellar initial mass function.' MNRAS 359 (May): 211–222.

Leinert, C., et al. 1993. 'A systematic approach for young binaries in Taurus.' A&A 278 (October): 129–149.

Levermore, C. D., and G. C. Pomraning. 1981. 'A flux-limited diffusion theory.' ApJ 248 (August): 321–334.

Liptai, D., D. J. Price, J. Wurster, and M. R. Bate. 2017. 'Does turbulence determine the initial mass function?' MNRAS 465 (February): 105–110.

Lomax, O., A. P. Whitworth, D. A. Hubber, D. Stamatellos, and S. Walch. 2015. 'Simulations of star formation in Ophiuchus - II. Multiplicity.' MNRAS 447 (February): 1550–1564.

Lorén-Aguilar, P., and M. R. Bate. 2014. 'Two-fluid dust and gas mixtures in smoothed particle hydrodynamics: a semi-implicit approach.' MNRAS 443 (September): 927–945.

———. 2015. 'Two-fluid dust and gas mixtures in smoothed particle hydrodynamics II: an improved semi-implicit approach.' MNRAS 454 (December): 4114–4119.

Lovelace, R. V. E., M. M. Romanova, and J. Contopoulos. 1993. 'Theory of jets from young stars.' ApJ 403 (January): 158–163.

Low, C., and D. Lynden-Bell. 1976. 'The minimum Jeans mass or when fragmentation must stop.' MNRAS 176 (August): 367–390.

Lucy, L. B. 1977. 'A numerical approach to the testing of the fission hypothesis.' AJ 82 (December): 1013–1024.

Luhman, K. L. 2007. 'The Stellar Population of the Chamaeleon I Star-forming Region.' ApJS 173 (November): 104–136.

Luhman, K. L., T. L. Esplin, and N. P. Loutrel. 2016. 'A Census of Young Stars and Brown Dwarfs in IC 348 and NGC 1333.' ApJ 827, 52 (August): 52.

Luhman, K. L., et al. 2003. 'New Low-Mass Members of the Taurus Star-forming Region.' ApJ 590 (June): 348–356.

Lynden-Bell, D. 1966. 'The role of magnetism in spiral structure.' *The Observatory* 86 (April): 57–60.

Mac Low, M.-M., R. S. Klessen, A. Burkert, and M. D. Smith. 1998. 'Kinetic Energy Decay Rates of Supersonic and Super-Alfvénic Turbulence in Star-Forming Clouds.' *Physical Review Letters* 80 (March): 2754–2757.

Machida, M. N., S.-i. Inutsuka, and T. Matsumoto. 2006. 'Second Core Formation and High-Speed Jets: Resistive Magnetohydrodynamic Nested Grid Simulations.' ApJL 647 (August): L151–L154.

———. 2008. 'High- and Low-Velocity Magnetized Outflows in the Star Formation Process in a Gravitationally Collapsing Cloud.' ApJ 676 (April): 1088–1108.

Machida, M. N., T. Matsumoto, T. Hanawa, and K. Tomisaka. 2005. 'Collapse and fragmentation of rotating magnetized clouds - II. Binary formation and fragmentation of first cores.' MNRAS 362 (September): 382–402.

Magnani, L., L. Blitz, and L. Mundy. 1985. 'Molecular gas at high Galactic latitudes.' ApJ 295 (August): 402–421.

Mason, B. D., W. I. Hartkopf, D. R. Gies, T. J. Henry, and J. W. Helsel. 2009. 'The High Angular Resolution Multiplicity of Massive Stars.' AJ 137 (February): 3358–3377.

Mason, B. D., et al. 1998. 'ICCD speckle observations of binary stars. XIX - an astrometric/spectroscopic survey of O stars.' AJ 115 (February): 821.

Mathieu, R. D. 1992. 'The eccentricity distribution of pre-main sequence binaries.' In *Binaries as Tracers of Star Formation*, edited by A. Duquennoy and M. Mayor, 155–169.

McCray, R., and M. Kafatos. 1987. 'Supershells and propagating star formation.' ApJ 317 (June): 190–196.

McCrea, W. H., and D. McNally. 1960. 'The formation of Population I stars, II. The formation of molecular hydrogen in interstellar matter.' MNRAS 121:238.

McDonald, J. M., and C. J. Clarke. 1995. 'The effect of star-disc interactions on the binary mass-ratio distribution.' MNRAS 275 (August): 671–684.

McKee, C. F., and S. S. R. Offner. 2010. 'The Protostellar Mass Function.' ApJ 716 (June): 167–180.

Mellon, R. R., and Z.-Y. Li. 2008. 'Magnetic Braking and Protostellar Disk Formation: The Ideal MHD Limit.' ApJ 681 (July): 1356–1376.

Mestel, L., and L. Spitzer Jr. 1956. 'Star formation in magnetic dust clouds.' MNRAS 116:503.

Mihalas, D., and B. W. Mihalas. 1984. *Foundations of radiation hydrodynamics.*

Monaghan, J. J. 1985. 'Particle methods for hydrodynamics.' *Computer Physics Reports* 3 (October): 71–124.

———. 1992. 'Smoothed particle hydrodynamics.' ARA&A 30:543–574.

———. 2005. 'Smoothed particle hydrodynamics.' *Reports on Progress in Physics* 68 (August): 1703–1759.

Monaghan, J. J., and J. C. Lattanzio. 1985. 'A refined particle method for astrophysical problems.' A&A 149 (August): 135–143.

Morris, J. P., and J. J. Monaghan. 1997. 'A Switch to Reduce SPH Viscosity.' *Journal of Computational Physics* 136 (September): 41–50.

Motte, F., P. Andre, and R. Neri. 1998. 'The initial conditions of star formation in the rho Ophiuchi main cloud: wide-field millimeter continuum mapping.' A&A 336 (August): 150–172.

Mouschovias, T. C. 1974. 'Stable equilibria of the interstellar gas and magnetic field in the galactic gravitational field.' In *Bulletin of the American Astronomical Society*, 6:262–263. BAAS. March.

———. 1976. 'Nonhomologous contraction and equilibria of self-gravitating, magnetic interstellar clouds embedded in an intercloud medium: Star formation. II - Results.' ApJ 207 (July): 141–158.

Mouschovias, T. C., F. H. Shu, and P. R. Woodward. 1974. 'On the Formation of Interstellar Cloud Complexes, OB Associations and Giant H II Regions.' A&A 33 (June): 73.

Myers, P. C., R. A. Linke, and P. J. Benson. 1983. 'Dense cores in dark clouds. I - CO observations and column densities of high-extinction regions.' ApJ 264 (January): 517–537.

Nakano, T., T. Hasegawa, J.-I. Morino, and T. Yamashita. 2000. 'Evolution of Protostars Accreting Mass at Very High Rates: Is Orion IRc2 a Huge Protostar?' ApJ 534 (May): 976–983.

Nakano, T., T. Hasegawa, and C. Norman. 1995. 'The Mass of a Star Formed in a Cloud Core: Theory and Its Application to the Orion A Cloud.' ApJ 450 (September): 183.

Nayakshin, S. 2006. 'Massive stars in subparsec rings around galactic centres.' MNRAS 372 (October): 143–150.

Nayakshin, S., S.-H. Cha, and A. Hobbs. 2009. 'Dynamic Monte Carlo radiation transfer in SPH: radiation pressure force implementation.' MNRAS 397 (August): 1314–1325.

Neuhaeuser, R., M. F. Sterzik, J. H. M. M. Schmitt, R. Wichmann, and J. Krautter. 1995. 'ROSAT survey observation of T Tauri stars in Taurus.' A&A 297 (May): 391.

Offner, S. S. R., R. I. Klein, C. F. McKee, and M. R. Krumholz. 2009. 'The Effects of Radiative Transfer on Low-Mass Star Formation.' ApJ 703 (September): 131–149.

Offner, S. S. R., and C. F. McKee. 2011. 'The Protostellar Luminosity Function.' ApJ 736, 53 (July): 53.

Oka, T., et al. 2001. 'Statistical Properties of Molecular Clouds in the Galactic Center.' ApJ 562 (November): 348–362.

Osterbrock, D. E., and G. J. Ferland. 2006. *Astrophysics of gaseous nebulae and active galactic nuclei.*

Ostriker, E. C., J. M. Stone, and C. F. Gammie. 2001. 'Density, Velocity, and Magnetic Field Structure in Turbulent Molecular Cloud Models.' ApJ 546 (January): 980–1005.

Ostriker, J. P., and C. F. McKee. 1988. 'Astrophysical blastwaves.' *Reviews of Modern Physics* 60:1–68.

Padoan, P., R. Jimenez, M. Juvela, and Å. Nordlund. 2004. 'The Average Magnetic Field Strength in Molecular Clouds: New Evidence of Super-Alfvénic Turbulence.' ApJL 604 (March): L49–L52.

Patience, J., A. M. Ghez, I. N. Reid, and K. Matthews. 2002. 'A High Angular Resolution Multiplicity Survey of the Open Clusters α Persei and Praesepe.' AJ 123 (March): 1570–1602.

Payne, D. G., and R. D. Blandford. 1981. 'Compton scattering in a converging fluid flow. III - Spherical supercritical accretion.' MNRAS 196 (September): 781–795.

Petr, M. G., V. Coudé du Foresto, S. V. W. Beckwith, A. Richichi, and M. J. McCaughrean. 1998. 'Binary Stars in the Orion Trapezium Cluster Core.' ApJ 500 (June): 825–837.

Pollack, J. B., C. P. McKay, and B. M. Christofferson. 1985. 'A calculation of the Rosseland mean opacity of dust grains in primordial solar system nebulae.' 64 (December): 471–492.

Preibisch, T., Y. Balega, K.-H. Hofmann, G. Weigelt, and H. Zinnecker. 1999. 'Multiplicity of the massive stars in the Orion Nebula cluster.' 4 (December): 531–542.

Price, D. J. 2012. 'Smoothed particle hydrodynamics and magnetohydrodynamics.' *Journal of Computational Physics* 231 (February): 759–794.

Price, D. J., and M. R. Bate. 2007. 'The impact of magnetic fields on single and binary star formation.' MNRAS 377 (May): 77–90.

———. 2008. 'The effect of magnetic fields on star cluster formation.' MNRAS 385 (April): 1820–1834.

Price, D. J., and J. J. Monaghan. 2004a. 'Smoothed Particle Magnetohydrodynamics - I. Algorithm and tests in one dimension.' MNRAS 348 (February): 123–138.

Price, D. J., and J. J. Monaghan. 2004b. 'Smoothed Particle Magnetohydrodynamics - II. Variational principles and variable smoothing-length terms.' MNRAS 348 (February): 139–152.

———. 2007. 'An energy-conserving formalism for adaptive gravitational force softening in smoothed particle hydrodynamics and N-body codes.' MNRAS 374 (February): 1347–1358.

Price, D. J., T. S. Tricco, and M. R. Bate. 2012. 'Collimated jets from the first core.' MNRAS 423 (June): L45–L49.

Price, N. M., and P. Podsiadlowski. 1995. 'Dynamical interactions between young stellar objects and a collisional model for the origin of the stellar mass spectrum.' MNRAS 273 (April): 1041–1068.

Pringle, J. E. 1989a. 'A boundary layer origin for bipolar flows.' MNRAS 236 (January): 107–115.

———. 1989b. 'On the formation of binary stars.' MNRAS 239 (July): 361–370.

Raghavan, D., et al. 2010. 'A Survey of Stellar Families: Multiplicity of Solar-type Stars.' ApJS 190 (September): 1–42.

Rees, M. J. 1976. 'Opacity-limited hierarchical fragmentation and the masses of protostars.' MNRAS 176 (September): 483–486.

Reipurth, B., and H. Zinnecker. 1993. 'Visual binaries among pre-main sequence stars.' A&A 278 (October): 81–108.

Richtmyer, R. D., and K. W. Morton. 1967. *Difference methods for initial-value problems.*

Rizzuto, A. C., et al. 2013. 'Long-baseline interferometric multiplicity survey of the Sco-Cen OB association.' MNRAS 436 (December): 1694–1707.

Robitaille, T. P., B. A. Whitney, R. Indebetouw, K. Wood, and P. Denzmore. 2006. 'Interpreting Spectral Energy Distributions from Young Stellar Objects. I. A Grid of 200,000 YSO Model SEDs.' ApJS 167 (December): 256–285.

Rogers, F. J., and C. A. Iglesias. 1992. 'Radiative atomic Rosseland mean opacity tables.' ApJS 79 (April): 507–568.

Salpeter, E. E. 1955. 'The Luminosity Function and Stellar Evolution.' ApJ 121 (January): 161.

Saumon, D. 1990. 'A Hydrogen Equation of State for Astrophysical Applications.' PhD diss., THE UNIVERSITY OF ROCHESTER.

Saumon, D., and G. Chabrier. 1991. 'Fluid hydrogen at high density - Pressure dissociation.' Phys. Rev. A 44 (October): 5122–5141.

———. 1992. 'Fluid hydrogen at high density - Pressure ionization.' Phys. Rev. A 46 (August): 2084–2100.

Scally, A., C. Clarke, and M. J. McCaughrean. 1999. 'Wide binaries in the Orion nebula cluster.' MNRAS 306 (June): 253–256.

Scoville, N. Z., and P. M. Solomon. 1975. 'Molecular clouds in the Galaxy.' ApJL 199 (July): L105–L109.

Shu, F. H. 1977. 'Self-similar collapse of isothermal spheres and star formation.' ApJ 214 (June): 488–497.

Shu, F. H., F. C. Adams, and S. Lizano. 1987. 'Star formation in molecular clouds - Observation and theory.' ARA&A 25:23–81.

Sicilia-Aguilar, A., et al. 2013. 'Protostars, multiplicity, and disk evolution in the Corona Australis region: a Herschel Gould Belt Study.' A&A 551, A34 (March): A34.

Simon, M., et al. 1995. 'A lunar occultation and direct imaging survey of multiplicity in the Ophiuchus and Taurus star-forming regions.' ApJ 443 (April): 625–637.

Smith, R. J., S. Longmore, and I. Bonnell. 2009. 'The simultaneous formation of massive stars and stellar clusters.' MNRAS 400 (December): 1775–1784.

Snell, R. L., L. G. Mundy, P. F. Goldsmith, N. J. Evans II, and N. R. Erickson. 1984. 'Models of molecular clouds. I - Multitransition study of CS.' ApJ 276 (January): 625–645.

Solomon, P. M., A. R. Rivolo, J. Barrett, and A. Yahil. 1987. 'Mass, luminosity, and line width relations of Galactic molecular clouds.' ApJ 319 (August): 730–741.

Spiniello, C., S. C. Trager, L. V. E. Koopmans, and Y. P. Chen. 2012. 'Evidence for a Mild Steepening and Bottom-heavy Initial Mass Function in Massive Galaxies from Sodium and Titanium-oxide Indicators.' ApJL 753, L32 (July): L32.

Spitzer, L., Jr. 1949. 'The Temperature of Interstellar Matter. II.' ApJ 109 (May): 337.

Stamatellos, D., D. A. Hubber, and A. P. Whitworth. 2007. 'Brown dwarf formation by gravitational fragmentation of massive, extended protostellar discs.' MNRAS 382 (November): L30–L34.

Stamatellos, D., and A. P. Whitworth. 2005. 'Monte Carlo radiative transfer in SPH density fields.' A&A 439 (August): 153–158.

———. 2009. 'The role of thermodynamics in disc fragmentation.' MNRAS 400 (December): 1563–1573.

Stamatellos, D., A. P. Whitworth, and D. A. Hubber. 2011. 'The Importance of Episodic Accretion for Low-mass Star Formation.' ApJ 730, 32 (March): 32.

———. 2012. 'Episodic accretion, protostellar radiative feedback, and their role in low-mass star formation.' MNRAS 427 (December): 1182–1193.

Strittmatter, P. A. 1966. 'Gravitational collapse in the presence of a magnetic field.' MNRAS 132:359.

Tan, J. C., and C. F. McKee. 2004. 'The Formation of the First Stars. I. Mass Infall Rates, Accretion Disk Structure, and Protostellar Evolution.' ApJ 603 (March): 383–400.

Tasker, E. J., and J. C. Tan. 2009. 'Star Formation in Disk Galaxies. I. Formation and Evolution of Giant Molecular Clouds via Gravitational Instability and Cloud Collisions.' ApJ 700 (July): 358–375.

Testi, L., A. I. Sargent, L. Olmi, and J. S. Onello. 2000. 'Star Formation in Clusters: Early Subclustering in the Serpens Core.' ApJL 540 (September): L53–L56.

Tobin, J. J., et al. 2016. 'The VLA Nascent Disk and Multiplicity Survey of Perseus Protostars (VANDAM). II. Multiplicity of Protostars in the Perseus Molecular Cloud.' ApJ 818, 73 (February): 73.

Tomida, K., et al. 2010. 'Radiation Magnetohydrodynamics Simulation of Proto-stellar Collapse: Two-component Molecular Outflow.' ApJL 714 (May): L58–L63.

Tomisaka, K. 2002. 'Collapse of Rotating Magnetized Molecular Cloud Cores and Mass Outflows.' ApJ 575 (August): 306–326.

Tout, C. A., M. Livio, and I. A. Bonnell. 1999. 'The ages of pre-main-sequence stars.' MNRAS 310 (December): 360–376.

Tout, C. A., and J. E. Pringle. 1992. 'Accretion disc viscosity - A simple model for a magnetic dynamo.' MNRAS 259 (December): 604–612.

Treu, T., et al. 2010. 'The Initial Mass Function of Early-Type Galaxies.' ApJ 709 (February): 1195–1202.

Truelove, J. K., et al. 1997. 'The Jeans Condition: A New Constraint on Spatial Resolution in Simulations of Isothermal Self-gravitational Hydrodynamics.' ApJL 489 (November): L179–L183.

Truelove, J. K., et al. 1998. 'Self-gravitational Hydrodynamics with Three-dimensional Adaptive Mesh Refinement: Methodology and Applications to Molecular Cloud Collapse and Fragmentation.' ApJ 495 (March): 821–852.

Tsukamoto, Y., K. Iwasaki, S. Okuzumi, M. N. Machida, and S. Inutsuka. 2015a. 'Bimodality of Circumstellar Disk Evolution Induced by the Hall Current.' ApJL 810, L26 (September): L26.

———. 2015b. 'Effects of Ohmic and ambipolar diffusion on formation and evolution of first cores, protostars, and circumstellar discs.' MNRAS 452 (September): 278–288.

Urban, A., N. J. Evans II, and S. D. Doty. 2009. 'A Parameter Study of the Dust and Gas Temperature in a Field of Young Stars.' ApJ 698, 1341-1356 (June): 1341–1356.

Urban, A., H. Martel, and N. J. Evans II. 2010. 'Fragmentation and Evolution of Molecular Clouds. II. The Effect of Dust Heating.' ApJ 710, 1343-1364 (February): 1343–1364.

van Kempen, T. A., et al. 2009a. 'APEX-CHAMP$^+$ high-J CO observations of low-mass young stellar objects. I. The HH 46 envelope and outflow.' A&A 501 (July): 633–646.

van Kempen, T. A., et al. 2009b. 'APEX-CHAMP$^+$ high-J CO observations of low-mass young stellar objects. II. Distribution and origin of warm molecular gas.' A&A 507 (December): 1425–1442.

van Kempen, T. A., et al. 2010. 'Origin of the hot gas in low-mass protostars. Herschel-PACS spectroscopy of HH 46.' A&A 518, L121 (July): L121.

Vazquez-Semadeni, E., T. Passot, and A. Pouquet. 1995. 'A turbulent model for the interstellar medium. 1: Threshold star formation and self-gravity.' ApJ 441 (March): 702–725.

Visser, R., et al. 2012. 'Modelling Herschel observations of hot molecular gas emission from embedded low-mass protostars.' A&A 537, A55 (January): A55.

Vorobyov, E. I., I. Baraffe, T. Harries, and G. Chabrier. 2013. 'The effect of episodic accretion on the phase transition of CO and CO_2 in low-mass star formation.' A&A 557, A35 (September): A35.

Vorobyov, E. I., and S. Basu. 2010. 'The Burst Mode of Accretion and Disk Fragmentation in the Early Embedded Stages of Star Formation.' ApJ 719 (August): 1896–1911.

Wakelam, V., et al. 2017. 'H_2 formation on interstellar dust grains: The viewpoints of theory, experiments, models and observations.' *Molecular Astrophysics* 9 (December): 1–36.

Wardle, M., and A. Koenigl. 1993. 'The structure of protostellar accretion disks and the origin of bipolar flows.' ApJ 410 (June): 218–238.

Weidner, C., and P. Kroupa. 2006. 'The maximum stellar mass, star-cluster formation and composite stellar populations.' MNRAS 365 (February): 1333–1347.

Whitehouse, S. C., and M. R. Bate. 2004. 'Smoothed particle hydrodynamics with radiative transfer in the flux-limited diffusion approximation.' MNRAS 353 (October): 1078–1094.

———. 2006. 'The thermodynamics of collapsing molecular cloud cores using smoothed particle hydrodynamics with radiative transfer.' MNRAS 367 (March): 32–38.

Whitehouse, S. C., M. R. Bate, and J. J. Monaghan. 2005. 'A faster algorithm for smoothed particle hydrodynamics with radiative transfer in the flux-limited diffusion approximation.' MNRAS 364 (December): 1367–1377.

Whitworth, A. P. 1998. 'The Jeans instability in smoothed particle hydrodynamics.' MNRAS 296 (May): 442–444.

Wichmann, R., et al. 1997. 'The T Tauri star population in the Lupus star forming region.' A&A 320 (April): 185–195.

Wiseman, J. J., and P. T. P. Ho. 1996. 'Heated gaseous streamers and star formation in the Orion molecular cloud.' Nature 382 (July): 139–141.

Wurster, J., M. R. Bate, and D. J. Price. 2018. 'The collapse of a molecular cloud core to stellar densities using radiation non-ideal magnetohydrodynamics.' MNRAS 475 (April): 1859–1880.

Wurster, J., D. J. Price, and M. R. Bate. 2016. 'Can non-ideal magnetohydrodynamics solve the magnetic braking catastrophe?' MNRAS 457 (March): 1037–1061.

———. 2017. 'The impact of non-ideal magnetohydrodynamics on binary star formation.' MNRAS 466 (April): 1788–1804.

Yıldız, U. A., et al. 2012. 'APEX-CHAMP$^+$ high-J CO observations of low-mass young stellar objects. III. NGC 1333 IRAS 4A/4B envelope, outflow, and ultraviolet heating.' A&A 542, A86 (June): A86.

Zhu, Z., L. Hartmann, and C. Gammie. 2009. 'Nonsteady Accretion in Protostars.' ApJ 694 (April): 1045–1055.

———. 2010. 'Long-term Evolution of Protostellar and Protoplanetary Disks. II. Layered Accretion with Infall.' ApJ 713 (April): 1143–1158.

Zinnecker, H. 1982. 'Prediction of the protostellar mass spectrum in the Orion near-infrared cluster.' *Annals of the New York Academy of Sciences* 395 (October): 226–235.